*Author:*
**Phelps, Ryan A**

*Title:*
**Exploring the Role of Solvents on the Chemical Dynamics of Reactive Intermediates using Ultrafast Transient Absorption Spectroscopy**

# Exploring the Role of Solvents on the Chemical Dynamics of Reactive Intermediates using Ultrafast Transient Absorption Spectroscopy


Ryan Phelps

A dissertation submitted to the University of Bristol in accordance with the requirements for award of the degree of Doctor of Philosophy in the Faculty of Science.

School of Chemistry

March 2021

Words count: ~48,000

**Abstract**

The research reported in this thesis explores how different types of solvent-solute interactions influence photochemical outcomes. The research combines ultrafast transient absorption spectroscopy (TAS) measurements with quantum chemical calculations to unravel competing reaction pathways for three chemical systems.

The ultraviolet (UV) photoexcitation of α-diazocarbonyl compounds produces ketenes by both concerted and stepwise Wolff rearrangements. The stepwise mechanism proceeds through singlet carbene intermediates which can also participate in bimolecular reactions. Transient absorption spectra provide direct evidence for competitive production of singlet α-carbonyl carbene and ketene intermediates, with ylide formation by carbene capture in aprotic nucleophilic solvents. A new enol-mediated pathway is identified in reactions of singlet α-carbonyl carbenes with alcohols, and a computed two-dimensional cut of the potential energy surface for the reaction with methanol shows that the enol forms without a barrier. This pathway is promoted by an intermolecular hydrogen bond from methanol to the carbonyl oxygen atom of the singlet α-carbonyl carbene.

Because of the zwitterionic character of ylides, they interact strongly with polar solvent molecules. Ultrafast TAS reveals the specific solvation dynamics of a tetrahydrofuran-derived ylide with various hydrogen-bond donor solvents. The specific interaction of ethanol with the ylide is further characterised using quantum chemical calculations and atom-centred density matrix propagation trajectories which show preferential hydrogen-bonding to an α-carbonyl group.

The final system studied by ultrafast TAS is the 255-nm UV photoexcitation of 2-aminothiazole, revealing competing N-H cleavage and heterocyclic ring-opening pathways. In non-polar solvents, the TAS data indicate that N-H cleavage outcompetes the ring-opening pathways. In contrast, polar solvents are shown to inhibit N-H fission, and ring-opening is the preferred pathway to photoproducts. Initial quantum chemical calculations suggest the height of the barrier to access the dissociative $\pi\sigma^*$ $S_1$-state responsible for N-H bond scission is highly sensitive to the solvent and controls the product branching.

## Acknowledgements

I would like to thank all those past and present at Bristol who have encouraged and supported me. I would like to thank my supervisor Andrew Orr-Ewing for not just his teachings, but for his belief and support in my work.

I would also like to take this time to thank Georgia Thornton. Her consistent encouragement and friendship throughout this PhD will always be treasured.

*"Sucking at something is the first step towards being sort-of good at something" – Jake the dog*

I declare that the work in this dissertation was carried out in accordance with the requirements of the University's *Regulations and Code of Practice for Research Degree Programmes* and that it has not been submitted for any other academic award. Except where indicated by specific reference in the text, the work is the candidate's own work. Work done in collaboration with, or with the assistance of, others, is indicated as such. Any views expressed in the dissertation are those of the author.

SIGNED: Ryan Phelps DATE: 22/03/2021

# Contents

# List of Figures

# List of Schemes

# List of Tables

# List of Abbreviations

| | |
|---|---|
| 2-Aminothiazole | 2-AT |
| 2-Iminothiazole | 2-IT |
| 5-Diazomeldrum acid | DMA |
| Absolute phase | ABS |
| Acetonitrile | ACN |
| Acetonitrile-ylide | ACN-Y |
| Barium borate | BBO |
| Beam splitter | BS |
| Conical intersection | CI |
| Coupled Cluster | CC |
| Coupled Cluster single, double and MP2 triple excitations | CCSD(T) |
| Density function theory | DFT |
| Diazonapthoquinone | DNQ |
| Dichloromethane | DCM |
| Difference frequency generation | DFG |
| Diphenlmethylene | DPM |
| Ethanol | EtOH |
| Ethanol-ylide | EtOH-Y |
| Ethyl Diazoacetate | EDA |
| Ethyl Diazoacetoacetate | EDAA |
| Excited state H-atom transfer | ESHT |
| Fourth order Perturbation | MP4 |
| Generalised gradient approximation | GGA |
| Ground state bleach | GSB |
| Group delay dispersion | GDP |
| Hartree-Fock | HF |
| Hydrogen bonded EDA | HB-EDA |
| Infrared | IR |
| Kohn-Sham orbitals | KS-orbitals |
| Local density approximation | LDA |
| Mercury cadmium telluride | MCT |
| Methanol | MeOH |
| Methanol-ylide | MeOH-Y |
| Möller-Plesset perturbation | MP |
| Optical parametric amplification | OPA |
| Photodiode | PD |
| Pockels cell | PC |
| Potential energy surface | PES |
| Synchronization and delay generator | SDG |
| Second harmonic generation | SHG |
| Second order Perturbation | MP2 |
| Sum frequency generation | SFG |
| Tertiary-butanol | t-BuOH |
| Tetrahydrofuran | THF |

| | |
|---|---|
| Tetrahydrofuran-ylide | THF-Y |
| Third order dispersion | TOD |
| Third order Perturbation | MP3 |
| Time independent Schrodinger equation | TISE |
| Time-dependent DFT | TD-DFT |
| Transient absorption spectroscopy | TAS |
| Transient electronic absorption spectroscopy | TEAS |
| Transient vibrational absorption spectroscopy | TVAS |
| Ultraviolet | UV |
| Visible | Vis |
| White light continuum | WLC |
| Wolff rearrangement | WR |
| X-ray transient absorption spectroscopy | XTAS |

# Chapter 1. Introduction

The photochemistry of molecules can often be rationalised in terms of their evolution along one or more potential energy surfaces (PESs) corresponding to different electronic states. Recent advances in theoretical modelling using quantum chemistry methods enable accurate predictions of ground and excited state properties of molecules, and can be used to predict outcomes and strengthen understanding about the photochemistry of molecules. In this thesis, the chemical dynamics of reactive intermediates and excited states formed photolytically are studied using ultrafast transient absorption spectroscopy (TAS), and these experimental measurements are complemented with theoretical calculations. To establish the background to these studies, this chapter introduces the topic of photochemistry and its study using ultrafast spectroscopic methods, the principle of the PES for describing the topography of the energy landscape over which chemical dynamics occur, and the use of theoretical methods for the computation of molecular properties.

## 1.1 Photochemistry

The field of photochemistry deals with the reactive and dynamical events that occur in molecules because of the excitation of discrete energy levels by absorption of a photon. Typically, transitions between energy levels are described as either electronic, vibrational, rotational, or nuclear and can be induced by absorption of light in the ultraviolet and visible (UV-Vis, 100 – 800 nm), infrared (IR, ~ 800 nm – 1 mm), microwave (~ 1 mm – 1 m) and radiowave (> 1 m) regions. However, coupling between transitions is a well-known phenomenon, such as the coupling between electronic, vibrational and rotational transitions, termed a ro-vibronic transition. The absorption of UV-Vis photons is of particular interest due to the rich chemistry that can be induced by promotion of electrons to higher energy orbitals, with some of these photochemical processes illustrated in Figure 1.1.[1] However, evidence exists that IR pulses can also promote chemical reactivity.[2]

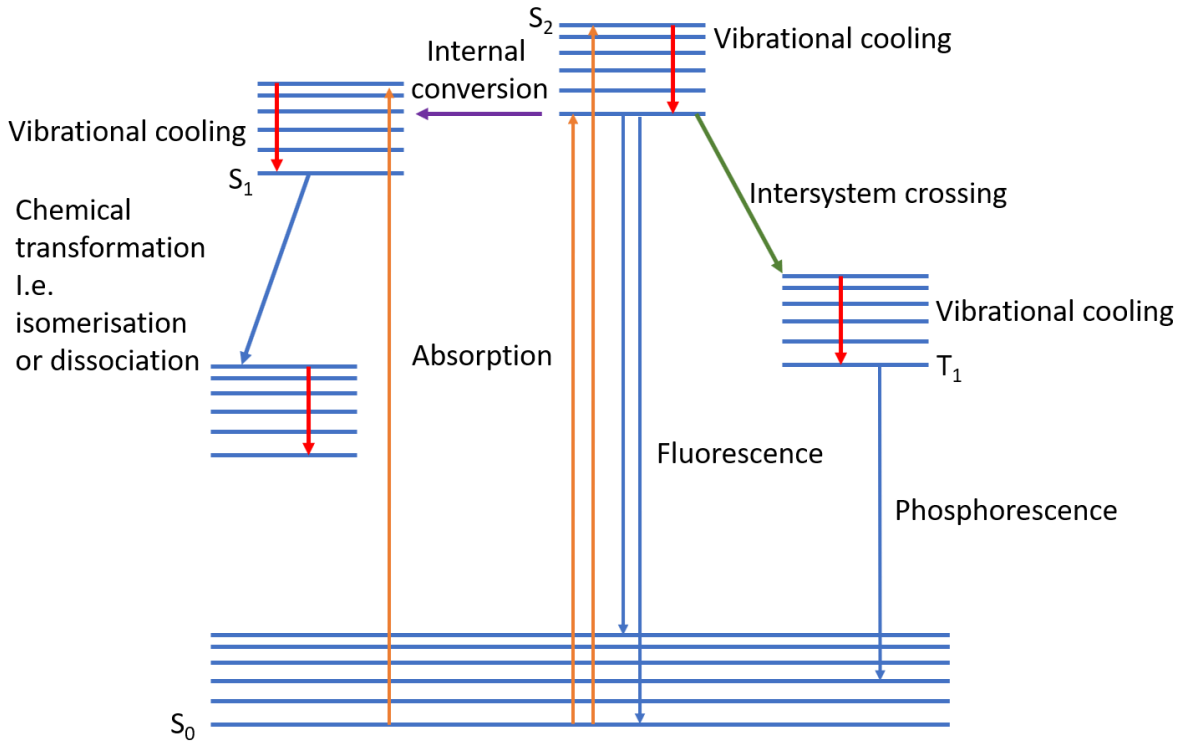


Figure 1.1 – Jablonski diagram showing various photochemical processes.

The use of light to induce chemistry is common throughout our universe. Molecules ranging from diatomics to large and complex polyatomics have been found to be ubiquitous in interstellar space despite surrounding temperatures which can be as low as ~10 K in molecular clouds.[3] Much of this chemistry is now thought to occur after photoexcitation, and large efforts are being made to unravel the mechanistic steps which give rise to the rich molecular universe.[4-6] Here on Earth, the sun provides a broad-wavelength source of light, emitting electromagnetic radiation from X-rays (~ 1 nm) to radiowaves (> 1 m),[7-9] forming high energy reactive intermediates which are thought to be fundamental to planetary atmospheres,[10] emergence of life on earth,[11-12] and photosynthesis.[13]

Today, photochemistry is in common use across synthetic chemistry laboratories, industrial processes, and technology, and its applications are the topic of numerous photosynthetic chemistry reviews.[14-17] The principles behind photochemistry are often used for the generation of reactive intermediates.[18] Still today, novel photochemical reaction pathways are being reported, with an aim to overcome great challenges in efficiency and selectivity.[19-22] A significant driving force for utilising light in chemical reactions is that it offers a more environmentally sustainable approach compared to the use of heavy metal catalysts.

The understanding about the mechanistic steps which lead to the generation of reactive intermediates is therefore paramount to improving and developing reactive processes and technology. To directly observe the mechanistic steps, various spectroscopy methods are frequently employed.

Since the field of spectroscopy deals with studying molecules by their interaction with electromagnetic radiation, it is not surprisingly a powerful and common technique in studying photochemistry. Spectroscopic experiments range from utilising high-energy X-rays to radiowaves to probe the various energy levels of a system which can be used as chemical signatures for the identification of photoproducts. Until the advent of flash photolysis,[23-24] spectroscopy methods were unable to probe short-lived excited states and intermediates, and these species were instead postulated on the basis of observed chemical outcomes. The more-recent development of ultrashort laser pulses has opened-up the possibility of a new wealth of experimental information that can be gained about reaction intermediates.[25]

### 1.2 Ultrafast spectroscopy

Over the past few decades, ultrafast spectroscopy has become a widely used technique to study molecular motions and dynamics which occur on femtosecond timescales.[26-31] Processes such as intersystem crossing,[32-35] solvation, electron-transfer,[36-38] structural rearrangements of liquids,[39-42] and reactive intermediate chemistry can be studied by ultrafast techniques.[43-46] Ultrafast spectroscopy encompasses a broad range of spectroscopic techniques, such as sum-frequency generation spectroscopy, 2-dimensional electronic spectroscopy, 2-dimensional infrared spectroscopy, and transient absorption spectroscopy. More recently, the field of attochemistry has been developed, and can capture the sub-femtosecond dynamics of electron motion.[47] The implementation of ultrafast TAS using femtosecond lasers is described in Chapter 3, and Chapters 4 – 6 of this thesis present measurements that provide new mechanistic insights into the formation and chemical dynamics of reaction intermediates formed after photoexcitation of stable molecules in solution by a UV-pulse.

### 1.3 Potential energy surfaces and non-adiabatic dynamics

One of the most important concepts for the study of photochemistry, reactions, and chemical dynamics is the adiabatic PES. In general, PESs are multidimensional, with the potential energy depending on several different coordinates such as bond distances and bond angles.

The adiabatic PES defines the potential energy of a system with respect to these nuclear coordinates and can be used to approximate various chemical and dynamical changes of a system.[48-50] A schematic one-dimensional plot along one such A – B internuclear separation (for example, for a diatomic AB molecule) is shown in Figure 1.2 and will be used to guide the discussion in this section. Construction of an adiabatic PES first begins with invoking the Born-Oppenheimer approximation to the time-independent Schrödinger equation (TISE). The Born-Oppenheimer approximation states that nuclei remain static on the timescale of changes in the positions of electrons, and hence their movements can be described as uncoupled. However, this assumption is only valid for slowly moving nuclei.

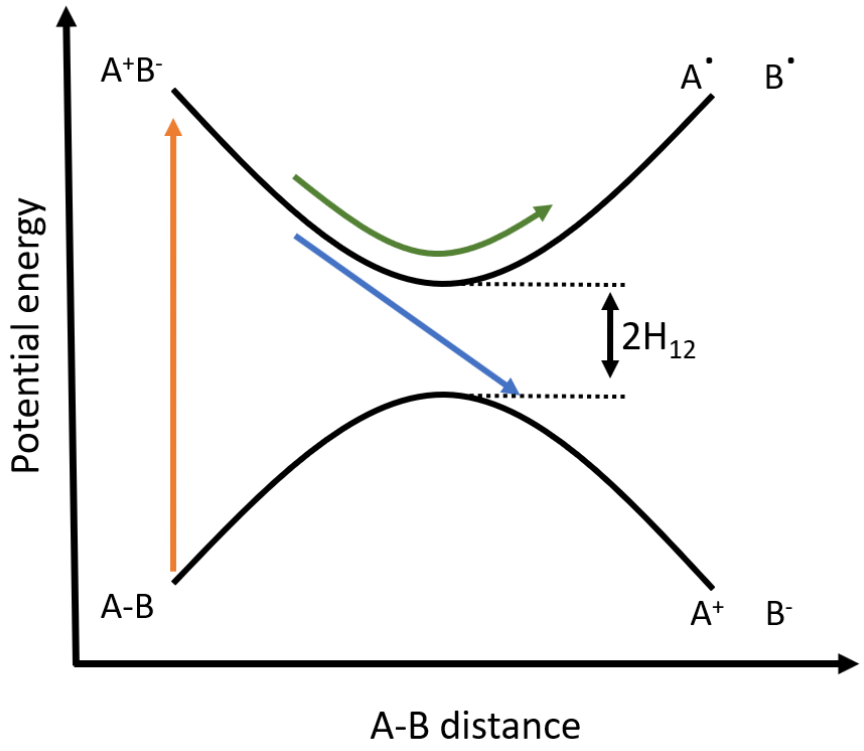


Figure 1.2 – Ground and first-excited state adiabatic PESs (black curves) of a molecule AB as a function of the distance between atoms A and B. The vertical excitation of molecule AB (orange) reaches an energetically unstable structure, illustrated here by charge transfer to make $A^+B^-$. Atoms A and B progress along the excited state potential energy surface to lower the potential energy of system (green or blue arrows). When the value of the diabatic coupling term $H_{12}$ is large, adiabatic dynamics are observed (green arrow). However, when the value of $H_{12}$ is small, the potential energy surfaces become close in energy which can result in non-adiabatic crossing from the excited state PES to the lower energy PES (blue arrow). The outcomes of the adiabatic and non-adiabatic pathways are different photoproducts, shown here as $A^{\cdot} + B^{\cdot}$ and $A^- + B^+$, respectively.

Non-adiabatic dynamics refer to events that occur when large couplings between nuclear and electronic motions cause a breakdown of the Born-Oppenheimer approximation, and hence are frequently referred to as non-Born-Oppenheimer molecular dynamics. The coupling of nuclear and electronic motions often becomes significant when two PESs are in close energy proximity. For a diatomic molecule, the fast movement of nuclei around the area of an avoided crossing of two electronic states allows passage from one to another adiabatic potential energy curve (Blue arrow in Figure 1.2). For polyatomic molecules, a switch onto a

different adiabatic PES typically occurs through a conical intersection (CI).[51-52] CIs are multi-dimensional topographical features that arise at specific geometries where degeneracy is reached between adiabatic PESs and can be described as molecular funnels. A schematic diagram illustrating a 3-dimensional representation of a conical intersection is shown in Figure 1.3. A common CI geometry is one with a high symmetry point group, where the electronic wavefunctions have different symmetry classifications and the coupling between the surfaces vanishes, allowing them to cross. Molecular distortions from the high symmetry structure break the symmetry and prevent crossings for other regions of the PESs. CIs are now known to be ubiquitous in polyatomic molecular systems, and often influence the photochemistry.[53-54] Prediction of non-adiabatic dynamics at CIs is a computationally expensive task, requiring calculation of coupling vectors between electronic and nuclear degrees of freedom. It is beyond the scope of this thesis to understand the various strategies that can be employed to simplify the problem, but is noteworthy that such non-adiabatic simulations are able to complement experimental observations, and predict various non-adiabatic processes.[55]

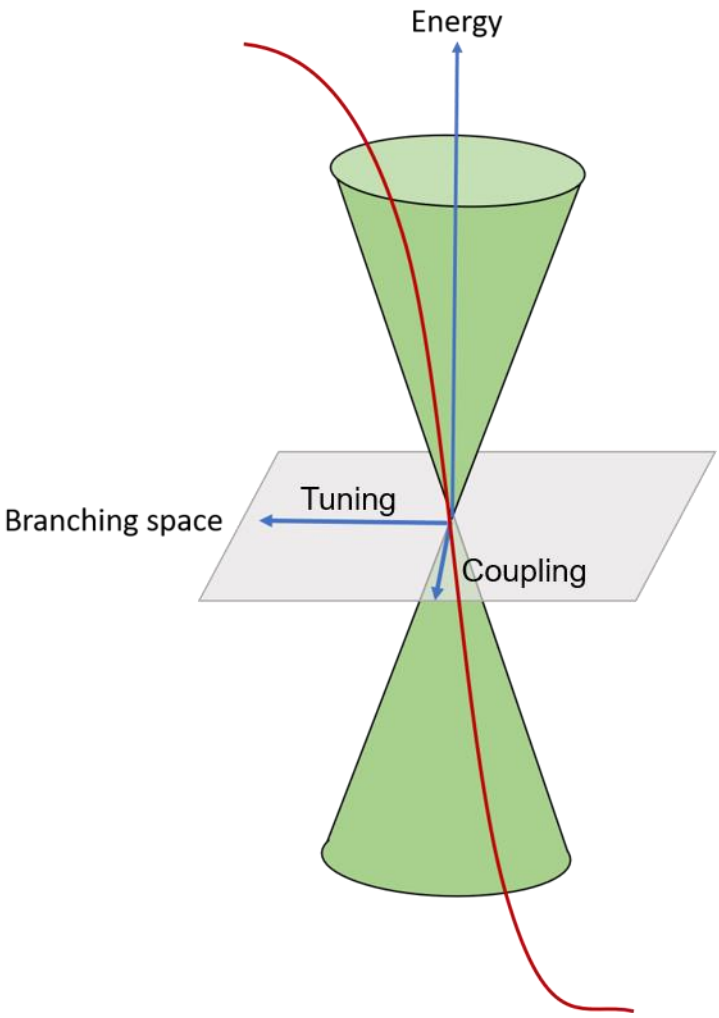


Figure 1.3– Schematic diagram of a CI. The grey region shows the branching space of molecular distortions that results in the lifting of degeneracy between the two electronic states shown in green. The red curve shows the movement through a conical intersection (green funnel) that results in the non-adiabatic crossing between PESs.

### 1.4 Theoretical methods

Today, with modern advances in super-computing, complex and elegant algorithms can routinely be applied to address various chemical problems. Accurate computations of chemical properties offer complementary information to support conclusions derived from experimental studies, and deepen mechanistic understanding. These computations now offer predictive tools to understand chemistry which would otherwise require expensive or potentially dangerous experiments to explore. Many of the theoretical methods discussed herein are routinely used to complement spectral assignments and offer profound insights into the formation and dynamics of various reaction intermediates discussed in later chapters.

It is beyond the scope of this thesis to provide an in-depth description of the various computational methods. Instead, a focus will be placed on their successes and their inadequacies when predicting chemical properties.

### 1.4.1 The variational principle and the Hartree-Fock method

The foundation to many ab initio methods which aim to solve the Time-independent Schrödinger equation (TISE) are based around the variational principle. The variational principle states that the true ground state energy is always less than or equal to the expectation energy $\langle E \rangle$ of a trial wavefunction $\Psi_n$ as shown in **equation 1.1.** Varying the trial wavefunction to minimise the expectation energy will provide a way to improve systematically the approximation of the exact wavefunction.

$$\langle E \rangle \geq \left\langle \Psi_n \middle| \widehat{H} \middle| \Psi^*{}_n \right\rangle \quad 1.1$$

The Hartree-Fock (HF) method is arguably one of the most utilised *ab initio* computational methods, and is the basis behind many methods such as Møller-Plesset perturbation (MP) theory and coupled cluster (CC) methods. The HF method assumes that the electronic wavefunction can be described by a single Slater determinant constructed with single electron spin-orbitals $\psi_n(\alpha \; or \; \beta \; spin)$ as shown for a 2-electron system in **equation 1.2**. This assumption will always overestimate the energy of a multi-electron system, and is called the HF energy. The difference between the HF energy and the exact solution to the TISE is known as electron correlation. Within the HF method, each electron is treated as experiencing an average repulsion from the other electrons in the molecule, and this treatment neglects the tendency for electrons to avoid one another by independent repulsions. This factor is also known as the Coulombic contribution to the electron correlation. The use of a Slater determinant within HF theory satisfies the Pauli-exclusion principle requiring that no two electrons with the same spin can occupy the same orbital at any one time, and so explicitly treats the so-called exchange correlation contribution to the electron correlation. Static correlation arises within the HF method (and many post HF methods) from the assumption that an electronic wavefunction can be described by a single Slater determinant. This assumption is satisfactory for systems which are dominated by a single reference wavefunction, but often gives poor predictions for systems which can only be described using several reference wavefunctions, for example, ground states which are quasi-degenerate with low-lying excited states.[56-58] Methods such as the *complete active space self-consistent*

*field* (CASSCF) approach instead use multiple Slater determinants to approximate the reference wavefunction.

$$\Psi = \frac{1}{\sqrt{2}}\begin{vmatrix}\psi_1(\alpha) & \psi_2(\beta)\\ \psi_1(\beta) & \psi_2(\alpha)\end{vmatrix} \qquad 1.2$$

### 1.4.2 Møller-Plesset perturbation theory

Post HF methods typically aim to retrieve the Coulombic contribution to the electron correlation, and begin by calculating the HF wavefunction. A commonly used post Hartree-Fock method is Møller-Plesset (MP) theory, which builds upon the HF method by recovering contributions from Coulombic electron correlation using Rayleigh-Schrödinger perturbation theory. By considering an unperturbed Hamiltonian $\widehat{H}_0$ from the solution to the HF equations, a small perturbation $\hat{V}$ can be applied, with $\lambda$ controlling the size of the perturbation as shown in **equation 1.3.** In MP theory the perturbation is in the form of excited Slater determinants, where for example, second-order MP perturbation theory (MP2) uses doubly excited slater determinants.

$$\widehat{H} = \widehat{H}_0 + \lambda\hat{V} \qquad 1.3$$

The success of MP theory is reflected by it being one of the most commonly used post Hartree-Fock methods. It remains as one of the least computationally expensive *ab initio* methods for computing electron correlation effects and can been used for systems where more computationally expensive methods (such as coupled cluster methods) are too costly. The most commonly used of the MP theories is MP2, and its computational performance has been improved considerably so that molecules consisting of several-hundreds of atoms can now be handled.[59] Third (MP3) and fourth (MP4) order corrections are available, but they are more costly, do not always provide more accurate predictions of chemical properties, and convergence can be erratic.[60-61] MP2 theory has been successful applied to hydrogen-bonded base pairs, reproducing the coupled cluster singles, doubles with MP2 triplet excitations (CCSD(T)) energies with good accuracy.[62] However, modelling of weaker interactions, such as dispersion forces is less reliable.[63]

### 1.4.3 Density Functional Theory

The methods outlined so far for describing the electronic wavefunction use constructs based on single electron wavefunctions. All have three spatial coordinates and one spin coordinate, which gives the N-electron wavefunction large dimensional complexity, and calculations

become very computationally expensive as the number of electrons increases. Density functional theory (DFT) aims to describe the electronic wavefunction by using a system's electron density rather than describing the individual electrons, simplifying the dimensionality to 3 spatial coordinates regardless of the size of the system. The foundation for DFT was formulated by Kohn and Hohenberg who established that the ground state energy can uniquely be determined by the electron density, and any trial electron density which is positive throughout space follows the variational principle.[64] However, even with exact knowledge of the electron density, the functional form which gives the energy is not known, in particular for the kinetic energy. Secondly, to obtain the electron density, the electronic wavefunction must be found. Kohn and Sham provided solutions to these problems, calculating the electron density from a series of non-interacting electrons, with an external potential applied such that the electron density calculated is the same as a series of interacting electrons.[65] This approach constructs the so-called Kohn-Sham orbitals (KS-orbitals), but generation of the KS-orbitals is not equivalent to determining the exact wavefunction.

Similarly to HF theory, the use of non-interacting single-electron wavefunctions creates shortcomings in correlating electronic motions. One of the simplest, and widely used functionals to determine electron correlation effects is the local density approximation (LDA). The LDA assumes the electron density can be treated as a uniform electron gas and has had success in calculations for solid state systems, but for molecular systems the LDA is considered as a framework for more complicated approximations to be made.[66-68] For example, the generalised gradient approximation (GGA) describes the electron density changing slowly with position. The importance of the GGA can be easily understood by considering the bonding between two atoms of different electronegativities where the electron density will not be uniformly distributed.

The greatest success of density functional theory is arguably the use of hybrid functionals, which contain a portion of exchange-correlation from HF theory combined with predicting electron correlation effects using functionals of the electron density (i.e. LDA and GGA). The portion of electron-correlation calculated by each method is typically determined using experimental values or comparison with high level methods. There are numerous benchmark studies which assess the accuracy of various DFT methods, and generally hybrid

functions have been found to perform well.[69-72] A failure of DFT has been in describing non-covalent interactions due to shortcomings in the description of dispersion forces.[73] Although, methods to improve the description of dispersion forces have been developed, such as D3[74] and wB97XD[75] functionals. Nevertheless, the largest benefit of using DFT is the low computational cost compared to more-expensive post-Hartree-Fock methods; DFT scales as ~$N^3$ compared to ~$N^5$ for MP2. A huge success of DFT has been the development of time-dependent density functional theory (TD-DFT) for computation of excited state properties, and this method can be used for the computation of excited state potential energy surfaces and vertical excitations.[76-77]

**References**


1. Turro, N. J.; Ramamurthy, V.; Scaiano, J. C., *Modern molecular photochemistry of organic molecules*. University Science Books: Sausalito, Calif., 2010.
2. Escobedo, R.; Miranda, R.; Martínez, J. Infrared Irradiation: Toward Green Chemistry, a Review. *Int J Mol Sci* **2016,** *17*, 453-453.
3. Ballesteros-Paredes, J.; André, P.; Hennebelle, P.; Klessen, R. S.; Kruijssen, J. M. D.; Chevance, M.; Nakamura, F.; Adamo, A.; Vázquez-Semadeni, E. From Diffuse Gas to Dense Molecular Cloud Cores. *Space Sci. Rev.* **2020,** *216*, 76.
4. Öberg, K. I. Photochemistry and Astrochemistry: Photochemical Pathways to Interstellar Complex Organic Molecules. *Chem. Rev.* **2016,** *116*, 9631-9663.
5. Arumainayagam, C. R.; Garrod, R. T.; Boyer, M. C.; Hay, A. K.; Bao, S. T.; Campbell, J. S.; Wang, J.; Nowak, C. M.; Arumainayagam, M. R.; Hodge, P. J. Extraterrestrial prebiotic molecules: photochemistry vs. radiation chemistry of interstellar ices. *Chem. Soc. Rev.* **2019,** *48*, 2293-2314.
6. Jørgensen, J. K.; Belloche, A.; Garrod, R. T. Astrochemistry During the Formation of Stars. *Annu. Rev. Astron. Astrophys.* **2020,** *58*, 727-778.
7. Del Zanna, G.; Mason, H. E. Solar UV and X-ray spectral diagnostics. Living Rev. Sol. Phys. **2018,** *15*, 5.
8. Meftah, M.; Damé, L.; Bolsée, D.; Hauchecorne, A.; Pereira, N.; Sluse, D.; Cessateur, G.; Irbah, A.; Bureau, J.; Weber, M.; Bramstedt, K.; Hilbig, T.; Thiéblemont, R.; Marchand, M.; Lefèvre, F.; Sarkissian, A.; Bekki, S. SOLAR-ISS: A new reference spectrum based on SOLAR/SOLSPEC observations. *A&A* **2018,** *611*.
9. Solar Radio Emissions. In *Handbook of the Solar-Terrestrial Environment*, Kamide, Y.; Chian, A., Eds. Springer Berlin Heidelberg: Berlin, Heidelberg, 2007; pp 133-151.
10. Plane, J. M. C. Yuk L. Yung and William B. DeMore: Photochemistry of Planetary Atmospheres. *J. Atmos. Chem.* **2001,** *39*, 215-216.
11. Ritson, D. J.; Mojzsis, S. J.; Sutherland, J. D. Supply of phosphate to early Earth by photogeochemistry after meteoritic weathering. *Nat. Geosci*. **2020,** *13*, 344-348.
12. Rapf, R. J.; Vaida, V. Sunlight as an energetic driver in the synthesis of molecules necessary for life. *Phys. Chem. Chem. Phys.* **2016,** *18*, 20067-20084.
13. Nobel, P. S., 5 - Photochemistry of Photosynthesis. In *Physicochemical and Environmental Plant Physiology (Third Edition)*, Nobel, P. S., Ed. Academic Press: Burlington, 2005; pp 219-266.
14. Introduction: Photochemistry in Organic Synthesis. *Chem. Rev.* **2016,** *116*, 9629-9630.
15. Cambié, D.; Bottecchia, C.; Straathof, N. J. W.; Hessel, V.; Noël, T. Applications of Continuous-Flow Photochemistry in Organic Synthesis, Material Science, and Water Treatment. *Chem. Rev.* **2016,** *116*, 10276-10341.

16. Yu, Y.; Guo, P.; Zhong, J.-S.; Yuan, Y.; Ye, K.-Y. Merging photochemistry with electrochemistry in organic synthesis. *Org. Chem. Front.* **2020,** *7*, 131-135.
17. Hoffmann, N. Photochemical Reactions as Key Steps in Organic Synthesis. *Chem. Rev.* **2008,** *108*, 1052-103.
18. Oelgemöller, M.; Hoffmann, N. Studies in organic and physical photochemistry – an interdisciplinary approach. *Org. Biomol. Chem.* **2016,** *14*, 7392-7442.
19. Deng, Y.; Yang, C.-P. H.; Smith Iii, A. B. Enantioselective Total Synthesis of (+)-Peniciketals A and B: Two Architecturally Complex Spiroketals. *J. Am. Chem. Soc.* **2021**, *143*, 1740–1744.
20. Chowdhury, R.; Yu, Z.; Tong, M. L.; Kohlhepp, S. V.; Yin, X.; Mendoza, A. Decarboxylative Alkyl Coupling Promoted by NADH and Blue Light. *J. Am. Chem. Soc.* **2020,** *142*, 20143-20151.
21. Becker, M. R.; Wearing, E. R.; Schindler, C. S. Synthesis of azetidines via visible-light-mediated intermolecular [2+2] photocycloadditions. *Nat. Chem.* **2020,** *12*, 898-905.
22. Guillou, A.; Earley, D. F.; Patra, M.; Holland, J. P. Light-induced synthesis of protein conjugates and its application in photoradiosynthesis of 89Zr-radiolabeled monoclonal antibodies. *Nat. Protoc.* **2020,** *15*, 3579-3594.
23. Porter, G.-N.; Norrish, R. G. W. Flash photolysis and spectroscopy. A new method for the study of free radical reactions. *Proc. R. Soc. Lond. A.* **1950,** *200*, 284-300.
24. Norrish, R. G. W. Kinetic spectoscopy and flash photolysis. *Am. Sci.* **1962,** *50*, 131-157.
25. Zewail, A. H. Femtochemistry: Atomic-Scale Dynamics of the Chemical Bond Using Ultrafast Lasers (Nobel Lecture). *Angew Chem Int Ed Engl.* **2000,** *39*, 2586-2631.
26. Zewail, A. H. Femtochemistry: Atomic-Scale Dynamics of the Chemical Bond. *J. Phys. Chem. A* **2000,** *104*, 5660-5694.
27. Dantus, M.; Zewail, A. Introduction: Femtochemistry. *Chem. Rev.* **2004,** *104*, 1717-1718.
28. Changenet, P.; Gustavsson, T.; Lampre, I. Introduction to Femtochemistry: Excited-State Proton Transfer from Pyranine to Water Studied by Femtosecond Transient Absorption. *J. Chem. Educ.* **2020,** *97*, 4482-4489.
29. Maiuri, M.; Garavelli, M.; Cerullo, G. Ultrafast Spectroscopy: State of the Art and Open Challenges. *J. Am. Chem. Soc.* **2020,** *142*, 3-15.
30. Hochstrasser, R. M. Ultrafast Spectroscopy of Protein Dynamics. *J. Chem. Educ.* **1998,** *75*, 559.
31. Alarcos, N.; Cohen, B.; Ziółek, M.; Douhal, A. Photochemistry and Photophysics in Silica-Based Materials: Ultrafast and Single Molecule Spectroscopy Observation. *Chem. Rev.* **2017,** *117*, 13639-13720.
32. Bhattacherjee, A.; Pemmaraju, C. D.; Schnorr, K.; Attar, A. R.; Leone, S. R. Ultrafast Intersystem Crossing in Acetylacetone via Femtosecond X-ray Transient Absorption at the Carbon K-Edge. *J. Am. Chem. Soc.* **2017,** *139*, 16576-16583.
33. Wang, J.; Kubicki, J.; Peng, H.; Platz, M. S. Influence of Solvent on Carbene Intersystem Crossing Rates. *J. Am. Chem. Soc.* **2008,** *130*, 6604-6609.
34. Sitzmann, E. V.; Langan, J.; Eisenthal, K. B. Intermolecular effects on intersystem crossing studied on the picosecond timescale: the solvent polarity effect on the rate of singlet-to-triplet intersystem crossing of diphenylcarbene. *J. Am. Chem. Soc.* **1984,** *106*, 1868-1869.
35. Giacobbe, E. M.; Mi, Q.; Colvin, M. T.; Cohen, B.; Ramanan, C.; Scott, A. M.; Yeganeh, S.; Marks, T. J.; Ratner, M. A.; Wasielewski, M. R. Ultrafast Intersystem Crossing and Spin Dynamics of Photoexcited Perylene-3,4:9,10-bis(dicarboximide) Covalently Linked to a Nitroxide Radical at Fixed Distances. *J. Am. Chem. Soc.* **2009,** *131*, 3700-3712.
36. Hubig, S. M.; Bockman, T. M.; Kochi, J. K. Identification of Photoexcited Singlet Quinones and Their Ultrafast Electron-Transfer vs Intersystem-Crossing Rates. *J. Am. Chem. Soc.* **1997,** *119*, 2926-2935.
37. Huang, J.; Huang, Z.; Yang, Y.; Zhu, H.; Lian, T. Multiple Exciton Dissociation in CdSe Quantum Dots by Ultrafast Electron Transfer to Adsorbed Methylene Blue. *J. Am. Chem. Soc.* **2010,** *132*, 4858-4864.

38. Brown, A. M.; Antila, L. J.; Mirmohades, M.; Pullen, S.; Ott, S.; Hammarström, L. Ultrafast Electron Transfer Between Dye and Catalyst on a Mesoporous NiO Surface. *J. Am. Chem. Soc.* **2016,** *138*, 8060-8063.
39. Ren, Z.; Ivanova, A. S.; Couchot-Vore, D.; Garrett-Roe, S. Ultrafast Structure and Dynamics in Ionic Liquids: 2D-IR Spectroscopy Probes the Molecular Origin of Viscosity. J. Phys. Chem. Lett. **2014,** *5*, 1541-1546.
40. Hunt, N. T.; Turner, A. R.; Tanaka, H.; Wynne, K. The Ultrafast Dynamics of Hydrogen-Bonded Liquids: Molecular Structure-Dependent Occurrence of Normal Arrhenius or Fractional Stokes−Einstein−Debye Rotational Diffusive Relaxation. *J. Phys. Chem. B* **2007,** *111*, 9634-9643.
41. Kraack, J. P.; Hamm, P. Surface-Sensitive and Surface-Specific Ultrafast Two-Dimensional Vibrational Spectroscopy. *Chem. Rev.* **2017,** *117*, 10623-10664.
42. Perakis, F.; Hamm, P. Two-Dimensional Infrared Spectroscopy of Supercooled Water. *J. Phys. Chem. B* **2011,** *115*, 5289-5293.
43. Platz, M. S. A Perspective on Physical Organic Chemistry. *J. Org. Chem.* **2014,** *79*, 2341-2353.
44. Burdzinski, G. T.; Wang, J.; Gustafson, T. L.; Platz, M. S. Study of Concerted and Sequential Photochemical Wolff Rearrangement by Femtosecond UV−vis and IR Spectroscopy. *J. Am. Chem. Soc.* **2008,** *130*, 3746-3747.
45. Burdzinski, G.; Platz, M. S. Ultrafast time-resolved studies of the photochemistry of diazo carbonyl compounds. *J. Phys. Org. Chem.* **2010,** *23*, 308-314.
46. Ihee, H.; Goodson, B. M.; Srinivasan, R.; Lobastov, V. A.; Zewail, A. H. Ultrafast Electron Diffraction and Structural Dynamics: Transient Intermediates in the Elimination Reaction of $C_2F_4I_2$. *J. Phys. Chem. A* **2002,** *106*, 4087-4103.
47. Nisoli, M.; Decleva, P.; Calegari, F.; Palacios, A.; Martín, F. Attosecond Electron Dynamics in Molecules. *Chem. Rev.* **2017,** *117*, 10760-10825.
48. Rangel, C.; Navarrete, M.; Corchado, J. C.; Espinosa-García, J. Potential energy surface, kinetics, and dynamics study of the $Cl+CH_4 \rightarrow HCl+CH_3$ reaction. *J. Chem. Phys.* **2006,** *124*, 124306.
49. Bytautas, L.; Bowman, J. M.; Huang, X.; Varandas, A. J. C. Accurate Potential Energy Surfaces and Beyond: Chemical Reactivity, Binding, Long-Range Interactions, and Spectroscopy. *Adv. Phys. Chem.* **2012,** *2012*, 679869.
50. Thomas, A. M.; Doddipatla, S.; Kaiser, R. I.; Galimova, G. R.; Mebel, A. M. A Barrierless Pathway Accessing the $C_9H_9$ and $C_9H_8$ Potential Energy Surfaces via the Elementary Reaction of Benzene with 1-Propynyl. *Sci. Rep.* **2019,** *9*, 17595.
51. Brouard, M.; Vallance, C.; Royal Society of, C., *Tutorials in molecular reaction dynamics*. Royal Society of Chemistry: Cambridge, 2010.
52. Yarkony, D. R., Conical intersections: Their description and consequences. In *Conical Intersections*, WORLD SCIENTIFIC: 2004; Vol. Volume 15, pp 41-127.
53. Domcke, W.; Yarkony, D. R. Role of Conical Intersections in Molecular Spectroscopy and Photoinduced Chemical Dynamics. *Annu. Rev. Phys. Chem.* **2012,** *63*, 325-352.
54. Schuurman, M. S.; Stolow, A. Dynamics at Conical Intersections. *Annu. Rev. Phys. Chem.* **2018,** *69*, 427-450.
55. Barbatti, M. Nonadiabatic dynamics with trajectory surface hopping method. Wiley Interdiscip. Rev. *Comp. Mol. Sci.* **2011,** *1*, 620-633.
56. Szalay, P. G.; Müller, T.; Gidofalvi, G.; Lischka, H.; Shepard, R. Multiconfiguration Self-Consistent Field and Multireference Configuration Interaction Methods and Applications. *Chem. Rev.* **2012,** *112*, 108-181.
57. Park, J. W.; Al-Saadon, R.; MacLeod, M. K.; Shiozaki, T.; Vlaisavljevich, B. Multireference Electron Correlation Methods: Journeys along Potential Energy Surfaces. *Chem. Rev.* **2020,** *120*, 5878-5909.
58. Lischka, H.; Nachtigallová, D.; Aquino, A. J. A.; Szalay, P. G.; Plasser, F.; Machado, F. B. C.; Barbatti, M. Multireference Approaches for Excited States of Molecules. *Chem. Rev.* **2018,** *118*, 7293-7361.

59. Cremer, D. Møller–Plesset perturbation theory: from small molecule methods to methods for thousands of atoms. Wiley Interdiscip. Rev. *Comp. Mol. Sci.* **2011,** *1*, 509-530.
60. Leininger, M. L.; Allen, W. D.; Schaefer, H. F.; Sherrill, C. D. Is Moller–Plesset perturbation theory a convergent ab initio method? *J. Chem. Phys.* **2000,** *112*, 9213-9222.
61. Helgaker, T.; Gauss, J.; Jorgensen, P.; Olsen, J. The prediction of molecular equilibrium structures by the standard electronic wave functions. *J. Chem. Phys.* **1997,** *106*, 6430-6440.
62. Jurečka, P.; Šponer, J.; Černý, J.; Hobza, P. Benchmark database of accurate (MP2 and CCSD(T) complete basis set limit) interaction energies of small model complexes, DNA base pairs, and amino acid pairs. *Phys. Chem. Chem. Phys.* **2006,** *8*, 1985-1993.
63. Riley, K. E.; Platts, J. A.; Řezáč, J.; Hobza, P.; Hill, J. G. Assessment of the Performance of MP2 and MP2 Variants for the Treatment of Noncovalent Interactions. *J. Phys. Chem. A* **2012,** *116*, 4159-4169.
64. Hohenberg, P.; Kohn, W. Inhomogeneous Electron Gas. *Phys. Rev.* **1964,** *136*, B864-B871.
65. Kohn, W.; Sham, L. J. Self-Consistent Equations Including Exchange and Correlation Effects. *Phys. Rev.* **1965,** *140*, A1133-A1138.
66. Ghosez, P.; Junquera, J. Handbook of Theoretical and comnputational Chemistry of Nanostructures. ASP, Stevenson Ranch**, 2006**.
67. Hasnip, P. J.; Refson, K.; Probert, M. I. J.; Yates, J. R.; Clark, S. J.; Pickard, C. J. Density functional theory in the solid state. *Philos. Trans. A. Math. Phys. Eng. Sci.* **2014,** *372*, 20130270.
68. Zhang, G.-X.; Reilly, A. M.; Tkatchenko, A.; Scheffler, M. Performance of various density-functional approximations for cohesive properties of 64 bulk solids. *New J. Phys.* **2018,** *20*, 063020.
69. Afzal, M. A. F.; Hachmann, J. Benchmarking DFT approaches for the calculation of polarizability inputs for refractive index predictions in organic polymers. *Phys. Chem. Chem. Phys.* **2019,** *21*, 4452-4460.
70. Brandenburg, J. G.; Maas, T.; Grimme, S. Benchmarking DFT and semiempirical methods on structures and lattice energies for ten ice polymorphs. *J. Chem. Phys.* **2015,** *142*, 124104.
71. Howard, J. C.; Enyard, J. D.; Tschumper, G. S. Assessing the accuracy of some popular DFT methods for computing harmonic vibrational frequencies of water clusters. *J. Chem. Phys.* **2015,** *143*, 214103.
72. Teale, A. M.; Lutnæs, O. B.; Helgaker, T.; Tozer, D. J.; Gauss, J. Benchmarking density-functional theory calculations of NMR shielding constants and spin–rotation constants using accurate coupled-cluster calculations. *J. Chem. Phys.* **2013,** *138*, 024111.
73. Ireta, J.; Neugebauer, J.; Scheffler, M. On the Accuracy of DFT for Describing Hydrogen Bonds: Dependence on the Bond Directionality. *J. Phys. Chem. A* **2004,** *108*, 5692-5698.
74. Grimme, S.; Antony, J.; Ehrlich, S.; Krieg, H. A consistent and accurate ab initio parametrization of density functional dispersion correction (DFT-D) for the 94 elements H-Pu. *J. Chem. Phys.* **2010,** *132*, 154104.
75. Chai, J.-D.; Head-Gordon, M. Long-range corrected hybrid density functionals with damped atom–atom dispersion corrections. *Phys. Chem. Chem. Phys.* **2008,** *10*, 6615-6620.
76. Shao, Y.; Mei, Y.; Sundholm, D.; Kaila, V. R. I. Benchmarking the Performance of Time-Dependent Density Functional Theory Methods on Biochromophores. *J. Chem. Theory. Comp.* **2020,** *16*, 587-600.
77. Laurent, A. D.; Jacquemin, D. TD-DFT benchmarks: A review. *Int. J. Quantum Chem* **2013,** *113*, 2019-2039.

# Chapter 2 Reactive Intermediates

Sections of this chapter have been published: Phelps, R.; Orr-Ewing, A. J. Direct Observation of Ylide and Enol Intermediates Formed in Competition with Wolff Rearrangement of Photoexcited Ethyl Diazoacetoacetate. *J. Am. Chem. Soc.* **2020,** *142*, 7836-7844.

Reactive intermediates are short-lived species which often determine the outcomes of chemical reactions and they are typically assigned to different classes. Examples of importance in organic chemistry are: photo-excited-states, radicals, carbenes, zwitterions, anions, and cations. Many of these intermediates are frequently invoked in reaction mechanisms, some of which will be addressed in in Chapters 4-6. Despite the long-standing importance of reactive intermediates in many fields, these elusive species are not often directly observable due to their short lifetimes. As much of this chapter will discuss, a combination of ultrafast spectroscopic techniques and computational investigations has offered new ways to investigate the formation, reactivity, and solvation of reaction intermediates.

### 2.1 Solvent effects on organic reactions

Organic synthesis heavily relies on conducting reactions in the solution phase. As a consequence, chemical industries have become one of the biggest consumers of organic solvents. The choice of solvent can have considerable effects on reaction outcomes, and therefore understanding the role solvents play in chemical reactivity is paramount to improving chemical processes. Bulk properties of solvents such as dielectric constants or viscosity can often be used to explain experimental observations. The effects of solvents in organic reactions have been the topic of numerous reviews,[1-3] and these effects can frequently be computationally reproduced using implicit solvent models.[4-6] Often harder to computationally model are specific interactions of solvent molecules with substrates, catalysts, intermediates and transition states. These interactions require an explicit treatment of one or more solvent molecules which becomes computationally expensive.[1, 7] The role of solvent in the formation and chemical dynamics of reaction intermediates will be a common theme throughout this thesis.

## 2.2 Diazo compounds, carbenes, ketenes, and ylides

In Chapters 4 and 5 of this thesis, ultrafast transient absorption spectroscopy measurements are reported and used to study the formation and chemical dynamics of intermediates formed from the photo-excitation of the diazo compounds shown in scheme 2.1. Commonly encountered intermediates are carbenes, ketenes, and ylides. Therefore, this section provides background information about diazo compounds and the intermediates formed from its photoexcitation.

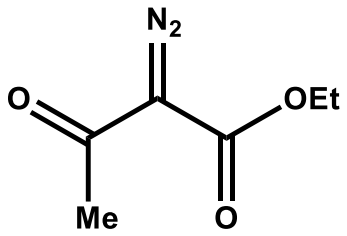


Ethyl diazoacetoacetate

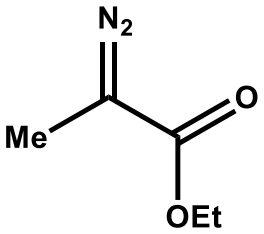


Ethyl diazoacetate

Scheme 2.1 – Structures of ethyl diazoacetoacetate and ethyl diazoacetate

Since the preparation of ethyl diazoacetate in 1883,[8] the formation of carbene and ketene intermediates from the photolysis, thermolysis, and metal catalysed initiation of diazo compounds has attracted mechanistic investigations.[9-13] Their frequent use in a variety of different reactions means understanding the formation and chemical dynamics of the reaction intermediates is essential to their efficient and controlled use in organic synthesis.[14-15] The metal catalysed initiation of diazo compounds has dominated their use,[16-18] but more-recent advances in spectroscopy have sparked interest in the photochemistry of diazo compounds and photoinitiated synthesis has begun to compete in the use of diazo compounds in modern synthesis.[14-15]

Carbenes have 6 valence electrons making them highly reactive and short-lived intermediates which partake in a wealth of chemical reactions. Examples include the Buchner rearrangement; C-H insertion; addition to C=C double bonds (cyclopropanation); O-H insertions; and C-X insertions (X = Halogens).[14-15, 19-20] Their mechanisms often remain elusive due to the short lifetimes of the intermediates involved.

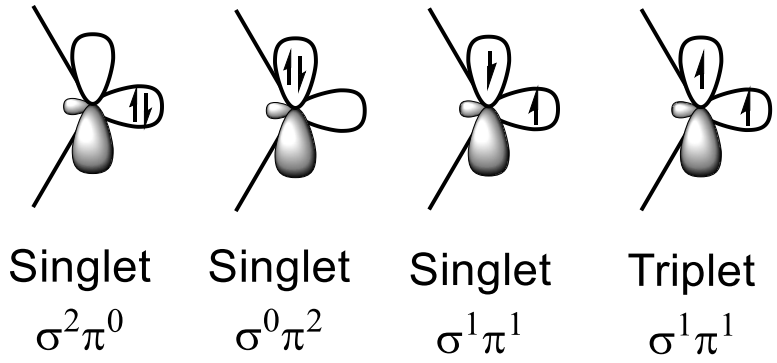


Scheme 2.2 – Electron configurations of carbenes.

**2.2.1 Triplet carbenes**

Carbenes typically adopt a triplet multiplicity in their ground states when substituents and solvents do not offer stabilisation to the singlet electron configurations. For non-stabilised carbenes the multiplicity is largely controlled by the trade-off between pairing electrons into the lower energy orbital or achieving maximum multiplicity. In the case of triplet carbenes, the energy to pair two electrons is often greater than the HOMO-LUMO energy gap, making the triplet configuration the ground state.

Triplet carbenes are biradicals, with single electrons placed into p and $sp^2$ orbitals, as illustrated for the triplet $\sigma^1\pi^1$ configuration in Scheme 2.2. They have been found to react with a variety of species via step-wise mechanisms: for example, the insertion into C=C double bonds shown in scheme 2.3 is assumed to pass through a biradical intermediate on the basis that products are found to be non-stereoselectively formed.[21]

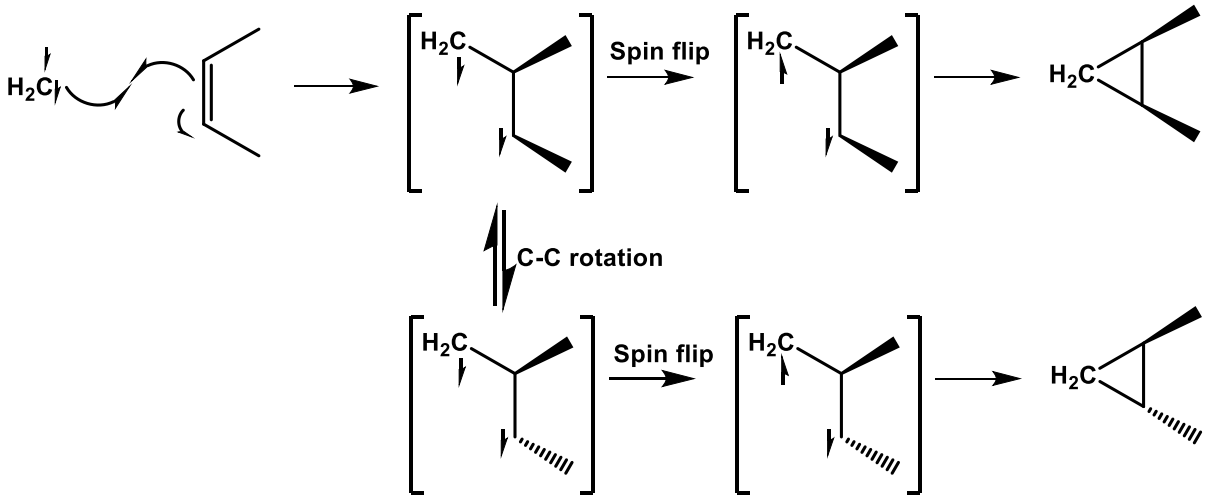


Scheme 2.3 – Stepwise mechanism for the reaction of triplet carbenes with alkenes via C=C insertion.

### 2.2.2 Singlet carbenes

The electronic configurations of singlet carbenes are outlined in scheme 2.2, and in their lowest energy singlet states these carbenes are typically described as having a $\sigma^2\pi^0$ electron configuration. However, accurate computations of the properties of singlet carbenes are often challenging, because of considerable contributions from other singlet configurations (shown in scheme 2.2) to the overall wavefunction. The computations of electronic states of carbenes have been the topic of numerous reviews and articles, and in general, stabilised carbenes can be accurately using single-reference methods.[22-29]

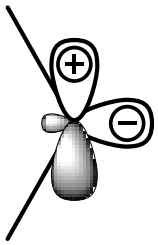

Scheme 2.4 – Zwitterionic structure of the singlet carbene

Singlet carbenes can undergo both electrophilic and nucleophilic reactions due to their zwitterionic structure, as is illustrated in scheme 2.4, and have therefore been found to react readily with nucleophiles to form ylides, electrophiles to form cations and participate in insertion reactions that retain the stereochemistry of the reactants,[21] suggesting a concerted mechanism which is illustrated for the insertion into a C=C double bond in scheme 2.5.

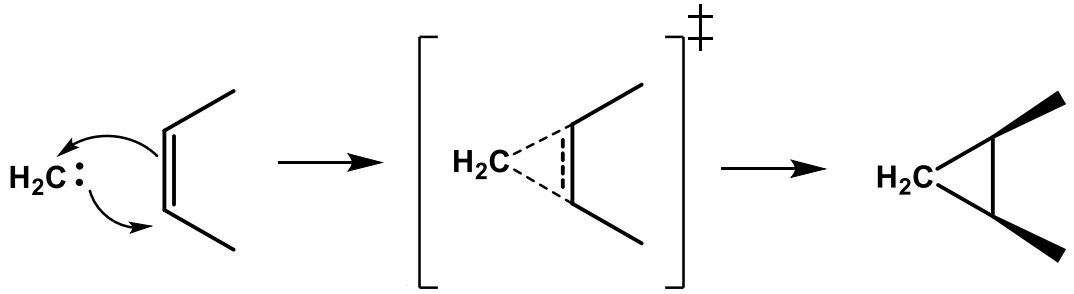


Scheme 2.5 – Concerted mechanism for the reaction of singlet carbenes with alkenes via C=C insertion.

Methods to stabilise singlet configurations have been proposed, such as functionalising the carbene with carbonyl groups to stabilise the singlet $\sigma^2\pi^0$ configuration[30] or incorporating the carbene into a 6-membered ring with two double bonds to stabilise the singlet $\sigma^0\pi^2$ configuration.[31] The formation of carbonyl carbenes is a commonly encountered theme in this

thesis; the conjugation of the electron lone pair of the carbene into the carbonyl functional group is achieved by having the carbene $sp_2$-orbital orthogonal to the carbonyl plane. This geometry allows the electron pair to donate into the carbonyl orbital, as is illustrated in scheme 2.6.

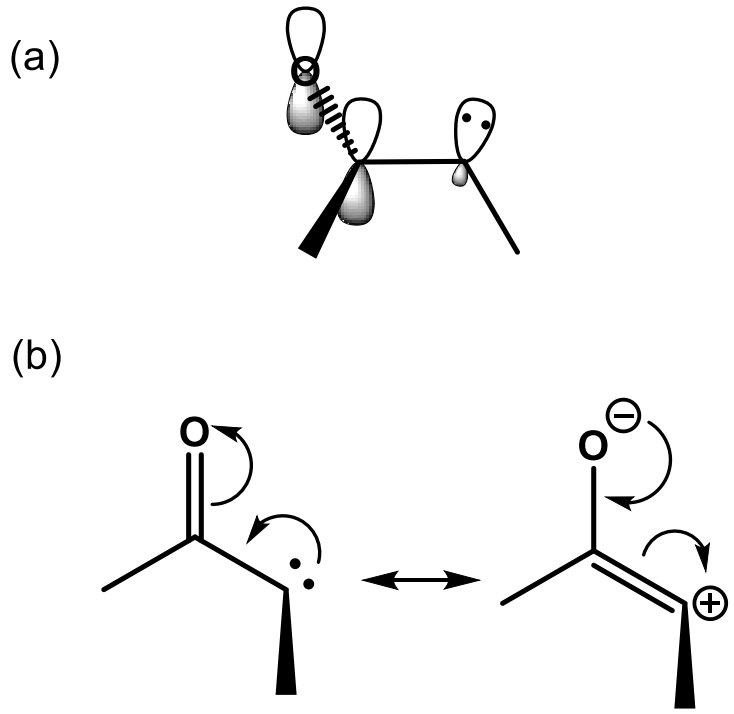


Scheme 2.6 – (a) Geometry of the carbene lone pair with respect to the carbonyl π atomic orbitals. (b) Resonance forms of carbonyl carbenes.

The ground state multiplicity of carbenes can also be altered by the choice of solvent. For example, Ar−C−$CO_2CH_3$ has a triplet ground state in cyclohexane, but a singlet ground state in acetonitrile or dichloromethane.[32] Tomioka and coworkers reported that the reactivity of phenylcarbene towards a mixture of alcohols could be altered by the use of dioxane as a solvent instead of cyclohexane.[33] They interpreted the change in reactivity as a result of specific interactions of dioxane with the carbene. Similar arguments were put forward for picosecond optical grating calorimetry experiments for the reaction of singlet methylene with benzene (Buchner ring-expansion), which identified two heat depositions suggesting the formation of an intermediate species. Carbene-benzene complexes were suggested to account for the observations. However, it is now thought the Buchner ring-expansion proceeds through a cyclopropane intermediate,[34] and therefore the two heat depositions are likely to arise from the formation of this intermediate and not the carbene-benzene complex. Nevertheless, the specific interaction of nucleophilic solvents with carbene

intermediates has been the focus of numerous studies.[35-37] However, these were often indirect and so did not provide direct evidence for carbene-solvent complexation.

With modern laser techniques, the solvation dynamics of carbenes can now be directly monitored by transient electronic absorption spectroscopy (TEAS). Platz and co-workers photoexcited samples of *p*-biphenylyltrifluoromethyl diazomethane in various solvents, and identified the development of a transient absorption band at ~400 nm within the instrument response (~300 fs) which they assigned to the formation of carbene intermediates. Over the course of several tens-of-picoseconds, they observed a progressive redshift in the peak maxima which they attributed to specific interactions of the solvent with the vacant p-orbital of the carbene.[35] This interaction is conceptually similar to ylide formation and will be referred to as an ylidic interaction herein. The ylidic interactions of nucleophiles with carbenes have also been computationally studied; for example, Hadad and co-workers examined the fluorocarbene-$(methanol)_3$ cluster using a stochastic sampling method to predict various cluster candidates, and characterised them using atoms-in-molecule analysis and natural bond orders.[38] They identified characteristic traits which distinguish ylide formation and ylidic interactions: notable characteristics include the $C_c$-O bond length and bond order, where $C_c$-O is the distance between the carbene-carbon and the donating oxygen atom of methanol. Ylides were found to have bond lengths of ~1.5-1.7 Å and bond orders of ~0.5, whereas ylidic interactions were found to have $C_c$-O distances greater than 2.2 Å with bond orders of ~0.2. The total cluster stabilisation for the ylidic interaction was found to be as high as ~145 kJ $mol^{-1}$.

Singlet carbenes are often formed because of spin-conservation after photoexciting or thermally activating diazo-compounds. The singlet carbene can then undergo reaction or intersystem crossing to the ground-state triplet species, complicating reaction outcomes. Therefore, carbene intersystem crossing rates have attracted the attention of numerous spectroscopy studies.[39-41] The intersystem crossing of diphenylmethylene (DPM) is a notably interesting case. DPM has a triplet ground state, however the energy gap to the first excited singlet state is as little as ~13 kJ $mol^{-1}$. As a consequence, a rapid equilibrium exists between population in the singlet and triplet states.[39] Solvation has been shown to alter intersystem crossing rates of carbenes, with more polar solvents stabilising the singlet state relative to the triplet state. Lowering the singlet-triplet energy gap was proposed to reduce the vibronic coupling between the two states, slowing the rate of intersystem crossing.[40] However further

work has identified that halogenated solvents also slowed the rate of intersystem crossing despite not following the trend in polarity. Instead, the coordination of the nucleophilic solvent to the vacant p-orbital of the carbene was suggested to cause significant geometry differences between the stabilised singlet carbenes and the triplet state, creating a barrier to intersystem crossing.[41]

### 2.2.3 Ketenes

Ketenes contain a >C=O=O functional group and can be generated by various chemical reactions.[42] However, this thesis focuses on the formation of ketene intermediates from the photoexcitation of diazo carbonyl compounds through the so-called Wolff-rearrangement.

The ketene-forming Wolff rearrangement (WR) of photo-excited α-diazocarbonyl compounds is shown in Scheme 2.7 and can follow either concerted or stepwise pathways, the latter via singlet carbonyl carbene intermediates which may also undergo competing reactions. This photochemical rearrangement is used in a range of synthetic processes including ring contractions,[43-44] and the Arndt-Eistert synthesis of carboxylic acids.[45] However, as is discussed in Section 2.2.2, direct observations of the carbenes, as well as other proposed intermediates in their reactions, remain rare because of their high reactivity and hence short lifetimes.

(a) Stepwise Wolff-rearrangment

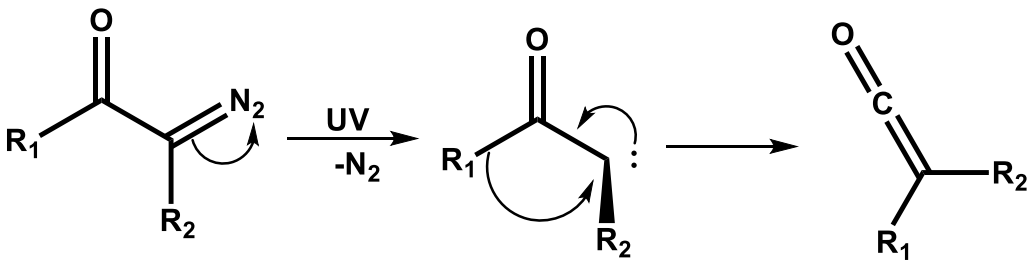


(b) Concerted Wolff-rearrangment

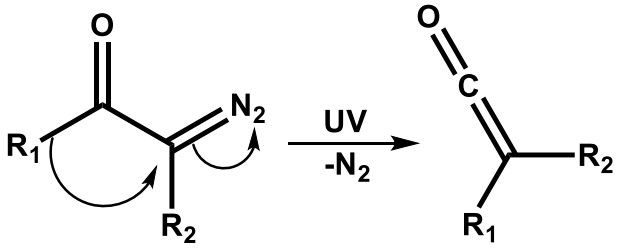


Scheme 2.7 – Proposed mechanisms for the formation of ketenes from the photoexcitation of α-diazo carbonyl compounds: (a) Stepwise Wolff-rearrangement; (b) Concerted Wolff-rearrangement.

One notable example of observation of WR pathways is the report by Platz and co-workers of transient absorption spectroscopy (TAS) measurements with infrared (IR) and ultraviolet (UV) probe wavelengths following the photoexcitation of the α-diazocarbonyl compound azibenzil in acetonitrile (ACN). WR was shown to occur on ultrafast (<0.3 ps) and slower (700 ps) timescales by monitoring the product ketene stretching mode at 2113 $cm^{-1}$, consistent with contributions from both the concerted and stepwise WR pathways after photoexcitation. This interpretation was supported by the observed kinetics of a near-UV transient absorption band at 370 nm which was assigned to a singlet carbene.[11] Platz and co-workers found further evidence for ketene formation from a carbene isomerisation in the photoexcitation of p-biphenylyl diazo ketone. The observed lifetime of the singlet carbene depended on the solvent, with ACN and tetrahydrofuran (THF) argued to stabilise the singlet carbene and suppress WR. In contrast, in methanol (MeOH) a shorter singlet carbene lifetime was postulated to be a consequence of reaction with the solvent in competition with Wolff rearrangement, but reaction products were not assigned.[46]

α-Diazocarbonyl compounds typically adopt locally planar geometries, and the partial double C-C bond character results in syn and anti-isomers.[47] Experimental evidence points to selectivity towards the concerted and stepwise WRs from the syn and anti-isomers respectively.[48] For example, photo-excited methyl 2-diazo-(2-naphthyl) acetate, 99% of which adopts an anti-form, undergoes only the stepwise WR,[49] [50] whereas the cyclic diazo-compounds diazonaphthoquinone (DNQ) and 5-diazomeldrum acid (DMA) (structures are shown in scheme 2.8), which are locked in their syn-isomers, favour concerted WR.[51-52]

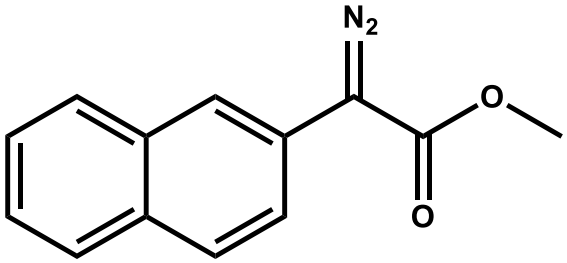


Methyl 2-diazo-(2-naphthyl) acetate

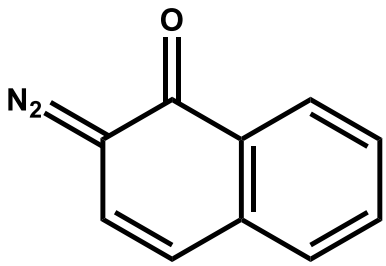


Diazonaphthoquinone (DNQ)

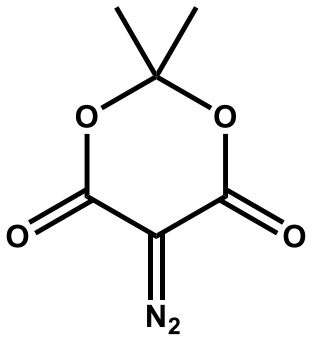


5-Diazomeldrum acid (DMA)

Scheme 2.8 – Structures of Methyl 2-diazo-(2-naphthyl_ acetate and 5-diazomeldrum acid

Computational methods have further explored the proposed mechanisms for the WR using electronically non-adiabatic trajectory simulations.[53] Figure 2.1 shows a schematic diagram of the potential energy surface and is used as a guide for the photodynamics observed. In these calculations, $S_2 \leftarrow S_0$ ($\pi^* \leftarrow \pi$) photo-excited DNQ showed rapid internal conversion to the $S_1$ state (with $\pi^*$ character localized on the diazo group), where C-N extension brought the molecule to an $S_1/S_0$ conical intersection.[53] After ultrafast decay to the $S_0$ state through this intersection, the C-N coordinate continued to extend to form a hot singlet carbene that either vibrationally cooled or rearranged to a ketene within ~10 ps. A competing pathway to ketene formation involving simultaneous C-C shortening and C-N elongation indicated concerted WR within 400 fs. Recent non-adiabatic trajectory calculations for photo-excited DMA identified similar mechanisms for WR as well as an $S_1$ pathway to singlet carbene formation.[54] The concerted WR in DMA happened within 500 fs, which is consistent with previous reports.[51]

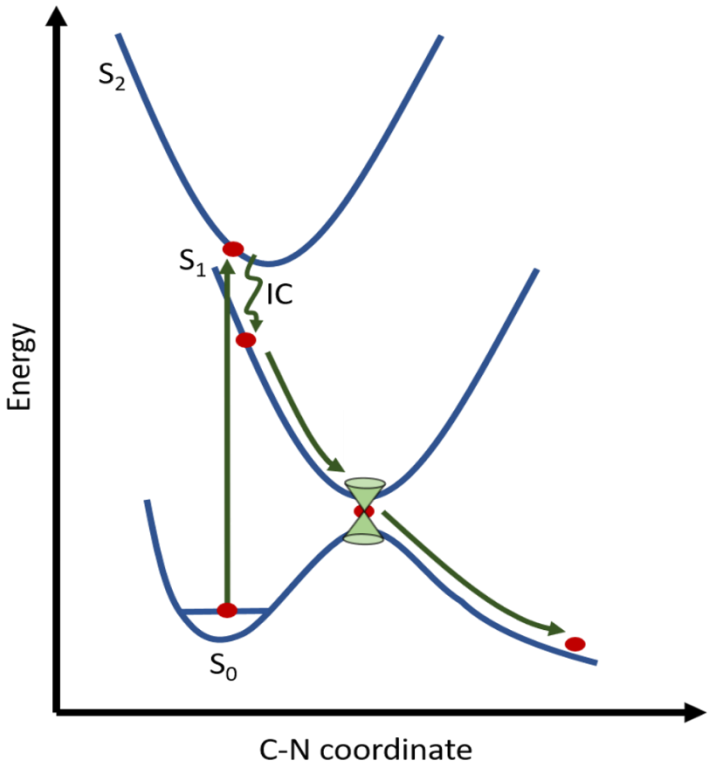


Figure 2.1 – Schematic potential energy curves for the photoinduced loss of $N_2$ from DNQ leading to a stepwise Wolff rearrangement. Red circles are used to track positions along the PES and green arrows show the reaction pathways. The green funnel shows the location of a conical intersection.

The extent to which Wolff rearrangement occurs is influenced by the nature of the migratory group.[55] Here, the focus is on the effect alkoxy groups have on the propensity for WR because of the relevance to studies reported in Chapters 4 and 5. In prior experimental studies of diazo-3-ketocaboxylates, the ester functionality was found not to migrate.[56-57] These conclusions derived from stable product analysis, but ultrafast time resolved spectroscopy offers direct observation of the reaction pathways. For example, photoexcitation of a biphenyl diazo ester produced a singlet carbene, with no evidence for Wolff rearrangement,[46] in contrast with the keto-derivative where both stepwise and concerted WR pathways were active.[10] The reluctance of alkoxy groups to migrate via WR is likely to be a consequence of higher activation barriers because of the energy required to break the ester resonance.[46]

### 2.2.4 Ylides

Ylides are examples of zwitterionic compounds which have positive and negative point charges in adjacent positions. Often these species are synthesised *in situ* due to their high reactivities, although methods of generating stabilised ylides are known.[58-60] Ylides are ubiquitous in synthetic chemistry as well being found as intermediates in biochemical processes. Arguably, the Wittig reagent is the most well-known ylide; it was discovered in 1954, and this discovery was recognized by a Nobel prize in 1979. The Wittig reagent consists of a phosphine substituent directly attached to a negatively charged carbon atom and is still widely used in modern synthetic reactions. However, great efforts are still being invested in understanding how the Wittig reagent, among other ylides and reactive intermediates, interacts with solvent molecules.

In the presence of alcohols, ethers, nitriles or other nucleophiles, singlet carbenes react to form ylides. Direct observation of ACN ylides has been reported in a low-temperature matrix,[61] but most evidence of ylide formation under ambient conditions is inferred from the reaction products. Exceptions include the use of Transient vibrational absorption spectroscopy (TVAS) to reveal spectral bands of intermediates from the photoexcitation of ethyl diazoacetate in ACN, one of which was attributed to an ylide on the basis of calculated vibrational mode frequencies.[12] Further such observations of ACN and dioxane derived ylides have also been reported.[12, 62] The mechanisms by which singlet carbenes react with alcohols to make ethers are thought to follow the three pathways shown in Scheme 2.9, with their relative significance depending on the electron donating or withdrawing character of $R_1$ and $R_2$ substituents.[14] Carbocation intermediates of the protonation of diphenylcarbene were previously identified by TAS with a probe spanning the near-UV and visible regions,[63-64] but the formation of the alcohol-ylide intermediate species has received less attention. Xue *et al*. presented direct evidence for an alcohol ylide, in this case from reaction of singlet carboethoxycarbene,[12] but used an ester carbene to suppress WR. Hence, any competition between WR and bimolecular reaction pathways was not examined.

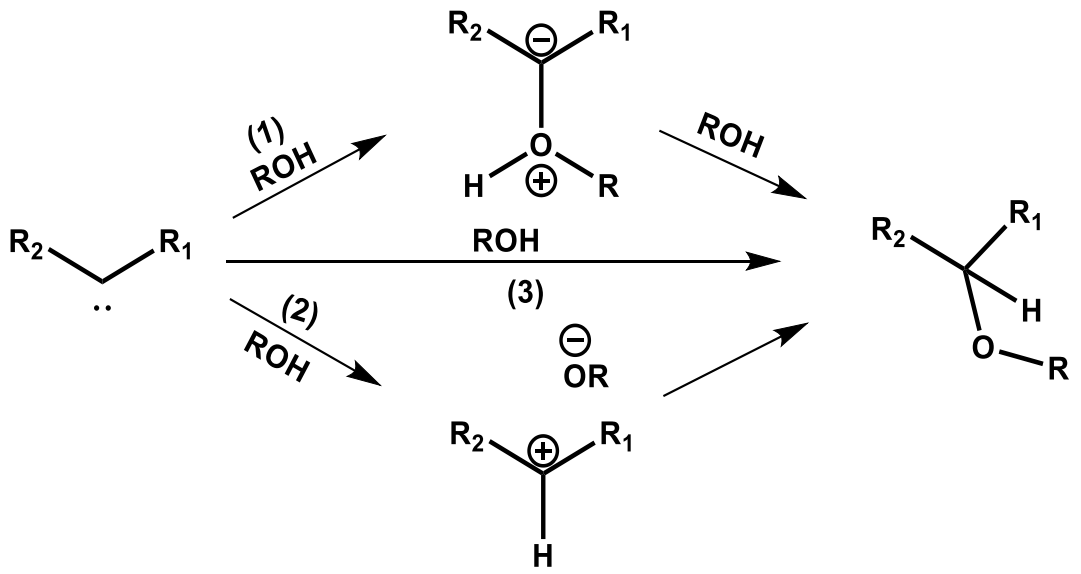


Scheme 2.9 – Proposed pathways for singlet carbene reaction with an alcohol to make an ether.

**2.3 Photochemistry of aromatic compounds**

Chapter 6 of this thesis describes an investigation of the photochemistry of the heterocyclic molecule 2-aminothiazole in various solvents. Therefore, this section introduces the photochemistry of aromatic compounds, and will be used to guide the interpretation of TAS datasets presented in Chapter 6.

The photochemistry of aromatic compounds has received considerable attention,[65-68] and has importance in synthetic[69-71] and biological chemistry.[68, 72-73] Of particular interest are πσ* states which refer to the PESs accessed by a σ*←π electronic transition, either directly or indirectly by passage through a conical intersection with a higher lying excited state. The importance of these dissociative πσ* states has been shown for numerous photochemical reactions.[65, 67, 74] For example, the πσ* PES of imidizole is dissociative with respect to the N-H bond, with a conical intersection with the $S_0$ state at planar geometries and extended N-H bond distances. Gas phase experiments have shown that direct photoexcitation to the πσ* state results in N-H bond fission to form an H atom and partner radicals with high kinetic energy release and a anisotropic recoil velocity distribution.[75] Similar N-H photofragmentation pathways have been found in pyrrole.[76] In both cases, the photoexcitation to the optically bright ππ* states leads to N-H bond fission with high and low total kinetic energy release components. The high kinetic energy release channel has an anisotropic recoil velocity distribution suggesting relaxation to the πσ* state and subsequent

N-H bond fission. The low total kinetic energy release component has no recoil anisotropy and that is suggestive of dissociation from vibrationally excited $S_0$ molecules.[75-76] Total kinetic energy release experiments and supporting theoretical studies have been used to show that phenol molecules excited to the bright ππ* state at wavelengths <248 nm rapidly pass through a high energy $^1$ππ*/$^1$πσ* conical intersection, resulting in O-H fission products with high translational energy. At longer wavelengths, products are formed with lower translational energy. The initially proposed explanation was that the $^1$ππ*/$^1$πσ* conical intersection cannot be reached, and instead 'slow' internal conversion from the $^1$ππ* state to the $S_0$ state places enough energy into the O-H stretching mode to reach the $^1$πσ* surface for O-H fission to occur, resulting in excess energy in certain vibrational modes of the products.[77-78] However, TEAS and velocity map imaging experiments suggest H-atom tunnelling to be responsible for the formation of photoproducts at longer wavelengths,[79-80] and this interpretation is supported by theoretical studies.[81-83] The findings in phenol were analogous to pyrrole,[84-85] suggesting common dissociation pathways involving $^1$πσ* states. The studies discussed so far have dealt with the photochemistry of isolated molecules; in reality, molecules are rarely isolated and the role of solvent on the photochemistry of such systems must also be considered.

### 2.3.1 The role of solvents in the photochemistry of heteroaromatic molecules

The influence of solvation on dissociative πσ* surfaces has recently started to be explored experimentally and computationally. For example, N-H bond fission on the πσ* surface has been shown to be less efficient in pyrrole-argon clusters compared to isolated monomers. Calculations suggest that the πσ* state is destabilised by the cluster, and the N-H coordinate is no longer fully dissociative, removing the πσ*/$S_0$ conical intersection at extended N-H distances and preventing dissociation.[86] Similar findings have been demonstrated for pyrrole-xenon clusters.[87-88] In contrast, pyrrole-ammonia clusters have been shown to undergo excited state H-atom transfer (ESHT) to the ammonia cluster.[89-90] David *et al.* used a supersonic jet to form the clusters and probe them in a time-of-flight mass spectrometer, from which they found a relatively long (~10 ps) lifetime of the excited pyrrole cluster and formation of $NH_4$-ammonia cluster products. With support from CASSCF calculations, the authors invoked an intermediate state to the ESHT process and, on this basis, discounted direct N-H rupture. They instead proposed an excited state proton transfer mechanism, whereby an electron was first transferred to the solvent, followed by the ejection of a proton

in a step-wise mechanism.[89] Rubio-Lago *et al.* used velocity map imaging to follow the same reaction, but found no evidence for the long-lived excited state. Instead, the authors preferred to invoke direct N-H rupture of the initially excited cluster.[90] TVAS measurements for the $\pi^* \leftarrow \pi$ excitation of phenol–$(NH_3)_3$ clusters identified the formation of $NH_4$ radical products, also suggestive of an ESHT from the phenol to the adjacent $NH_3$.[91] Theoretical studies suggested that the ESHT occurred through the $^1\pi\pi^*/^1\pi\sigma^*$ conical intersection and found the $^1\pi\sigma^*$ state of phenol to be stabilised by hydrogen bond formation, reducing the energy required to reach the $^1\pi\pi^*/^1\pi\sigma^*$ conical intersection.[92-93] Although the study of small clusters can give insights into the role solvents play in the photochemistry of heteroaromatic molecules, a fluctuating solution phase environment is more dynamical, and bulk solvent properties can influence the photochemistry of species.

Solution phase TAS measurements of adenine in $D_2O$ revealed contrasting photochemistry compared to gas phase experiments. The gas phase photochemistry of adenine showed N-H bond fission,[94] but solution phase experiments found no evidence that such a pathway exists.[95] The solution phase photochemistry of phenol in cyclohexane was similar to in the gas-phase.[96] In $H_2O$, phenol still shows O-H bond fission, but also the formation of solvated electrons.[74] Whether the bond fission pathway undergoes excited state proton transfer, H-atom transfer, autoionisation, or an excited-state proton-coupled transfer has been investigated by Oliver *et al.*, who provided evidence for the formation of $PhOH^+$ from the 200-nm photoexcitation of phenol in <200 fs; the fast decay of $PhOH^+$ to form $PhO^\cdot$ radicals and solvated electrons suggested an autoionisation pathway. Interestingly, the 267 nm excitation of phenol also showed the formation of $PhO^\cdot$ radicals and solvated electrons, but on ~ns timescales. Here, sub-ps autoionisation was not observed, and instead the $S_1$ state vibrationally cooled over a picosecond timescale, reducing the energy of the system. Oliver *et al*. argued that the total energy of the system lies near the threshold for autoionisation, reflecting the slower yield of $PhO^\cdot$ radicals.[74]

Dissociative $\pi\sigma^*$ states have also been suggested to contribute to the ring-opening of heterocyclic molecules.[67, 97-100] The challenge for such gas-phase experiments is that although mass spectrometry photochemical studies are well suited to detection of H atom ejection and dissociation pathways because the masses of photoproducts are distinguishable from the parent molecule, they cannot identify ring-opening isomerisation and tautomerisation

pathways. More recent experiments in solution have utilised substituted heterocyclic molecules bearing 'reporter' groups. For example, 2-thiophenone has a carbonyl substituent which is well suited for TVAS studies in solution. These experiments by Ashfold and coworkers provided unambiguous evidence for the photoinduced ring-opening in the solution phase, identifying ketene stretching modes of a ring-opened product. In this case, ~60% of photoexcited molecules were predicted to ring-closed again after photoexcitation. Similar ring-opening pathways of carbonyl bearing heterocyclic molecules were also found.[67] The model compound 1,3-cyclohexadiene has been subjected to extensive investigation for its photoinduced ring-opening pathways,[101-110] but observation of ring-opening of aromatic non-substituted heterocycles still remains scarce in solution phase experiments.

As mentioned earlier, pyrrole exhibits ultrafast N-H bond fission,[76] and theory suggests the presence of conical intersections at ring-extended geometries and ring-distortions.[111] However, ring extensions and deformations involving heavier atoms are too slow to compete with N-H bond fission. In contrast, N-methylpyrrole exhibits a slower, several-hundred picosecond, N-Me dissociation pathway. Excitation at longer wavelengths was found to reduce the lifetime of N-methylpyrrole, and the kinetic energy of methyl fragments decreased, which was rationalised by contributions from competing ring-extension and ring-puckering pathways at these longer excitation wavelengths.[112-113] Ring-opening and ring-puckering pathways have also been suggested to compete with N-H bond fission in 2-aminooxazole,[114-115] where non-adiabatic trajectories found 20% of photoexcited molecules underwent a proton transfer mechanism (where an electron is first transferred to the solvent, followed by a proton in a stepwise mechanism) with the remaining fraction relaxing through ring-opening or ring-puckering channels.[115]

**2.4 Conclusion**

Photo-excited diazo compounds are a rich source of reactive intermediates which, due to their intrinsic short-lived lifetimes, can only be directly observed using ultrafast spectroscopy methods. The role of solvation in the chemical dynamics of carbene intermediates has attracted considerable interest, but the mechanistic steps for the reactions of carbenes and the solvation dynamics of ylides still require further investigation. Chapters 4 and 5 address some of these topics using ultrafast transient absorption spectroscopy, and provide deep new

insights into the role of solvents on the chemical dynamics of intermediates formed from the photoexcitation of diazo compounds.

Furthermore, the photo-dynamics of aromatic compounds has been extensively studied in the gas phase,[65, 68] with some studies also investigating the photodynamics in solution, but the role solvents play in the photochemistry of these aromatic compounds remains incompletely understood. Chapter 6 reports solution-phase TAS measurements of 2-aminothiazole and provides new insights about competing N-H fission and ring-opening pathways of amino-heterocycles.

**References**


1. Varghese, J. J.; Mushrif, S. H. Origins of complex solvent effects on chemical reactivity and computational tools to investigate them: a review. *React. Chem. Eng.* **2019,** *4*, 165-206.
2. Balakrishnan, G.; Sahoo, S. K.; Chowdhury, B. K.; Umapathy, S. Understanding solvent effects on structure and reactivity of organic intermediates: a Raman study. *Faraday Discuss.* **2010,** *145*, 443-466.
3. Reichardt, C. Solvents and Solvent Effects: An Introduction. *Org. Process Res. Dev.* **2007,** *11*, 105-113.
4. Truong, T. N. Solvent Effects on Structure and Reaction Mechanism: A Theoretical Study of [2 + 2] Polar Cycloaddition between Ketene and Imine. *J. Phys. Chem. B* **1998,** *102*, 7877-7881.
5. Capurso, M.; Gette, R.; Radivoy, G.; Dorn, V. The Sn2 Reaction: A Theoretical-Computational Analysis of a Simple and Very Interesting Mechanism. *Proc.* **2019,** *41*, 81.
6. Onufriev, A. V.; Case, D. A. Generalized Born Implicit Solvent Models for Biomolecules. *Annu Rev Biophys* **2019,** *48*, 275-296.
7. Boereboom, J. M.; Fleurat-Lessard, P.; Bulo, R. E. Explicit Solvation Matters: Performance of QM/MM Solvation Models in Nucleophilic Addition. *J. Chem. Theory. Comp.* **2018,** *14*, 1841-1852.
8. Curtius, T. Ueber die Einwirkung von salpetriger Säure auf salzsauren Glycocoläther. *Berichte der deutschen chemischen Gesellschaft* **1883,** *16*, 2230-2231.
9. Burdzinski, G.; Platz, M. S. Ultrafast time-resolved studies of the photochemistry of diazo carbonyl compounds. *J. Phys. Org. Chem.* **2010,** *23*, 308-314.
10. Burdzinski, G. T.; Wang, J.; Gustafson, T. L.; Platz, M. S. Study of Concerted and Sequential Photochemical Wolff Rearrangement by Femtosecond UV−vis and IR Spectroscopy. *J. Am. Chem. Soc.* **2008,** *130*, 3746-3747.
11. Burdzinski, G.; Zhang, Y.; Wang, J.; Platz, M. S. Concerted Wolff Rearrangement in Two Simple Acyclic Diazocarbonyl Compounds. *J. Phys. Chem. A* **2010,** *114*, 13065-13068.
12. Xue, J.; Luk, H. L.; Platz, M. S. Direct Observation of a Carbene-Alcohol Ylide. *J. Am. Chem. Soc.* **2011,** *133*, 1763-1765.
13. Platz, M. S. A Perspective on Physical Organic Chemistry. *J. Org. Chem.* **2014,** *79*, 2341-2353.
14. Nuno R. Candeias; Carlos A. M. Afonso Developments in the Photochemistry of Diazo Compounds. *Curr. Org. Chem.* **2009,** *13*, 763-787.
15. Ciszewski, Ł. W.; Rybicka-Jasińska, K.; Gryko, D. Recent developments in photochemical reactions of diazo compounds. *Org. Biomol. Chem.* **2019,** *17*, 432-448.
16. Xiang, Y.; Wang, C.; Ding, Q.; Peng, Y. Diazo Compounds: Versatile Synthons for the Synthesis of Nitrogen Heterocycles via Transition Metal-Catalyzed Cascade C–H Activation/Carbene Insertion/Annulation Reactions. *Adv. Synth. Catal.* **2019,** *361*, 919-944.

17. Anciaux, A. J.; Demonceau, A.; Noels, A. F.; Hubert, A. J.; Warin, R.; Teyssie, P. Transition-metal-catalyzed reactions of diazo compounds. 2. Addition to aromatic molecules: catalysis of Buchner's synthesis of cycloheptatrienes. *J. Org. Chem.* **1981,** *46*, 873-876.
18. Zhu, S.-F.; Zhou, Q.-L. Iron-catalyzed transformations of diazo compounds. *Natl. Sci. Rev.* **2014,** *1*, 580-603.
19. Candeias, N. R.; Gois, P. M. P.; Veiros, L. F.; Afonso, C. A. M. C−H Carbene Insertion of α-Diazo Acetamides by Photolysis in Non-Conventional Media. *J. Org. Chem.* **2008,** *73*, 5926-5932.
20. Ford, A.; Miel, H.; Ring, A.; Slattery, C. N.; Maguire, A. R.; McKervey, M. A. Modern Organic Synthesis with α-Diazocarbonyl Compounds. *Chem. Rev.* **2015,** *115*, 9981-10080.
21. Singh, M. S., Reactive Intermediates in Organic Chemistry : Structure and Mechanism. Wiley-VCH: 2014.
22. Gerbig, D.; Ley, D. Computational methods for contemporary carbene chemistry. Wiley Interdiscip. Rev. *Comp. Mol. Sci.* **2013,** *3*, 242-272.
23. Luk, H. L.; Vyas, S.; Hadad, C. M., Computational Methods for the Study of Carbenes and their Excited States. In *Contemporary Carbene Chemistry*, 2013; pp 107-130.
24. Kassaee, M. Z.; Shakib, F. A.; Momeni, M. R.; Ghambarian, M.; Musavi, S. M. Carbenes with Reduced Heteroatom Stabilization: A Computational Approach. *J. Org. Chem.* **2010,** *75*, 2539-2545.
25. Rahmi, K.; Kassaee, M. Z.; Khorshidvand, N. Comparison of bis(alkylthio)carbenes by density functional and Second-order Møller–Plesset perturbation theory. *J. Phys. Org. Chem.* **2021,** *34*, e4122.
26. Koohi, M.; Bastami, H. Substituted Hammick carbenes: The effects of fused rings and hetero atoms through DFT calculations. *J. Phys. Org. Chem.* **2020,** *33*, e4023.
27. Haerizade, B. N.; Kassaee, M. Z.; Zandi, H.; Koohi, M.; Ahmadi, A. A. Ylide stabilized carbenes: a computational study. *J. Phys. Org. Chem.* **2014,** *27*, 902-908.
28. Kassaee, M. Z.; Koohi, M.; Mohammadi, R.; Ghavami, M. 2,2,9,9-Tetramethylcyclonona-3,5,7-trienylidene vs. its heterocyclic analogues: A quest for stable carbenes at DFT. *Struct. Chem.* **2013,** *26*, 908-916.
29. Ghafarian Shirazi, R.; Neese, F.; Pantazis, D. A. Accurate Spin-State Energetics for Aryl Carbenes. *J. Chem. Theory. Comp.* **2018,** *14*, 4733-4746.
30. Scott, A. P.; Platz, M. S.; Radom, L. Singlet−Triplet Splittings and Barriers to Wolff Rearrangement for Carbonyl Carbenes. *J. Am. Chem. Soc.* **2001,** *123*, 6069-6076.
31. Chen, B.; Rogachev, A. Y.; Hrovat, D. A.; Hoffmann, R.; Borden, W. T. How to Make the $\sigma_0\pi_2$ Singlet the Ground State of Carbenes. *J. Am. Chem. Soc.* **2013,** *135*, 13954-13964.
32. Wang, J.; Burdzinski, G.; Kubicki, J.; Platz, M. S. Ultrafast UV−Vis and IR Studies of p-Biphenylyl Acetyl and Carbomethoxy Carbenes. *J. Am. Chem. Soc.* **2008,** *130*, 11195-11209.
33. Tomioka, H.; Ozaki, Y.; Izawa, Y. Modification of singlet carbene reactivities by solvent. *Tetrahedron* **1985,** *41*, 4987-4993.
34. McNamara, O. A.; Maguire, A. R. The norcaradiene–cycloheptatriene equilibrium. *Tetrahedron* **2011,** *67*, 9-40.
35. Wang, J.; Kubicki, J.; Gustafson, T. L.; Platz, M. S. The Dynamics of Carbene Solvation: An Ultrafast Study of p-Biphenylyltrifluoromethylcarbene. *J. Am. Chem. Soc.* **2008,** *130*, 2304-2313.
36. Standard, J. M. Effects of Solvation and Hydrogen Bond Formation on Singlet and Triplet Alkyl or Aryl Carbenes. *J. Phys. Chem. A* **2017,** *121*, 381-393.
37. Hadad, C. Z.; Jenkins, S.; Flórez, E. Unusual solvation through both p-orbital lobes of a carbene carbon. *J. Chem. Phys.* **2015,** *142*, 094302.
38. Gómez, S.; Restrepo, A.; Hadad, C. Z. Theoretical tools to distinguish O-ylides from O-ylidic complexes in carbene–solvent interactions. *Phys. Chem. Chem. Phys.* **2015,** *17*, 31917-31930.
39. Eisenthal, K. B.; Turro, N. J.; Sitzmann, E. V.; Gould, I. R.; Hefferon, G.; Langan, J.; Cha, Y. Singlet-triplet interconversion of diphenylmethylene. Energetics, dynamics and reactivities of different spin states. *Tetrahedron* **1985,** *41*, 1543-1554.

40. Sitzmann, E. V.; Langan, J.; Eisenthal, K. B. Intermolecular effects on intersystem crossing studied on the picosecond timescale: the solvent polarity effect on the rate of singlet-to-triplet intersystem crossing of diphenylcarbene. *J. Am. Chem. Soc.* **1984,** *106*, 1868-1869.
41. Wang, J.; Kubicki, J.; Peng, H.; Platz, M. S. Influence of Solvent on Carbene Intersystem Crossing Rates. *J. Am. Chem. Soc.* **2008,** *130*, 6604-6609.
42. Allen, A.; Tidwell, T. Recent advances in ketene chemistry. *Arkivoc* **2016,** *2016*, 415-490.
43. Simon, R.; Jurij, S.; Branko, S. Ring Contractions of 4-Oxoquinolizine-3-diazonium Tetrafluoroborates, by an Aza Wolff Rearrangement, to Alkyl Indolizine3carboxylates. *Eur. J. Org. Chem.* **2001,** *2001*, 3705-3709.
44. Wang, B.; Xie, Y.; Yang, Q.; Zhang, G.; Gu, Z. Total Synthesis of Aquatolide: Wolff Ring Contraction and Late-Stage Nozaki–Hiyama–Kishi Medium-Ring Formation. *Org. Lett.* **2016,** *18*, 5388-5391.
45. Wilds, A. L.; Meader, A. L. The Use of Higher Diazohydrocarbons in the Arndt-Eistert Synthesis. *J. Org. Chem.* **1948,** *13*, 763-779.
46. Wang, J.; Burdzinski, G.; Kubicki, J.; Platz, M. S. Vis and IR Studies of p-Biphenylyl Acetyl and Carbomethoxy Carbenes. *J. Am. Chem. Soc.* **2008,** *130*, 11195-11209.
47. Pecile, C.; Föffani, A.; Ghersetti, S. The Interaction of Diazocarbonyl Compounds with Hydroxylic Solvents. *Tetrahedron* **1964,** *20*, 823-829.
48. Kaplan, F.; Meloy, G. K. The Structure of Diazoketones. A Study of Hindered Internal Rotation1,2. *J. Am. Chem. Soc.* **1966,** *88*, 950-956.
49. Wang, Y.; Yuzawa, T.; Hamaguchi, H.-O.; Toscano, J. P. Time-Resolved IR Studies of 2-Naphthyl(carbomethoxy)carbene: Reactivity and Direct Experimental Estimate of the Singlet/Triplet Energy Gap. *J. Am. Chem. Soc.* **1999,** *121*, 2875-2882.
50. Zhu, Z.; Bally, T.; Stracener, L. L.; McMahon, R. J. Reversible Interconversion between Singlet and Triplet 2-Naphthyl(carbomethoxy)carbene. *J. Am. Chem. Soc.* **1999,** *121*, 2863-2874.
51. Lippert, T.; Koskelo, A.; Stoutland, P. O. Direct Observation of a Photoinduced Wolff Rearrangement in PMMA Using Ultrafast Infrared Spectroscopy. *J. Am. Chem. Soc.* **1996,** *118*, 1551-1552.
52. Wolpert, D.; Schade, M.; Brixner, T. Femtosecond midinfrared study of the photoinduced Wolff rearrangement of diazonaphthoquinone. *J. Chem. Phys.* **2008,** *129*, 094504.
53. Cui, G.; Thiel, W. Photoinduced Ultrafast Wolff Rearrangement: A NonAdiabatic Dynamics Perspective. *Angew. Chem. Int. Ed.* **2013,** *52*, 433-436.
54. Xu, C.; Gu, F. L.; Zhu, C. An excited-state Wolff rearrangement reaction of 5-diazo Meldrum's acid: an ab initio on-the-fly nonadiabatic dynamics simulation. *Phys. Chem. Chem. Phys.* **2018,** *20*, 22681-22688.
55. Ogata, Y.; Sawaki, Y.; Ohno, T. Mechanism for oxidation of phenylacetylenes with peroxymonophosphoric acid. Oxirene as an intermediate inconvertible to ketocarbene. *J. Am. Chem. Soc.* **1982,** *104*, 216-219.
56. Gallucci, R. R.; Jones, M. Photolysis of methyl 3-diazo-2-oxopropionate. Wolff migration of the carbomethoxy group. *J. Org. Chem.* **1985,** *50*, 4404-4405.
57. Maier, G.; Reisenauer, H. P.; Sayrac, T. Oxirene - Intermediate or Transition state - Matrix Irradiation of Diazoketones. *Chem. Ber. Recl.* **1982,** *115*, 2192-2201.
58. Cuadro, A. M.; Novella, J. L.; Molina, A.; Alvarez-Builla, J.; Vaquero, J. J. Synthesis of highly stabilised ylides from N- [2- (1,3-benzazolylmethyl)]pyridinium salts. *Tetrahedron* **1990,** *46*, 6033-6046.
59. Oost, R.; Neuhaus, J. D.; Merad, J.; Maulide, N., Sulfur Ylides in Organic Synthesis and Transition Metal Catalysis. In *Modern Ylide Chemistry: Applications in Ligand Design, Organic and Catalytic Transformations*, Gessner, V. H., Ed. Springer International Publishing: Cham, 2018; pp 73-115.
60. Tamura, Y.; Miyamoto, T.; Eiho, J.; Taniguchi, H.; Nishimura, T.; Kita, Y. Synthesis of ylides stabilised by the 3-oxocyclohex-1-enyl group. *J. Chem. Soc., Perkin Trans. 1* **1974**, 105-107.

61. Naito, I.; Nakamura, K.; Kumagai, T.; Oku, A.; Hori, K.; Matsuda, K.; Iwamura, H. Formation of Nitrile Ylide by Addition of Carbene with Acetonitrile in a Low-Temperature Argon Matrix. *J. Phys. Chem. A* **1999,** *103*, 8187-8192.
62. Hoijemberg, P. A.; Moss, R. A.; Krogh-Jespersen, K. Reversible O-Ylide Formation in Carbene/Ether Reactions. *J. Phys. Chem. A* **2012,** *116*, 358-363.
63. Peon, J.; Polshakov, D.; Kohler, B. Solvent Reorganization Controls the Rate of Proton Transfer from Neat Alcohol Solvents to Singlet Diphenylcarbene. *J. Am. Chem. Soc.* **2002,** *124*, 6428-6438.
64. Belt, S. T.; Bohne, C.; Charette, G.; Sugamori, S. E.; Scaiano, J. C. Carbocation Formation via Carbene Protonation Studied by the Technique of Stopped-flow Laser-flash Photolysis. *J. Am. Chem. Soc.* **1993,** *115*, 2200-2205.
65. Ashfold, M. N. R.; King, G. A.; Murdock, D.; Nix, M. G. D.; Oliver, T. A. A.; Sage, A. G. πσ* excited states in molecular photochemistry. *Phys. Chem. Chem. Phys.* **2010,** *12*, 1218-1238.
66. Ashfold, M. N. R.; Murdock, D.; Oliver, T. A. A. Molecular Photofragmentation Dynamics in the Gas and Condensed Phases. *Annu. Rev. Phys. Chem.* **2017,** *68*, 63-82.
67. Ashfold, M. N. R.; Bain, M.; Hansen, C. S.; Ingle, R. A.; Karsili, T. N. V.; Marchetti, B.; Murdock, D. Exploring the Dynamics of the Photoinduced Ring-Opening of Heterocyclic Molecules. *J. Phys. Chem. Lett.* **2017,** *8*, 3440-3451.
68. Roberts, G. M.; Stavros, V. G. The role of πσ* states in the photochemistry of heteroaromatic biomolecules and their subunits: insights from gas-phase femtosecond spectroscopy. *Chem. Sci.* **2014,** *5*, 1698-1722.
69. Yang, Q.; He, Y.; Wang, T.; Zeng, L.; Zhang, Z. Synthesis of 3-heteroarylchromones via a photochemical reaction. *Mol. Divers.* **2016,** *20*, 9-16.
70. Elliott, L. D.; Berry, M.; Orr-Ewing, A. J.; Booker-Milburn, K. I. The Intramolecular Photometathesis of Pyrroles. *J. Am. Chem. Soc.* **2007,** *129*, 3078-3079.
71. Koovits, P. J.; Knowles, J. P.; Booker-Milburn, K. I. Conformationally Driven Two- and Three-Photon Cascade Processes in the Stereoselective Photorearrangement of Pyrroles. *Org. Lett.* **2016,** *18*, 5608-5611.
72. Görner, H. Photochemistry of DNA and related biomolecules: quantum yields and consequences of photoionization. *Journal of photochemistry and photobiology. B, Biology* **1994,** *26*, 117-39.
73. Li, J.-H.; Zuehlsdorff, T. J.; Payne, M. C.; Hine, N. D. M. Photophysics and Photochemistry of DNA Molecules: Electronic Excited States Leading to Thymine Dimerization. *J. Phys. Chem. C* **2018,** *122*, 11633-11640.
74. Oliver, T. A. A.; Zhang, Y.; Roy, A.; Ashfold, M. N. R.; Bradforth, S. E. Exploring Autoionization and Photoinduced Proton-Coupled Electron Transfer Pathways of Phenol in Aqueous Solution. *J. Phys. Chem. Lett.* **2015,** *6*, 4159-4164.
75. Devine, A. L.; Cronin, B.; Nix, M. G. D.; Ashfold, M. N. R. High resolution photofragment translational spectroscopy studies of the near ultraviolet photolysis of imidazole. *J. Chem. Phys.* **2006,** *125*, 184302.
76. Cronin, B.; Nix, M. G. D.; Qadiri, R. H.; Ashfold, M. N. R. High resolution photofragment translational spectroscopy studies of the near ultraviolet photolysis of pyrrole. *Phys. Chem. Chem. Phys.* **2004,** *6*, 5031-5041.
77. Nix, M. G. D.; Devine, A. L.; Cronin, B.; Dixon, R. N.; Ashfold, M. N. R. High resolution photofragment translational spectroscopy studies of the near ultraviolet photolysis of phenol. *J. Chem. Phys.* **2006,** *125*, 133318.
78. Ashfold, M. N. R.; Devine, A. L.; Dixon, R. N.; King, G. A.; Nix, M. G. D.; Oliver, T. A. A. Exploring nuclear motion through conical intersections in the UV photodissociation of phenols and thiophenol. *Proc. Natl. Acad. Sci.* **2008,** *105*, 12701.
79. Roberts, G. M.; Chatterley, A. S.; Young, J. D.; Stavros, V. G. Direct Observation of Hydrogen Tunneling Dynamics in Photoexcited Phenol. *J. Phys. Chem. Lett.* **2012,** *3*, 348-352.

80. Woo, K. C.; Kim, S. K. Multidimensional H Atom Tunneling Dynamics of Phenol: Interplay between Vibrations and Tunneling. *J. Phys. Chem. A* **2019,** *123*, 1529-1537.
81. Xie, C.; Ma, J.; Zhu, X.; Yarkony, D. R.; Xie, D.; Guo, H. Nonadiabatic Tunneling in Photodissociation of Phenol. *J. Am. Chem. Soc.* **2016,** *138*, 7828-7831.
82. Yang, K. R.; Xu, X.; Zheng, J.; Truhlar, D. G. Full-dimensional potentials and state couplings and multidimensional tunneling calculations for the photodissociation of phenol. *Chem. Sci.* **2014,** *5*, 4661-4680.
83. Dixon, R. N.; Oliver, T. A. A.; Ashfold, M. N. R. Tunnelling under a conical intersection: Application to the product vibrational state distributions in the UV photodissociation of phenols. *The J. Chem. Phys.* **2011,** *134*, 194303.
84. Roberts, G. M.; Williams, C. A.; Yu, H.; Chatterley, A. S.; Young, J. D.; Ullrich, S.; Stavros, V. G. Probing ultrafast dynamics in photoexcited pyrrole: timescales for 1πσ* mediated H-atom elimination. *Faraday Discuss.* **2013,** *163*, 95-116.
85. Xie, W.; Domcke, W.; Farantos, S. C.; Grebenshchikov, S. Y. State-specific tunneling lifetimes from classical trajectories: H-atom dissociation in electronically excited pyrrole. *J. Chem. Phys.* **2016,** *144*, 104105.
86. Poterya, V.; Profant, V.; Fárník, M.; Slavíček, P.; Buck, U. Experimental and theoretical study of the pyrrole cluster photochemistry: Closing the πσ* dissociation pathway by complexation. *J. Chem. Phys.* **2007,** *127*, 064307.
87. Rubio-Lago, L.; Zaouris, D.; Sakellariou, Y.; Sofikitis, D.; Kitsopoulos, T. N.; Wang, F.; Yang, X.; Cronin, B.; Devine, A. L.; King, G. A.; Nix, M. G. D.; Ashfold, M. N. R.; Xantheas, S. S. Photofragment slice imaging studies of pyrrole and the Xe···pyrrole cluster. *J. Chem. Phys.* **2007,** *127*, 064306.
88. Lipciuc, M. L.; Wang, F.; Yang, X.; Kitsopoulos, T. N.; Fanourgakis, G. S.; Xantheas, S. S. Cluster-Controlled Photofragmentation: The Case of the Xe–Pyrrole Cluster. *ChemPhysChem* **2008,** *9*, 1838-1841.
89. David, O.; Dedonder-Lardeux, C.; Jouvet, C.; Kang, H.; Martrenchard, S.; Ebata, T.; Sobolewski, A. L. Hydrogen transfer in excited pyrrole–ammonia clusters. *J. Chem. Phys.* **2004,** *120*, 10101-10110.
90. Rubio-Lago, L.; Amaral, G. A.; Oldani, A. N.; Rodríguez, J. D.; González, M. G.; Pino, G. A.; Bañares, L. Photodissociation of pyrrole–ammonia clusters by velocity map imaging: mechanism for the H-atom transfer reaction. *Phys. Chem. Chem. Phys.* **2011,** *13*, 1082-1091.
91. Ishiuchi, S.-i.; Sakai, M.; Daigoku, K.; Ueda, T.; Yamanaka, T.; Hashimoto, K.; Fujii, M. Picosecond time-resolved infrared spectra of photo-excited phenol–$(NH_3)_3$ cluster. *Chem. Phys. Lett.* **2001,** *347*, 87-92.
92. Ishiuchi, S.-i.; Daigoku, K.; Saeki, M.; Sakai, M.; Hashimoto, K.; Fujii, M. Hydrogen transfer in photo-excited phenol/ammonia clusters by UV–IR–UV ion dip spectroscopy and ab initio molecular orbital calculations. II. Vibrational transitions. *J. Chem. Phys.* **2002,** *117*, 7083-7093.
93. Daigoku, K.; Ishiuchi, S.-i.; Sakai, M.; Fujii, M.; Hashimoto, K. Photochemistry of phenol–$(NH_3)_n$ clusters: Solvent effect on a radical cleavage of an OH bond in an electronically excited state and intracluster reactions in the product $NH_4(NH_3)_{n-1}$ ($n \leqslant 5$). *J. Chem. Phys.* **2003,** *119*, 5149-5158.
94. Nix, M. G. D.; Devine, A. L.; Cronin, B.; Ashfold, M. N. R. Ultraviolet photolysis of adenine: Dissociation via the $\pi_1\sigma^*$ state. *J. Chem. Phys.* **2007,** *126*, 124312.
95. Roberts, G. M.; Marroux, H. J. B.; Grubb, M. P.; Ashfold, M. N. R.; Orr-Ewing, A. J. On the Participation of Photoinduced N–H Bond Fission in Aqueous Adenine at 266 and 220 nm: A Combined Ultrafast Transient Electronic and Vibrational Absorption Spectroscopy Study. *J. Phys. Chem. A* **2014,** *118*, 11211-11225.
96. Zhang, Y.; Oliver, T. A. A.; Ashfold, M. N. R.; Bradforth, S. E. Contrasting the excited state reaction pathways of phenol and para-methylthiophenol in the gas and liquid phases. *Faraday Discuss.* **2012,** *157*, 141-163.

97. Schalk, O.; Galiana, J.; Geng, T.; Larsson, T. L.; Thomas, R. D.; Fdez. Galván, I.; Hansson, T.; Vacher, M. Competition between ring-puckering and ring-opening excited state reactions exemplified on 5H-furan-2-one and derivatives. *J. Chem. Phys.* **2020,** *152*, 064301.
98. Schalk, O.; Geng, T.; Hansson, T.; Thomas, R. D. The ring-opening channel and the influence of Rydberg states on the excited state dynamics of furan and its derivatives. *J. Chem. Phys.* **2018,** *149*, 084303.
99. Miyazaki, J.; Takiyama, H.; Nakata, M. Isocyano compounds newly recognized in photochemical reaction of thiazole: matrix-isolation FT-IR and theoretical studies. *RSC Adv.* **2017,** *7*, 4960-4974.
100. Geng, T.; Ehrmaier, J.; Schalk, O.; Richings, G. W.; Hansson, T.; Worth, G.; Thomas, R. D. Time-Resolved Photoelectron Spectroscopy Studies of Isoxazole and Oxazole. *J. Phys. Chem. A* **2020,** *124*, 3984-3992.
101. Trulson, M. O.; Dollinger, G. D.; Mathies, R. A. Excited state structure and femtosecond ring-opening dynamics of 1,3-cyclohexadiene from absolute resonance Raman intensities. *J. Chem. Phys.* **1989,** *90*, 4274-4281.
102. Reid, P. J.; Doig, S. J.; Wickham, S. D.; Mathies, R. A. Photochemical ring-opening reactions are complete in picoseconds: a time-resolved UV resonance Raman study of 1,3-cyclohexadiene. *J. Am. Chem. Soc.* **1993,** *115*, 4754-4763.
103. Reid, P. J.; Lawless, M. K.; Wickham, S. D.; Mathies, R. A. Determination of Pericyclic Photochemical Reaction Dynamics with Resonance Raman Spectroscopy. *J. Phys. Chem.* **1994,** *98*, 5597-5606.
104. Pullen, S.; Walker, L. A.; Donovan, B.; Sension, R. J. Femtosecond transient absorption study of the ring-opening reaction of 1,3-cyclohexadiene. *Chem. Phys. Lett.* **1995,** *242*, 415-420.
105. Lawless, M. K.; Wickham, S. D.; Mathies, R. A. Resonance Raman View of Pericyclic Photochemical Ring-Opening Reactions: Beyond the Woodward-Hoffmann Rules. *Acc. Chem. Res.* **1995,** *28*, 493-502.
106. Pullen, S. H.; Anderson, N. A.; Walker, L. A.; Sension, R. J. The ultrafast photochemical ring-opening reaction of 1,3-cyclohexadiene in cyclohexane. *J. Chem. Phys.* **1998,** *108*, 556-563.
107. Lochbrunner, S.; Fuss, W.; Schmid, W. E.; Kompa, K.-L. Electronic Relaxation and Ground-State Dynamics of 1,3-Cyclohexadiene and cis-Hexatriene in Ethanol. *J. Phys. Chem. A* **1998,** *102*, 9334-9344.
108. Fuß, W.; Schikarski, T.; Schmid, W. E.; Trushin, S.; Kompa, K. L. Ultrafast dynamics of the photochemical ring opening of 1,3-cyclohexadiene studied by multiphoton ionization. *Chem. Phys. Lett.* **1996,** *262*, 675-682.
109. Fuß, W.; Schmid, W. E.; Trushin, S. A. Time-resolved dissociative intense-laser field ionization for probing dynamics: Femtosecond photochemical ring opening of 1,3-cyclohexadiene. *J. Chem. Phys.* **2000,** *112*, 8347-8362.
110. Dudek, R. C.; Weber, P. M. Ultrafast Diffraction Imaging of the Electrocyclic Ring-Opening Reaction of 1,3-Cyclohexadiene. *J. Phys. Chem. A* **2001,** *105*, 4167-4171.
111. Barbatti, M.; Vazdar, M.; Aquino, A. J. A.; Eckert-Maksić, M.; Lischka, H. The nonadiabatic deactivation paths of pyrrole. *J. Chem. Phys.* **2006,** *125*, 164323.
112. Sage, A. G.; Nix, M. G. D.; Ashfold, M. N. R. UV photodissociation of N-methylpyrrole: The role of 1πσ∗ states in non-hydride heteroaromatic systems. *J. Chem. Phys.* **2008,** *347*, 300-308.
113. Woo, K. C.; Kim, S. K. Mode-specific excited-state dynamics of N-methylpyrrole. *Phys. Chem. Chem. Phys.* **2019,** *21*, 14387-14393.
114. Szabla, R.; Tuna, D.; Góra, R. W.; Šponer, J.; Sobolewski, A. L.; Domcke, W. Photochemistry of 2-Aminooxazole, a Hypothetical Prebiotic Precursor of RNA Nucleotides. *J. Phys. Chem. Lett.* **2013,** *4*, 2785-2788.
115. Szabla, R.; Šponer, J.; Góra, R. W. Electron-Driven Proton Transfer Along H2O Wires Enables Photorelaxation of πσ* States in Chromophore–Water Clusters. *J. Phys. Chem. Lett.* **2015,** *6*, 1467-1471.

# Chapter 3. Ultrafast transient absorption spectroscopy experiments

The direct investigation of reaction intermediates formed from the photoexcitation of molecules can give mechanistic insights which can be used to understand, develop, and improve reactive processes. Many of these reactions are in solution, and therefore the role solvents play within reactions can often be crucial to understanding reaction outcomes. Since reaction intermediates are typically short lived, their direct observations typically require ultrafast time-durations. Ultrafast transient absorption spectroscopy (TAS) is a commonly used technique to monitor the kinetics of molecules within the femtosecond-picosecond regime. Conceptually, TAS is relatively simple. An initiation step is required, and can be in the form of an electric discharge, pressure change, heat or light; here, the focus will be on use of a short laser pulse to access ultrafast timescales. A pump pulse, typically in the UV-Vis region, is used to generate an excited state population. The sample is then probed by an additional pulse at various delay times. Probing techniques which use X-rays (X-ray transient absorption spectroscopy, XTAS), UV-Vis light (transient electronic absorption spectroscopy, TEAS) or IR light (transient vibrational absorption spectroscopy, TVAS) pulses have become well-established.[1-2] The probe pulse is weak enough not to induce a population change in the sample.

In the University of Bristol laboratory,[3] TEAS and TVAS experiments use the same laser source. A < 50 fs 800-nm pulse is generated from a Ti:Sapphire laser and converted into more useful wavelengths using methods such as optical parametric amplification within individual UV- and Mid-IR-generating optical parametric amplifiers (referred to as UV OPA and IR OPA respectively herein) or by generating a white-light supercontinuum by focusing the 800-nm fundamental radiation into a $CaF_2$ window, which gives a broadband UV-Vis probe pulse for TEAS experiments. Figure 3.1 schematically shows the optical set-up for TAS experiments at the University of Bristol and will be used as a guide throughout this chapter. Subsections address the various aspects of the optical layout, data acquisition, and spectral decomposition.

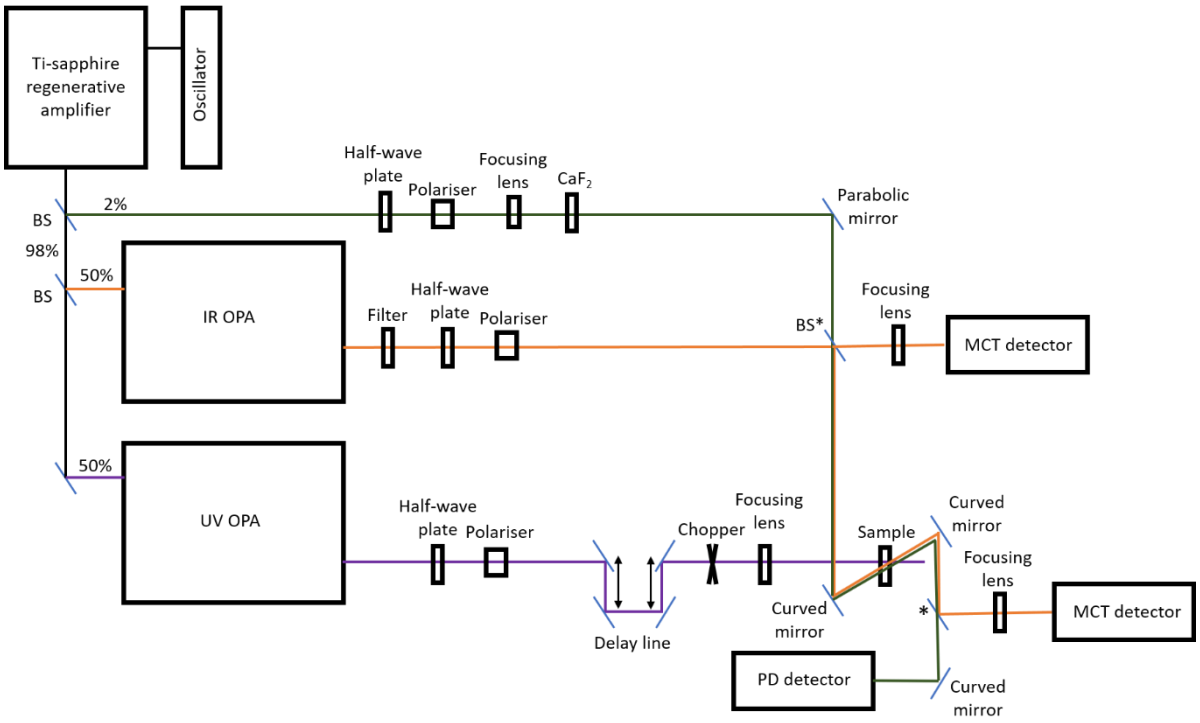


Figure 3.1 – Schematic optical layout for the University of Bristol TAS setup. The beam lines are indicated by different colours: black shows the 800-nm output of the amplifier; green shows the WLC generation stage; orange shows the IR beam line; purple shows the UV pump laser beam line. A * indicates a removable optic to switch between TEAS and TVAS experiments.

### 3.1 Oscillator and amplifier

In the University of Bristol laboratory, a commercial Coherent Vitara-S Ti:Sapphire oscillator is used to generate mode-locked laser pulses centred at a wavelength of 800 nm, at a repetition rate of 80 MHz. A Pockels cell optical switch reduces the repetition rate to 1 kHz, and is triggered by a synchronization and delay generator (SDG). The selected femtosecond pulses are amplified by a commercial Coherent Legend Elite HE+ regenerative amplifier in which the pulses are first stretched to the picosecond regime by an optical stretcher, which consists of two gratings to spatially separate the individual wavelength components. A schematic diagram of this grating-based stretcher is shown in Figure 3.2(a). Each wavelength takes a different pathlength causing a temporal frequency chirp within the pulse. The stretcher reduces the peak power to avoid nonlinear optical effects and optical damage inside the amplifier cavity. The amplifier cavity is schematically shown in Figure 3.2(b) and includes a Ti:Sapphire crystal, pumped by a Q-switched Evolution pump laser that operates at 532 nm by frequency doubling a 1064 nm Nd:YLF laser using an LBO crystal. Inside the cavity, the

stretched pulses circulate and gain intensity by stimulated emission in the Ti:Sapphire crystal. Using a photodiode which measures a small leakage of intensity from inside the cavity, the pulses are monitored until the crystal is saturated and maximum pulse intensity is reached. Once maximum gain is achieved, a Pockels cell triggered by the SDG changes the polarization of the pulse. The thin film polarizer reflects the amplified pulse, which leaves the cavity and is directed to an optical compressor. The compressor follows the same principles as the stretcher, consisting of a pair of gratings to compress the pulses down to durations below 40 fs with pulse energies of ~5 mJ per pulse.

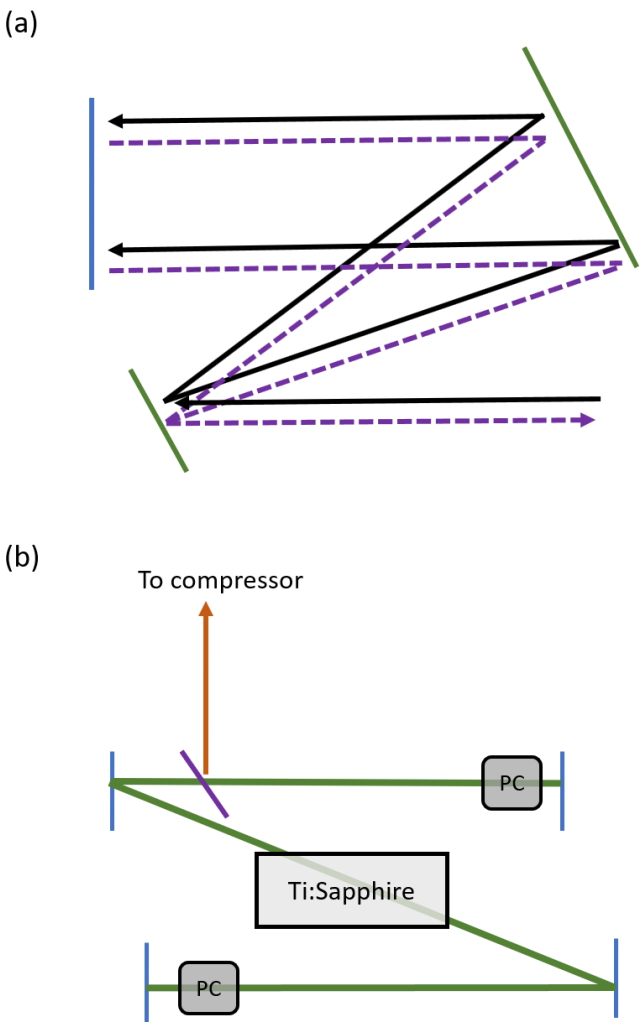


Figure 3.2 – (a) Optical layout of a grating-based stretcher or compressor. The incoming pulse is shown in black and is dispersed onto two gratings (Green) to spatially separate the individual wavelength components. A temporal chirp is achieved by making each wavelength take a different pathlength to a periscope (Blue). The spatially and temporally chirped pulse returns (Purple) and is spatially recombined and recollimated using the same two gratings. (b) schematic diagram of the layout for a Ti:Sapphire regenerative amplifier cavity. The green line shows the beam path for the multiple trips of intracavity pulses, causing repeated stimulated emission in the Ti:Sapphire crystal. Mirrors are shown in blue and the polariser is shown in purple. Triggering of a Pockels cell (PC) switches the polarisation of the pulse so that it is reflected out of the cavity and towards the compressor.

### 3.2 Optical parametric amplifiers

Optical parametric amplifiers convert the 800-nm output of the Ti:Sapphire laser to a range of tuneable wavelengths from deep-UV to mid-IR through parametric amplification using a

white-light-continuum (WLC), followed by second harmonic generation (SHG), sum-frequency generation (SFG) or difference-frequency generation (DFG). Figure 3.3 shows a schematic representation of the optical layout of an OPA and is used to guide the discussion in this section. The non-linear processes used to convert the 800-nm output of the amplifier to more useful wavelengths are illustrated in Figure 3.4.

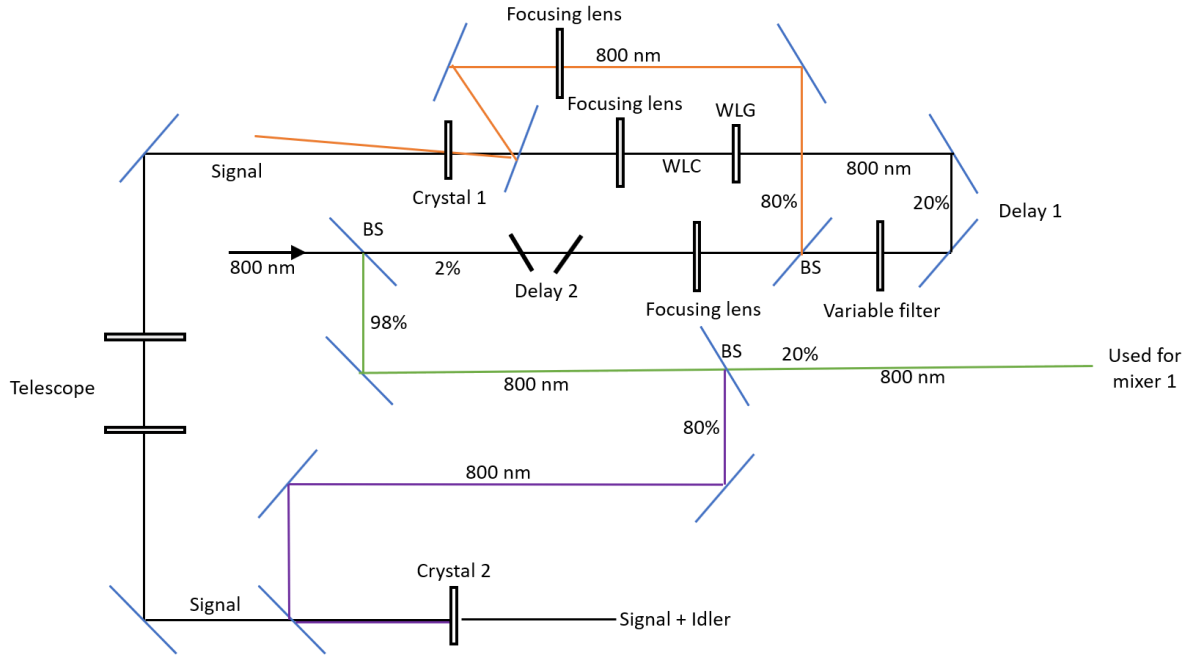


Figure 3.3 – Optical layout for the amplification of a white-light continuum. The black arrow shows the input 800-nm fundamental beam from the Ti:Sapphire amplifier.

In the Bristol laboratory, the 800-nm pulses are each split into three beams, with a weaker (2%) portion used for the generation of a WLC probe for TEAS experiments. The remaining two beams are used to seed two commercial Coherent OPERA-SOLO OPAs, one in a UV-generating configuration (UV OPA) to provide a UV pump pulse for TAS, and a second for IR generation (IR OPA) with the mid-IR pulses used as probes in TVAS experiments. Both OPAs generate amplified signal and idler pulses via a similar optical set-up (shown in Figure 3.3) and differ in their mixing stages.

### 3.2.2 Signal and idler generation

Inside the OPAs, the 800-nm pump pulse is divided using a series of beam splitters (BS), with each beam path shown using a different colour in Figure 3.3. A small portion (~2%) is used to generate the WLC by focusing into a sapphire plate. A variable filter and iris are used to control the intensity and beam diameter to enable the production of a stable WLC. Portions of the

remaining 800-nm pulses are used to pump two type-2 phase matching β-barium borate (BBO) crystals. Crystal 1 serves as a preamplification stage with the overlap of the focused 800-nm pump pulse and less intense WLC producing signal (~1160-1600 nm) and idler (~1600-2600 nm) pulses via DFG (see Figure 3.4). The delivery of the pulses into Crystal 1 is set in a non-collinear geometry to enable the separation of the signal beam from residual 800-nm and sum-frequency pulses. The signal is passed through a telescope for recollimation and directed into crystal 2, along with another 800-nm pump pulse for parametric amplification of the signal. The temporal overlaps of the signal seed and 800-nm pump pulses in crystal 1 and crystal 2 are controlled by two motorised delay stages and the crystal angle is rotated to achieve the phase matching angle for the desired centre wavelength.

### 3.2.3 Mixing stages

The UV-OPA offers two colinear mixing stages, each fitted with a BBO crystal of type 1 phase matching to allow various combinations of SFG and SHG to produce tuneable wavelengths from ~230-1300 nm. The IR OPA utilises a single non-collinear mixer stage, fitted with a non-collinear $AgGaS_2$ crystal to produce a broadband mid-IR probe pulse with centre wavelengths that can span the range 2600-20,000 nm.

## 3.3 White light continuum probe

A small portion (~ 2%) of the 800-nm beam produced by the amplifier is focused using a 200-mm focusing lens into a 3-mm thick $CaF_2$ window to produce a WLC probe spanning 340-750 nm. A half-wave plate and polariser combination is used to regulate the intensity of the 800-nm beam, and an iris controls the beam diameter and beam profile. The resulting WLC is recollimated using a parabolic mirror.

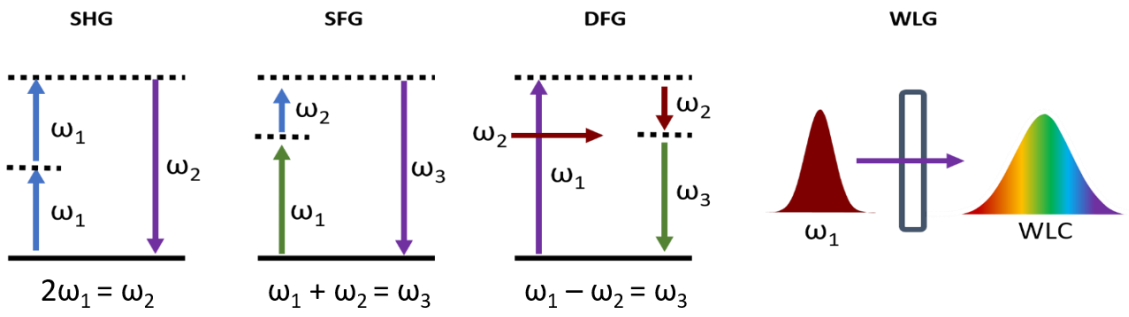


Figure 3.4 - Non-linear optical processes used to generate UV pump, and UV-visible and mid-IR probe pulses. The horizontal red arrow ($\omega_2$) shows the use of a seed pulse for DFG.

### 3.4 Transient electronic absorption spectroscopy

Measurements are made by photoexciting a sample in a Harrick cell assembled from two 1.5-mm thick $CaF_2$ windows separated by Teflon spacers, with the sample circulating constantly from a reservoir to avoid photodegradation. Continuous circulation is driven by a peristaltic pump. All spectra are obtained under aerobic conditions, with dissolved oxygen only expected to affect the photochemistry on timescales >100 ns that are much longer than the temporal window probed.[4] The photoexcited samples are probed by spatially overlapping a WLC probe, and the transmitted WLC probe pulses are dispersed into a Andor spectrometer (Shamrock 163) fitted with a 1024-element photodiode array (Entwicklungsbüro Stresing). Spectra are calibrated by scaling to known spectral signatures of holmium oxide glass. An optical delay line is used to provide a pump-probe delay of up to 1.3 ns. To achieve a time-dependent change in intensity as a function of time (see Equation 3.1), pump-on and pump-off spectra are collected using a mechanical chopper (Thorlabs, MC2000) which intersect the pump pulse at a repetition rate of 500 Hz.

$$\Delta A(\lambda, t) = -log \frac{I_{Pump-on}}{I_{Pump-off}} \qquad 3.1$$

The expression for change in absorbance ($\Delta A$) of the probe pulse in equation 3.1 shows that a reduction in the amount of light absorbed by a sample causes negative features in the transient spectra. Typically, these negative features are a result of a fraction of the sample being placed into an excited state, and there are now fewer sample molecules in the ground state to absorb given wavelengths ($\lambda$) of the probe light. Typically, these features are referred to as ground state bleaches (GSB) and can be monitored to understand kinetics and relaxation mechanisms which reform the sample ground state. Other causes are known for negative ($\Delta A$) features, such as stimulated emission, and reaction of other probed molecules which overall result in more light reaching the detector. Positive signals arise due to greater absorption of light, and indicate the gain of new species, such as excited-state molecules, transient intermediates and stable products.

### 3.5 Transient vibrational absorption spectroscopy

TVAS experiments are carried out in a similar way to TEAS experiments described in 3.4, but using 300 $cm^{-1}$ bandwidth mid-IR pulses to probe the sample instead of the WLC pulses. Following transmission through the sample, these mid-IR probe pulses are dispersed in a spectrometer (HORIBA Scientific, iHR320) fitted with a 128-element mercury-cadmium-

telluride array detector (Infrared Associates Inc., MCT-10−128) and fast read-out electronics (Infrared Systems Development Corp, FPAS-0144). Before reaching the sample, a portion of the IR beam is split using a 50:50 beam splitter and directed to a spectrometer of matching configuration to provide a reference for each individual probe pulse so that shot-to-shot pulse intensity fluctuations can be divided out of the final data. To remove IR spectral features from water vapour in ambient air, the IR beamlines are sealed in plastic tubing and purged with dry $N_2$ gas. Spectra are converted from ΔA (mOD) per pixel into ΔA (mOD) per $cm^{-1}$ by matching the spectra to a compound with known spectral signatures. For example, Trans-stilbene at ~6000 nm and ACN at ~5000 nm are convenient calibration references.

**3.6 Data acquisition, spectral decomposition, and chirp correction**

For both TEAS and TVAS experiments, data are collected using a LabView code which was previously developed at the University of Bristol. For a fixed pump-probe delay, spectra are collected and averaged until good signal to noise is obtained. Various delay times are scanned in a randomised order to avoid any long-term changes to signal intensity altering the kinetic information, such as temperature fluctuations and photodegradation of the sample. Each data set is acquired by repeatedly cycling through a series of delay times, and averaged until kinetic information is of the desired quality. The number of averages and cycles required will vary depending on laser stability and signal to noise levels.

Transient absorption experiments give the time-evolution of an absorption spectrum which can be used to interpret the dynamics of chemical processes. The absorption spectra often contain overlapped signals from ground states, excited states, reaction intermediates, solvent complexes, and products. To extract meaningful information, the experimentally measured spectrum must first be disentangled. Decomposing a spectrum into its individual spectral components is a non-trivial task, and several methods are possible.[5] Spectral target analysis is the most commonly used method to decompose the spectra presented in this thesis, with example spectral decompositions to be found in the supporting information sections to Chapters 4-6.

Using KOALA software, [6] the absorption spectra of individual species can be measured in isolation, and used as basis functions for modelling contributions to the time-evolution of the transient spectra. Because this thesis is concerned with the chemical dynamics of reaction intermediates, it is often not possible to measure such absorption spectra in an FTIR or UV-

Vis spectrometer. Instead, transient spectra can be recorded at different time delays (e.g. short and longer times) and used as basis functions to approximate the absorption profiles of different intermediate species. When intermediates are not formed in isolation, their absorption bands can often be well-modelled using Gaussian functions. At its simplest, KOALA[6] performs a Linear Least Squares regression to fit basis functions to the spectral intensity. The principle behind this method is that each transient spectrum can be decomposed as a sum of spectral components of varying amplitudes and residual signals which are not captured by the spectral target analysis. The best fit is obtained when the residual signals are minimized. Linear Least Squares regression is only suitable when absorption profiles do not vary in position or shape over time. However, on femtosecond to picosecond timescales, processes such as vibrational cooling and solvation often manifest themselves by shifting the centre wavelength or changing the breadth of a band. To model processes such as vibrational cooling and solvation, further Gaussian functions can be added and their centre wavelength and half-width maximum parameters can be allowed to change during a fit. The time-evolution of the centre wavelength or half-width at half maximum amplitude can then be used to extract kinetic information about the dynamical processes.

Spectral chirp is a common issue for TEAS experiments, and occurs because each wavelength of the WLC probe has a unique time-zero ($t_0$); i.e. the different spectral components of the WLC pulse are temporally displaced from each other. This chirp arises because the refractive indices of materials used in transmissive optics depend on the wavelength of the light. The effect of chirp on representative TEAS spectra is shown in Figure 3.5(a).

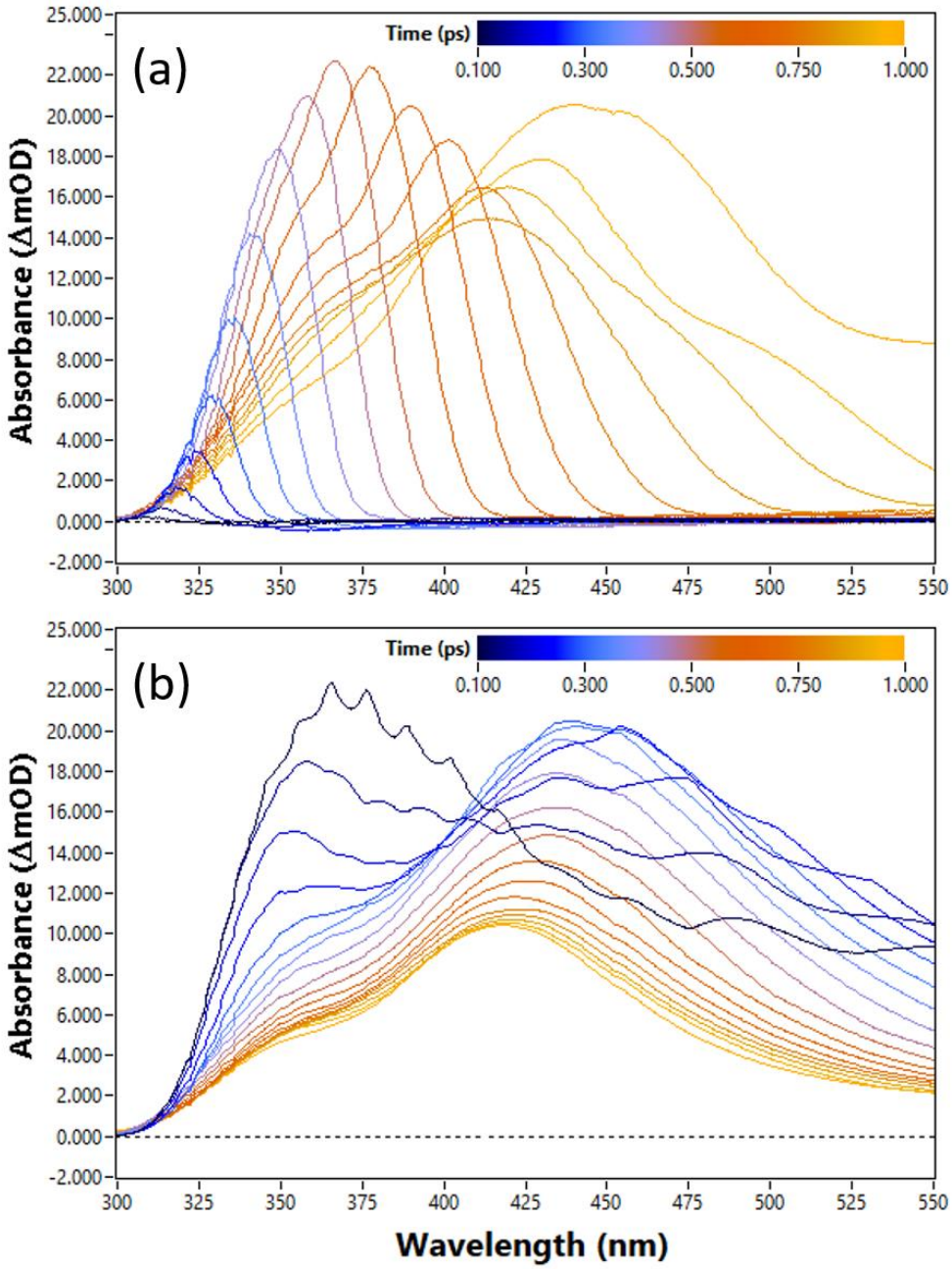


Figure 3.5 – Chirp correction in KOALA.[6] (a) Raw spectra of 10 mM 2-Aminothiazole in DCM at time delays of 0.1 – 1 ps without chirp correction; b) spectra after chirp correction using values: ABP = 1047 fs, GDD = 119 $fs^2$ $rad^{-1}$, TOD = -91 $fs^3$ $rad^{-1}$. Early time spectra are shown in blue and evolve into orange for later time delays.

Using KOALA,[6] the spectral chirp is corrected post data collection. In brief, a unique time zero is selected for each wavelength, and is defined as the moment when a selected absorbance level is reached. A plot of the time-zero values as a function of wavelength is used to determine the absolute phase (ABP), the group delay dispersion (GDD), and the third order

dispersion (TOD) by using equation 3.2. The absorbance values for each wavelength of a particular time delay are then reassigned to another set of spectra, correcting for the delayed time-zero.

$$t_0(\lambda) = \mathrm{ABP} + \mathrm{GDD}\left(\frac{2\pi c}{\lambda}\right) + \frac{1}{2}\mathrm{TOD}\left(\frac{2\pi c}{\lambda}\right)^2 \qquad 3.2$$

This type of correction is not required prior to analysis of the transient infra-red spectra reported in this thesis.

## References


1. Geneaux, R.; Marroux, H. J. B.; Guggenmos, A.; Neumark, D. M.; Leone, S. R. Transient absorption spectroscopy using high harmonic generation: a review of ultrafast X-ray dynamics in molecules and solids. *Philos. Trans. R. Soc. A* **2019,** *377*, 20170463.
2. Berera, R.; van Grondelle, R.; Kennis, J. T. M. Ultrafast transient absorption spectroscopy: principles and application to photosynthetic systems. *Photosynth. Res.* **2009,** *101*, 105-118.
3. Roberts, G. M.; Marroux, H. J. B.; Grubb, M. P.; Ashfold, M. N. R.; Orr-Ewing, A. J. On the Participation of Photoinduced N–H Bond Fission in Aqueous Adenine at 266 and 220 nm: A Combined Ultrafast Transient Electronic and Vibrational Absorption Spectroscopy Study. *J. Phys. Chem. A* **2014,** *118*, 11211-11225.
4. Koyama, D.; Donaldson, P. M.; Orr-Ewing, A. J. Femtosecond to microsecond observation of the photochemical reaction of 1,2-di(quinolin-2-yl)disulfide with methyl methacrylate. *Phys. Chem. Chem. Phys.* **2017,** *19*, 12981-12991.
5. van Stokkum, I. H. M.; Larsen, D. S.; van Grondelle, R. Global and target analysis of time-resolved spectra. *Biochim. Biophys. Acta. Bioenerg.* **2004,** *1657*, 82-104.
6. Grubb, M. P.; Orr-Ewing, A. J.; Ashfold, M. N. R. KOALA: A program for the processing and decomposition of transient spectra. *Rev. Sci. Instrum.* **2014,** *85*, 064104.

# Chapter 4. Direct Observation of Ylide and Enol Intermediates Formed in Competition with Wolff Rearrangement of Photo-Excited Ethyl Diazoacetoacetate

The data and results presented in this chapter have been published: Phelps, R.; Orr-Ewing, A. J. Direct Observation of Ylide and Enol Intermediates Formed in Competition with Wolff Rearrangement of Photoexcited Ethyl Diazoacetoacetate. *J. Am. Chem. Soc.* **2020,** *142*, 7836-7844. I performed all experiments and computations, and analysed the data sets presented.

### 4.1. Introduction

The photochemistry of diazo compounds bearing carbonyl groups to form carbene and ketene intermediates have been discussed in chapter 2. The mechanisms to Wolff-rearrangement (WR) has been widely investigated, and in this chapter the competition between the WR of carbene intermediates and reactions of carbene intermediates with solvent molecules will be discussed.

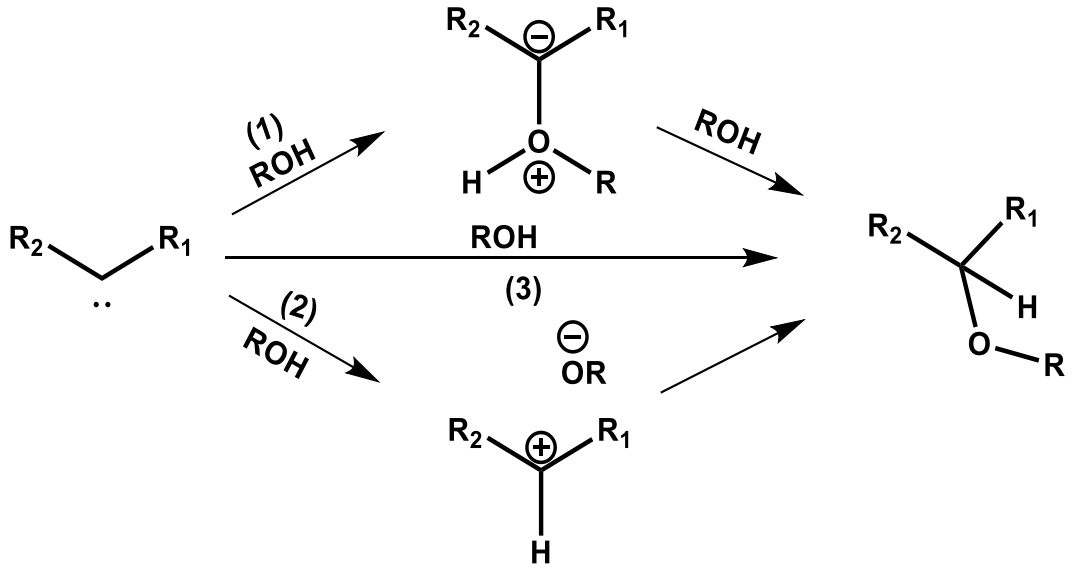


Scheme 4.1 – Proposed pathways for singlet carbene reaction with an alcohol to make an ether. For $\alpha$-carbonyl carbenes.

The reaction of carbenes with alcohols has attracted significant attention in the literature, and both the ylide (path 1) and carbocation (path 2) intermediate pathways shown

in scheme 4.1 are widely accepted,[1] although in the 1960s Strausz *et al*. proposed the formation of an enol intermediate in carbonyl carbene – alcohol reactions.[2] This idea of carbonyl involvement was revisited in the 1990s by Platz and co-workers, but they preferred to assign a transient electronic absorption band to an ylide structure on the basis that they did not find a kinetic isotope effect to its formation.[3] Evidence has been presented of enol formation by carbonyl carbene insertion into O-H bonds of $H_2O$ (Scheme 4.2),[4-5] but this mode of reactivity has yet to be demonstrated for alcohols.

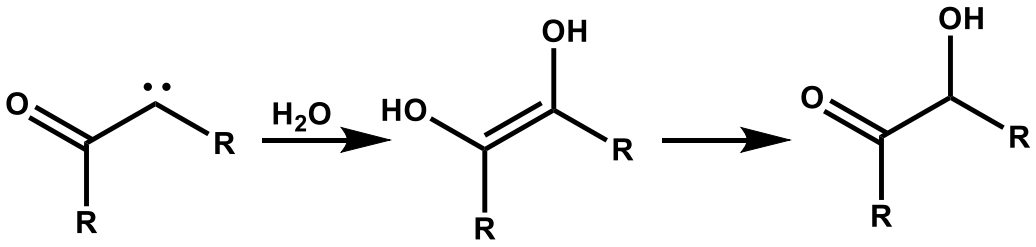


Scheme 4.2 – Reaction of $H_2O$ with a singlet carbonyl carbene to produce an enol intermediate.

Here, direct evidence is presented from TVAS measurements for singlet carbonyl carbene formation and reaction in competition with concerted WR of a UV photo-excited α-diazo carbonyl compound, ethyl diazoacetoacetate (EDAA). Furthermore, this chapter will report the competitive formation of a previously unobserved alcohol-derived enol as an intermediate to ether formation, and compare the nucleophilic reactivity of the singlet carbene in a range of solvents.

## 4.2. Method

**A. Experiment.** The photoinduced chemistry of ethyl diazoacetoacetate was studied in cyclohexane and several nucleophilic solvents using TVAS with a broadband IR probe. Spectra were collected following the photoexcitation at 256 nm of 3.2 mM samples of EDAA (Sigma Aldrich, ≤100%) used as received. At this UV wavelength, absorption is assigned to the $S_4 \leftarrow S_0$ excitation, orbital contributions for which are shown in Figure S4.10 of the Supporting Information. With a sample path length of 380 μm, an absorbance at 256 nm of approximately 0.6 was obtained. Measurements were made for EDAA solutions in cyclohexane (Fisher Scientific, extra pure, SLR grade), tetrahydrofuran (Fisher Scientific, extra pure, SLR grade, stabilised with 0.025% BHT), acetonitrile (Fisher Scientific, HPLC gradient grade, <99.9%),

ethanol ((EtOH) Sigma Aldrich, ACS reagent grade, >99.5%), and tertiary butanol ((t-BuOH) Sigma Aldrich, anhydrous, ≥99.5%). Steady-state FTIR and UV absorption spectra for these EDAA solutions are shown in Figures S4.10 and S4.11 of the Supporting Information.

**B. Computational details.** Assignments of transient IR bands were supported by gas phase anharmonically corrected vibrational frequencies computed with density functional theory (DFT). These calculations used the B3LYP functional and the 6-311++G(d,p) basis set for all the species considered in this study. Accurate geometries[6] and anharmonically corrected vibrational frequencies[7-8] of organic molecules have been reported using this chosen level of theory. Calculations achieved respective accuracies within 9 $cm^{-1}$ and 33 $cm^{-1}$ in reproducing experimental ketone and ester carbonyl stretching frequencies for EDAA in all the solvents studied. A solvent correction in the form of the polarisable continuum model (PCM) can lead to erronous results with anharmonic frequency calculations,[9] and was not applied. Because of the accuracy of the calculated carbonyl stretching band wavenumbers, detection and assignment of transient intermediates largely relied on comparisons of experimental measurements and computational simulation of bands observed in this spectral window. Comparisons with measured spectra in the ketene stretching region around 2100 $cm^{-1}$ provided further evidence for certain product pathways. Proposed assignments were also supported by experimentally derived kinetic data and computed energies of intermediates and products.

To provide further understanding of the mechanism of singlet carbene insertion into alcohols, relaxed potential energy scans were calculated at the B3LYP/6-311++G(d,p) level to map out the potential energy surface for reaction of MeOH with the EDAA-derived singlet carbene. In these scans, two coordinates were varied and all other geometric parameters were relaxed. The two coordinates chosen were the distance of the oxygen atom of MeOH from the carbene carbon atom, which was incremented over 175 steps with a stepsize of 0.01 Å, and the MeOH O-H distance which was increased with a stepsize of 0.05 Å over 10 steps. All calculations were performed for species in the gas phase using the Gaussian 09 computational package.[10]

**C. Specral decomposition**

The spectral decomposition was carried out using the KOALA program.[11] An example fitting procedure for the decomposition of the overlapping enol, ketene and GSB bands for the 256-nm photoexcitation of EDAA in EtOH is shown in Figure 4.1. In brief, an early time basis

function is superimposed on the experimental data and has fixed intensity. Contributions from GSB recovery are neglected to simplify the data analysis, but are expected to contribute at most 15% to the GSB recovery on the basis of data obtained in cyclohexane. To decompose carbene, ylide and enol bands, Gaussian functions with fixed centres and widths are overlapped with the early time basis function to best describe the experimental data. To decompose the ketene band and the effect of vibrational cooling on the spectrum, the Gaussian centre and width are floated.

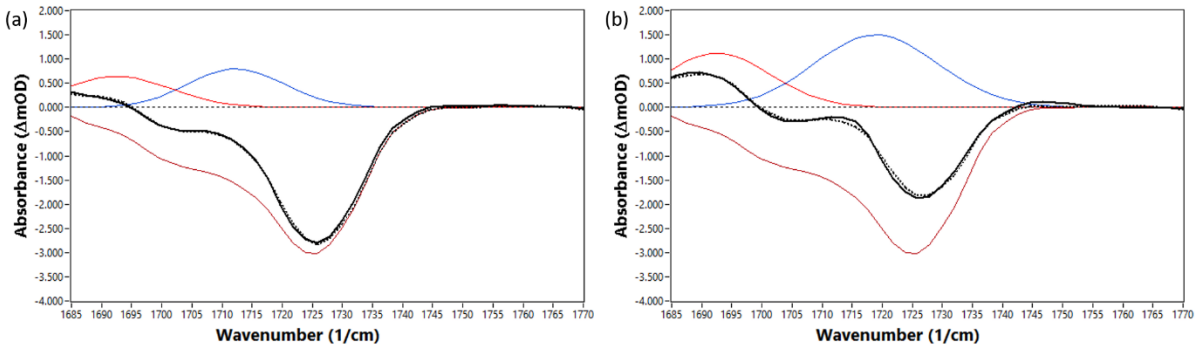


Figure 4.1 – Example fitting procedure for the decomposition of the overlapping enol, ketene and GSB bands for the 256-nm photoexcitation of EDAA in EtOH. Transient spectra are shown at: (a) 4 ps; and (b) 1100 ps time delays. An early time basis function (dark red) is superimposed on the experimental data (solid black line) and has a fixed intensity. Gaussian functions are then overlapped to produce the simulated curve (dotted line) which best describes the experimental data. The ketene absorption (solid blue line) is fitted to a shifting and narrowing Gaussian function to simulate the effects of vibrational cooling on the spectrum. The enol is fitted to a Gaussian function with fixed centre and width (solid red line).

### 4.3. Results and Discussion

Scheme 4.3 serves as a guide for the discussion of the observed photochemical pathways of EDAA in a range of solvents. At equilibrium, EDAA exists in 4 different isomers, with calculated gas-phase Gibbs energies (see Table S4.2 of the Supporting Information) that show 87 % exists as the Z,E-isomer (shown as (1) in scheme 4.3). The photolysis of EDAA (1) is expected to retain this stereochemistry, forming the more stable anti-isomer of the carbene (shown as (2) in scheme 4.3). Conjugation of the carbene lone pair of electrons into the α-carbonyl groups hinders internal rotation, preventing rearrangement to other carbene

stereoisomers. Similar arguments apply to the isomers of potential reaction products, as is discussed further below.

This section begins with IR bands associated with the primary photoproducts observed in non-reactive cyclohexane, and will then report alternative photochemical channels that arise in various nucleophilic solvents. Summaries of the observed band positions and measured time constants for the various intermediates are presented respectively in Table 4.1 and Table S4.1 (Supporting Information). No evidence was found for triplet carbene participation in any of the experiments, consistent with computational prediction of a singlet carbene ground state for species (2). Reference to carbenes hereafter thus implies only the singlet species.

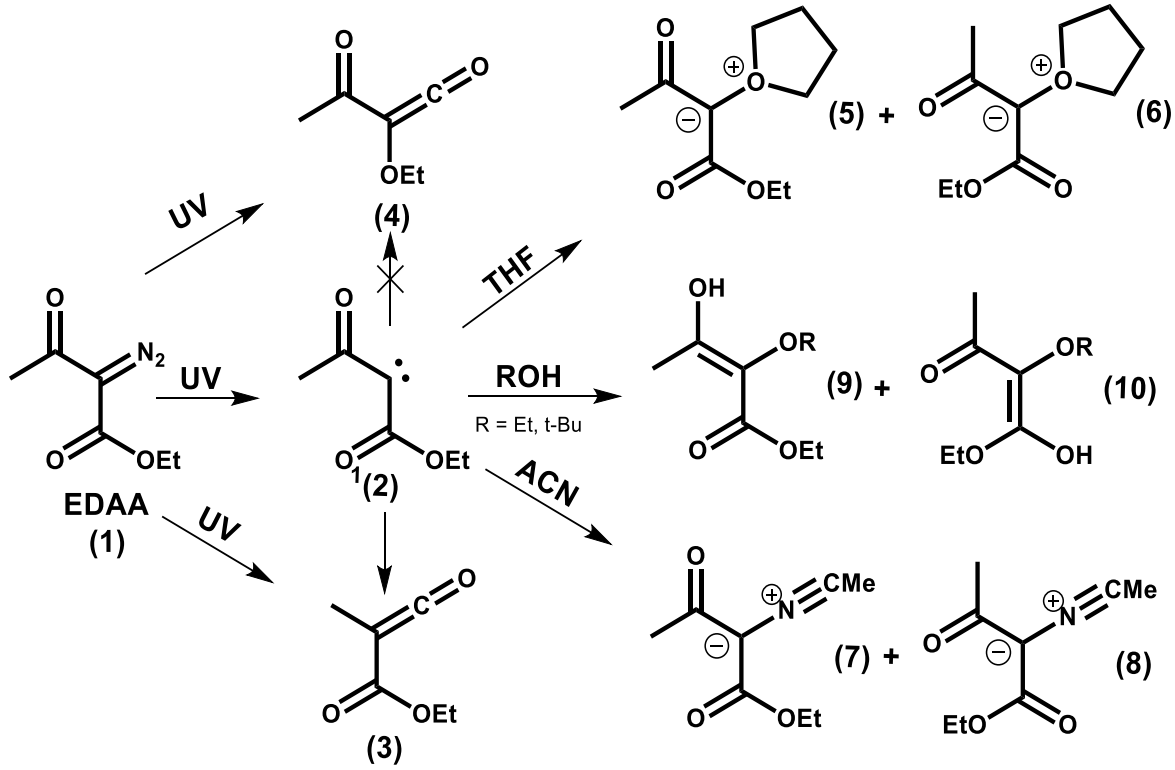


Scheme 4.3 – The photochemical pathways of EDAA in solution determined by transient vibrational absorption spectroscopy. Carbene (2) has a singlet ground-state, emphasized here by the $^1$(2) notation.

Table 4.1 – Band Positions of the Intermediates Observed in the Five Solvents Studied. Intermediates are Identified by Bold Numbers in Parentheses Corresponding to the Labels Used in Scheme 4.3.

| | Cyclohexane ($cm^{-1}$) | THF ($cm^{-1}$) | ACN ($cm^{-1}$) | EtOH ($cm^{-1}$) | t-BuOH ($cm^{-1}$) |
|---|---|---|---|---|---|
| Ketene (**3**) | 2125 | 2130 | 2130 | 2130 | 2130 |
| | 1722 | 1715 | 1711 | 1720 | 1722 |
| Ketene (**4**) | 2105 | | | | |
| Carbene (**2**) | 1645 | 1646 | 1627 | | 1636 |
| Ylide | | 1586 (**5**) | 1625 (**7**) | | |
| | | 1635 (**6**) | | | |
| Enol (**9**) | | | | 1694 | 1694 |

### 4.3.1 Wolff rearrangement

Figures 4.1 and 4.2 show TVAS spectra, obtained in two different probe wavenumber regions, for the photoexcitation of EDAA in a variety of solvents. Negative-going bands centred around 2130 $cm^{-1}$ (diazo stretch) (Figure 4.2(a)), and 1670 $cm^{-1}$ (ketone stretch) and 1730 $cm^{-1}$ (ester stretch) (Figure 4.3(a)) in cyclohexane are assigned to ground state bleaches (GSB) of EDAA vibrational bands on the basis of steady-state IR absorption spectra (Figure S4.9). A 15% GSB recovery of the 1670 $cm^{-1}$ band implies 85% conversion of photo-excited EDAA to photoproducts. Regeneration of ground state EDAA can therefore be discounted as the only cause of the observed 50-75% recovery in the 1730 $cm^{-1}$ and 2130 $cm^{-1}$ GSBs, which must instead be a result of overlapping photoproduct bands. Data-fitting to decompose these bands into their overlapping components is shown in Figure 4.1 and Figure S4.8 of the Supporting Information.

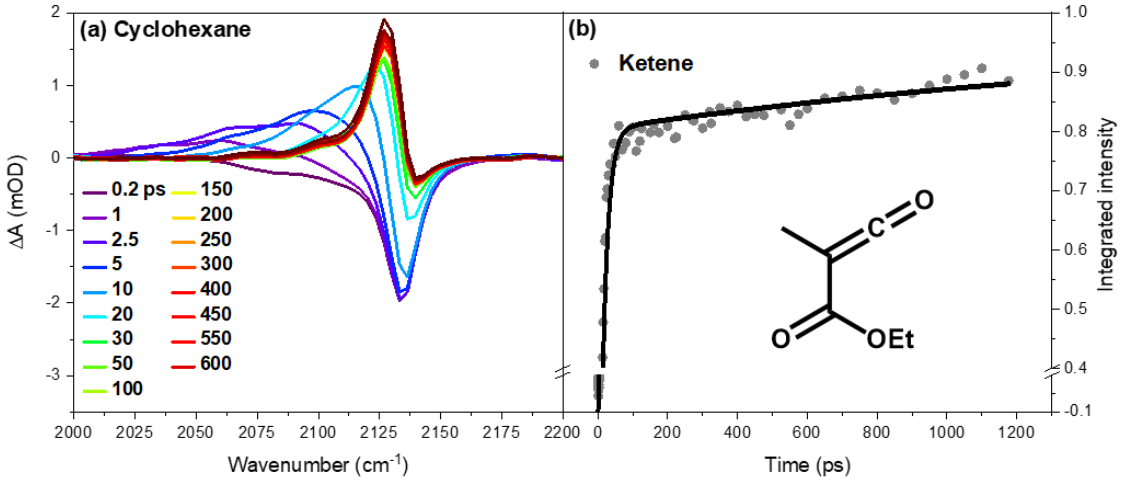


Figure 4.2 – Photoinduced ketene formation from EDAA: (a) TVAS spectra for the 256-nm photoexcitation of EDAA in cyclohexane. Spectra were obtained by monitoring the C=C=O ketene stretching region from 2000 – 2200 $cm^{-1}$. The inset key shows the colour scheme identifying transient spectra obtained at different time delays after the UV excitation laser pulse. (b) A kinetic fit to the growth of integrated intensity of the 2125 $cm^{-1}$ band corresponding to a vibrationally cooled ground-state ketene. The inset structure shows the preferred assignment of the 2125 $cm^{-1}$ band to ketene (3). Grey circles are experimental measurements and the solid line is a fit to a biexponential function giving time constants of 17 ± 1 ps and >1 ns.

Table 4.2 – Time Constants for the Production of Ketene (3) after UV Photoexcitation of EDAA in Various Solvents, and Percentage Contributions of the Stepwise WR.

| Solvent | $\tau_1$/ ps | $\tau_2$/ ps | Stepwise WR fraction / % |
|---|---|---|---|
| Cyclohexane | 17 ± 1 | > 1000 | 20 ± 8 |
| ACN | 15.7 ± 0.6 | ≈ 1000 | 4 ± 2 |
| THF | 11.5 ± 0.3 | 180 ± 100 | 4 ± 2 |
| EtOH | 11.0 ± 0.3 | | 0 |
| t-BuOH | 10.9 ± 0.4 | | 0 |

EDAA has two carbonyl groups adjacent to the diazo group (i.e. in $\alpha$ positions), and two alternative WR reactions are therefore possible, as shown in Scheme 4.3. Rearrangement involving the ketone functionality yields ketene (3), whereas rearrangement of the ester functionality produces ketene (4). Ketene photoproducts are unambiguously identified by monitoring the characteristic IR bands associated with the C=C=O stretching modes and indicate two isomers with bands at 2125 and 2105 $cm^{-1}$ in cyclohexane (Figure 4.2(a)). The ketene molecules are born within the instrument response time (i.e. < 300 fs) and with excess vibrational energy, as is evident from the breadth of the bands at early times and their narrowing and shift to higher wavenumber with increasing time delay as excess internal energy dissipates to the solvent. The prompt ketene formation is consistent with a concerted WR reaction. A further long-term growth in intensity is observed for the 2125 $cm^{-1}$ band (Figure 4.2(b) and Supporting Information, Figure S4.3) over time-delays extending to beyond 1 ns, which suggests a contribution to the ketene yield from the stepwise WR and hence the participation of carbene intermediates.

Similar observations of ketene formation were made in all the chosen nucleophilic solvents (see Supporting Information, Figure S4.1). Time constants associated with the growth of the 2125 $cm^{-1}$ band, as well as the percentage contribution from the stepwise WR, are summarized in Table 4.2. The faster of the two observed time constants is attributed to the dynamics of vibrational cooling of promptly formed hot ketene molecules after concerted WR, with the longer time constant a direct measure of the product ketene growth associated with the stepwise WR. The observed suppression of the stepwise WR in nucleophilic solvents results from solvent molecules intercepting the carbene intermediates before this WR pathway can occur. Kinetic analysis at early times (<20 ps) could not be performed for the weaker 2105 $cm^{-1}$ band because of overlap by the broad absorption associated with vibrationally hot ketene molecules. However, no detectable long-term growth of the 2105 $cm^{-1}$ band implies that stepwise WR does not occur for the associated ketene on these time scales (Supporting Information, Figure S4.3).

Computations of single point energies and transition states identify that ketene (3) lies 113 kJ $mol^{-1}$ below ketene (4) in energy, and the former has a 13.7 kJ $mol^{-1}$ lower activation energy for formation from the intermediate carbene (2) (shown in Table S4.5 of supporting information). These arguments favour ketene (3) as the product of the stepwise WR pathway, hence the 2125 $cm^{-1}$ band is assigned to it, with ketene (4) proposed to be responsible for the

band around 2105 $cm^{-1}$. These assignments are consistent with vibrational frequency calculations that predict ketene stretching frequencies to be higher for product (3) than for product (4).

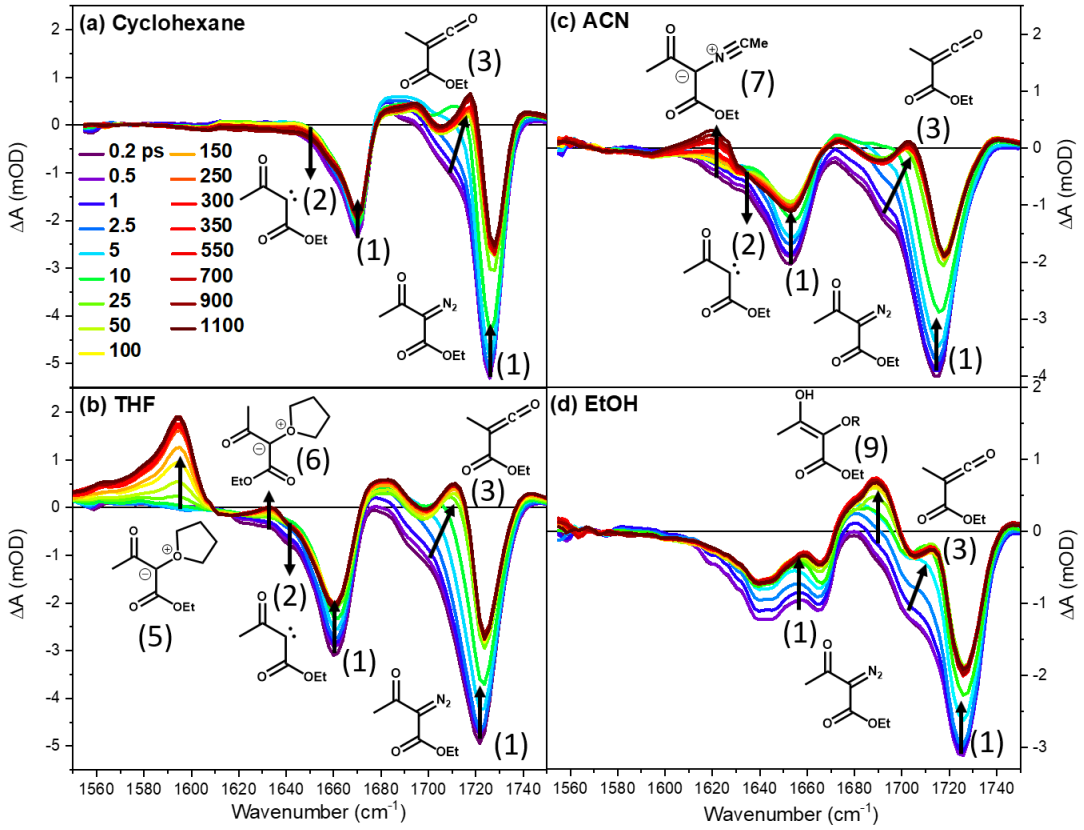


Figure 4.3 – Spectroscopic evidence for various intermediates from carbene reactions in different solvents. TVAS spectra are shown for 3.2 mM EDAA solutions after photoexcitation at 256 nm. The solvents used are (a) cyclohexane; (b) THF; (c) ACN; (d) EtOH. The inset colour key in panel (a) identifies spectra obtained at different time delays, and black arrows show the directions of change of spectral features with time. Numbers in parentheses provide band assignments to structures in Scheme 4.3.

A positive-going band indicative of photoproducts is centred between 1700 and 1725 $cm^{-1}$ but overlaps the EDAA parent molecule GSB (e.g. Figure 4.3(a)). This band is observed both in the unreactive cyclohexane solvent and in all the nucleophilic solvents studied. The

associated photoproduct is born vibrationally hot and undergoes vibrational cooling, as shown by the band narrowing and shifting to higher wavenumber with increasing time delay. The band is further found to increase over longer times in cyclohexane, ACN, and THF. For the alcohol solvents studied, after its initial rise the band intensity remains constant for the duration of the experiment. Assignment of this band to carbene (2) can be discounted because it does not decay by reaction with nucleophilic solvents or stepwise WR. Photoisomerization of EDAA to a diazirine could account for the prompt band appearance, with predicted product vibrational frequencies of 1725 and 1740 $cm^{-1}$, but this does not explain the long-term growth of the band. A more plausible assignment is to ketene (3), which has a predicted vibrational band at 1732 $cm^{-1}$ (ester stretch), because the kinetics of growth of the 1725 $cm^{-1}$ band at longer time delays match those of the ketene band at 2125 $cm^{-1}$ in all solvents.

### 4.3.2 Ylide formation

To investigate the photoinduced reactions of singlet carbenes with nucleophiles and the possible generation of ylide intermediates, TVAS measurements were performed for EDAA solutions in THF and ACN. These solvents were chosen in part because they contain no acidic hydrogen atoms, hence ruling out formation of carbocation intermediates of the type shown in Scheme 4.1. Transient IR bands associated with ylide intermediates and insertion reaction products are therefore more readily identified.

Bands centred at 1586 $cm^{-1}$ in THF (Figure 4.3(b)) and 1625 $cm^{-1}$ in ACN (Figure 4.3(c)) are assigned to the respective ylides (5) and (7) in Scheme 4.3, based upon good agreement with calculated vibrational frequencies of the ketone stretching modes at 1564 $cm^{-1}$ and 1634 $cm^{-1}$ respectively. An additional weaker band in THF at 1635 $cm^{-1}$ is assigned to the E,Z-isomer (6), which is formed when the THF molecule approaches the carbonyl anti to the ketone functionality. Isomer (6) sits 32.4 kJ $mol^{-1}$ higher in energy (see Table S4.4 of Supporting Information) and is therefore expected to be a minor contributor. The ylides are formed with time constants of 140 ± 6 ps in THF, and ≈ 1 ns in ACN by solvent nucleophilic attack at the carbene centre. The lifetimes of the ylides are longer than the 1.3-ns time limit of the experiment. The E,Z-isomer of the ACN ylide (8) has a predicted IR band at 1653 $cm^{-1}$ which is likely to overlap other bands in the transient spectra. This isomer is also expected to be only a minor product on energetic grounds, and it remains unassigned in the measured spectra.

The observation of ylides provides further evidence for carbene (2) production by photoexcitation of EDAA, and hence for competition between photoinduced carbene formation and concerted WR pathways. TVAS measurements for EDAA in alcohol solutions do not show such clear-cut evidence for ylide bands in the probe spectral window, and alternative reaction pathways are discussed in section 4.3.3.

### 4.3.3 Enol formation

For photo-excited solutions of EDAA in EtOH, a transient absorption band identified at 1694 $cm^{-1}$ has a 35 ± 2 ps time constant for growth (Figure 4.3(d)). A similar feature is observed for EDAA in t-BuOH with a corresponding time constant of 160 ± 30 ps (see Figure S4.4 of Supporting Information). Calculated vibrational frequencies for the alcohol ylide suggest bands should be observable at 1598 $cm^{-1}$ and 1736 $cm^{-1}$, i.e. at the lower and upper edges of the spectral regions shown in Figure 4.3, but the TVAS experiments were unable to detect any such bands close to the predicted features in measurements covering 1550 - 1800 $cm^{-1}$. It can be argued against the assignment of the 1694 $cm^{-1}$ band to an alcohol ylide because the discrepancies with the bands computed to appear at 1598 $cm^{-1}$ (a ketone stretch) and 1736 $cm^{-1}$, both assigned to isomer 2 in Table S4.7 of Supporting Information, lie outside the level of agreement with computational predictions demonstrated for ylide bands in THF and ACN. Solvation of the EtOH ylide might account for a significant shift to lower wavenumber than the predicted 1736 $cm^{-1}$ band position. However, this proposition is argued against because THF ylides formed in THF:EtOH mixtures show no more than -10 $cm^{-1}$ shifts upon displacement of THF by EtOH in the solvation shell of the ylide (see Figure S4.6 of Supporting Information). For such modest solvent shifts with alcohols, it would still be expected to see the absorption band computed to appear at 1598 $cm^{-1}$ in the spectral window covered by the experimental measurements, but it is not observed. Further, indirect arguments against an ylide assignment of the 1694 $cm^{-1}$ band are presented in Figure S4.6 of Supporting Information.

An alternative assignment is therefore needed for the 1694 $cm^{-1}$ band. A cation absorption (Scheme 4.1) is ruled out because in this spectral region the only expected band has a predicted wavenumber of 1740 $cm^{-1}$. Assuming bimolecular reaction with solvent is responsible for the 1694 $cm^{-1}$ band in EtOH solution, the rate of growth identifies an apparently diffusion-controlled reaction rate coefficient. Measurements in cyclohexane:EtOH

mixtures of different ratios indicate a rate coefficient $k$ = (4.3 ± 0.3) × $10^{10}$ $dm^3$ $mol^{-1}$ $s^{-1}$ (Supporting Information, Figure S4.5). TVAS measurements in THF:EtOH mixtures reveal direct competition between growth of the 1694 $cm^{-1}$ band and the band identifying the THF ylide (Supporting Information, Figure S4.6), confirming that the 1694 $cm^{-1}$ band derives from reaction of carbene (2).

To investigate further the mechanism for the reaction between carbene (2) and alcohols, a two-dimensional relaxed potential energy surface was computed for the reaction with a MeOH molecule. The outcome is shown in Figure 4.4 and reveals barrierless formation of an enol species, as well as suggesting involvement of one of the carbonyl groups in the reaction. The $\alpha$-carbonyl group appears to promote the enol pathway by a hydrogen bonding interaction with the alcohol which facilitates a barrierless proton transfer along the intermolecular hydrogen bond. The ylide is computed to lie higher in energy than the enol, and it is connected to the enol by a pathway which is monotonically downhill in potential energy. The pathway to the carbocation is an energetically uphill process that is likely to be inaccessible. Single point energy calculations predict enol (9) to be 146 kJ $mol^{-1}$ more stable than the ylide isomer of the type shown in Scheme 4.1. Computed vibrational frequencies of the enol identify a strong band at 1713 $cm^{-1}$ (an ester carbonyl stretch) which agrees satisfactorily with the experimentally observed 1694 $cm^{-1}$ feature. For these reasons, the preferred assignment of this band is to enol (9).

Alcohol reaction anti to the ketone functionality of carbene (2) yields enol (10) by a barrierless pathway involving the ester carbonyl group (see Figure S4.12 of Supporting Information). Enol (10) has a predicted vibrational band at 1694 $cm^{-1}$ (the ketone stretch), but lies 73.8 kJ $mol^{-1}$ higher in energy than enol (9) and is therefore expected to only be a minor contributor to the band intensity. Another solvent dependent band is observed in Figure 4.3(d) between 1650 and 1670 $cm^{-1}$, with the EtOH concentration dependence of its growth rate establishing a diffusion-limited rate coefficient consistent with that found for enol (9). Several minima were identified in the theoretical calculations corresponding to different isomers of enol (9). In particular, its Z,Z-isomer (isomer 4, Supporting Information, Table S4.7) is only 3.3 kJ $mol^{-1}$ higher in energy and forms from the syn-isomer of the carbene. Isomer 4 (Supporting Information, Table S4.7) has a predicted IR-active mode at 1648 $cm^{-1}$ (ester stretch), making it a plausible candidate for the feature lying between 1650 and 1670 $cm^{-1}$.

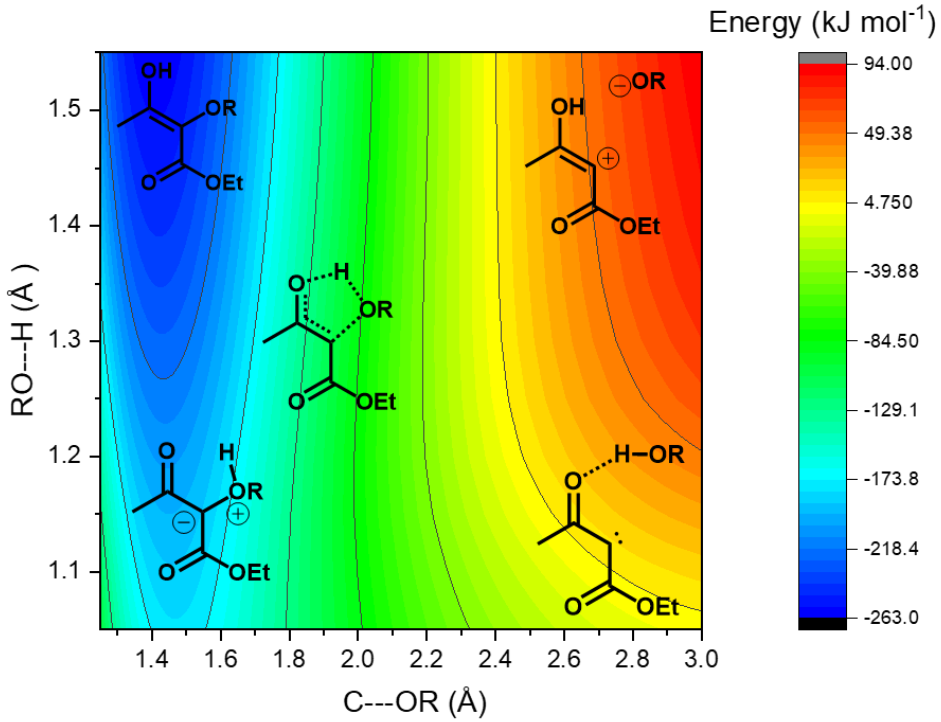


Figure 4.4 – A computed two-dimensional relaxed potential energy surface showing the minimum energy pathway for the reaction of MeOH with the EDAA-derived carbene (2). The plotted coordinates are C---OR, the distance between the O atom of MeOH and the carbene centre atom, and RO---H, the distance between the O and H atoms originating from the MeOH.

The findings suggest enol formation is the preferred pathway for the reaction of α-carbonyl carbenes with alcohols. This deduction contrasts with the report by Xue *et al.* of direct observation of an alcohol ylide derived from an α-carbonyl carbene.[12] This latter study used a carboethoxy carbene, but calculations (Figure S4.12 of Supporting Information) indicate that reactions of such carbenes with an alcohol to form an enol from an ester group remain barrierless. Instead, a structural argument could account for the different experimental observations. The carboethoxy carbene employed by Xue *et al*. can react anti with respect to the carbonyl to form an E-isomer of the ylide which does not have a carbonyl group in the correct orientation for the enol-forming proton transfer reaction. Conjugation of the negative charge of the ylide gives an enolate-like structure which introduces an energy barrier to rotation, therefore preventing rearrangement to the lower-energy enol.[12] In contrast,

reactions from both syn and anti faces of the α-carbonyl carbene employed in the experiments presented in this chapter offer carbonyl groups in the right orientation to form enols which cannot be spectroscopically distinguished here.

### 4.3.4 Singlet carbene

The evidence presented so far of carbene (2) formation is indirectly obtained by monitoring the growth of its reaction products. Direct observation of carbene spectral signatures is complicated by the overlap of spectral features from several species involved in the reactions. However, in ACN the experiments detect a weak band centred at 1638 $cm^{-1}$ that is in accord with an expected singlet carbene band at 1627 $cm^{-1}$. The kinetics of the decay of the band match the growth of the ACN ylide band intensity, as shown in Figure 4.5. Similar observations were made in THF, with a band identified at 1646 $cm^{-1}$ that decays on a timescale consistent with formation of the THF ylide. The shift in the observed wavenumbers of these bands from computational predictions can be explained by solvent-specific interactions at the carbene centre to form an ylidic complex in which there is partial electron donation from the nucleophile to the vacant p-orbital of the carbene centre.[13] Previous reports have identified similar solvent-dependent shifts in the electronic spectra of singlet carbenes.[14]

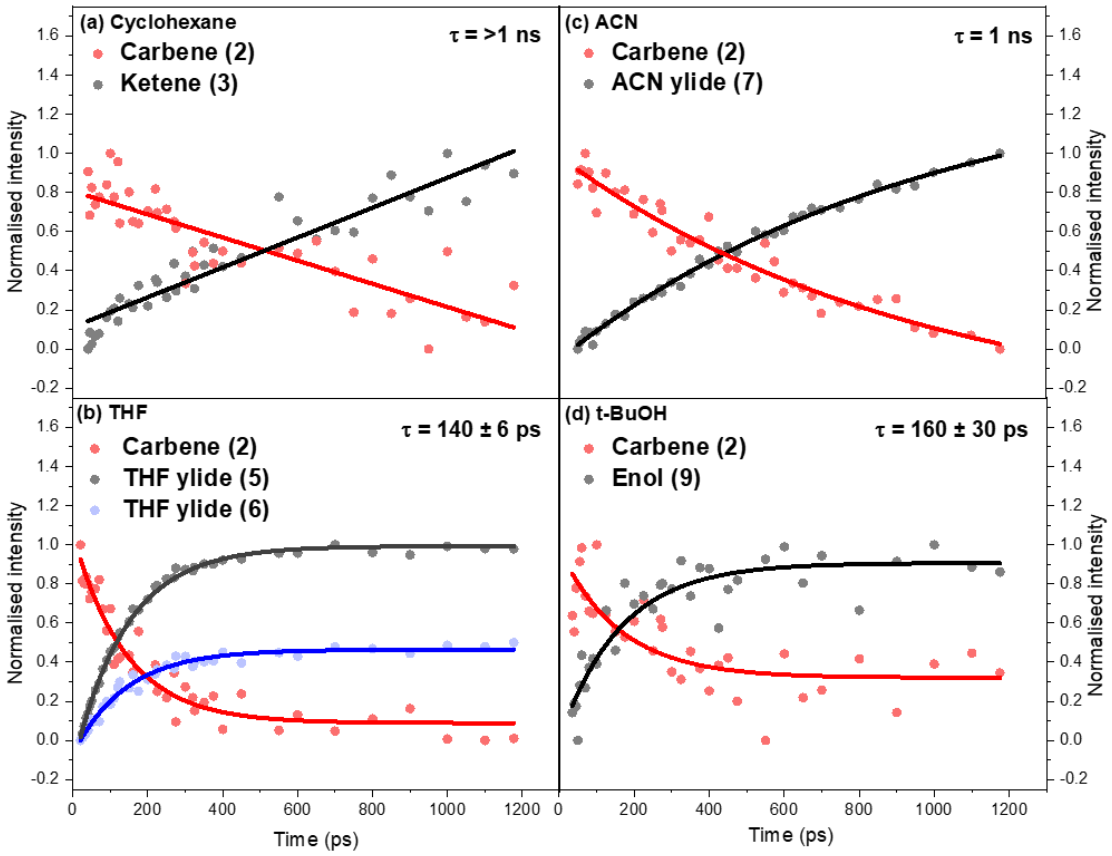


Figure 4.5 – Kinetics of carbene (2) reactions derived from direct spectroscopic observations following 256-nm excitation of 3.2 mM EDAA solutions. In all panels, normalised intensities for bands assigned to carbene (2) are shown in red, and reaction products are in black or blue. Circles are experimental measurements and solid lines are fits to single exponential functions. (a) decay of the 1620-1650 $cm^{-1}$ band assigned to the carbene (red) and growth of the 1725 $cm^{-1}$ ketene (3) band (black) in cyclohexane. Solid lines are global fits which establish a common exponential time constant of $\tau > 1$ ns. (b) Carbene band decay at 1646 $cm^{-1}$ (red) and growth of the THF ylide (5) band at 1586 $cm^{-1}$ (black) and THF ylide (6) (Blue, ×0.5) (Supporting Information, Table S4.4, Isomer 4) at 1635 $cm^{-1}$ in THF, $\tau = 140 \pm 6$ ps. (c) Carbene band decay at 1638 $cm^{-1}$ and growth of the ACN ylide band at 1625 $cm^{-1}$ (black) in ACN $\tau = 1$ ns. (d) Carbene band decay at 1636 $cm^{-1}$ (red) and growth of the enol band at 1694 $cm^{-1}$ (black) in t-BuOH, $\tau = 160 \pm 30$ ps.

The identification and analysis of carbene (2) bands in alcohols is challenging because of the spectral overlap of transient absorption and GSB features in the region where

calculations predict a singlet carbene band will appear. However, the slower reaction of the singlet carbene in t-BuOH than in EtOH, evident from the comparative rates of growth of the enol bands, allows separation of the decay of the transient feature centred between 1636 $cm^{-1}$ and the GSB recovery. The decay of the feature in t-BuOH can be fitted to the same time constant as the growth of the enol band (Figure 4.5(d)), and it may therefore correspond to loss of the singlet carbene.

In cyclohexane, decay of singlet carbene bands should be dominated by the stepwise WR because reaction with solvent is not expected. In accord with this expectation, no evidence for carbene insertion into C-H bonds of cyclohexane was found within the 1.3 ns timescale of the measurements. A weak but prompt growth of an absorption band at 1645 $cm^{-1}$ (Figure 4.3(a)) could correspond to the singlet carbene but overlaps the wing of a stronger GSB. Its slow decay (Figure 4.5(a)) is compatible with the stepwise WR route to ketene products.

The prompt formation of bands proposed to arise from singlet carbene (2) in all the different solvents studied supports direct competition between carbene formation and the concerted Wolff rearrangement for photo-excited EDAA. The kinetics of decay of these bands match the growth of products of the stepwise WR and of products of carbene reactions with the solvent. This combination of spectroscopic and kinetic evidence is consistent with carbene (2) being a precursor to stepwise WR reactions, and supports the proposition of competition between this structural rearrangement and bimolecular reaction with solvent molecules.

**4.5 Conclusion**

The UV photoexcitation of ethyl diazo acetoacetate and loss of $N_2$ leads to ultrafast production of two isomers of a ketene photoproduct via a Wolff rearrangement. The photochemistry also makes a singlet carbonyl carbene intermediate, IR bands of which are identified, and this carbene avoids the rearrangement pathway by rapid reaction with nucleophilic solvents. In tetrahydrofuran or acetonitrile solutions, these reactions produce ylides which are observed via characteristic IR absorption bands at 1586 $cm^{-1}$ and 1625 $cm^{-1}$ respectively. However, in EtOH or t-BuOH, alternative reaction pathways of the singlet carbene are identified. The α-carbonyl group of the carbene influences these O-H insertion reactions by promoting enol formation via a cyclic structure, resembling a pericyclic reaction

pathway that is computed to be barrierless. The enol formation is monitored experimentally via a band at 1694 $cm^{-1}$. The measurements made show no spectroscopic signatures between 1550 $cm^{-1}$ and 1800 $cm^{-1}$ in the measurements of EDAA photochemistry to support a previously proposed alcohol ylide pathway.

**References**


1. Kirmse, W. 100 Years of the Wolff Rearrangement. *Eur. J. Org. Chem.* **2002,** *2002*, 2193-2256.
2. Strausz, O. P.; Thap, D. M.; Gunning, H. E. Rearrangement and Polar Reaction of Carbethoxymethylene in 2-Propanol. *J. Am. Chem. Soc.* **1968,** *90*, 1660-1661.
3. Toscano, J. P.; Platz, M. S.; Nikolaev, V.; Popic, V. Carboethoxycarbene. A Laser Flash Photolysis Study. *J. Am. Chem. Soc.* **1994,** *116*, 8146-8151.
4. Chiang, Y.; Jefferson, E. A.; Kresge, A. J.; Popik, V. V.; Xie, R. Q. Conjugate addition of water to acarbonylcarbenes. *J. Phys. Org. Chem.* **1998,** *11*, 610-613.
5. Chiang, Y.; Eustace, S. J.; Jefferson, E. A.; Kresge, A. J.; Popik, V. V.; Xie, R.-Q. Flash photolysis of 4-diazoisochroman-3-one in aqueous solution. Hydration of the carbene produced by loss of nitrogen and ketonization of the enol hydration product. *J. Phys. Org. Chem.* **2000,** *13*, 461-467.
6. Wiberg, K. B. Basis set effects on calculated geometries: 6-311++G** vs. aug-cc-pVDZ. *J. Comput. Chem.* **2004,** *25*, 1342-1346.
7. Rani, U.; Oturak, H.; Sudha, S.; Sundaraganesan, N. Molecular Structure, Harmonic and Anharmonic Frequency Calculations of 2,4-Dichloropyrimidine and 4,6-Dichloropyrimidine by HF and Density Functional Methods. *Spectrochim. Acta A* **2011,** *78*, 1467-1475.
8. Frey, J. A.; Leist, R.; Tanner, C.; Frey, H.-M.; Leutwyler, S. 2-pyridone: The role of out-of-plane vibrations on the $S_1 \leftrightarrow S_0$ spectra and $S_1$ state reactivity. *J. Chem. Phys.* **2006,** *125*, 114308-114322.
9. Broda, M. A.; Buczek, A.; Kupka, T.; Kaminsky, J. Anharmonic vibrational frequency calculations for solvated molecules in the B3LYP Kohn–Sham basis set limit. *Vib. Spectrosc* **2012,** *63*, 432-439.
10. Frisch, M. J.; Trucks, G. W.; Schlegel, H. B.; Scuseria, G. E.; Robb, M. A.; Cheeseman, J. R.; Scalmani, G.; Barone, V.; Mennucci, B.; Petersson, G. A.; Nakatsuji, H.; Caricato, M.; Li, X.; Hratchian, H. P.; Izmaylov, A. F.; Bloino, J.; Zheng, G.; Sonnenberg, J. L.; Hada, M.; Ehara, M.; Toyota, K.; Fukuda, R.; Hasegawa, J.; Ishida, M.; Nakajima, T.; Honda, Y.; Kitao, O.; Nakai, H.; Vreven, T.; Montgomery, J. A., Jr.;; Peralta, J. E.; Ogliaro, F.; Bearpark, M.; Heyd, J. J.; Brothers, E.; Kudin, K. N.; Staroverov, V. N.; Kobayashi, R.; Normand, J.; Raghavachari, K.; Rendell, A.; Burant, J. C.; Iyengar, S. S.; Tomasi, J.; Cossi, M.; Rega, N.; Millam, N. J.; Klene, M. K., J. E.;; Cross, J. B.; Bakken, V.; Adamo, C.; Jaramillo, J.; Gomperts, R.; Stratmann, R. E.; Yazyev, O.; Austin, A. J.; Cammi, R.; Pomelli, C.; Ochterski, J. W.; Martin, R. L.; Morokuma, K.; Zakrzewski, V. G.; Voth, G. A.; Salvador, P.; Dannenberg, J. J.; Dapprich, S.; Daniels, A. D.; Farkas, O.; Foresman, J. B.; Ortiz, J. V.; Cioslowski, J.; Fox, D. J. *Gaussian 09, revision D.01*, Gaussian, Inc: Wallingford, CT, 2013.
11. Grubb, M. P.; Orr-Ewing, A. J.; Ashfold, M. N. R. KOALA: A program for the processing and decomposition of transient spectra. *Rev. Sci. Instrum.* **2014,** *85*, 064104.
12. Xue, J.; Luk, H. L.; Platz, M. S. Direct Observation of a Carbene-Alcohol Ylide. *J. Am. Chem. Soc.* **2011,** *133*, 1763-1765.
13. Gómez, S.; Restrepo, A.; Hadad, C. Z. Theoretical tools to distinguish O-ylides from O-ylidic complexes in carbene–solvent interactions. *Phys. Chem. Chem. Phys.* **2015,** *17*, 31917-31930.
14. Wang, J.; Kubicki, J.; Gustafson, T. L.; Platz, M. S. The Dynamics of Carbene Solvation: An Ultrafast Study of p-Biphenylyltrifluoromethylcarbene. *J. Am. Chem. Soc.* **2008,** *130*, 2304-2313.

**Chapter 4 – Supporting information**

S1 – Supporting experimental data and fitting

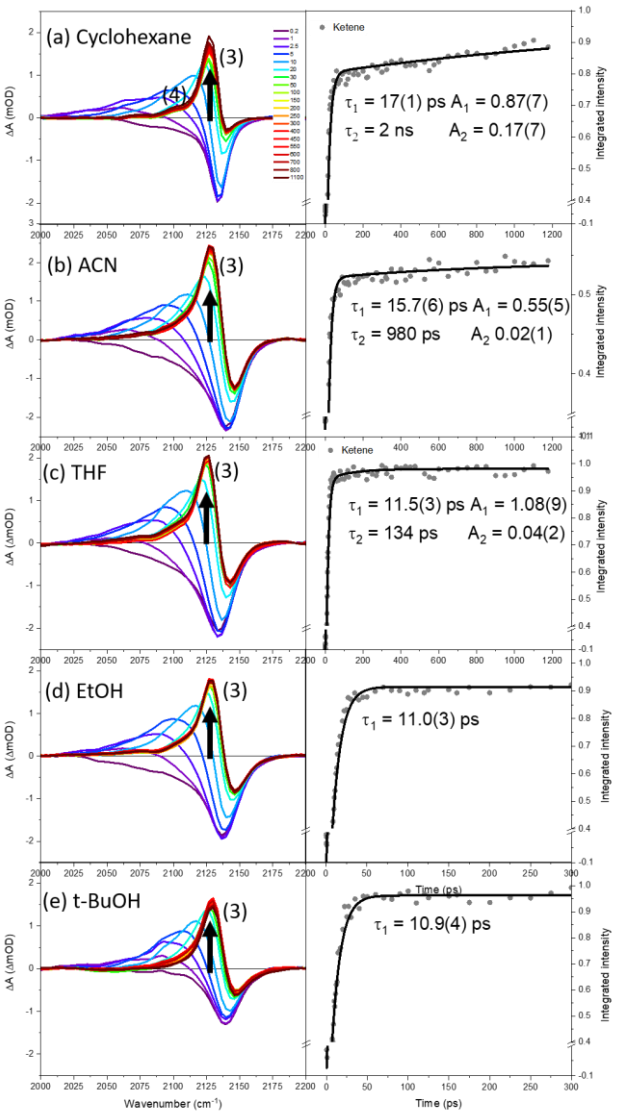


Figure S4.1 – Left column - TVAS spectra obtained in the ketene stretching region from 2000 – 2200 $cm^{-1}$ for the UV ($\lambda$ = 256 nm) photoexcitation of ethyl diazoacetoacetate (EDAA) in: (a) Cyclohexane; (b) ACN; (c) THF; (d) EtOH; (e) t-BuOH. Ketene structures (3) and (4) to which bands are assigned are shown in Scheme 4.3 of the main text. Right column – Time-dependent growths of the integrated intensities for the ketene band at 2125 $cm^{-1}$ in the corresponding solvents (grey circles), and fits (solid lines) to biexponential functions to obtain time constants $\tau_1$ and $\tau_2$. The corresponding relative amplitudes of the two time components are given by values $A_1$ and $A_2$. Numbers in parentheses are fitting uncertainties within a 95% confidence interval. The uncertainties in $A_1$ values are predicted to be ± 7.5% due to the overlapping GSB recovery which could account for up to 15% of the amplitude.

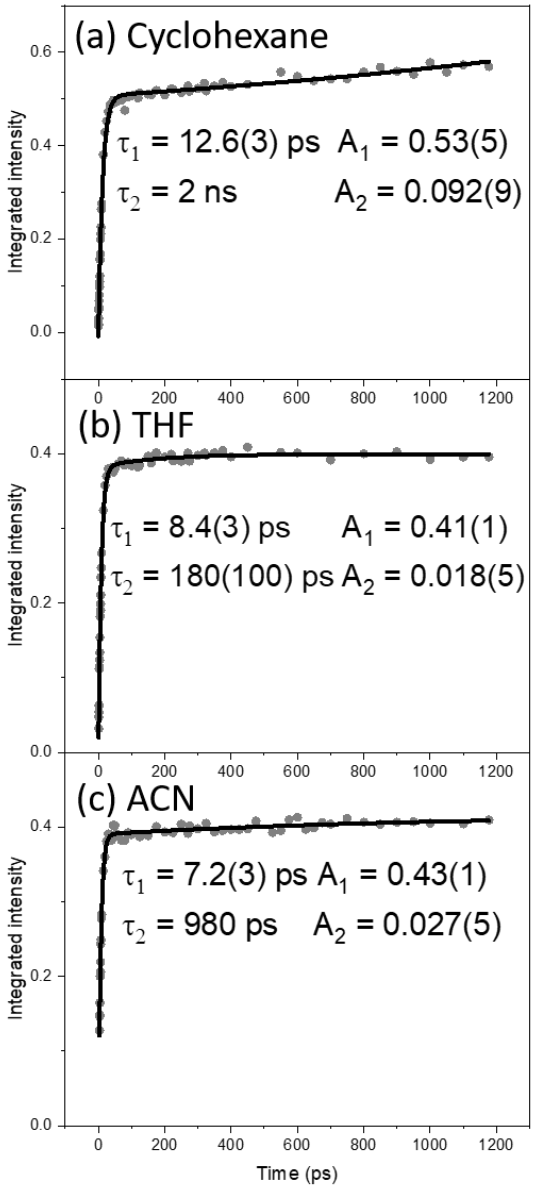


Figure S4.2 - Kinetic plots for the growth in intensity of the 1725 $cm^{-1}$ band assigned to a ketene photoproduct of 256-nm UV excitation of EDAA in: (a) Cyclohexane; (b) THF; (c) ACN. Circles are experimental measurements and solid lines are fits to a biexponential growth function with time constants $\tau_1$ and $\tau_2$ and respective amplitudes $A_1$ and $A_2$. Numbers in parentheses are fitting uncertainties within a 95% confidence interval.

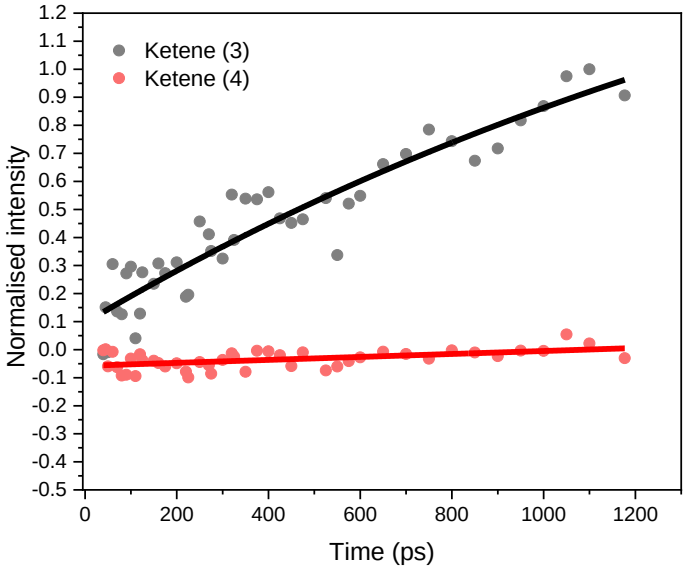


Figure S4.3 – Kinetic analysis of the intensities of bands attributed to ketenes (3) and (4) (see Scheme 4.3 of the main text) in Figure S4.1(a) produced by the stepwise Wolff rearrangement. Circles are experimental measurements and solid lines are fits to an exponential growth function to give a ≈2 ns time constant for ketene (3) and no observable growth of ketene (4). Data are plotted for time delays after 40 ps, a period after the vibrational cooling of hot ketene molecules. The data set has been renormalized to a maximum value of unity to highlight the stepwise Wolff-rearrangement component in the growth of the ketene (3) band. No measurable contribution from the stepwise Wolff-rearrangement was found for the ketene (4) band.

Kinetics of growth of the enol band in EtOH, t-BuOH and THF:EtOH mixtures

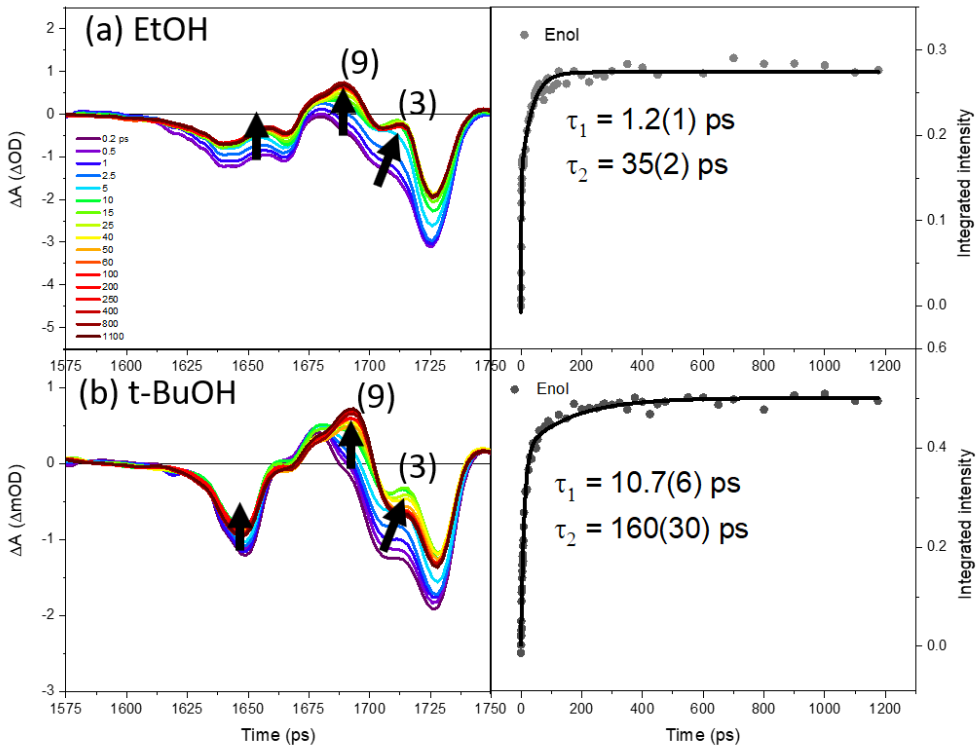


Figure S4.4 – Left: TVAS spectra measured from 1575 – 1750 $cm^{-1}$ following the 256-nm photoexcitation of EDAA in: (a) EtOH; (b) t-BuOH. Right: Kinetic plots associated with the growth of the enol band at ~1694 $cm^{-1}$ in the corresponding solvents (circles) and fits (solid lines) to biexponential growth functions to give time constants $\tau_1$ and $\tau_2$. The enol is shown as species (9) in Scheme 4.3 of the main text. Species (3) is a ketene photoproduct.

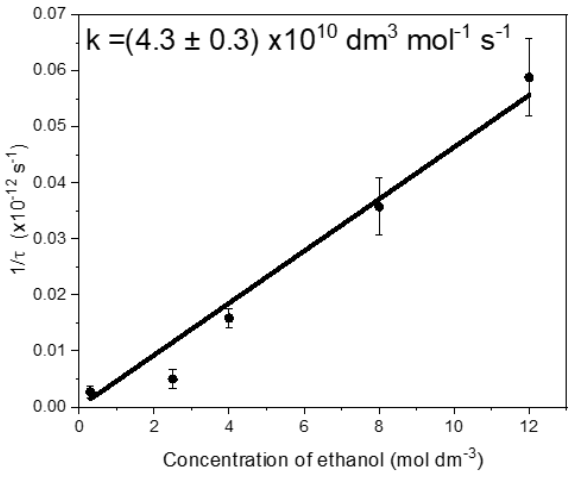

Figure S4.5 – Pseudo-first order kinetic analysis for singlet carbene (2) (see Scheme 4.3) reaction with EtOH. The plot shows pseudo first-order rate coefficients given by 1/τ (where τ is an exponential growth time constant) as a function of EtOH concentration in cyclohexane. The product enol is shown as Enol (9) in Scheme 4.3 of the main text and Enol isomer (9) in Section S2 Table S4.7.

The growth of the enol band at 1694 $cm^{-1}$ in EtOH and t-BuOH solutions (Figure S4.4) can be fitted to a biexponential function. The faster component is likely to derive from overlap with the ketene (3) absorption which extends to lower wavenumber at earlier times because it is produced with excess vibrational energy. The second component (with larger time constant $\tau_2$) is attributed to the formation of the enol. However, it is not possible to discount the faster $\tau_1$ component also containing a contribution from the reaction of vibrationally hot carbene molecules with the alcohol.

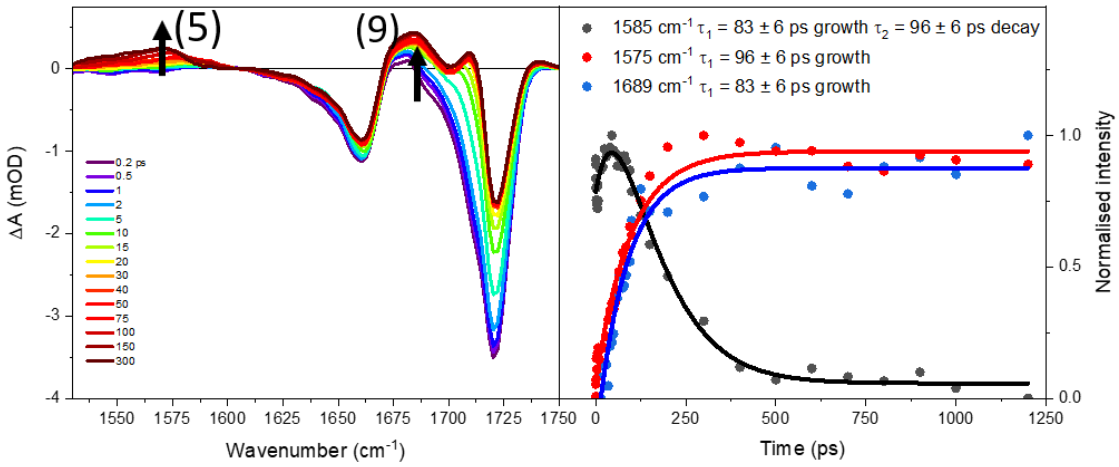


Figure S4.6 – Left – TVAS spectra measured between 1530 and 1750 $cm^{-1}$ for the 256-nm photoexcitation of EDAA in a 3:2 THF:EtOH mixture. Right – Kinetic plots showing the competition between formation of the THF ylide (shown as (5) in Scheme 4.3 of the main text) at 1585 $cm^{-1}$ and the EtOH enol (shown as (9) in Scheme 4.3 of main text) at 1689 $cm^{-1}$. A global fit of the growth of both bands gives a time constant of 83 ± 6 ps. The decay of the 1585 $cm^{-1}$ band and the growth of the 1575 $cm^{-1}$ band give a time constant of 96 ± 6 ps which is assigned to solvent reorganization around the THF ylide. Solid symbols are experimental measurements and lines are fits to an exponential growth function.

Indirect support for the assignment of enol (9) to the 1694 $cm^{-1}$ is given by comparing the solvation dynamics of the 1694 $cm^{-1}$ band (in neat EtOH) to those of the THF ylide in THF:EtOH mixtures (compare Figure S4.6 with the TVAS spectra obtained in neat THF or EtOH in Figure 4.2 of the main text). In the THF mixtures, THF ylide (5) gives rise to a broad band at 1585 $cm^{-1}$ which grows with an 83 ± 6 ps time constant. The band position matches the 1586 $cm^{-1}$ ylide band found in neat THF. The 1585 $cm^{-1}$ band subsequently shifts to 1575 $cm^{-1}$ with a 96 ± 6 ps time constant, which is attributed to solvent reorganization around the THF ylide as EtOH displaces THF in the ylide solvent shell. In contrast, a 1689 $cm^{-1}$ band in THF:EtOH mixtures (corresponding to the 1694 $cm^{-1}$ band in neat EtOH attributed to an enol) forms promptly and shows no further time-dependent band shifts. With changing THF and EtOH ratios, the bands assigned to an enol and to a THF ylide shift in opposite directions (compare Figure S4.6 with TVAS spectra obtained in neat THF or EtOH). These observations are consistent with different types of bonding adjacent to the carbonyl group responsible for the IR band.

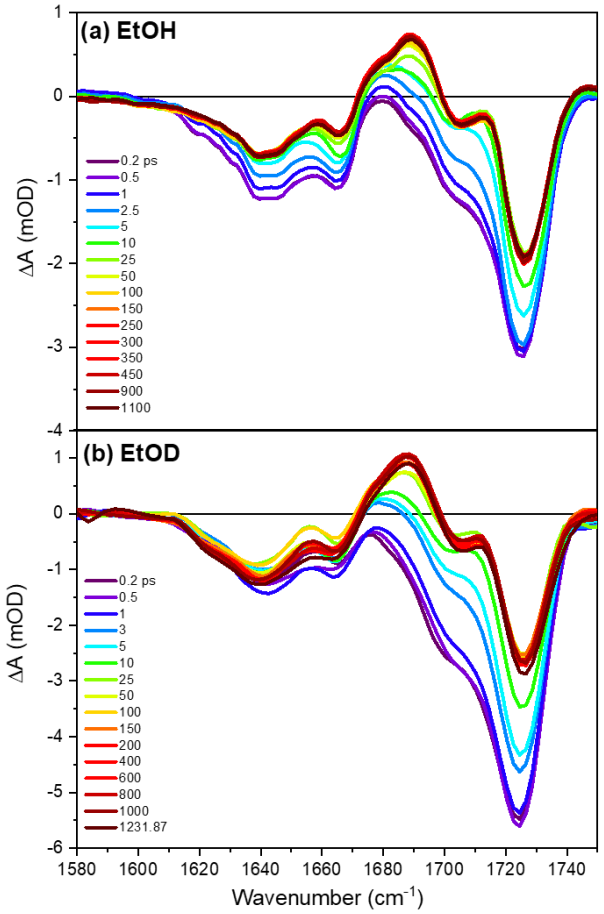


Figure S4.7 – Comparison of TVAS spectra for the 256 nm photoexcitation of EDAA in (a) EtOH and (b) EtOD

The isotopic substitution of EtOH for EtOD shown in Figure S4.7 identifies that there is no perturbation to the carbonyl stretching frequency of the transient absorption band centred at 1694 $cm^{-1}$. This observation is in agreement with the calculated vibrational frequencies of the deuterated enol (shown as (9) in Scheme 4.3 of main text), and supports the deductions of the preferred formation of intramolecularly non-hydrogen bonded enol and ylide isomers.

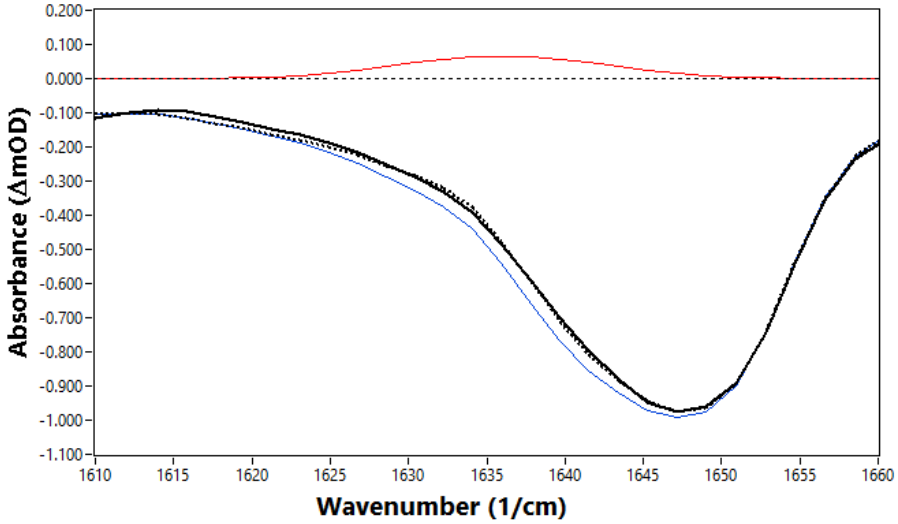


Figure S4.8 – Example fitting procedure for the decomposition of the overlapping carbene band (red) and the ground state bleach (blue) following the 256-nm photoexcitation of EDAA in t-BuOH. The example spectrum is taken at 35 ps. The basis function for the ground state bleach was taken at 1175 ps, corresponding to completion of any GSB recovery and with no remaining overlapping signal from the carbenes because they have fully reacted with solvent molecules. The basis function is set to be invariant in all fits and a Gaussian function is overlapped and fitted to account for absorption by the carbene band (red) at early time. Spectral decomposition was carried out using the KOALA program.[1]

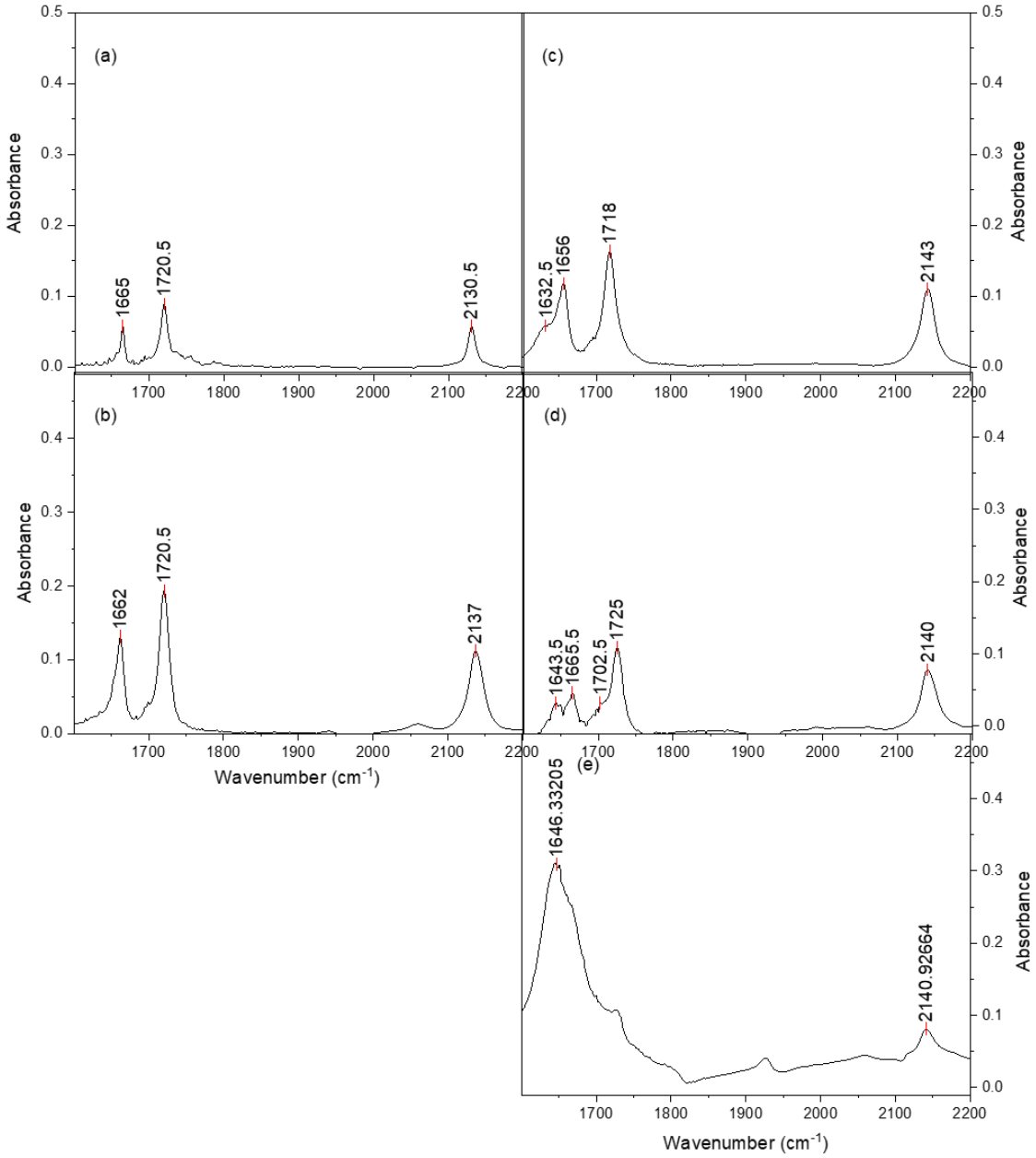


Figure S4.9 – Steady state FTIR spectra in the 1600 – 2200 $cm^{-1}$ region for 3.2 mM EDAA in: (a) Cyclohexane; (b) THF; (c) ACN; (d) EtOH; (e) t-BuOH.

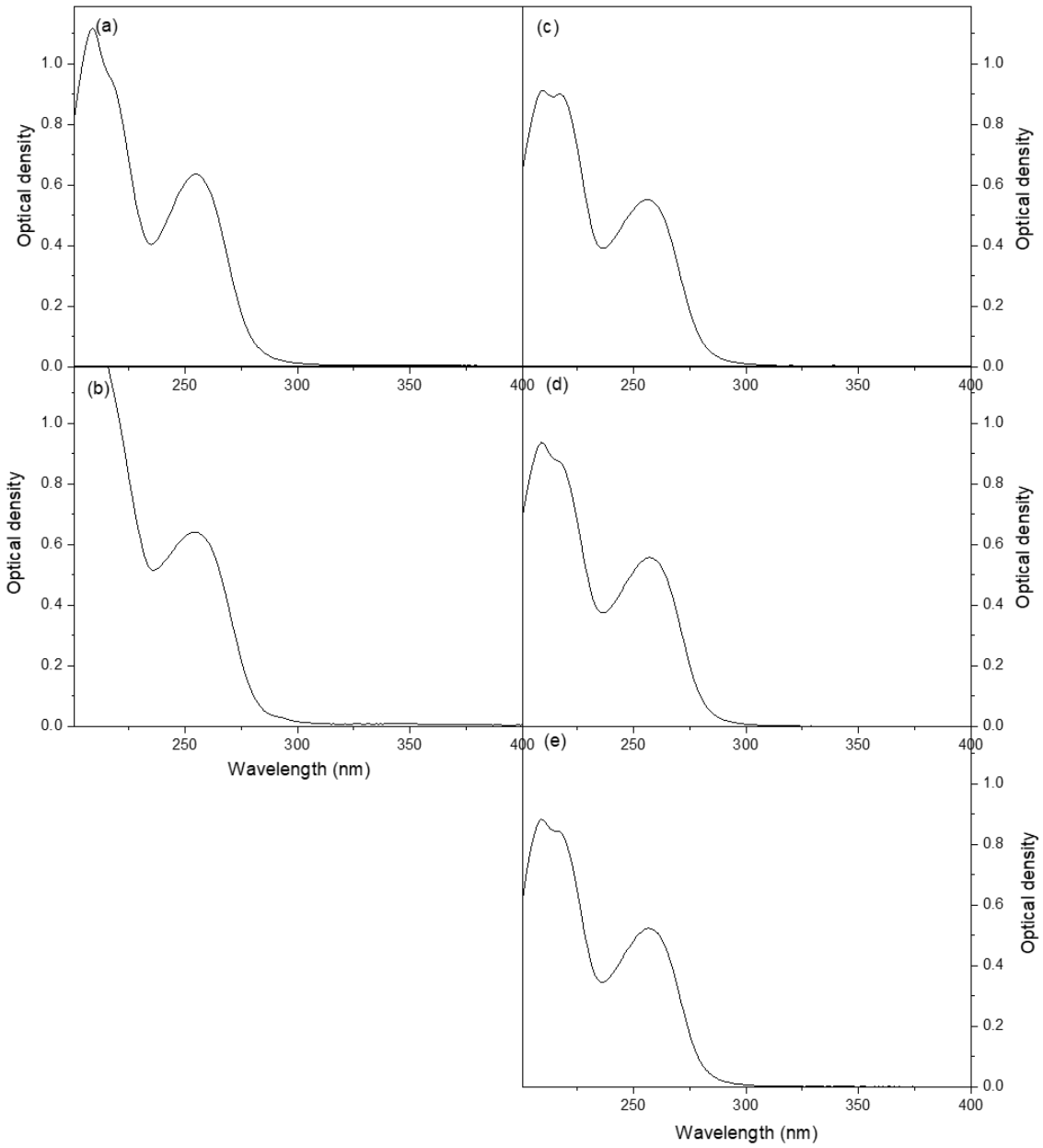


Figure S4.01 – Steady state UV-Vis absorption spectra in the 200 – 400 nm wavelength region for 3.2 mM EDAA in: (a) cyclohexane; (b) THF; (c) ACN; (d) EtOH; (e) t-BuOH.

Table S4.1 – Time constants for the growth and decay of various reactive intermediates (identified by their numbers in Scheme 4.3) in the different solvents studied. Uncertainties in time constants from the kinetic fitting are specified in parentheses.

| | Cyclohexane (ps) | THF (ps) | ACN (ps) | EtOH (ps) | t-BuOH (ps) |
|---|---|---|---|---|---|
| Ketene (3) Growth | $\tau_1$ = 17(1)<br>$\tau_2 \geq$ 1000 | $\tau_1$ = 11.5(3)<br>$\tau_2$ = 180(100) | $\tau_1$ = 15.7(6)<br>$\tau_2 \geq$ 1000 | $\tau_1$ = 11.0(3) | $\tau_1$ = 10.9(4) |
| Carbene (2) Decay | $\tau_1 \geq$1000 | $\tau_1$ = 140(6) | $\tau_1 \geq$ 1000 | | $\tau_1$ = 160(30) |
| Ylide Growth | | $\tau_1$ = 140(6) | $\tau_1 \geq$ 1000 | | |
| Enol (9) Growth | | | | $\tau_1$ = 35(2) | $\tau_1$ = 160(30) |

S2. Computational results

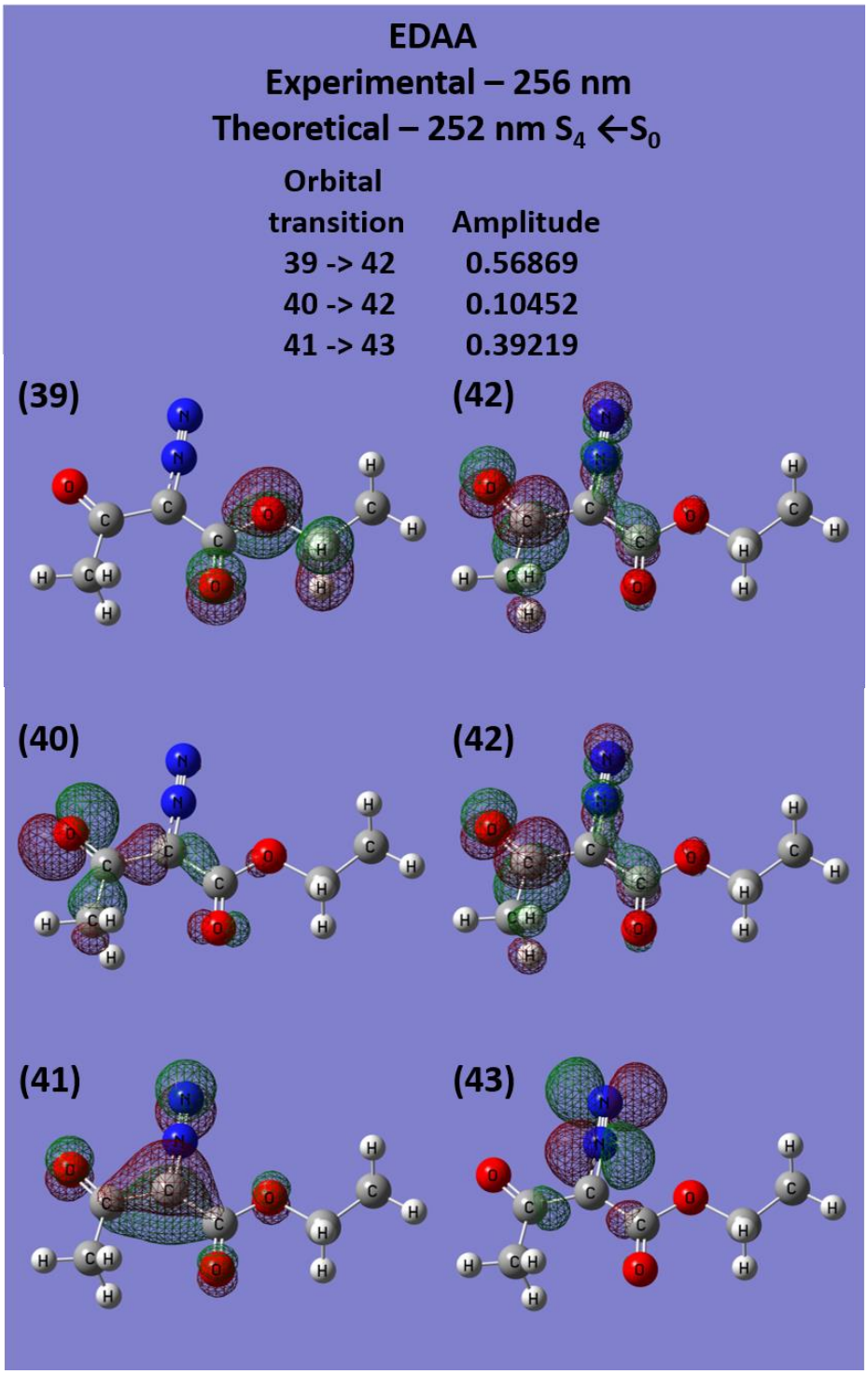


Figure S4.11 – Visualisation of the molecular wavefunctions involved in the 256-nm $S_4 \leftarrow S_0$ transition of EDAA. The corresponding orbital numbers are given in parethenses.

Table S4.2 – EDAA isomer structures, energies, frequencies and gas phase mole fractions

| EDAA Isomer | Energy[a] (kJ mol$^{-1}$) | Computed frequency[b] (cm$^{-1}$) | Structure | ΔG (kJ mol$^{-1}$) | Mole fraction | Observed frequency (cm$^{-1}$) | | | | |
|---|---|---|---|---|---|---|---|---|---|---|
| | | | | | | $C_6H_{12}$ | THF | ACN | EtOH | t-BuOH |
| 1 | 7.19 | 1710 (188)<br>1675 (372)<br>2224 (275) | 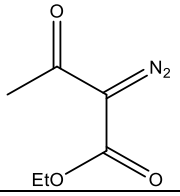 | 4.6 | 0.131 | | | | | |
| 2 | 0.00 | 1730 (359)<br>1689 (190)<br>2205 (315) | 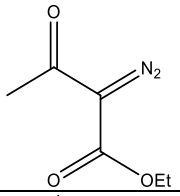 | 0 | 0.868 | 1721<br>1665<br>2131 | 1721<br>1662<br>2137 | 1718<br>1656<br>2143 | 1725<br>1665<br>2140 | ≈1650 (Very broad) |
| 3 | 23.5 | 1773 (347)<br>1689 (190)<br>2205 (315) | 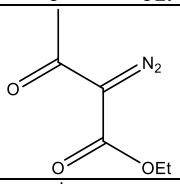 | 19.3 | 0.0003 | | | | | |
| 4 | 21.5 | 1717 (364)<br>1705 (84)<br>2182 (178) | 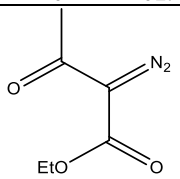 | 18.6 | 0.0004 | | | | | |

[a]B3LYP/6-311++G(d,p) energies for various isomers of EDAA are specified relative to Isomer 2.

[b]Anharmonically corrected vibrational frequencies for selected vibrational modes in the spectral regions covered by the experiments are also listed, and for Isomer 2 are compared to experimental values. Numbers in parentheses are IR transition intensities in km mol$^{-1}$.

Table S4.3 – Acetonitrile ylide structures, energies and vibrational frequencies

| ACN ylide Isomer | Energy[a] (kJ mol$^{-1}$) | Computed frequency[b] (cm$^{-1}$) | Structure | Observed frequency (cm$^{-1}$) |
|---|---|---|---|---|
| 1 | 2.89 | 1677 (145)<br>1626 (309) | 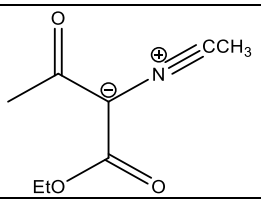 | |
| 2 | 0.00 | 1707 (139)<br>1634 (182) | 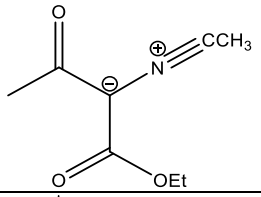 | 1625 |
| 3 | 34.2 | 1757 (391)<br>1675 (23) | 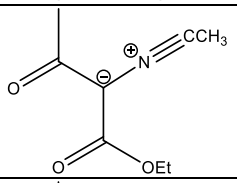 | |
| 4 | 25.9 | 1676 (84)<br>1653 (228) | 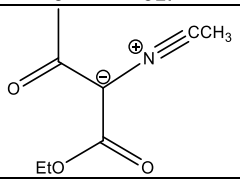 | |

[a]B3LYP/6-311++G(d,p) energies are specified for a variety of possible ACN-ylide isomers relative to the energy of Isomer 2.

[b]Anharmonically corrected vibrational frequencies within the experimentally studied spectral region are also listed and compared to experimental data. Values in parentheses are computed IR band intensities in km mol$^{-1}$.

Table S4.4 - THF ylide structures, energies and vibrational frequencies

| THF ylide Isomer | Energy[a] (kJ mol$^{-1}$) | Computed frequency[b] (cm$^{-1}$) | Structure | Observed frequency (cm$^{-1}$) |
|---|---|---|---|---|
| 1 | -0.68 | 1666 (99)<br>1563 (279) | 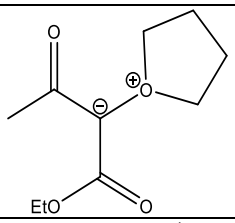 | |
| 2 | 0 | 1698 (135)<br>1564 (236) | 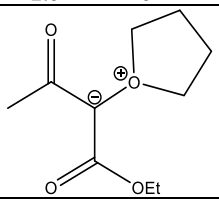 | 1586 |
| 3 | 54.7 | 1622 (73)<br>1744 (374) | 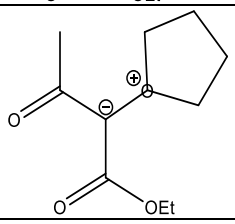 | |
| 4 | 32.4 | 1643 (76)<br>1604 (16) | 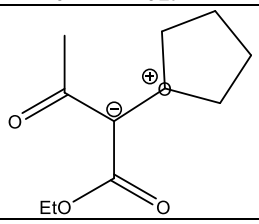 | 1635 |

[a]B3LYP/6-311++G(d,p) energies are specified for a variety of possible THF-ylide isomers relative to the energy of Isomer 2.

[b]Anharmonically corrected vibrational frequencies within the experimentally studied spectral region are also listed and compared to experimental data. Values in parentheses are computed IR band intensities in km mol$^{-1}$.

THF ylide Isomer 1 is predicted to be the lowest energy isomer, in contrast to the corresponding ACN-ylide for which Isomer 2 is the lowest energy form. This difference is likely to derive from steric repulsion from the bulky THF group. Isomer 2 is the preferred assignment of the band at 1586 cm$^{-1}$ in THF (Figure 4.2(b), main paper) on the basis that the corresponding anti carbene isomer is the most stable, and reaction to form Isomer 1 requires a significant rearrangement. The minor band at 1635 cm$^{-1}$ is assigned to Isomer 4.

Table S4.5 - Energies and vibrational frequencies of the photoproducts of EDAA.

| Isomer | Energy[a] (kJ mol$^{-1}$) | Computed frequency[b] (cm$^{-1}$) | Observed frequency (cm$^{-1}$) |
|---|---|---|---|
| Singlet carbene (syn) | 11.55 | 1712 (227)<br>1606 (4) | |
| Singlet carbene ((2) in scheme 4.3) (anti | 0 | 1627 (19)<br>1597 (62) | |
| Ketene 1 (syn) | -267 | 2172 (769)<br>1703 (177) | |
| Ketene 1 ((3) in scheme 4.3) (anti) | -274<br>$E_a$ = 16.9[c] | 2163 (744)<br>1732 (62) | 2125<br>1725 |
| Ketene 2 (syn) | -160 | 2154 (665)<br>1674 (201) | |
| Ketene 2 ((4) in scheme 4.3) (anti) | -162<br>$E_a$ = 30.7[c] | 2142 (618)<br>1699 (318) | 2105 |
| Triplet carbene (syn) | 23.9 | 1645 (44)<br>1538 (68) | |
| Triplet carbene (anti) | 14.1 | 1638 (83)<br>1561 (62) | |

[a]B3LYP/6-311++G(d,p) energies are specified relative to the singlet carbene (anti) product.

[b]Anharmonically corrected vibrational frequencies in the spectral regions studied are listed for a series of isomers potentially produced by the loss of $N_2$ from photoexcited EDAA. Values in parentheses are computed IR band intensities in km mol$^{-1}$.

[c] The activation energy for the formation of ketene calculated from carbene (2)

Table S4.6 – B3LYP/6-311++G(d,p) computed and anharmonically corrected vibrational frequencies in the IR probe region studied for other possible products of the UV photoexcitation of EDAA.

| Molecule | Frequency[a] (cm$^{-1}$) |
|---|---|
| Diazirine | 1748 (297)<br>1732 (29) |
| Cation | 1740 (154) |

[a]Values in parentheses are computed IR band intensities in km mol$^{-1}$.

Table S4.7 – Predicted energies and vibrational frequencies for potential isomeric enol and ylide products of the EDAA derived carbene (2) insertion into EtOH.

| Isomer | Energy[a] (kJ mol$^{-1}$) | Frequency[b] (cm$^{-1}$) | Geometry | Isomer | Energy[a] (kJ mol$^{-1}$) | Frequency[b] (cm$^{-1}$) | Geometry |
|---|---|---|---|---|---|---|---|
| 1 | 14.9 | 1732 (5)<br>1613 (84) | 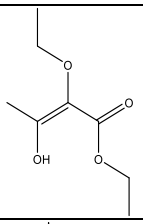 | 7 | 208 | 1790 (218)<br>1643 (100) | 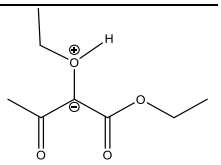 |
| 2 | 163 | 1736 (88)<br>1598 (176) | 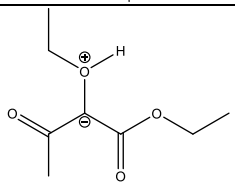 | 8 | 90.5 | 1699 (206)<br>1581 (133) | 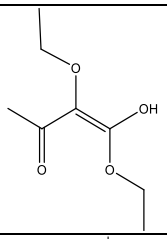 |
| 3 | 77.8 | 1704 (2)<br>1628 (44) | 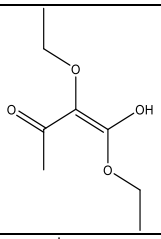 | 9 | 16.7 | 1713 (100)<br>1612 (78)<br>1712 (70)[c]<br>1606 (126)[c] | 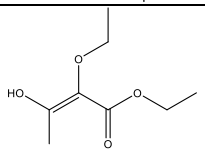 |
| 4 | 20.0 | 1648 (57)<br>1606 (11) | 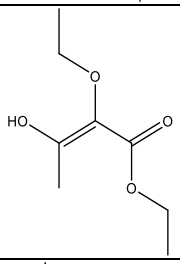 | 10 | 133.2 | 1712 (105)<br>1600 (116) | 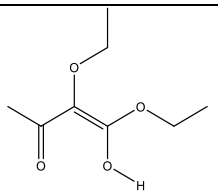 |
| 5 | 0 | 1733 (275)<br>1629 (76) | 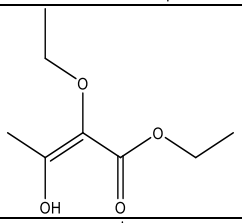 | 11 | 57.7 | 1590 (199)<br>1590 (22) | 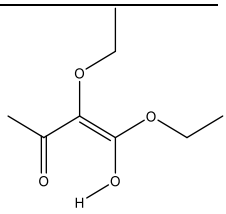 |
| 6 | 239 | 1790 (218)<br>1643 (101) | 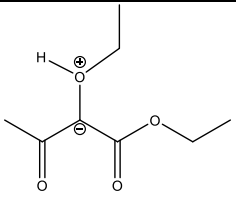 | 12 | 224 | 1669 (163)<br>1625 (76) | 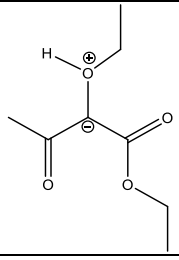 |

[a] All energies are expressed relative to Enol 5.

[b] Numbers in parentheses are IR band intensities in km mol$^{-1}$.

[c] Deuterium was used for the explicit hydrogen shown in the structure for the optimization and anharmonically corrected vibrational frequencies.

Several possible product isomers were identified for the insertion of the singlet carbene ((2) in Scheme 4.3) into EtOH. Single point energies and anharmonically corrected vibrational frequencies were determined at the B3LYP/6-311++G(d,p) level using very tight convergence criteria and are reported in Table S4.7. Isomers 4, 6, 7 and 8 can be discounted because they arise from either the syn isomer of the carbene which is not expected to be favoured, or through a large rearrangement across a partial double bond which is unfavourable. Isomers 1, 5, 10 and 11 can also be discounted as products because of the large rearrangement energies required to rotate around the enol double bond after the concerted addition. The barrier to this rotation is calculated to be ~255 kJ $mol^{-1}$. Isomers 9 and 8 are the most energetically accessible products for their respective syn and anti (with respect to the ketone functionality) approach by MeOH.

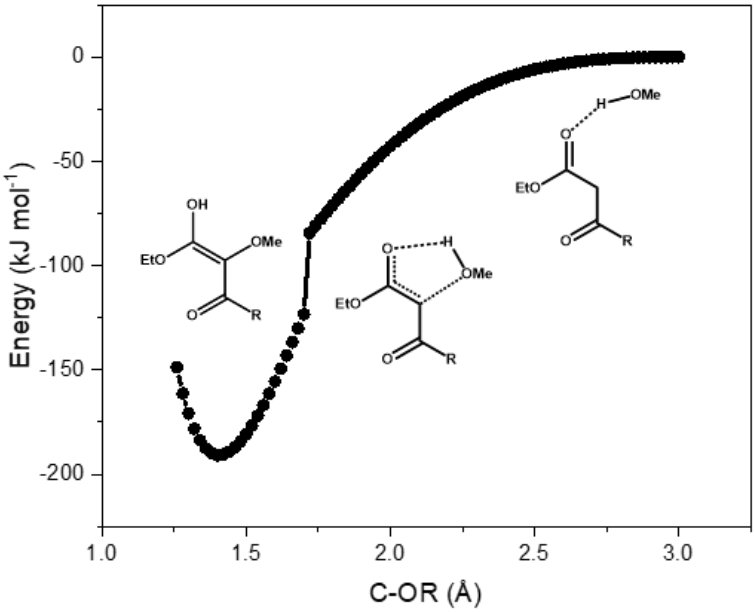


Figure S4.12 – PE curve showing the pathway for reaction of a MeOH molecule with singlet carbene (2) in which the MeOH interacts with the ester moiety. The discontinuous change in energy at a C-OR distance around 1.75 Å is the point when the proton transfer becomes barrierless, forming the enol (shown as (10) in scheme 4.3 of the main text) and structure 8 in Table S4.7).

Additional information

Full computational details and data files are available at the University of Bristol data repository, data.bris, at https://doi.org/10.5523/bris.iqt2f0tmjtut2m0wgxbtsopdo

## References

1. Grubb, M. P.; Orr-Ewing, A. J.; Ashfold, M. N. R. KOALA: A program for the processing and decomposition of transient spectra. *Rev. Sci. Instrum.* **2014,** *85*, 064104.

# Chapter 5. Direct Observation of the Dynamics of Ylide Solvation by Hydrogen-bond Donors using Transient vibrational absorption Spectroscopy

## 5.1. Introduction

Much of the synthesis of fine chemicals, pharmaceutical compounds and agrochemicals relies on reactions conducted in organic solvents, but the choice of solvent affects the thermodynamics and kinetics, and hence the outcomes of chemical reactions. In the solutions used for synthesis, different types of solute-solvent interactions will influence the rates, product yields and selectivity of the chemistry.[1-3] Many of these solvent-induced effects are attributed to bulk properties such as the solvent's dielectric constant; for example, polar solvents stabilise polar or charged intermediates and nucleophiles. However, these bulk properties are not always sufficient to account for solvent-induced trends in chemical reactivity because, at the molecular level, specific solute-solvent interactions can be significant. Such behaviour is common for protic solvents such as water and alcohols, for which the influence of hydrogen bonding has to be considered to understand how the solvent influences a reaction.[4-6] Efforts to understand hydrogen-bonding and its effects on the stability, molecular structure and reactivity of reaction intermediates in solution are therefore important across chemistry and biochemistry.

Zwitterions are dipolar neutral molecules carrying both formal negative and positive charges, and this polarity makes them particularly sensitive to their solvent environment.[7-10] Zwitterions come in many forms; for example, ylides and betaines are frequently invoked, short-lived intermediates for a variety of synthetic reactions.[11-15] Ylides have further been proposed as key intermediates in a series of biochemical transformations.[16-18] Lee *et al.* studied the effect of the solvent on sulfur-ylide mediated epoxidation, and found the use of 0.15 M methanol in non-polar solvents changed the stereochemistry, which they argued to be a result of specific betaine-methanol interactions.[19] Protic solvents have further been demonstrated to alter the selectivity in a series of Wittig reactions involving phosphonium ylides,[20-21] demonstrating a wider need to understand solvent interactions with such zwitterionic intermediates.

Several theoretical and computational studies have examined ylides as hydrogen-bond (HB) acceptors.[22-25] For example, Rozas *et al.* and Platts and Howard established that ylide complexes could be formed with a series of strong and weak HB donors. Their calculations identified that even the weak HB donor $C_2H_2$ could form stable ylide complexes with HB strengths of 16 – 34 kJ $mol^{-1}$,[23-24] and $CH_4$ formed such HBs with binding energies of 3-5 kJ $mol^{-1}$.[24] Further evidence for these types of C-H HBs with ylides came from the crystal structure of triphenylphosphonium benzylide, which showed a pairwise alignment suggestive of C-H HB donation to an acceptor atom in the ylide.[22] Despite the propensity for ylides to act as HB acceptors, direct experimental evidence of solvent-ylide complexes is scarce, as is evidence for the structural and electronic changes that result from hydrogen-bonded complexation.

α-Diazocarbonyl compounds can be used as precursors for singlet α-carbonyl carbenes by photolytic elimination of $N_2$,[26] and these carbenes have been shown to form in direct competition with the concerted Wolff-rearrangement to ketene intermediates.[27] Partial double C-C bond character within the local diazocarbonyl group results in syn and anti conformers,[28] with the syn-conformers favouring concerted Wolff-rearrangement,[29-30] whereas the anti-conformers form singlet carbene intermediates.[31-32] For diazoesters, the Wolff-rearrangement is largely suppressed,[33-34] and in Chapter 4 the Wolff-rearrangement of the ester functionality of Ethyl diazoacetoacetate was reported to only occur by a concerted Wolff-rearrangement mechanism.[27] Here, these findings are used to guide the interpretation of new experimental observations for the reaction and solvation dynamics of intermediates resulting from ultraviolet (UV) photoexcitation of Ethyl diazoacetate (EDA), as summarized in Scheme 5.1. Singlet carbenes from the photoexcitation of diazo compounds have been shown to insert into a variety of functional groups such as C=C, C-H and C-X (X = Cl, Br, I), and O-H bonds,[35-36] with the mechanism of insertion typically inferred from the stereochemistry of the products.

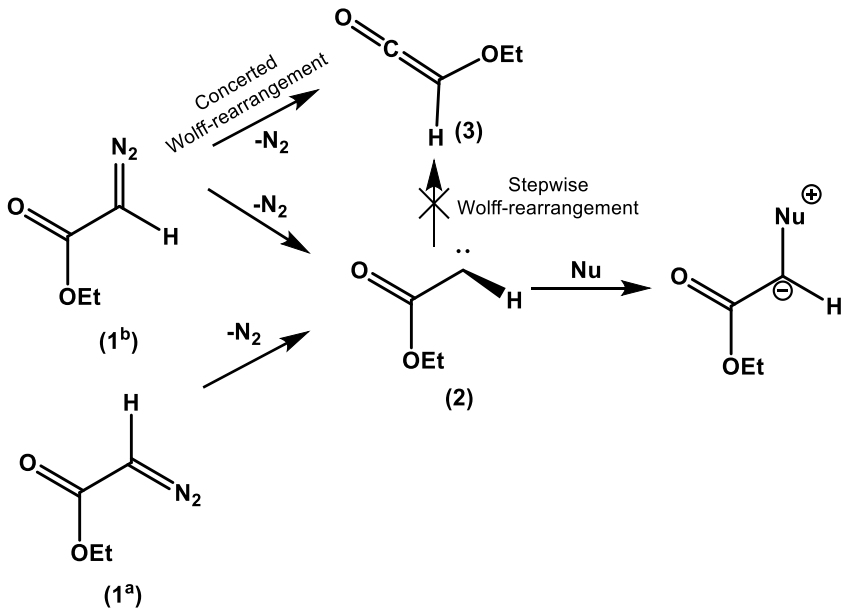


Scheme 5.1 – Photolytic decomposition of ethyl diazoacetate to produce singlet carbene intermediates in competition with ketenes, and the reaction of the singlet carbene with nucleophiles (Nu) to form ylides.

By monitoring the C=O stretching modes using transient vibrational absorption spectroscopy,[37] Xue *et al*. demonstrated that a variety of ylides could be directly observed from the reaction of the singlet α-carbonyl carbene formed by EDA photolysis with nucleophilic solvents such as tetrahydrofuran (THF), acetonitrile (ACN) and deuterated methanol (MeOD). Similarly, in Chapter 4 bands observed by TVAS were assigned to ylides produced following the photoexcitation of ethyl diazoacetoacetate in several aprotic nucleophilic solvents. In addition, the involvement of the α-carbonyl group in the reactivity of the α-carbonyl carbene with alcohols was identified, and provided experimental and computational evidence for an enol-forming pathway that bypasses the alcohol ylide.[27] Solvation of reacting carbenes has been the focus of several prior experimental and theoretical studies,[38-42] but the solvation dynamics of the ylide intermediates of carbene reactions have yet to be examined.

Here, spectroscopic evidence is presented which shows specific solvent interactions of EDA-derived THF ylides (THF-Y) with ethanol, chloroform, dichloromethane and cyclohexane HB donors, and by using TVAS the kinetics of solvation are characterize using IR band shifts. In combination with quantum chemical calculations and dynamical trajectory simulations, the TVAS measurements identify the structural changes to the ylide

intermediates induced by the solvent complexation, and provide new insights about how ylide-solvent interactions affect the ylide-mediated reaction mechanisms.

## 5.2. Method

**A. Experiment.** The photoinduced chemistry of ethyl diazoacetate was studied in several solvents and solvent mixtures using TVAS with a broadband mid-IR probe. The TVAS spectra were collected according to the instrumental set-up reported in Chapter 3. Spectra were collected following the photoexcitation at 270 nm of 65 mM samples of EDA (Sigma Aldrich, ≤100%) used as received. Samples were flowed through Harrick cells constructed with a 150 µm spacer. Absorption at 270 nm is assigned to the $S_2 \leftarrow S_0$ excitation with ππ* character to the diazo functional group. With a sample path length of 150 µm, an absorbance at 270 nm < 0.8 OD was obtained. Measurements were made for EDA solutions in cyclohexane (Fisher Scientific, extra pure, SLR grade), tetrahydrofuran (THF, Fisher Scientific, extra pure, SLR grade, stabilised with 0.025% BHT), acetonitrile (ACN, Fisher Scientific, HPLC gradient grade, <99.9%), ethanol (EtOH, Sigma Aldrich, ACS reagent grade, >99.5%), methanol (MeOH, ACS reagent grade, >99.5%), dichloromethane (DCM, Analytical grade, ≥99%) and chloroform (anhydrous, ≥99%, stabilised with <1% ethanol). Steady-state FTIR and UV absorption spectra for these EDA solutions are shown in Figures S5.1 and S5.2 of Section S1 of the Supporting Information.

**B. Computational details.** All calcuations were performed using the Gaussian 09 computational package.[43] Assignments of transient bands in TVAS spectra were supported by scaled harmonic vibrational frequencies computed at the MP2 level using a 6-311++G(d,p) basis set for the majority of the species considered in this study. A frequency scaling factor was determined from anharmonically corrected vibrational frequency calcuations of EDA, which reproduced the carbonyl stretching frequency to within 9 $cm^{-1}$ in cyclohexane, and was applied to all other species. Structures and vibrational frequencies of THF-ylide complexes were calculated using methanol as the HB donor in place of the ethanol used in the experiments to reduce the computational demands. Accurate computation of the properties of singlet carbenes often requires multi-reference methods because of their low lying singlet and triplet excited states. Single reference calcuations have been shown to be inadequate for accurate geometries and vibrational frequencies for non-substituted carbenes.[44] However, the bonding in carbonyl carbenes reduces their multi-reference character, and these species

can therefore be described satisfactorily by single-reference methods. For example, the CCSD(T) level of theory has been shown to give reasonable results for non-conjugated substituted carbenes.[45-46] Here, α-carbonyl carbene band frequencies were predicted at the CCSD/6-311++G(d,p) level of theory with adequate accuracy.

To explore the complexation of alcohols to ylides, and guide the interpretation of experimental measurements, binding energies were calcuated for various methanol complexes with the THF-ylide using MP2/6-311++G(d,p) geometries and MP2/aug-cc-pVTZ single point energies (with the large basis set chosen to minimize the consequences of basis set superposition error). The THF bath was included using a polarizable continuum model (PCM). Atom-centred density matrix propogation (ADMP) trajectories were calcuated for the various complexes using the B3LYP functional with the 6-31+G(d) basis set and inclusion of the THF bath using a PCM. A step size of 0.25 fs was used until the hydrogen bond length exceeded 3.1 Å, or for a maximum propagation time of 5 ps. The fictitious electron mass was set to 0.1 amu. All trajectories were simulated at 300 K, with a constant temperature maintained by a Gaussian isokinetic thermostat, and were computed for the hydrogen-bonded complex structures optimised at the B3LYP/6-31+G(d) level of theory. To extract typical behaviour, trajectories were computed 25 times for complexes 1 and 2 described later, and 40 times for complex 3 (see below) with randomised starting conditions. More trajectories are required to assess typical behaviour statistically, but were limited by the computational cost of running such calculations

**C. Specral decomposition**

The spectral decomposition was carried out using the KOALA program.[47] An example fitting procedure for the decomposition of the overlapping bands are shown in Figures 5.1 and 5.2.

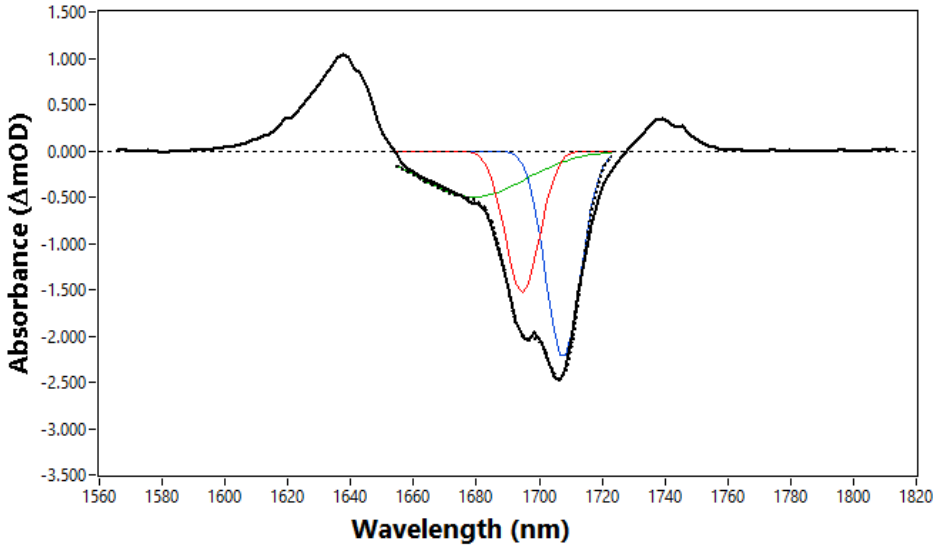


Figure 5.1 – Example fitting procedure for the decomposition of the overlapping ground state bleaches (GSB) of syn- (red) and anti-EDA (blue) following the 270-nm photoexcitation of EDA in THF. The example spectrum is taken at 1200 ps. Gaussian functions with fixed positions at 1697 $cm^{-1}$ and 1706 $cm^{-1}$ were superimposed onto each experimental spectrum, which simulated the peak of the negative-going bands well (black dotted line). The weaker-wing of the GSB around 1680 $cm^{-1}$ overlaps strongly with the carbene band and could not individually be decomposed by this method (See Figure 2 for the decomposition of photoproduct bands). Because the decomposition here is concerned with extracting kinetics from the recovery of ground state syn- and anti-EDA, a single Gaussian function was superimposed around 1670 $cm^{-1}$ (green) to account for any overlapping signal contribution from the weaker GSB wing and carbene band.

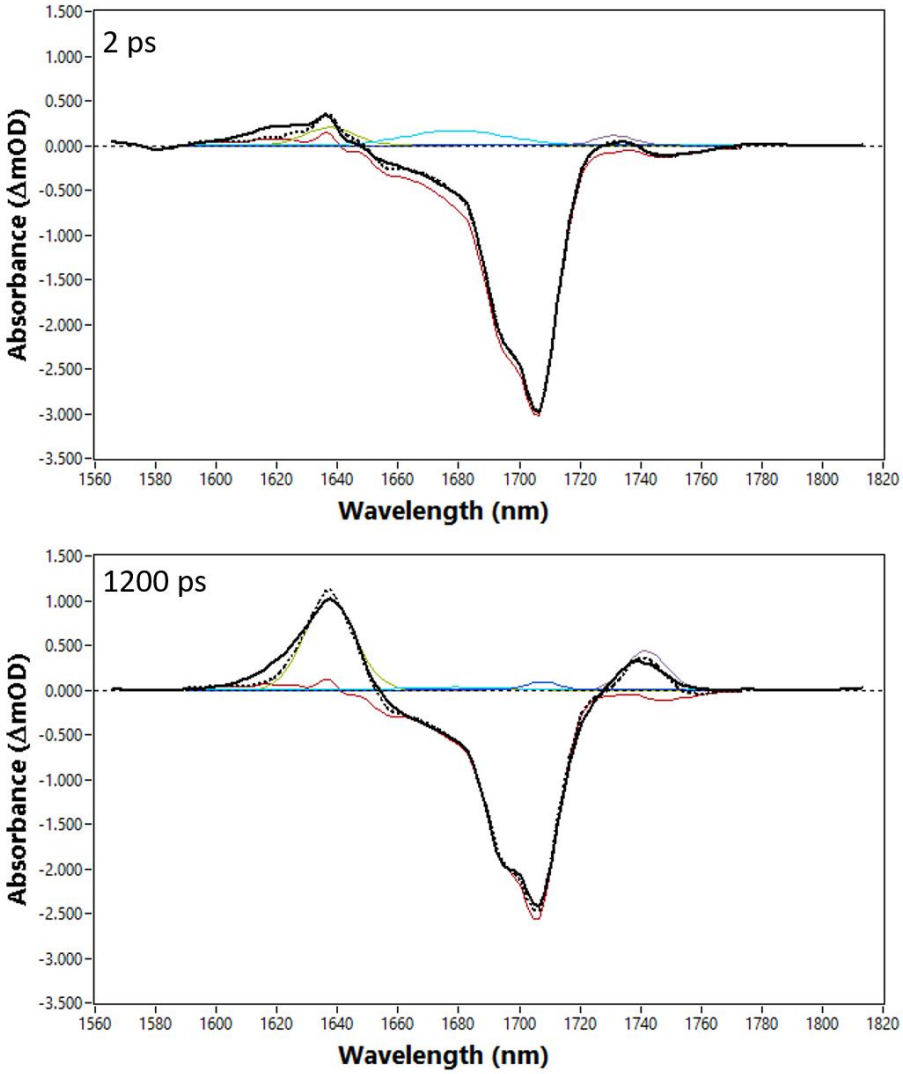


Figure 5.2 – Example fitting procedure for the decomposition of the overlapping photoproduct bands with the GSBs following the 270-nm photoexcitation of EDA in THF. The example spectra are taken at 2 ps (top panel) and 1200 ps (bottom panel). An early time basis function (red) was recorded before photoproduct formation and superimposed onto each experimental spectrum. An additional gaussian function (dark blue) was centred over the 1706 $cm^{-1}$ GSB to account for the different GSB recovery amplitudes and rates, but was not used to extract kinetic information about the EDA isomers (see Figure 1 for the decomposition of the EDA isomer GSBs). The THF-ylide (green) and carbene (light blue) were fit to gaussian functions with fixed positions and widths whereas the C-H insertion product (grey) was fit to a Gaussian function with the position and width floated to simulate the effects of vibrational cooling on the spectrum. The simulated spectrum is shown as the black-dotted line.

## 5.3. Results

This section begins by outlining the findings for the photoexcitation of EDA in various neat solvents. Sub-sections 5.3.1 – 5.3.7 address the different reaction pathways observed, which may be common to more than one solvent. Schemes 5.1 - 5.5 report the photoproduct channels and Tables 5.1 and 5.2 provides a summary of exponential time constants associated with the photochemical pathways identified. The procedures used for band assignments, spectral decomposition, kinetic fitting, and computational results can be found in the supporting information.

Table 5.1 – Band positions and time constants for intermediate and product species identified following 270-nm photoexcitation of EDA in cyclohexane, THF and ACN. Solvent-Y denotes a solvent-ylide.

| Species | Band wavenumber ($cm^{-1}$) | $\tau_1$ (ps) | $\tau_2$ (ps) |
|---|---|---|---|
| Cyclohexane | | | |
| (1[a]) Anti-EDA (GSB) | 1716 | 5.8 ± 0.7 recovery | |
| (1[b]) Syn-EDA (GSB) | 1705 | 1.7 ± 0.4 recovery | |
| (2) Carbene | 1678 | 0.5 ± 0.1 growth | 12.6 ± 0.4 decay |
| (3) Ketene (thermalized) | 2106 | 5.7 ± 0.3 growth | |
| (4) C-H insertion product | 1745 | 12.6 ± 0.4 growth | |
| THF | | | |
| (1[a]) Anti-EDA (GSB) | 1706 | 8.9 ± 0.8 recovery | |
| (1[b]) Syn-EDA (GSB) | 1697 | 2.3 ± 0.3 recovery | |
| (2) Carbene | 1681 | 0.7 ± 0.1 growth | 8.4 ± 0.3 decay |
| (3) Ketene | 2106 | 7.2 ± 0.5 growth | |
| (5) C-H insertion product | 1739 | 8.4 ± 0.3 growth | |
| (9) THF-Y | 1636 | 8.4 ± 0.3 growth | |
| ACN | | | |
| (1[a]) Anti-EDA (GSB) | 1700 | 10 ± 0.2 recovery | |
| (1[b]) Syn-EDA (GSB) | 1688 | 4.3 ± 0.6 recovery | |
| (2) Carbene | 1677 | - | 6.8 ± 0.2 decay |
| (8) ACN-Y | 1642 | 6.8 ± 0.2 growth | |

Table 5.2 – Band positions and time constants for intermediate and product species identified following 270-nm photoexcitation of EDA in EtOH, MeOH, chloroform, and DCM. Solvent-Y denotes a solvent-ylide.

| Species | Band wavenumber ($cm^{-1}$) | $\tau_1$ (ps) | $\tau_2$ (ps) |
|---|---|---|---|
| EtOH | | | |
| ($1^a$) Anti-EDA (GSB) | 1696 | 6.1 ± 0.4 recovery | |
| ($1^b$) Syn-EDA (GSB) | 1709 | ≈ 10 ps recovery | ≈ 10 ps bleaching |
| HB EDA (GSB) | 1674 | 11 ± 2 recovery | |
| (10) EtOH-Y | 1617 | 5.1 ± 0.3 growth | 80 ± 7 decay |
| (6) C-H insertion product | 1735 | 5.1 ± 0.3 growth | |
| (13) Ether | 1745 | 80 ± 7 growth | |
| (14) Enol | 1722 | 5.1 ± 0.3 growth | 80 ± 7 growth |
| MeOH | | | |
| ($1^a$) Anti-EDA (GSB) | 1696 | 7.9 ± 0.7 recovery | |
| ($1^b$) Syn-EDA (GSB) | 1709 | ≈ 10 ps recovery | ≈ 10 ps bleaching |
| HB EDA (GSB) | 1674 | 10 ± 2 recovery | |
| (10) MeOH-Y | 1618 | 5.1 ± 0.4 growth | 26 ± 3 Decay |
| (13) Ether | 1745 | 26 ± 3 growth | |
| (14) Enol | 1718 | 5.1 ± 0.4 growth | 26 ± 3 growth |
| Chloroform | | | |
| (2) Carbene | 1677 | ≈ 0.3 growth | 1.7 ± 0.4 decay |
| (11) Chloroform-Y | 1642 | 1.7 ± 0.4 growth | 27 ± 4 decay |
| (12) C-Cl insertion product | 1655 | 27 ± 4 growth | |
| (7) C-H insertion | 1626 | - | - |
| DCM | | | |
| (2) Carbene | 1677 | < 0.3 growth | 7 ± 3 decay |
| (11) DCM-Y | 1642 | 7 ± 3 growth | 17 ± 4 decay |
| (12) C-Cl insertion product | 1657 | 17 ± 4 growth | |
| (7) C-H insertion | 1637 | - | - |

### 5.3.1 Wolff rearrangement

Figure 5.3 shows TVAS spectra spanning 2020-2150 $cm^{-1}$ and obtained following the 270-nm photoexcitation of 65 mM EDA in Cyclohexane. Ketene molecules are identified by monitoring the characteristic mid-IR band associated with the C=C=O stretching mode at 2106 $cm^{-1}$ which forms a shoulder feature to the lower wavenumber side of a negative band corresponding to the GSB of EDA.

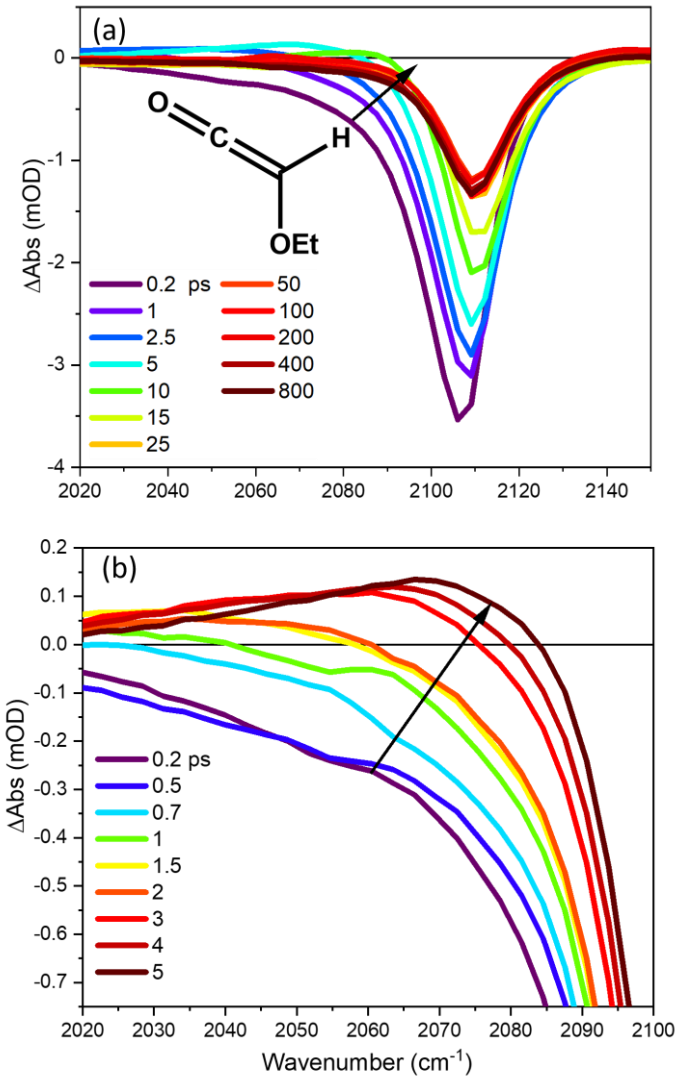


Figure 5.3 – (a) TVAS spectra measured in the wavenumber range 2020-2150 $cm^{-1}$ for the photoexcitation of 65 mM EDA in cyclohexane. (b) an expanded view to illustrate the formation of vibrationally hot ketene molecules. Note the change in the colour scheme for time points shown in the insets to panels (a) and (b). The black arrows indicate the overall directions of change in intensity over time.

The ketene molecules are born within the instrument response (< 300 fs) and with excess energy, as is evident from the breadth of the bands at early time delays, and their shift to higher wavenumber as excess energy is transferred to the solvent bath. As the ketene relaxes to lower vibrational levels, its mid-IR absorption band increasingly overlaps the GSB of the parent EDA, causing a reduction in the depth of this GSB feature. This vibrational energy transfer populates the vibrational ground state of the ketene with a 5.7 ± 0.3 ps time constant. The prompt formation of hot ketene molecules is consistent with a concerted Wolff-

rearrangement, and no evidence was found for contribution from a stepwise pathway. Similar results were obtained in THF (see Figure S5.4 of the supporting information).

### 5.3.2 Carbene formation

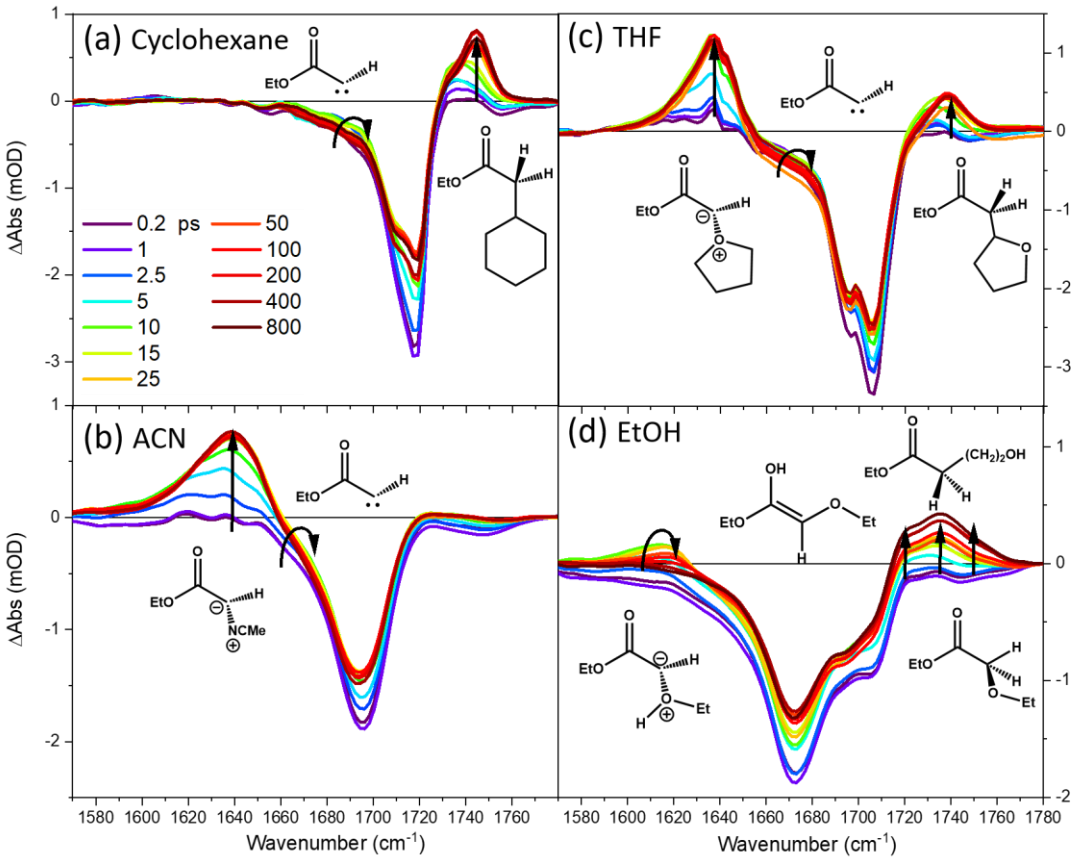


Figure 5.4 - TVAS spectra spanning the 1570-1780 $cm^{-1}$ wavenumber range, obtained for the photoexcitation of 65 mM EDA in: (a) Cyclohexane; (b) ACN; (c) THF; (d) EtOH. Black arrows illustrate the directions of change in intensity of spectral features over time.

Figure 5.4 shows TVAS spectra spanning 1550-1780 $cm^{-1}$ following the 270-nm photoexcitation of 65 mM EDA in Cyclohexane, ACN, THF and EtOH solutions. After the photolysis of EDA in cyclohexane, a weak positive-going band centred at 1678 $cm^{-1}$ develops with a time constant of 0.5 ± 0.1 ps and overlaps the wing of the stronger adjacent GSB feature. This band is assigned to the singlet carbene on the basis of its rapid growth, and the timescale for its decay, which matches that for the formation of reaction products as illustrated in Figure 5.5 and Table 5.1 and 5.2. The triplet carbene is discounted because it would not form so promptly after the laser pulse. The band position is in reasonable

agreement with a computed carbonyl stretching frequency of 1668 $cm^{-1}$ obtained for the singlet carbene at the CCSD/6-311++G(d,p) level of theory in a PCM treatment of cyclohexane solution. Similarly, singlet carbene bands are observed in ACN at 1677 $cm^{-1}$ and THF at 1680 $cm^{-1}$. In each case, the time constant for decay of intensity of the band assigned to the singlet carbene matches the time constant for formation of ylide and C-H insertion products. The carbene band could not be located in the TVAS spectra obtained in EtOH because of greater overlap with the GSB of EDA. The transient IR spectra provide no evidence for triplet carbene intermediates within the time-delay and detection wavenumber windows probed.

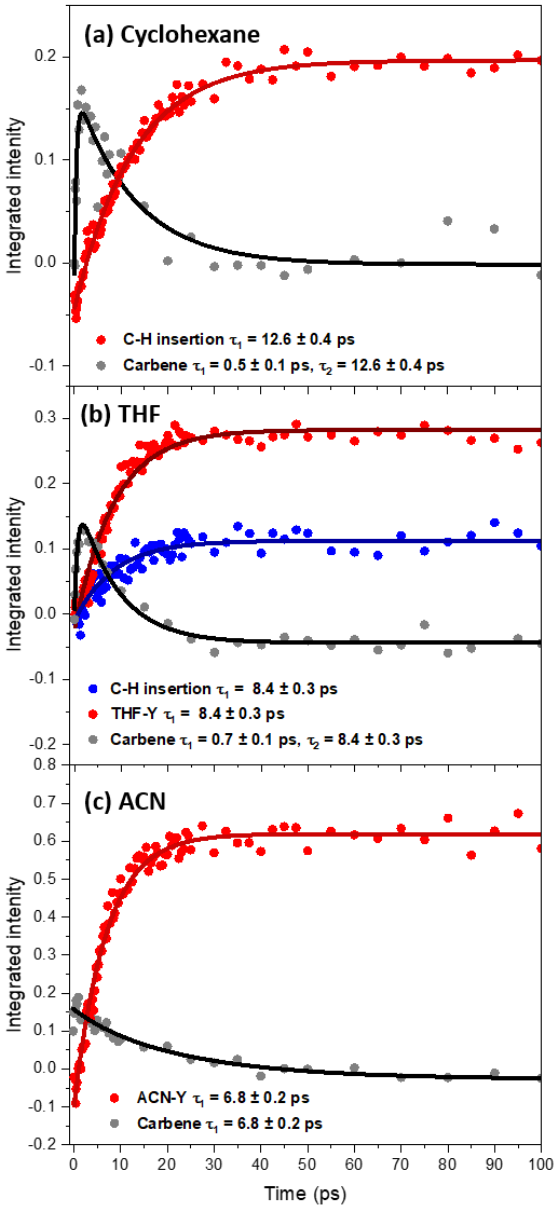


Figure 5.5 – Kinetic fitting of carbene and photoproduct TVAS bands obtained in (a) Cyclohexane, (b) THF, and (c) ACN solutions following EDA photolysis. Dots are experimental data points, and for each solution ylide and C-H insertion product kinetics are globally fitted with single functions shown as solid curves. The kinetics for the carbene were fitted to single or bi-exponential functions with the decay fixed to match the kinetics of growth of the ylide and C-H insertion products. The growth of the carbene in ACN solutions was not resolved from the spectra. Note, the kinetics plotted for ylide and C-H insertion products were obtained from repeated spectra in which the weak carbene bands were not spectroscopically resolved because of overlapping spectral artifacts. For the original kinetic plots see Figure S5.5 of the supporting information.

### 5.3.3 Ground state bleach recovery of EDA conformers

The 270-nm photoexcitation of EDA results in negative-going bands in Figures 5.3 and 5.4, and these are assigned to the GSBs of EDA (1) on the basis of steady state absorption spectra. EDA exists in both anti and syn conformations, made evident by two IR active carbonyl stretches centred at 1716 $cm^{-1}$ and 1705 $cm^{-1}$ in cyclohexane solutions and illustrated in Scheme 5.1. FTIR spectra can be found in Figure S5.2 of the supporting information. The bands are respectively assigned to the anti ($1^a$) and syn ($1^b$) conformers of ground state EDA, with support from computed vibrational frequencies of 1725 $cm^{-1}$ and 1710 $cm^{-1}$. The band intensity ratio for the syn- and anti-EDA conformers indicates that with the addition of increasing amounts of ethanol to cyclohexane solutions of EDA, there is a greater preference for the EDA to adopt the syn-conformation. The higher polarity of the syn-EDA means it is stabilised more effectively in solvents with higher dielectric constants.

Kinetic analysis shown in Figure 5.6 for the GSB recovery of the 1706 $cm^{-1}$ (syn-EDA) and 1716 $cm^{-1}$ (anti-EDA) bands in cyclohexane (Figure 5.6(a)) indicates syn-EDA undergoes 74% conversion to photoproducts compared to just 61% for anti-EDA. Geminate recombination of carbene and $N_2$ photofragments is considered unlikely; instead, the GSB recovery is more plausibly attributed to internal conversion of photoexcited EDA back to the $S_0$ state and dissipation of excess vibrational energy to the solvent. The greater photoconversion of syn-EDA is likely to be a result of a competing pathway to concerted Wolff-rearrangement, which was previously shown to occur selectively from photoexcited syn α-diazocarbonyl compounds.[48] Time constants for the recovery of ground-state syn-EDA and anti-EDA are 5.8 ± 0.7 ps and 1.7 ± 0.4 ps, respectively. Time constants for GSB recovery appear to be slower than photoproduct formation because they include the vibrational cooling of electronically ground state EDA to recover thermalized parent molecules. Similar observations are made in THF, ACN, EtOH, and MeOH solutions, with solvent dependent shifts in the EDA band positions (see Table 5.1). The percentage conversion to photoproducts increases to 84% for syn-EDA and 74% for anti-EDA in THF, and 81% and 77% respectively in ACN. The larger photoconversion in THF and ACN could be because solvents with higher dielectric constants stabilise the polar transition state for the loss of $N_2$, which is supported by ≈35% greater intensity of the ketene band relative to the GSB feature for photoexcitation of EDA in THF compared to in cyclohexane, indicating a higher ketene quantum yield. A greater

preference for the syn conformer in THF compared to cyclohexane can be discounted as the cause of the higher ketene yield because the FTIR spectra show <5% change in the intensities of syn and anti EDA bands for the two conformers (see Figure S5.2 of Section S1 in the supporting information).

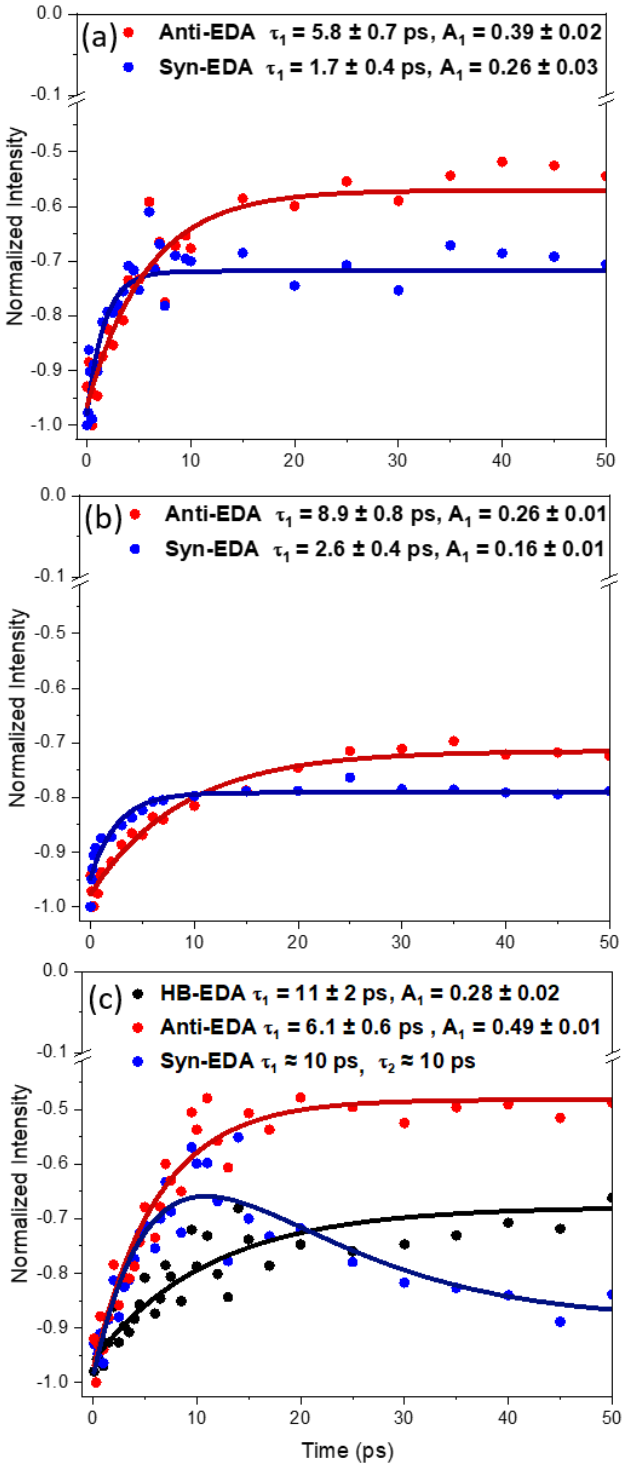


Figure 5.6 – Kinetic fitting of the EDA conformer ground state bleach recoveries in: (a) Cyclohexane; (b) THF; (c) EtOH. Dots are experimental data points normalized to a maximum depth of -1.0 and are fitted with single or bi-exponential functions shown by solid curves. The kinetics are shown for Syn-EDA (Blue), Anti-EDA (Red) and Hydrogen-bonded EDA (HB-EDA, Black).

In solutions containing added ethanol, a third GSB feature centred at 1675 $cm^{-1}$ is observed alongside those of the syn and anti conformers of EDA. Its intensity increases relative to the syn and anti EDA GSB features as more ethanol is added to the cyclohexane solutions. For this reason, the 1675 $cm^{-1}$ band is assigned to a hydrogen-bonded complex of EDA (HB-EDA) with ethanol. The HB-EDA GSB shows only a 28% recovery, with a time constant of 11 ± 2 ps. Syn- and anti-conformers of the HB-EDA complex are not spectroscopically resolved. The GSB assigned to non-H-bonded syn-EDA in ethanol recovers and further deepens, both with approximately 10 ps time constants. This additional depletion of syn-EDA after the initial photoexcitation is attributed to the re-establishment of the dynamic equilibrium between free and HB-EDA after photoexcitation. The direction of change suggests complexation of syn-EDA to ethanol increases the yield of photoproducts.

### 5.3.4 C-H bond insertion

TVAS spectra in Figure 5.4(a) (for EDA in cyclohexane) show the formation of a band at 1745 $cm^{-1}$ which grows with the same time constant as the decay of the singlet carbene band (12 ± 1 ps). Similar signatures are found in THF (5) at 1739 $cm^{-1}$ and ethanol (6) at 1735 $cm^{-1}$ and develop in competition with ylide intermediates (see section 5.3.5). Time constants for these reactions are reported in Tables 5.1 and 5.2. Assignment to the triplet carbene is discounted on the basis that, at the CCSD/6-311++G(d,p) level of theory, its computed carbonyl stretching frequency is 1677 $cm^{-1}$, well outside the level of agreement achieved between computation and TVAS observations for the singlet carbene. Instead, these bands are assigned to C-H insertion products from the reaction of the singlet carbene with solvent molecules and are shown in scheme 5.2. The magnitudes of the time constants in all three solvents suggest rapid reaction of the singlet carbene with a molecule in its first solvent shell. The assignments are supported by stable product analysis which found C-H insertion products after the photoexcitation of EDA in propanol,[49] and the good agreement of the band positions with known IR spectra of possible C-H insertion products (see Table S5.3 of section S2 in the supporting information).[50-52] Further C-H insertion signatures are found in DCM (7) at 1737 $cm^{-1}$ and chloroform (7) around 1726 $cm^{-1}$. Spectra taken in chloroform are shown in Figure 5.7, but the features of interest are strongly overlapped by absorption bands of vibrationally hot photoproducts. In a prior study, only trace amounts of C-H insertion products were found following EDA photolysis in methanol.[53] Thus, such species are not expected to make

significant contributions to the intensities of bands found around 1735 $cm^{-1}$ in the TVAS measurements conducted in methanol-containing solutions.

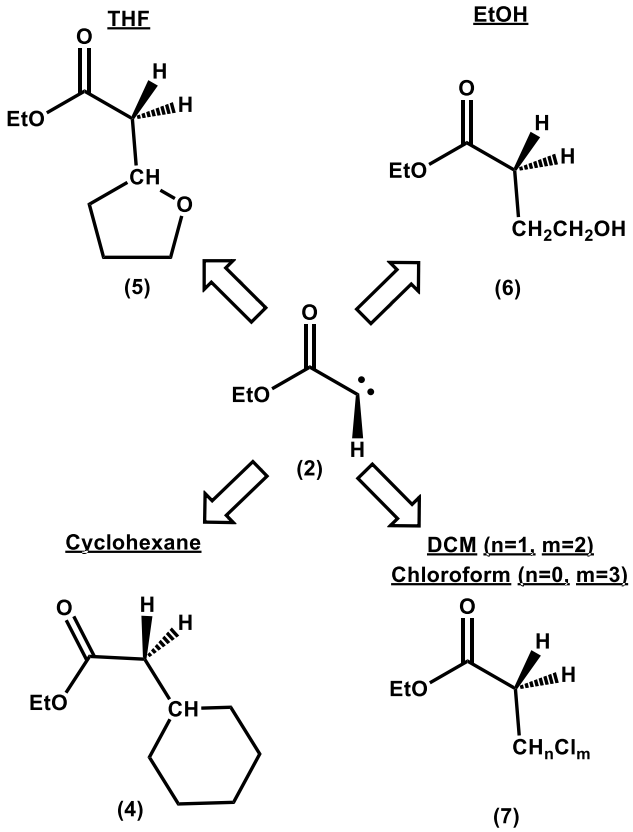


Scheme 5.2 – Structures of C-H insertion products formed from the reactions of the singlet carbene (2) with different solvents. Structures for C-H insertion into THF or EtOH are shown for one product only, and insertion into other C-H bonds is also expected.

### 5.3.5 Ylide formation

Reaction of the singlet carbene (**2**) with nucleophilic solvents can form ylides in competition with pathways such as C-H insertion discussed in Section 5.3.4. Scheme 5.3 summaries the ylide products argued here to be formed in the various solvents studied. Their kinetics of production are reported in Tables 5.1 and 5.2.

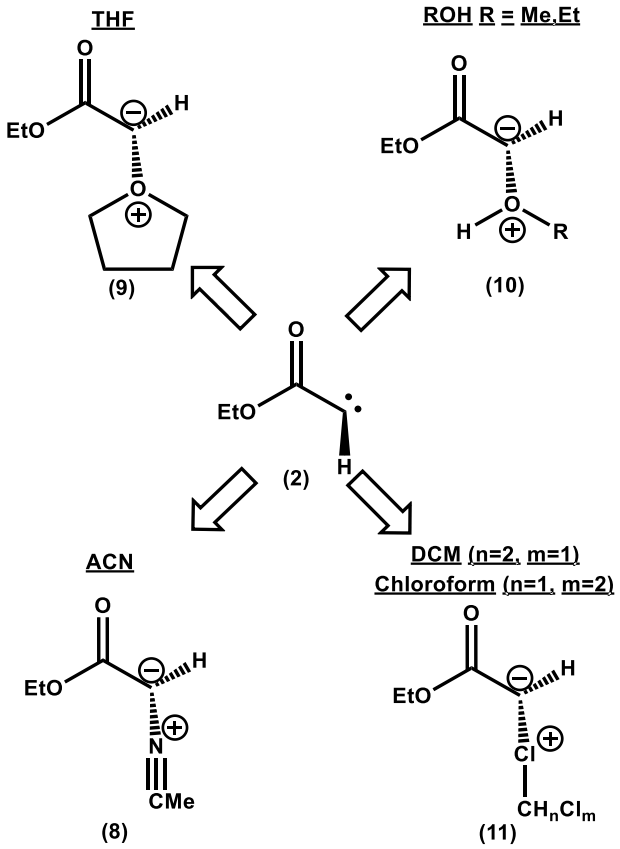


Scheme 5.3 – Structures of ylides formed from the reaction of carbene (2) with various solvent molecules

TVAS spectra in Figure 5.4 for ACN, THF, and ethanol, and in Figure 5.8 for methanol solutions are consistent with a previous report by Xue *et al.* They respectively show the formation of an ACN-ylide (ACN-Y) (8) with a characteristic absorption band at 1642 $cm^{-1}$, a THF-ylide (THF-Y (9), 1636 $cm^{-1}$), an EtOH-ylide (EtOH-Y (10), 1617 $cm^{-1}$) and a MeOH-ylide (MeOH-Y (10), 1618 $cm^{-1}$). Computed vibrational frequencies for the carbonyl stretching modes of THF-Y (1642 $cm^{-1}$) and ACN-Y (1643 $cm^{-1}$) are in good agreement with the observed band positions. However, the computed frequency of the corresponding MeOH-Y vibrational mode (1673 $cm^{-1}$) lies outside the levels of agreement with experimental observation demonstrated for THF-Y and ACN-Y. The experimentally observed frequency is shifted to lower wavenumber which could be because of solvent specific interactions similar to those described in section 5.3.8, or by deprotonation to form an anion which has a computed absorption band at 1618 $cm^{-1}$. The ACN-Y, THF-Y, EtOH-Y and MeOH-Y ylides form with respective time constants of 6.8 ± 0.2 ps, 8.4 ± 0.3 ps, 5.1 ± 0.2 ps and 5.1 ± 0.3 ps (Table 5. 1). The bands assigned to the carbonyl stretching of the EtOH-Y and MeOH-Y intermediates further decay with respective time constants of 80 ± 7 ps and 26 ± 3 ps, matching the time constants for growth of new

bands at 1745 $cm^{-1}$. The 1745 $cm^{-1}$ bands are assigned to the ether products of EtOH-Y and MeOH-Y (13) rearrangements shown in Scheme 5.5 on the basis of steady-state irradiation experiments and alcohol concentration dependence data in measurements by Xue *et al*. for Methanol-$d_1$ and t-Butanol in ACN mixtures.[37] The intensities and centre wavenumbers of bands assigned to the THF-Y and ACN-Y species remain unchanged over the 1.3 ns time window probed.

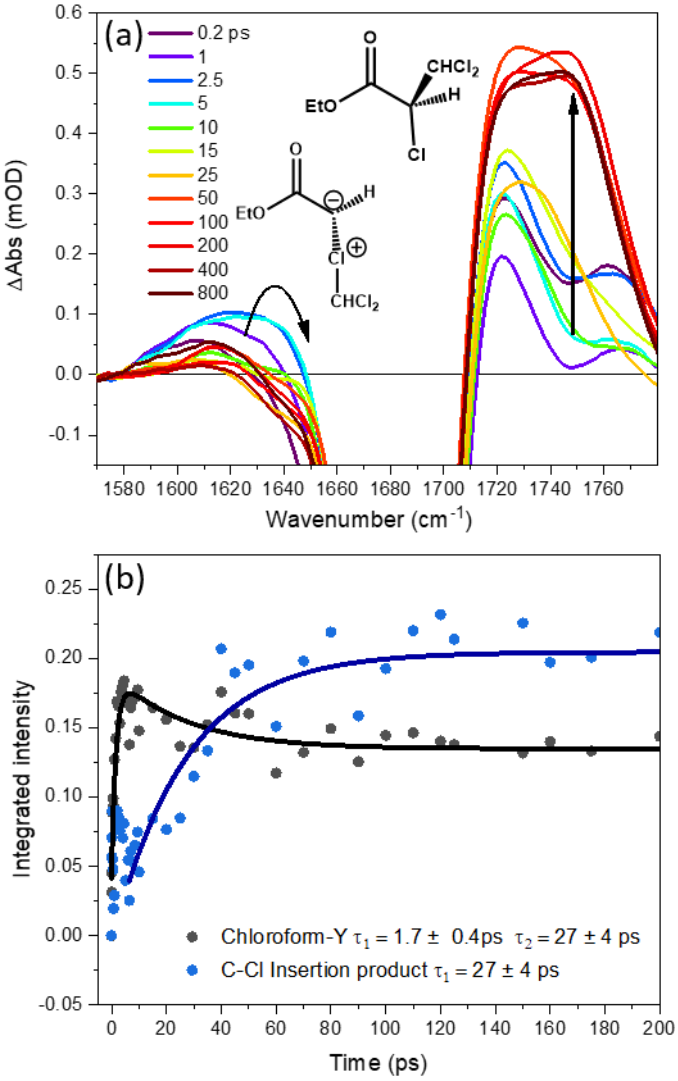


Figure 5.7 – (a) TVAS spectra obtained in the wavenumber range 1570-1780 $cm^{-1}$ following the 270-nm photoexcitation of 65 mM EDA in Chloroform. Black arrows illustrate formation of ylide and C-Cl insertion products, the proposed structures of which are shown. (b) Time-dependence of integrated band intensities and kinetic fitting for the ylide Chloroform-Y (black) and C-Cl insertion product (blue) with the structures shown in panel (a).

Figure 5.7 shows the outcomes of 270-nm photoexcitation of EDA in chloroform, with the growth of a band at 1643 $cm^{-1}$ with a 1.7 ± 0.4 ps time constant that matches the decay of the singlet carbene band (Table 5.2). A similar band is observed in DCM at 1657 $cm^{-1}$ which grows with a 7 ± 4 ps time constant. The similar positioning of the bands to those encountered for the various other ylides identified within this section suggests assignment of the 1643 $cm^{-1}$ band in chloroform to the chloroform ylide (Chloroform-Y, (11)), and the 1657 $cm^{-1}$ band in in DCM to the DCM ylide (DCM-Y, (11)), with support from the computed carbonyl stretching frequency of chloroform-Y at 1638 $cm^{-1}$ and DCM-Y at 1656 $cm^{-1}$. The Chloroform-Y and DCM-Y bands further decay in intensity with 27 ± 4 ps and 17 ± 4 ps time constants to form photoproducts which are further discussed in section 5.3.6.

### 5.3.6 C-Cl bond insertion

Figure 5.7(a) shows the growth of a broad TVAS band centred at 1750 $cm^{-1}$ that is attributed to a reaction product formed by the loss of the Chloroform-Y ylide intermediate. Evidence from calculated vibrational frequencies points to this being a C-Cl insertion product ((12), shown in Scheme 5.3) of the singlet carbene reaction with chloroform, for which the computed carbonyl stretching frequency is 1747 $cm^{-1}$. Similarly, the analogous C-Cl insertion product (12) is identified in DCM by the growth of a TVAS band at 1750 $cm^{-1}$. In each case, a concerted mechanism to formation of the C-Cl insertion product is discounted because this would then occur in direct competition with ylide (11) formation and C-H insertion. Instead, a delayed growth of the C-Cl insertion product is found, with a time constant that matches the ylide decay, suggesting C-Cl insertion proceeds through an ylide intermediate as illustrated in Scheme 5.4.

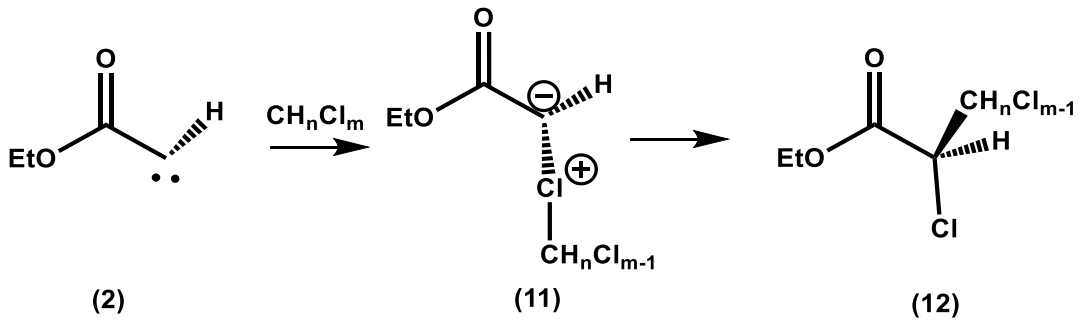


Scheme 5.4 – Stepwise mechanism for the C-Cl insertion reaction of the singlet carbene with DCM.

### 3.7 Enol formation

Chapter 4 reports evidence for the preferential formation of enol intermediates over ylides or carbocations during the reaction of an ethyl diazoacetoacetate derived $\alpha$-carbonyl carbene with alcohols.[27] Here, evidence of a similar reaction pathway for the EDA-derived singlet $\alpha$-carbonyl carbene is presented. Figure 5.8 shows the photoexcitation of 65 mM EDA in methanol, in which a transient IR absorption band at 1718 $cm^{-1}$ initially rises with the same time constant as the MeOH-Y band at 1618 $cm^{-1}$, suggesting a competing reaction pathway of the singlet carbene. The 1718 $cm^{-1}$ band continues to grow with a time constant that matches the decay of the MeOH-Y feature at 1618 $cm^{-1}$ and the growth of the product ether band at 1745 $cm^{-1}$. For this reason, assignment of the 1718 $cm^{-1}$ band to the C-H insertion product which is computed to show a band at 1735 $cm^{-1}$ is discounted,[50] because it is not expected to form sequentially from the MeOH-Y intermediate. Instead, the 1718 $cm^{-1}$ band is assigned to a mixture of E (14) and Z (15) isomers of an enol, with support from the computed carbonyl stretching frequencies for the E and Z enol isomers of 1726 $cm^{-1}$ and 1722 $cm^{-1}$ respectively. The kinetics suggest concerted and prompt formation of the Enol (14), but prompt formation of Enol (15) is unlikely on stereochemical grounds. Instead, it is likely that Enol (15) forms by proton transfer in Ylide (10) in competition with ether formation. A corresponding Enol band is similarly observed in ethanol at 1722 $cm^{-1}$ which also forms with a bi-exponential time constant that matches the kinetics observed for the EtOH-Y. The proposed mechanism of reaction of the singlet carbene with alcohols is summarised in Scheme 5.5.

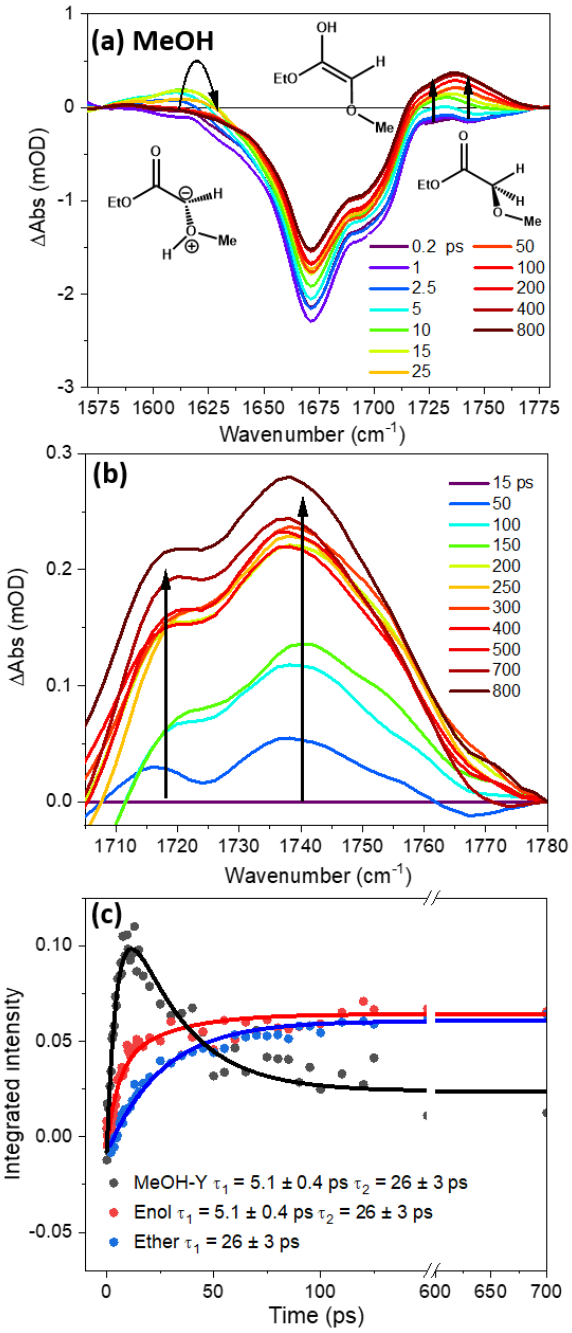


Figure 5.8 – (a) TVAS spectra obtained in the wavenumber range 1570-1780 $cm^{-1}$ following the 270-nm photoexcitation of 65 mM EDA in methanol. Black arrows illustrate formation of photoproducts, the structures of which are shown. (b) Expanded view of the TVAS spectra in the wavenumber range of 1710-1780 $cm^{-1}$, after subtraction of the TVAS spectrum obtained at a time delay of 15 ps to remove any possible signatures of C-H insertion products and highlight the formation of Enol and Ether products at later times (c) Time-dependence of integrated band intensities and kinetic fitting for the ylide MeOH-Y (black), Enol (red), and Ether (blue) with the structures shown in panel (a).

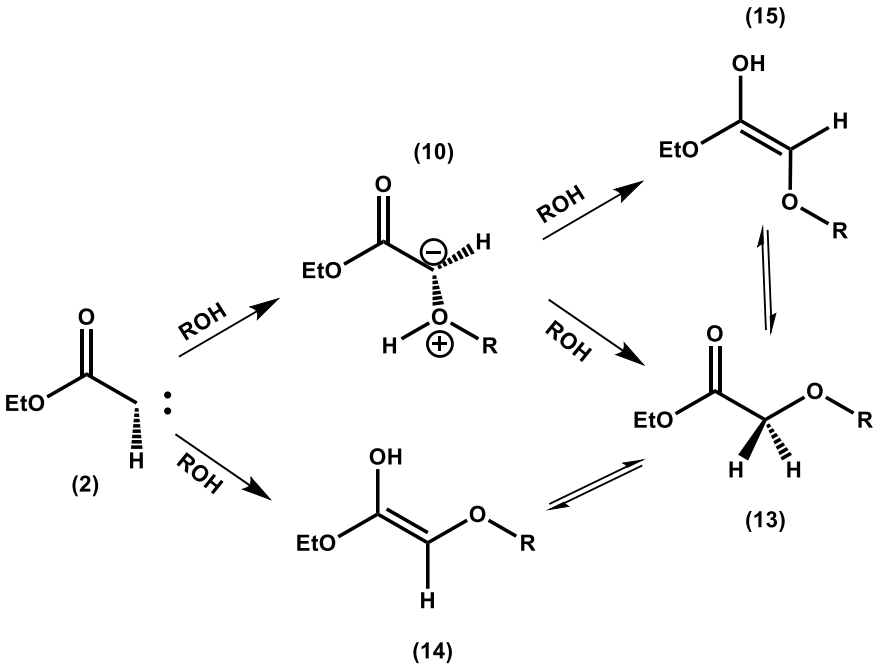


Scheme 5.5 – Production of Enol intermediates in competition with alcohol-ylide and Ether formation for the reaction of the singlet carbene with alcohols.

### 5.3.8 Ylide solvation dynamics in binary solvents

The dynamics of THF-Y formation were further studied by dilution of the THF using aprotic solvents. Figure 5.9 shows TVAS spectra obtained in a mixed solution of ≈2:3 molar ratios of THF: ACN. Both THF-Y and ACN-Y form in direct competition, as shown by bands observed between 1627 $cm^{-1}$ and 1651 $cm^{-1}$ which grow with a common 6.6 ± 0.1 ps time constant. The ylide bands persist over longer time durations than the 1.3 ns experimental limit, with no changes to the band intensity or position, and therefore show no evidence for electrostatic interactions of the positively charged oxygen atom of the THF-Y with other THF or ACN molecules. Addition of 2 M ACN causes a minor increase in the band intensity at 1624 $cm^{-1}$, but electrostatic complexation is unlikely to be the cause because similar effects are observed in non-polar solvents such as cyclohexane. Instead, a more-likely reason is because of hydrogen-bonding from the slightly polar C-H bonds which are further discussed in section 5.3.10.

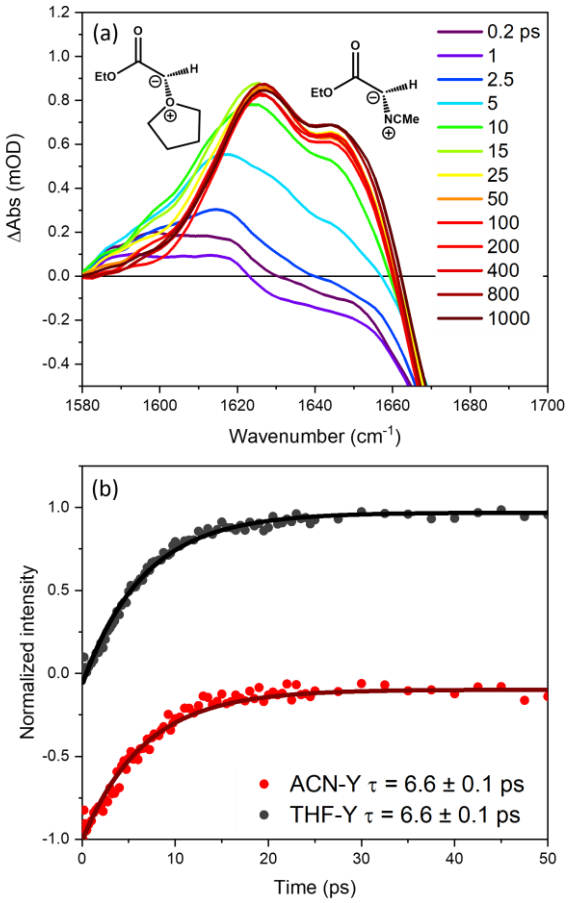


Figure 5.9 – (a) TVAS spectra obtained at wavenumbers from 1570-1780 $cm^{-1}$ for the photoexcitation of 65 mM EDA in a mixed solvent comprising 2:3 molar ratios of THF: ACN. Black arrows illustrate the directions of change in intensity of the observed bands, and the structures identify assignments to THF-Y and ACN-Y species. (b) Time-dependence of band intensities normalized to 0 - 1 and global kinetic fitting for the THF-Y (Black) and ACN-Y (Red), with structures shown in panel (a). The red data points have been vertically offset by -1.

In contrast, the dynamics of interaction of THF-Y with protic solvent molecules are revealed by TVAS spectra obtained for THF:EtOH mixtures. Figure 5.10 shows example TVAS spectra in the 1670-1780 $cm^{-1}$ wavenumber window measured for different THF:EtOH ratios. For EtOH concentrations above 1.7 M, three partially overlapping bands are identified between 1600 $cm^{-1}$ and 1650 $cm^{-1}$, with centres at 1636 $cm^{-1}$, 1621 $cm^{-1}$ and 1608 $cm^{-1}$. At a lower EtOH concentration of 0.4 M, only bands centred at 1636 $cm^{-1}$ and 1617 $cm^{-1}$ are observed. At any given EtOH concentration, all the bands initially form with the same time

constants but reveal further dynamics at later times which will be the focus of the discussion here.

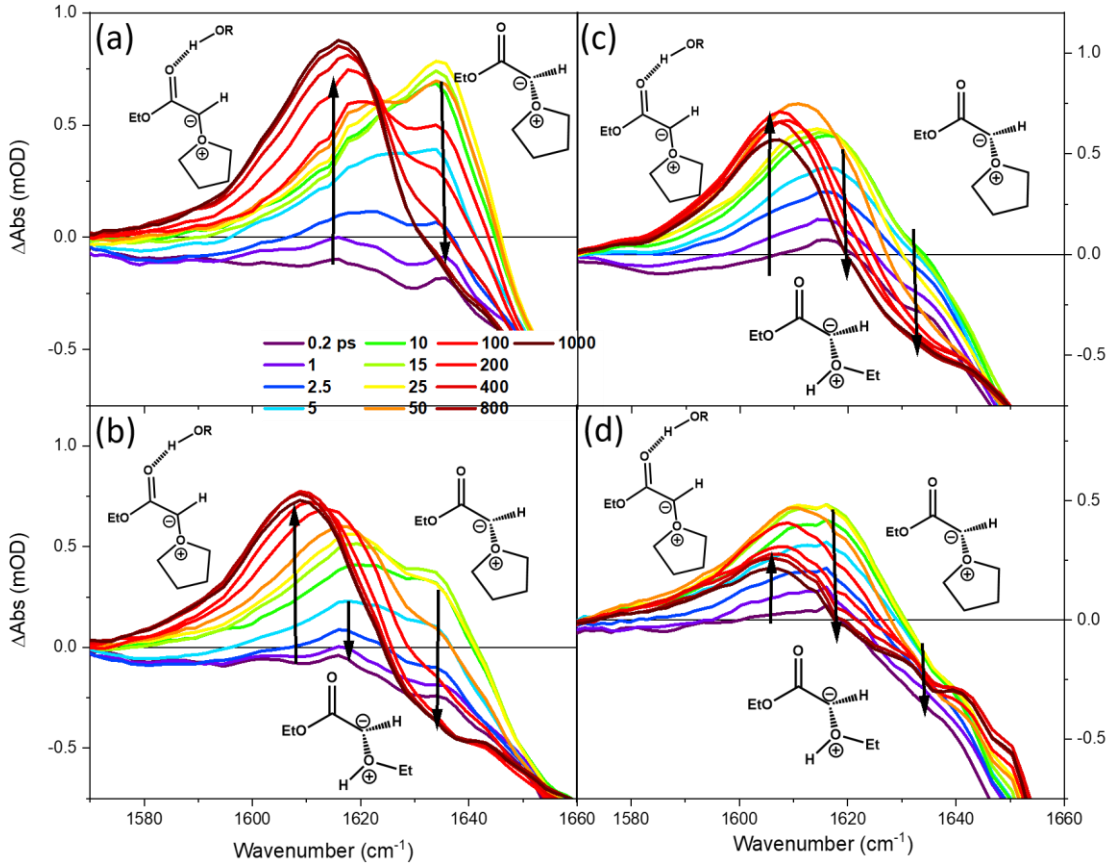


Figure 5.10 – TVAS spectra measured in the wavenumber range 1570-1780 $cm^{-1}$ for the photoexcitation of 65 mM EDA in mixed EtOH/THF solutions of different ratios. a) 0.4 M EtOH; b) 1.7 M EtOH; c) 4.6 M EtOH; d) 13.7 M EtOH. Black arrows illustrate the directions of change in intensity of spectral features for time delays greater than 20 ps.

The formation of the ether product of the EtOH-Y rearrangement is tracked using the carbonyl stretching band at 1746 $cm^{-1}$, and the kinetics are globally fitted to the same time constant as the decay of the 1621 $cm^{-1}$ band for each concentration of EtOH used. Therefore the 1621 $cm^{-1}$ band in the mixed solvent is assigned to the EtOH-Y intermediate which is a precursor to the ether. The band at 1636 $cm^{-1}$ is assigned to the THF-Y, on the basis of close correspondence with the THF-Y band shown in Figure 5.4(c), as well as dependence of the maximum band intensity on THF concentration. These assignments show the competitive formation of both THF and EtOH solvent derived ylides in the mixed THF:EtOH solvents.

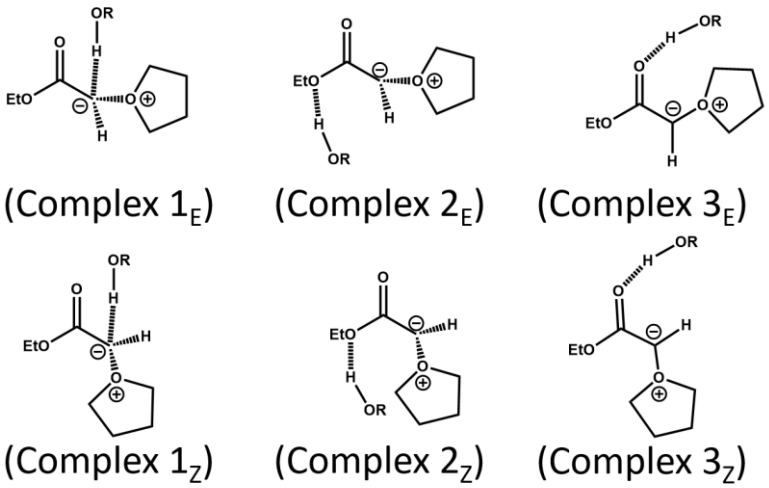


Scheme 5.6 – Schematic structures computed for possible hydrogen-bond donor-acceptor complexes of methanol and the E or Z isomers of THF-Y. Sub-scripts identify the stereochemistry of the ylide. In the calculations for each structure, R = Me, but R= Et was used in experiments.

Figure 5.10 shows that the bands at 1617 $cm^{-1}$ (in 0.4 M EtOH) and 1608 $cm^{-1}$ (in >1.7 M EtOH) initially form with the same time constant as the EtOH-Y and THF-Y ylides (shown as $\tau_1$ in Figure 5.11(a)), and continue to grow steadily with the same time constant as the decay of the THF-Y bands (shown as $\tau_2$ in Figure 5.11(a)). The kinetic analysis presented in Figure 5.11(b) demonstrates a first order dependence on the concentration of EtOH for the $\tau_2$ time constant shown in Figure 5.11(a). Both the 1617 $cm^{-1}$ (in 0.4 M EtOH) and 1608 $cm^{-1}$ (in >1.7M EtOH) bands are assigned to an IR signature for a hydrogen-bonded complex of the THF-ylide with EtOH (referred to hereafter as a THF-Y HB complex). This assignment is supported by observation in steady state FTIR spectra of the formation of a hydrogen bonded complex of ground state EDA with EtOH, characterized by a 19 $cm^{-1}$ downward shift in the carbonyl vibrational frequency relative to free syn-EDA. The various candidates considered for assignment of the hydrogen-bonded complex of the THF-ylide with EtOH are shown in Scheme 5.6 and further discussed in section 5.3.9.

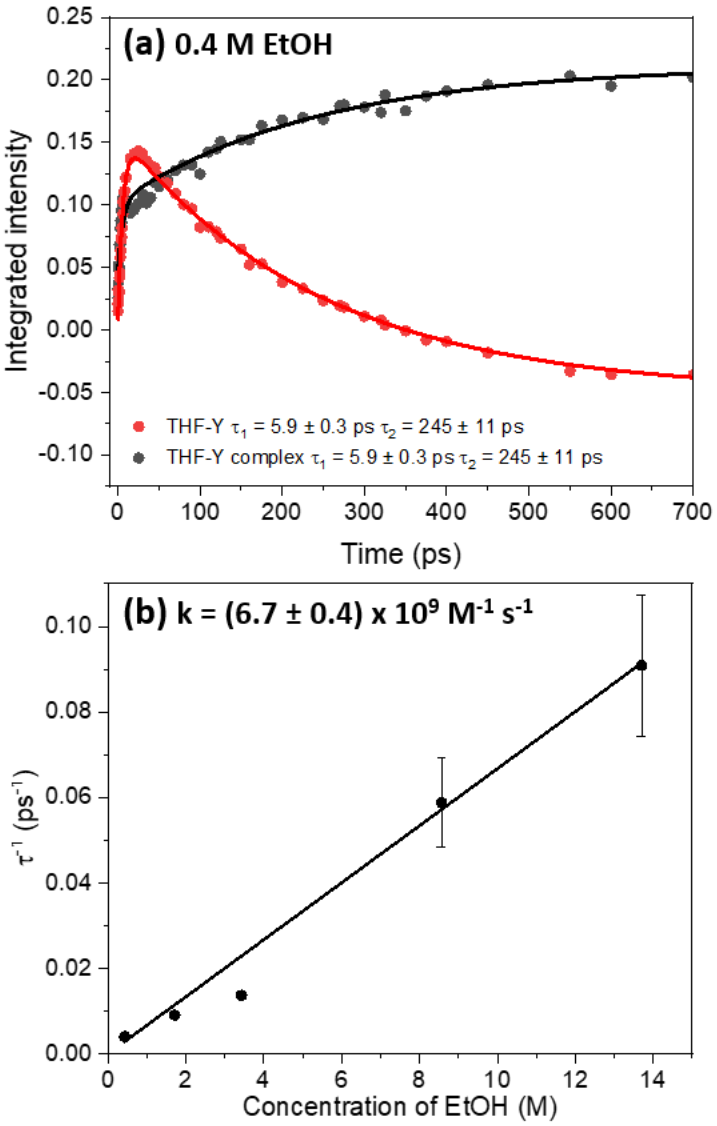


Figure 5.11 – Kinetics of formation of THF-Y ylides and their solvent complexes in a mixed THF/EtOH solution. (a) Fitting of integrated intensities of TVAS bands assigned to the THF-Y (Red) and THF-Y HB complex (Black) formed after photoexcitation of 65 mM EDA in a mixed solution of 0.4 M EtOH in THF. Dots represent experimental data points and solid lines are bi-exponential fits. (b) Dependence of pseudo-first order rate coefficients, 1/τ, for the growth of the THF-Y HB complex on EtOH concentration. Error bars on experimental data points show the uncertainties from the kinetic fits and do not consider errors arising from the spectral decomposition. For this reason, they were not used to weight the linear fit to extract a bimolecular rate coefficient. Error bars for data points between 0 M and 4 M ethanol concentrations are smaller than the data points.

The complete decay of the unbound THF-Y band (Figure 5.11(a)) shows that diffusive escape of H-bonded EtOH does not occur over the timescale probed (i.e. 1.3 ns), and that there is a greater propensity for the THF-Y to exist in its ethanol-complexed form. The position of equilibrium suggests that if any thermal dissociation of the THF-Y HB complex occurs, the hydrogen-bond donor and THF-Y will be confined as a pair within a solvent cage, illustrated by [THF-Y + EtOH] in Scheme 5.7, and can rapidly reform the hydrogen-bonded complex. This interpretation is supported by the pseudo first-order kinetic analysis of the exponential growth of complexes of THF-Y with EtOH solvent molecules shown in Figure 5.11(b), which yields a value for the bimolecular rate coefficient, $k = (6.7 \pm 0.4) \times 10^9$ $M^{-1}$ $s^{-1}$, which is close to diffusion limited, and confirms the formation of the hydrogen-bond to be a rapid process.

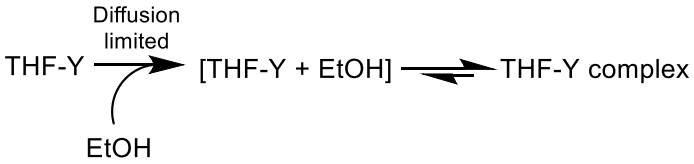


Scheme 5.7 – Reaction scheme for hydrogen-bond formation of the THF-Y with EtOH.

**5.3.9 – Structure of the hydrogen bonded complex**

To gain a deeper understanding of the hydrogen-bonded structure with IR signatures at 1617 $cm^{-1}$ (<0.4M EtOH) and 1608 $cm^{-1}$ (>1.7M EtOH) (Figure 5.10), various properties of the hydrogen-bonded structures are computed for the Z isomer of the THF-Y (see Scheme 5.6). A summary is presented in Table 5.3, and is used to guide the assignment of the structure for the THF-Y HB complex described in section 5.3.8. The calculations of the properties reported in Table 5.3 used methanol as a protic solvent in place of ethanol to reduce the computational expense, but they are expected to inform about similar intermolecular interactions in solutions containing EtOH.

Table 5.3 – Computed properties for the various hydrogen-bonded structures illustrated in Scheme 5.6 for the Z isomer of the THF-Y

| Complex | Enthalpy of complexation[a] (kJ mol$^{-1}$) | Median Hydrogen-bond lifetime[b] (ps) | Computed carbonyl vibrational frequency[c] (cm$^{-1}$) |
|---|---|---|---|
| Free THF-$Y_Z$ | - | - | 1642 |
| $1_Z$ | -38.0 | 0.30 | 1649 |
| $2_Z$ | -29.9 | 0.61 | 1657 |
| $3_Z$ | -33.8 | 2.6 | 1623 |

[a] Computed using MP2/6-311++G(d,p) geometries and MP2/aug-cc-pVTZ single point energies
[b] Computed at the B3LYP/6-31+G(d) level of theory
[c] Computed at the MP2/6-311++G(d,p) level of theory

Computations for the enthalpy of complexation indicates all 3 complexes experience a large thermodynamic stabilization compared to the uncomplexed THF-Y, but to gain deeper insights into the kinetic stability of the complexes dynamical simulations were perfomed. ADMP trajectories were propagated starting from complexes $1_Z$ - $3_Z$ at constant temperature (300 K) until the hydrogen bond length exceeded 3.1 Å, or for a maximum duration of 5 ps. 25 trajectories were computed for complexes $1_Z$ and $2_Z$, and 40 for the $3_Z$ isomer, all with randomised starting conditions. The statistics of computed lifetimes for the complexes are shown in Figure 5.12, together with representative trajectories. Of the three starting structures, complex $3_Z$ shows an enhanced kinetic stability compared to complexes $1_Z$ and $2_Z$. The median THF-Y HB lifetimes (see Table 5. 3) for the complexes were 0.30 ps (Complex $1_Z$), 0.61 ps (Complex $2_Z$) and 2.6 ps (Complex $3_Z$). Of the trajectories computed from a starting structure corresponding to Complex $3_Z$, 9 out of 40 showed a hydrogen-bond lifetime exceeding 5 ps. Overall, the trajectories suggest a greater propensity for complex 3 in a solution at dynamic equilibrium.

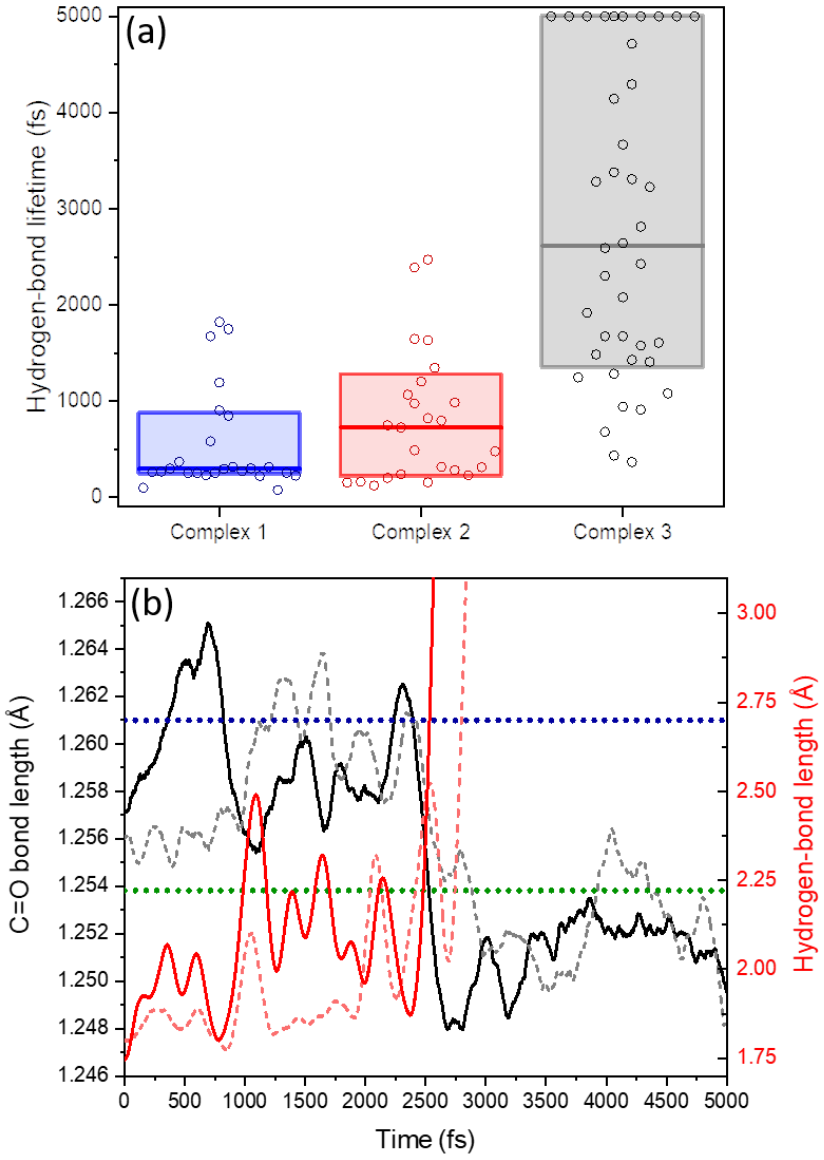


Figure 5.12 – Trajectory simulation outcomes for THF-Y complexes with methanol at 300 K. a) the hydrogen-bond lifetimes computed for multiple trajectories initiated from complexes $1_Z$ - $3_Z$. Box-plots show the mean hydrogen-bond lifetimes (centre horizontal lines) and the middle 80 percentile (box length). b) Evolution of C=O and H---O internuclear distances during representative trajectories for dissociation of complex $3_Z$. Dashed and solid traces show the outputs of two different trajectories. The time-dependent variation of the C=O bond length is shown in Black, and the hydrogen-bond length is show in red, with both smoothed by a 250-fs moving average. Horizontal dotted lines show computed C=O bond lengths for the $3_Z$ complex of THF-Y with methanol (Blue) and uncomplexed THF-Y (Green).

The experiments observe the change in stretching frequency of the THF-Y carbonyl group, and the results from the trajectories support the idea that the hydrogen-bonding environment is connected to changes in carbonyl bond length, and hence vibrational frequency. The calculations therefore support the interpretation that the complexed and free forms are spectroscopically distinguishable species. Moreover, the trajectories indicate that the solvent interactions with THF-Y undergo spontaneous fluctuations on few-ps timescales. The computed evolutions of C=O bond and hydrogen-bond lengths are shown in Figure 5.12(b) for two trajectories corresponding to the thermal break-up of complex $3_Z$, which shows a significant shift in the average C=O bond length at a time interval of ≈2500 fs in both trajectories. The combined results from multiple trajectory simulations show complexation to the carbonyl to be the most probable H-bonding site of the three options considered. The computed vibrational frequency of complex $3_Z$ (1623 $cm^{-1}$) is in good agreement with the observed 1617 $cm^{-1}$ band in Figure 5.10 and reproduces the -17 $cm^{-1}$ shift from the uncomplexed THF-Y observed in experiments and summarized in Table 5. 3.

The shift in band position of the THF-Y complex with ethanol from 1617 $cm^{-1}$ to 1608 $cm^{-1}$ for higher concentrations of EtOH could be a result of a microscopically heterogenous distribution of EtOH in THF. More specifically, the THF-Y preferentially forms within a locally THF dominated environment, but can diffuse to a locally EtOH rich environment where it forms complexes $3_E$ and $3_Z$. This interpretation is supported by computed carbonyl stretching bands of complex $3_Z$ at 1623 $cm^{-1}$ in THF and 1614 $cm^{-1}$ in MeOH (again using MeOH as a substitute for EtOH in the computations, and a PCM treatment of further solvent interactions). These calculations predict a shift of this band to lower wavenumber in the alcohol solution of the same magnitude as the experimental observations, as shown in Table 5.4. Any further assignment to complexes 1 and 2 is discounted because computed vibrational frequencies instead predict a shift in the carbonyl stretching band to higher wavenumber for these specific forms of interaction with an alcohol solvent molecule.

### 5.3.10 C-H hydrogen-bonding

The HB acceptor properties of the THF-Y were further explored using weaker HB donors than EtOH. Figure 5.13 shows the TVAS spectra obtained for Chloroform:THF, Dichloromethane:THF, ACN:THF and Cyclohexane:THF mixtures. The findings are summarised in Table 5.4.

The use of weaker hydrogen bond donors than EtOH also results in the formation of THF-Y HB complexes with bimolecular rate coefficients consistent with diffusion limited kinetics, and values are reported in Figure 5.13. The ylide HB complexes show a smaller shift in the carbonyl stretching frequency relative to THF-Y than observed in EtOH. The smallest shift is found for the weakest hydrogen-bond donor, cyclohexane. The equilibrium between free and HB-complexed THF-Y still favours the complexed ylide in the case of chloroform, which shows ≈100% complexation. However, with DCM, ACN, and cyclohexane, just 24%, 32% and 12% respectively of ylides apparently adopt the H-bonded complex form.

Table 5.4 – TVAS band positions for THF-Y and its complexes with various hydrogen-bond donors

| | THF-Y band ($cm^{-1}$) | THF-Y HB complex band ($cm^{-1}$) | Shift ($cm^{-1}$) |
|---|---|---|---|
| EtOH | 1636 | 1617/1608[a] | -19/-28[a] |
| Chloroform | 1636 | 1622 | -14 |
| DCM | 1636 | 1626 | -10 |
| ACN | 1633 | 1624 | -9 |
| Cyclohexane | 1636 | 1628 | -8 |

[a] At higher concentrations of EtOH

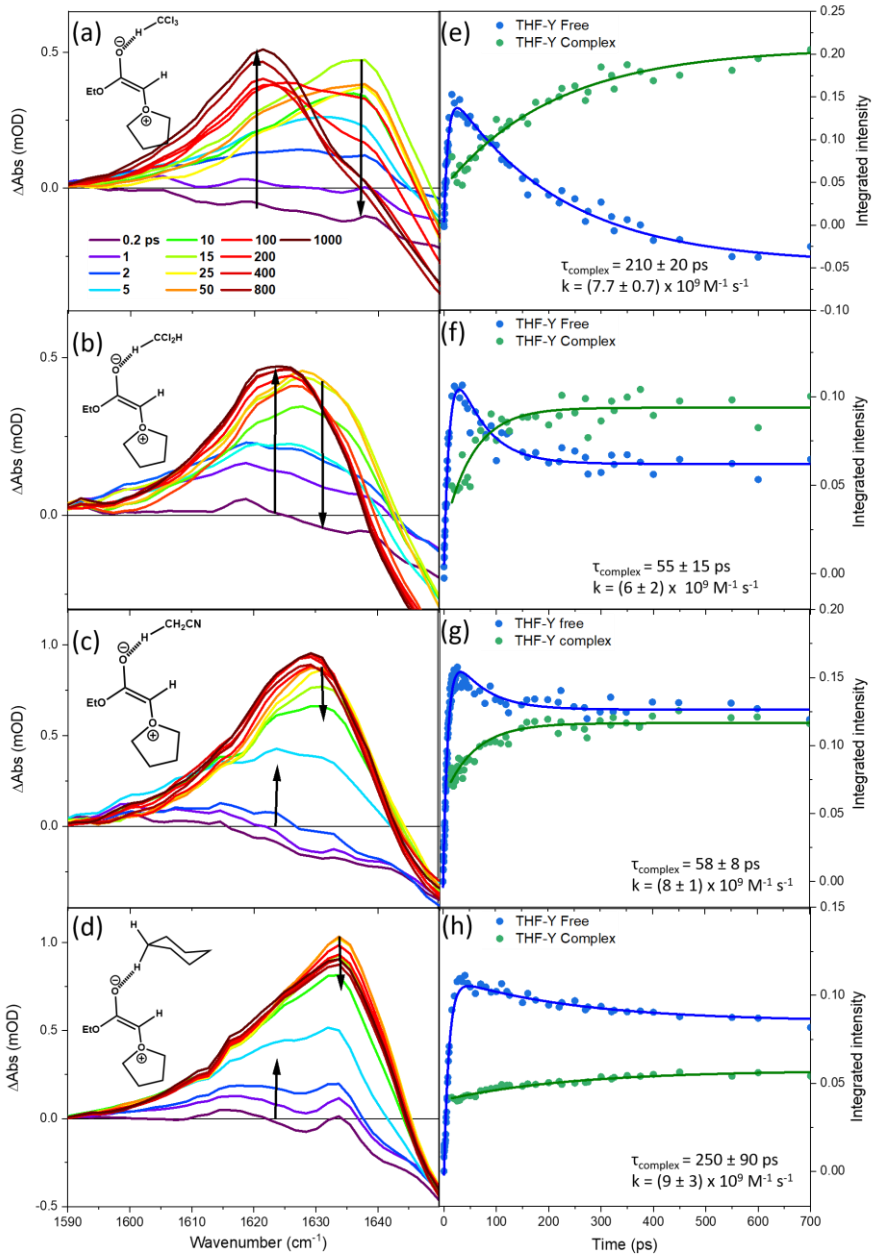


Figure 5.13 – Evidence from TVAS spectra for C-H hydrogen bond donation to THF-Y species in mixed solutions of THF and either $CHCl_3$, $CH_2Cl_2$ or cyclohexane. Left column: TVAS spectra for the wavenumber range from 1570-1780 $cm^{-1}$ for the photoexcitation of 65 mM EDA solutions of: (a) 0.62 M Chloroform in THF; (b) 3.1 M DCM in THF; (c) 1.9 M ACN; (d) 0.46 M Cyclohexane in THF. Right: Exponential fitting for the growth and decay of IR band intensities assigned to THF-Y (Blue), and for the growth of the solvent-complexed ylide (green). Inset numbers report the exponential time constants and bimolecular rate coefficients for solvent complexation.

## 5.4. Conclusions

The UV photoexcitation of ethyl diazoacetate and resulting elimination of $N_2$ forms singlet $\alpha$-carbonyl carbene intermediates which rapidly react with solvent molecules by insertion into C-H bonds. In nucleophilic solvents, the carbene can also competitively react with the electron donating groups of the solvent to produce ylides. In this study, these competing processes were resolved by ultrafast TVAS spectroscopy. The interaction of the THF ylide with ethanol molecules was experimentally monitored in EtOH:THF solvent mixtures via the growth of a band at 1617 $cm^{-1}$ (in 0.4M EtOH) and 1608 $cm^{-1}$ (>1.7M EtOH). This spectral feature was assigned to the hydrogen-bonded complex of the THF ylide. To characterise the interaction further, atom centred density matrix propagation trajectories were performed at 300 K for various complexes with methanol. These dynamical simulations identified hydrogen bond donation to the carbonyl group of the THF ylide to have enhanced kinetic stability over complexes in which the H-bond donation is to other acceptor sites. Further TVAS spectra revealed that THF ylides also interact with chloroform, dichloromethane, acetonitrile, and cyclohexane by accepting a C-H hydrogen bond, as is evidenced by IR bands downshifted in wavenumber from the uncomplexed THF ylide band. The magnitudes of the shifts reduce with weaker hydrogen bond donors. In each ylide-solvent system studied, the kinetics of ylide formation, ylide-solvent complexation, and further ylide reaction were all established directly from the TVAS measurements. The outcomes reveal the dynamical behaviour of these elusive intermediates in a range of organic solvents commonly used in synthetic chemistry.

## References


1. Reichardt, C. Solvents and Solvent Effects: An Introduction. *Org. Process Res. Dev.* **2007,** *11*, 105-113.
2. Slakman, B. L.; West, R. H. Kinetic solvent effects in organic reactions. *J. Phys. Org. Chem.* **2019,** *32*, e3904.
3. Varghese, J. J.; Mushrif, S. H. Origins of complex solvent effects on chemical reactivity and computational tools to investigate them: a review. *React. Chem. Eng.* **2019,** *4*, 165-206.
4. Knorr, J.; Sokkar, P.; Costa, P.; Sander, W.; Sanchez-Garcia, E.; Nuernberger, P. How Protic Solvents Determine the Reaction Mechanisms of Diphenylcarbene in Solution. *J. Org. Chem.* **2019,** *84*, 11450-11457.
5. Saleheen, M.; Verma, A. M.; Mamun, O.; Lu, J.; Heyden, A. Investigation of solvent effects on the hydrodeoxygenation of guaiacol over Ru catalysts. *Cat. Sci. Tech.* **2019,** *9*, 6253-6273.
6. Jayasree, E. G.; Sreedevi, S. A DFT study on protic solvent assisted tautomerization of heterocyclic thiocarbonyls. *Chem. Phys.* **2020,** *530*, 110650.
7. Koyambo-Konzapa, S. J.; Minguirbara, A.; Nsangou, M. Solvent effects on the structures and vibrational features of zwitterionic dipeptides: L-diglycine and L-dialanine. *J. Mol. Model.* **2015,** *21*, 189.

8. Hall, N.; Smith, B. Solvation Effects on Zwitterion Formation. *J. Phys. Chem. A* **1998,** *102*, 3985-3990
9. Runser, C.; Fort, A.; Barzoukas, M.; Combellas, C.; Suba, C.; Thiébault, A.; Graff, R.; Kintzinger, J. P. Solvent effect on the intramolecular charge transfer of zwitterions. Structures and quadratic hyperpolarizabilities. *Chem. Phys.* **1995,** *193*, 309-319.
10. Crittenden, D. L.; Chebib, M.; Jordan, M. J. T. Stabilization of Zwitterions in Solution: γ-Aminobutyric Acid (GABA). *J. Phys. Chem. A* **2004,** *108*, 203-211.
11. Wang, Y.-M.; Zhang, H.-H.; Li, C.; Fan, T.; Shi, F. Catalytic asymmetric chemoselective 1,3-dipolar cycloadditions of an azomethine ylide with isatin-derived imines: diastereo- and enantioselective construction of a spiro[imidazolidine-2,3'-oxindole] framework. *Chem. Commun.* **2016,** *52*, 1804-1807.
12. Li, F.; He, F.; Koenigs, R. Catalyst-Free [2,3]-Sigmatropic Rearrangement Reactions of Photochemically Generated Ammonium Ylides. *Synthesis* **2019,** *51*, 4348-4358
13. Yan, X.; Li, C.; Xu, X.; He, Q.; Zhao, X.; Pan, Y. Sulfonium ylide formation and subsequent CS bond cleavage of aromatic isopropyl sulfide catalyzed by hemin in aqueous solvent. *Tetrahedron* **2019,** *75*, 3081-3087.
14. Byrne, P. A.; Gilheany, D. G. The modern interpretation of the Wittig reaction mechanism. *Chem. Soc. Rev.* **2013,** *42*, 6670-6696.
15. Ford, A.; Miel, H.; Ring, A.; Slattery, C. N.; Maguire, A. R.; McKervey, M. A. Modern Organic Synthesis with α-Diazocarbonyl Compounds. *Chem. Rev.* **2015,** *115*, 9981-10080.
16. Iwig, D. F.; Grippe, A. T.; McIntyre, T. A.; Booker, S. J. Isotope and Elemental Effects Indicate a Rate-Limiting Methyl Transfer as the Initial Step in the Reaction Catalyzed by Escherichia coli Cyclopropane Fatty Acid Synthase. *Biochem.* **2004,** *43*, 13510-13524.
17. Iwig, D. F.; Booker, S. J. Insight into the Polar Reactivity of the Onium Chalcogen Analogues of S-Adenosyl-l-methionine. *Biochem.* **2004,** *43*, 13496-13509.
18. Kinzie, S. D.; Thern, B.; Iwata-Reuyl, D. Mechanistic Studies of the tRNA-Modifying Enzyme QueA: A Chemical Imperative for the Use of AdoMet as a "Ribosyl" Donor. *Org. Lett.* **2000,** *2*, 1307-1310.
19. Lee, H.-Y.; Bae, I.-H.; Min, K.-H. Solvent Effect on Sulfur Ylide Mediated Epoxidation Reaction. *Bull. Korean Chem. Soc.* **2007,** *28*, 2051-2055
20. Aksnes, G.; Berg, T. J.; Gramstad, T. Temperature and solvent effects in Wittig reactions. *Phosphorus, Sulfur, and Silicon and the Related Elements* **1995,** *106*, 79-84.
21. Salem, R. Anionic activation of the Wittig reaction using a solid-liquid phase transfer: Examination of the medium-, temperature-, base- and phase-transfer catalyst effects. *ARKIVOC XII,.* **2006,** *2006*, 1-22.
22. Batsanov, A. S.; Davidson, M. G.; Howard, J. A. K.; Lamb, S.; Lustig, C. Phosphonium ylides as hydrogen bond acceptors: intermolecular C–H···C interactions in the crystal structure of triphenylphosphonium benzylide. *Chem. Commun.* **1996**, 1791-1792.
23. Rozas, I.; Alkorta, I.; Elguero, J. Behavior of Ylides Containing N, O, and C Atoms as Hydrogen Bond Acceptors. *J. Am. Chem. Soc.* **2000,** *122*, 11154-11161.
24. A. Platts, J.; T. Howard, S. C–H · · · C Hydrogen bonding involving ylides. *J Chem. Soc., Perkin Trans. 2* **1997**, 2241-2248.
25. Zabardasti, A.; Kakanejadifard, A.; Ghasemian, M.; Jamshidi, Z. Theoretical study of molecular interactions of sulfur ylide with HF, HCN, and $HN_3$. *Struct. Chem.* **2013,** *24*, 271-277
26. Candeias, N.; Afonso, C. Developments in the Photochemistry of Diazo Compounds. *Curr. Org. Chem.* **2009,** *13*, 763-787.
27. Phelps, R.; Orr-Ewing, A. J. Direct Observation of Ylide and Enol Intermediates Formed in Competition with Wolff Rearrangement of Photoexcited Ethyl Diazoacetoacetate. *J. Am. Chem. Soc.* **2020,** *142*, 7836-7844.
28. Pecile, C.; Föffani, A.; Ghersetti, S. The Interaction of Diazocarbonyl Compounds with Hydroxylic Solvents. *Tetrahedron* **1964,** *20*, 823-829.

29. Wolpert, D.; Schade, M.; Brixner, T. Femtosecond midinfrared study of the photoinduced Wolff rearrangement of diazonaphthoquinone. *J. Chem. Phys.* **2008,** *129*, 094504.
30. Lippert, T.; Koskelo, A.; Stoutland, P. O. Direct Observation of a Photoinduced Wolff Rearrangement in PMMA Using Ultrafast Infrared Spectroscopy. *J. Am. Chem. Soc.* **1996,** *118*, 1551-1552.
31. Wang, Y.; Yuzawa, T.; Hamaguchi, H.-O.; Toscano, J. P. Time-Resolved IR Studies of 2-Naphthyl(carbomethoxy)carbene: Reactivity and Direct Experimental Estimate of the Singlet/Triplet Energy Gap. *J. Am. Chem. Soc.* **1999,** *121*, 2875-2882.
32. Zhu, Z.; Bally, T.; Stracener, L. L.; McMahon, R. J. Reversible Interconversion between Singlet and Triplet 2-Naphthyl(carbomethoxy)carbene. *J. Am. Chem. Soc.* **1999,** *121*, 2863-2874.
33. Gallucci, R. R.; Jones, M. Photolysis of methyl 3-diazo-2-oxopropionate. Wolff migration of the carbomethoxy group. *J. Org. Chem.* **1985,** *50*, 4404-4405.
34. Maier, G.; Reisenauer, H. P.; Sayrac, T. Oxirene - Intermediate or Transition state - Matrix Irradiation of Diazoketones. *Chem. Ber. Recl.* **1982,** *115*, 2192-2201.
35. Ciszewski, Ł. W.; Rybicka-Jasińska, K.; Gryko, D. Recent developments in photochemical reactions of diazo compounds. *Org. Biomole. Chem.* **2019,** *17*, 432-448.
36. Candeias, N. R.; Gois, P. M. P.; Veiros, L. F.; Afonso, C. A. M. C−H Carbene Insertion of α-Diazo Acetamides by Photolysis in Non-Conventional Media. *J. Org. Chem.* **2008,** *73*, 5926-5932.
37. Xue, J.; Luk, H. L.; Platz, M. S. Direct Observation of a Carbene-Alcohol Ylide. *J. Am. Chem. Soc.* **2011,** *133*, 1763-1765.
38. Wang, J.; Kubicki, J.; Gustafson, T. L.; Platz, M. S. The Dynamics of Carbene Solvation: An Ultrafast Study of p-Biphenylyltrifluoromethylcarbene. *J. Am. Chem. Soc.* **2008,** *130*, 2304-2313.
39. Gómez, S.; Restrepo, A.; Hadad, C. Z. Theoretical tools to distinguish O-ylides from O-ylidic complexes in carbene–solvent interactions. *Phys. Chem. Chem. Phys.* **2015,** *17*, 31917-31930.
40. Hadad, C. Z.; Jenkins, S.; Flórez, E. Unusual solvation through both p-orbital lobes of a carbene carbon. *J. Chem. Phys.* **2015,** *142*, 094302.
41. Wang, J.; Kubicki, J.; Peng, H.; Platz, M. S. Influence of Solvent on Carbene Intersystem Crossing Rates. *J. Am. Chem. Soc.* **2008,** *130*, 6604-6609.
42. Standard, J. M. Effects of Solvation and Hydrogen Bond Formation on Singlet and Triplet Alkyl or Aryl Carbenes. *J. Phys. Chem. A* **2017,** *121*, 381-393.
43. Frisch, M. J.; Trucks, G. W.; Schlegel, H. B.; Scuseria, G. E.; Robb, M. A.; Cheeseman, J. R.; Scalmani, G.; Barone, V.; Mennucci, B.; Petersson, G. A.; Nakatsuji, H.; Caricato, M.; Li, X.; Hratchian, H. P.; Izmaylov, A. F.; Bloino, J.; Zheng, G.; Sonnenberg, J. L.; Hada, M.; Ehara, M.; Toyota, K.; Fukuda, R.; Hasegawa, J.; Ishida, M.; Nakajima, T.; Honda, Y.; Kitao, O.; Nakai, H.; Vreven, T.; Montgomery, J. A., Jr.;; Peralta, J. E.; Ogliaro, F.; Bearpark, M.; Heyd, J. J.; Brothers, E.; Kudin, K. N.; Staroverov, V. N.; Kobayashi, R.; Normand, J.; Raghavachari, K.; Rendell, A.; Burant, J. C.; Iyengar, S. S.; Tomasi, J.; Cossi, M.; Rega, N.; Millam, N. J.; Klene, M. K., J. E.;; Cross, J. B.; Bakken, V.; Adamo, C.; Jaramillo, J.; Gomperts, R.; Stratmann, R. E.; Yazyev, O.; Austin, A. J.; Cammi, R.; Pomelli, C.; Ochterski, J. W.; Martin, R. L.; Morokuma, K.; Zakrzewski, V. G.; Voth, G. A.; Salvador, P.; Dannenberg, J. J.; Dapprich, S.; Daniels, A. D.; Farkas, O.; Foresman, J. B.; Ortiz, J. V.; Cioslowski, J.; Fox, D. J. *Gaussian 09, revision D.01*, Gaussian, Inc: Wallingford, CT, 2013.
44. Hajgató, B.; Nguyen, H. M. T.; Veszprémi, T.; Nguyen, M. T. Triplet–singlet energy gaps in iodo-carbenes (I–C–X): Remarkable discrepancy between theory and experiment. *Phys. Chem. Chem. Phys.* **2000,** *2*, 5041-5045.
45. Matzinger, S.; Fuelscher, M. P. Methyl Substitution in Carbenes. A Theoretical Prediction of the Singlet-Triplet Energy Separation of Dimethylcarbene. *J. Phys. Chem.* **1995,** *99*, 10747-10751.
46. Wang, X.; Agarwal, J.; Schaefer Iii, H. F. Characterizing a nonclassical carbene with coupled cluster methods: cyclobutylidene. *Phys. Chem. Chem. Phys* **2016,** *18*, 24560-24568.
47. Grubb, M. P.; Orr-Ewing, A. J.; Ashfold, M. N. R. KOALA: A program for the processing and decomposition of transient spectra. *Rev. Sci. Instrum.* **2014,** *85*, 064104.

48. Kaplan, F.; Meloy, G. K. The Structure of Diazoketones. A Study of Hindered Internal Rotation1,2. *J. Am. Chem. Soc.* **1966,** *88*, 950-956.
49. Strausz, O. P.; Thap, D. M.; Gunning, H. E. Rearrangement and Polar Reaction of Carbethoxymethylene in 2-Propanol. *J. Am. Chem. Soc.* **1968,** *90*, 1660-1661.
50. Drioli, S.; Nitti, P.; Pitacco, G.; Tossut, L.; Valentin, E. Enantiomerically pure tetrahydro-5-oxo-2-furancarboxylic esters from dialkyl 2-oxoglutarates. *Tetrahedron: Asymmetry* **1999,** *10*, 2713-2728.
51. Bellur, E.; Freifeld, I.; Böttcher, D.; Bornscheuer, U. T.; Langer, P. Synthesis of (tetrahydrofuran-2-yl)acetates based on a 'cyclization/hydrogenation/enzymatic kinetic resolution' strategy. *Tetrahedron* **2006,** *62*, 7132-7139.
52. Upadhya, T. T.; Sudalai, A. A short and efficient enantioselective synthesis of cyclohexylnorstatine, a key component of a renin inhibitor. *Tetrahedron: Asymmetry* **1997,** *8*, 3685-3689.
53. Chaimovich, H.; Vaughan, R. J.; Westheimer, F. H. Rearrangement accompanying the photolysis of diazoacyl esters. *J. Am. Chem. Soc.* **1968,** *90*, 4088-4093.

**Chapter 5 – Supporting information**

Section S1 – Experimental

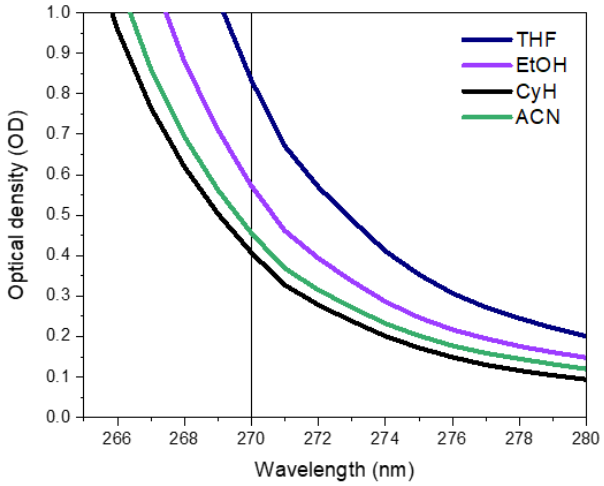


Figure S5.1 – UV-Vis spectra measured in the 255-280 nm range of 65mM EDA in Cyclohexane (black), Ethanol (Purple), acetonitrile (green), and Tetrahydrofuran (Blue). The sample path length was 150 µm. The vertical line shows the photoexcitation wavelength (270 nm) chosen for the TVAS studies reported in the main paper.

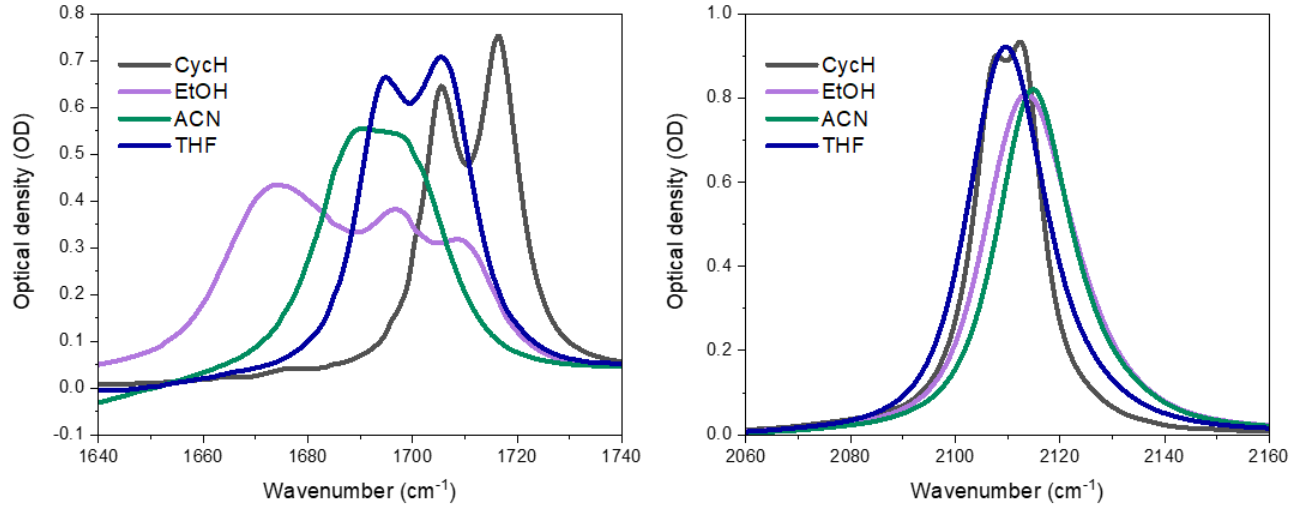


Figure S5.2 – FTIR spectra measured in the wavenumber ranges 1640-1740 $cm^{-1}$ (Left) and 2060-2160 $cm^{-1}$ (Right) for a 65 mM EDA solution in cyclohexane (Black), Ethanol (Purple), acetonitrile (green), and Tetrahydrofuran (Blue). The sample path length was 150 µm.

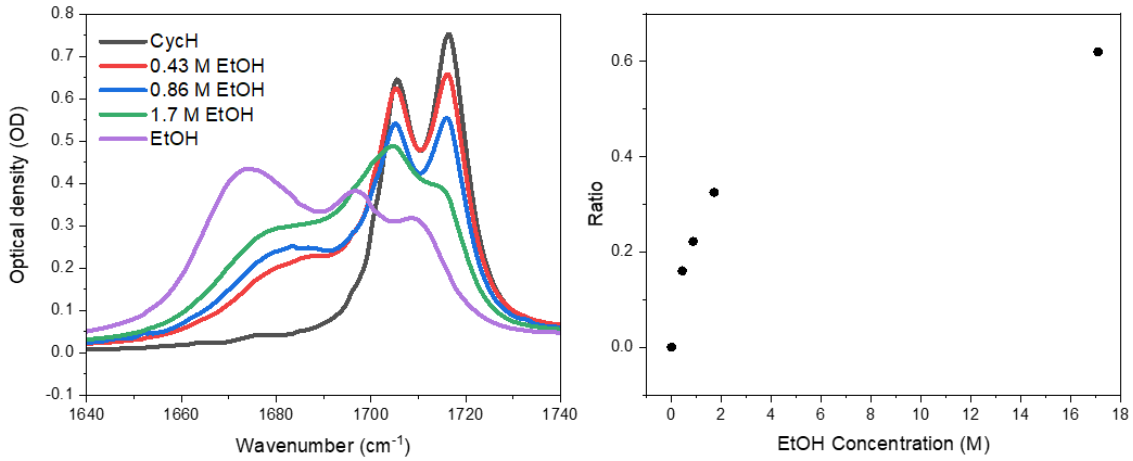


Figure S5.3 – FTIR spectra measured in the wavenumber range 1640-1740 $cm^{-1}$ for 65 mM EDA solutions with various concentrations of ethanol (EtOH) in cyclohexane (CycH). The sample path length was 150 µm. Right – Hydrogen-bonded EDA : uncomplexed-EDA IR band intensity ratio as a function of Ethanol concentration. The inset key shows the solvent compositions. The sample path length was 150 µm.

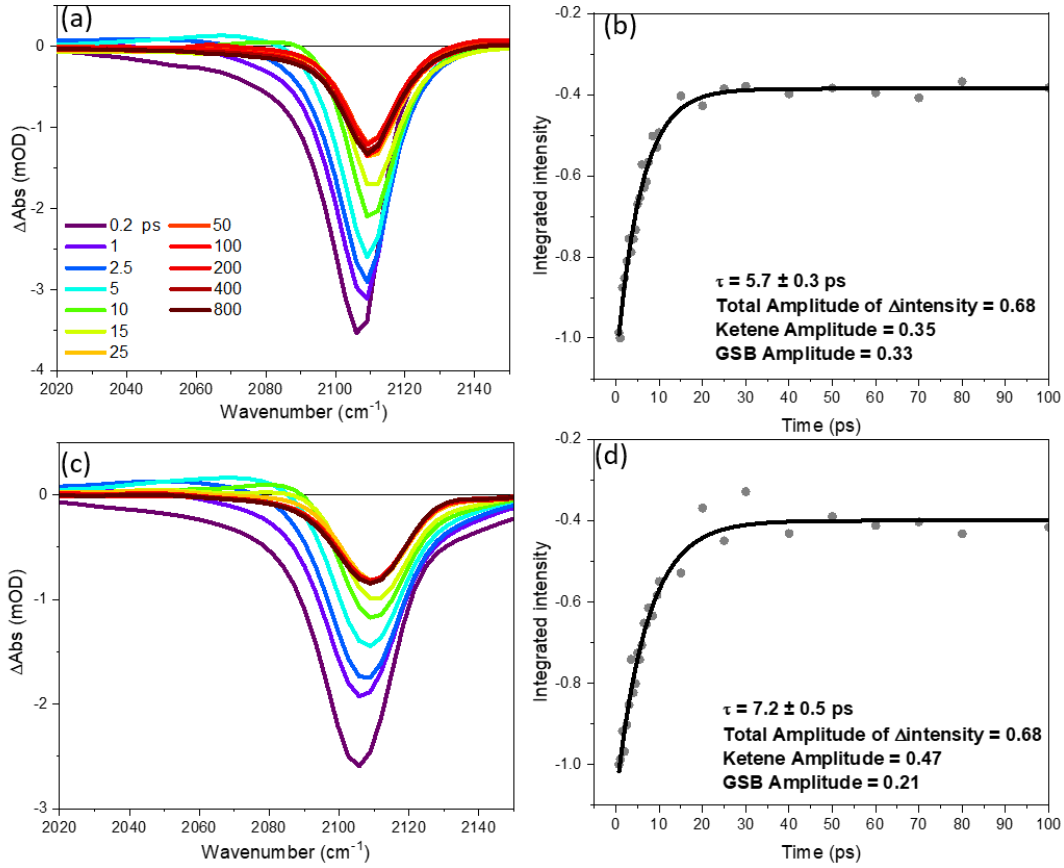


Figure S5.4 – TVAS spectra measured in the wavenumber range 2020-2150 $cm^{-1}$ for the 270-nm photoexcitation of 65 mM EDA in (a) Cyclohexane and (b) THF. The TVAS measurements used a 150-µm sample thickness. Time dependent growths for ketene bands are monitored in the range 2095-2125 $cm^{-1}$, where they overlap the negative GSB feature, and are plotted in (c) for cyclohexane and (d) for THF. Dots are experimental data points, fitted with single exponential functions shown as the solid curves. The GSB recovery amplitudes for the less overlapped ~1650 $cm^{-1}$ GSB (shown in Figure 5.4 of the main paper) are shown inset in Figures S5.4 (b) and (d) and used to determine the overall ketene amplitudes. The inset to Figures S5.4 (a) and (c) identifies the delay times for each TVAS spectrum.

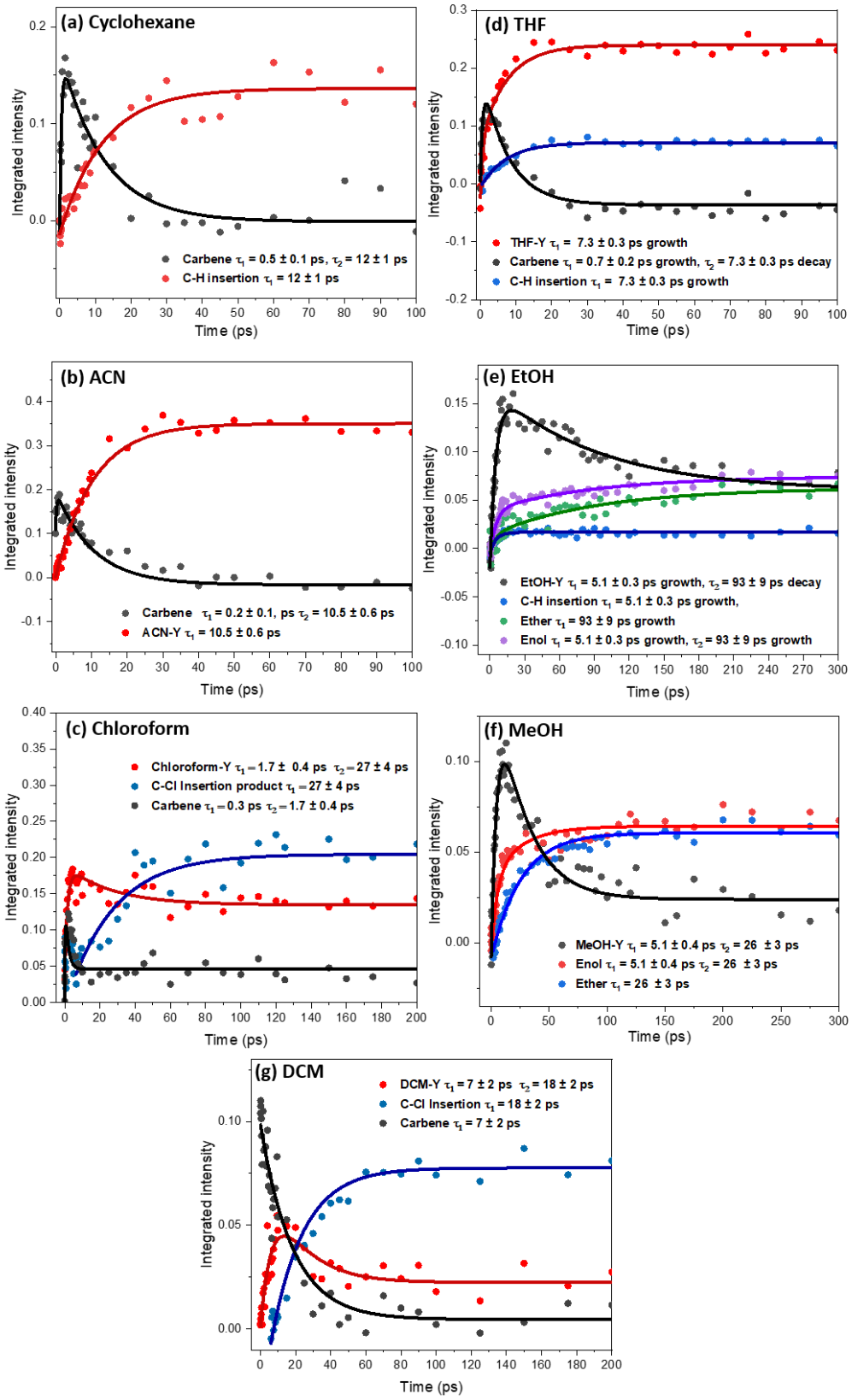


Figure S5.5 – Time-dependent growths of the integrated intensities for photoproduct bands formed from the 270-nm photoexcitation of EDA in: Cyclohexane (a); ACN (b); Chloroform (c);

THF (d); EtOH (e); MeOH (f); DCM (g). Dots are experimental data points, which are fitted with single or bi-exponential functions shown as solid curves. Inset are colour keys identifying the different photoproducts.

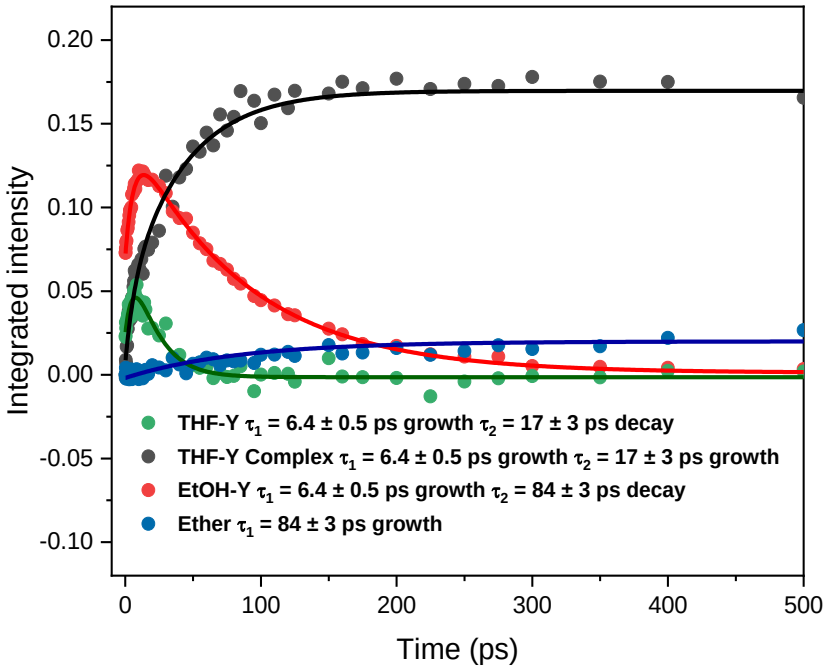


Figure S5.6 – Example kinetic fitting for: THF-Y (Green); THF-Y HB Complex (Black); EtOH-Y (Red); Ether (Blue) for the 270-nm photoexcitation of EDA in a 4.6 M EtOH solution in THF. Dots are experimental data points, and are fitted to single or biexponential functions shown as solid curves. Inset are colour keys identifying the different photoproducts.

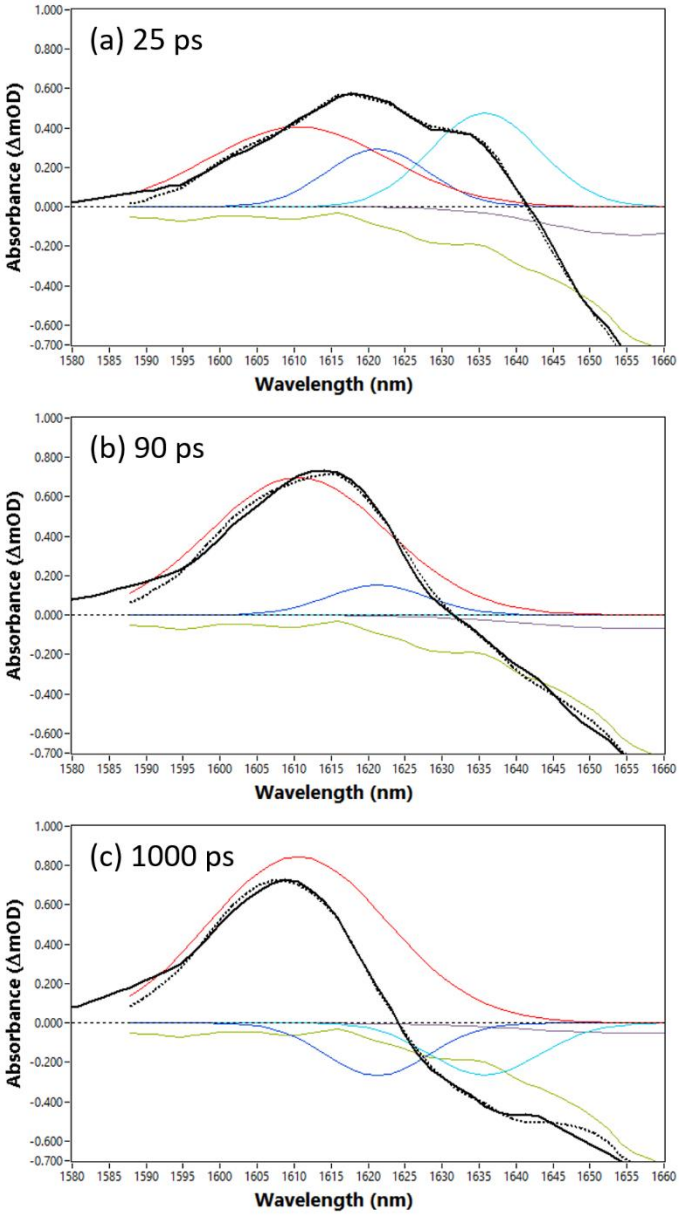


Figure S5.7 – Example fitting procedure for the decomposition of overlapping EtOH-Y, THF-Y, and THF-Y HB complex bands arising from the photoexcitation of 65 mM EDA in a solution of 1.7 M EtOH in THF. Transient spectra are shown by solid black lines at: (a) 25 ps; (b) 90 ps; and (c) 1000 ps. An early time basis function (light green) is used to fit the GSB recovery of EDA, and is overlapped with Gaussian functions of fixed widths and centres to produce the simulated curve (dotted-line) which best describes the experimental data. The colour scheme for the Gaussian functions is: cyan for THF-Y; blue for EtOH-Y; and red for the THF-Y HB complex. The spectral decomposition was carried out using the KOALA program. [1]

Section S2 – Computed vibrational frequencies

The majority of vibrational frequencies were computed at the MP2/6-311++G(d,p) level of theory with inclusion of the stated solvent using a polarizable continuum model (PCM). Harmonic frequencies were scaled by a factor of 0.9827 to account for anharmonicity. The anharmonicity scaling factor was computed for both isomers of EDA and applied to all other species.

Table S5.1 – Computed and observed vibrational frequencies for EDA isomers in various solvents

| Species | Solvent | Computed vibrational frequency | Observed vibrational frequency |
|---|---|---|---|
| Syn-EDA | Cyclohexane | 1710 | 1705 |
| Anti-EDA | Cyclohexane | 1725 | 1716 |
| Syn-EDA | THF | - | 1695 |
| Anti-EDA | THF | - | 1705 |
| Syn-EDA | ACN | - | 1688 |
| Anti-EDA | ACN | - | 1700 |
| Syn-EDA | EtOH | - | 1696 |
| Anti-EDA | EtOH | - | 1709 |
| HB-EDA | EtOH | - | 1674 |

Table S5.2 – Computed and observed vibrational frequencies for carbene and ketene intermediates formed in various solvents

| Species | Solvent | Computed vibrational frequency | Observed vibrational frequency |
|---|---|---|---|
| Ketene | Cyclohexane | - | 2130 |
| Ketene | THF | - | 2130 |
| Singlet Carbene | Cyclohexane | 1668[a] | 1678 |
| Singlet Carbene | THF | - | 1680 |
| Singlet Carbene | ACN | - | 1677 |
| Triplet Carbene | - | 1677[a] | - |

[a]Computed at the CCSD/6-311++G(d,p) level of theory without inclusion of a PCM treatment of solvent and scaled by a factor of 0.9695 (derived from the observed vibrational frequency of syn-EDA).

Table S5.3 – Literature and experimentally observed vibrational frequencies of C-H insertion products formed in various solvents

| Species | Solvent | Vibrational frequency (literature) | Observed vibrational frequency |
|---|---|---|---|
| C-H insertion | Cyclohexane | 1740[2] | 1745 |
| C-H insertion | THF | 1738[3] | 1739 |
| C-H insertion | EtOH | 1735[4] | 1735 |
| C-H insertion | MeOH | 1735[4] | - |
| C-H insertion | DCM | - | 1737 |
| C-H insertion | Chloroform | - | 1726 |

Table S5.4 – Computed and observed vibrational frequencies of Ylide and Enol intermediates formed in various solvents

| Species | Solvent | Computed vibrational frequency | Observed vibrational frequency |
|---|---|---|---|
| THF-Y | THF | 1642 | 1636 |
| ACN-Y | ACN | 1643 | 1642 |
| EtOH-Y | EtOH | - | 1617 |
| MeOH-Y | MeOH | 1673 | 1618 |
| Enol | MeOH | 1727 | 1722 |
| Enol | EtOH | - | 1726 |
| Chloroform-Y | Chloroform | 1638 | 1643 |
| DCM-Y | DCM | 1656 | 1657 |

Table S5.5 – Computed and observed vibrational frequencies of hydrogen-bonded complexes of the THF-Y with various hydrogen-bond donors

| Hydrogen-bond donor | Solvent | Computed vibrational frequency | Observed vibrational frequency |
|---|---|---|---|
| EtOH | THF | 1623 | 1619 |
| EtOH | EtOH | 1614 | 1608 |
| Chloroform | THF | - | 1622 |
| DCM | THF | - | 1622 |
| Cyclohexane | THF | - | 1628 |

**References**


1. Grubb, M. P.; Orr-Ewing, A. J.; Ashfold, M. N. R. KOALA: A program for the processing and decomposition of transient spectra. *Rev. Sci. Instrum.* **2014,** *85*, 064104.
2. Upadhya, T. T.; Sudalai, A. A short and efficient enantioselective synthesis of cyclohexylnorstatine, a key component of a renin inhibitor. *Tetrahedron: Asymmetry* **1997,** *8*, 3685-3689.
3. Bellur, E.; Freifeld, I.; Böttcher, D.; Bornscheuer, U. T.; Langer, P. Synthesis of (tetrahydrofuran-2-yl)acetates based on a 'cyclization/hydrogenation/enzymatic kinetic resolution' strategy. *Tetrahedron* **2006,** *62*, 7132-7139.
4. Drioli, S.; Nitti, P.; Pitacco, G.; Tossut, L.; Valentin, E. Enantiomerically pure tetrahydro-5-oxo-2-furancarboxylic esters from dialkyl 2-oxoglutarates. *Tetrahedron: Asymmetry* **1999,** *10*, 2713-2728.

# Chapter 6. Competing photochemical pathways in 2-aminothiazole revealed using ultrafast transient absorption spectroscopy

## 6.1. Introduction

The pursuit to discover the origins of life has remained one of the most controversial topics across scientific disciplines.[1-3] A central unanswered question is the construction of DNA from simple molecules in prebiotic conditions, and 2-aminoazoles were recently proposed to have played a critical role.[4-5] UV-light has been suggested to be a potential source of energy for prebiotic reactions and evidence exists that UV-light could have been involved in the selection of molecules incorporated into biology.[6-7] Therefore, the photochemistry and photostability of 2-aminoazoles are of significant interest.

The photochemistry of small heteroaromatic molecules has recently attracted a lot of attention, with a particular focus on their relaxation pathways.[8] For 5-membered heterocycles, such as thiazole, pyrrole and furan, relaxation pathways typically occur through conical intersections by either ring-puckering or ring-opening structural changes. However, which pathway occurs is often difficult to determine.[9-13] Recent time-resolved photoelectron spectroscopy measurements and quantum chemical calculations by Schalk *et al.* suggested a preference for a ring-opening pathway for the relaxation of furan.[14] However, Adachi *et al.* argued ring-puckering still dominates.[15] Solution phase transient infrared absorption spectroscopy measurements by Ashfold and coworkers provided unambiguous evidence for the ring-opening of various heterocyclic compounds bearing a carbonyl 'reporter' group by identifying the ketene stretching mode of ring-opened products.[16] When heterocycles bear an $NH_2$ group, an additional H-atom ejection pathway has also been suggested to contribute to the photochemistry.[17-21] Similarly, the N-H group in pyrrole undergoes UV-induced H-atom ejection.[22]

Szabla et al. computed a series of excited state potential energy surfaces for the gas-phase photochemistry of 2-aminooxazole (2-AO), and suggested the photochemistry to be dominated by the repulsive $^1\pi\sigma_{NH}^*$ surface which results in ultrafast nonradiative deactivation, phototautomerization, or photo-induced loss of a hydrogen atom from the $NH_2$ group.[18] The photochemistry of 2-AO in $H_2O$ clusters was further computationally explored,

identifying effective $S_0 \leftarrow S_1$ deactivation through the $^1\pi\sigma_{NH}^*$ surface by electron driven proton transfer (EDPT) along $H_2O$ wires, but also found 36% of the trajectories resulted in the C=N ring opening channel.[20] Other ring opening channels have also been suggested for azoles.[11, 23] To address the photostability of 2-aminoazoles, Todd *et al.* photo-irradiated aqueous samples of 2-aminooxazole and 2-aminothiazole (2-AT) and found 2-AT to be relatively more photostable, but identified that both 2-aminoazoles can be destroyed by prolonged exposure to UV-light.[24] Todd *et al.* speculated that the photo-destruction of the 2-aminoazoles occurred through ring-opening channels, however no photoproducts were observed. Although there are clear differences in their photostabilities, very little is known about the photochemistry of 2-aminothiazole, and why it may present as more photostable than 2-aminooxazole.

2-Aminothiazole forms a Hydrogen-bonded dimer in solutions of $CCl_4$ for concentrations as low as 0.002 M.[25] The dimer has been computationally found to catalyse tautomerisation of 2-AT to 2-iminothiazole (2-IT) through interaction of the $NH_2$ group of one 2-AT molecule with the N atom in the azole ring of its partner, as is shown in Scheme 6.1, and will initially form a 2-IT dimer ($(2\text{-IT})_2$). These computational results agreed with parallel experimental studies that found the relative concentration of 2-IT to be higher in more concentrated solutions of 2-AT.[26] Despite the propensity for 2-AT to dimerise at low concentrations, the photochemistry of the aminothiazole dimer has yet to be explored. Herein, femtosecond transient electronic absorption spectroscopy (TEAS) and transient vibrational absorption spectroscopy (TVAS) are used to probe the photochemical pathways of both the 2-AT monomer and the dimer in solution. New observations of competing ultrafast dynamical pathways are interpreted with the aid of quantum chemical computational studies of the excited state properties.

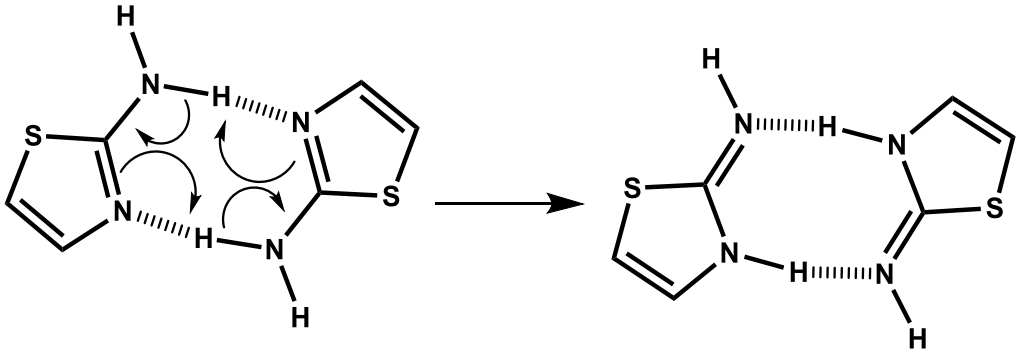

Scheme 6.1- Tautomerisation of $(2\text{-AT})_2$ to $(2\text{-IT})_2$.

## 6.2. Methods

**A. Experiment.** The photoinduced chemistries of the 2-AT monomer and its dimer were studied in several solvents using TEAS and TVAS. Using the setup discussed in Chapter 2, transient spectra for 2-AT monomer were collected following photoexcitation at 255 nm of 5-10 mM samples of 2-AT (Sigma Aldrich, ≤97%) used as received. With a sample pathlength of 300 μm, an absorbance at 255 nm < 0.9 OD was obtained for 5 mM 2-AT in dichloromethane (DCM) and pathlengths for TEAS and TVAS experiments were chosen accordingly to keep the optical density below 0.9 OD. Spectra for the dimer were collected at the same photoexcitation wavelength, but using a 120 mM solution of 2-AT in a Harrick cell with a 12 μm pathlength. Measurements were made for 2-AT solutions in cyclohexane (Fisher Scientific, extra pure, SLR grade), tetrahydrofuran (Fisher Scientific, extra pure, SLR grade, stabilised with 0.025% BHT), acetonitrile (Fisher Scientific, HPLC gradient grade, <99.9%), ethanol ((EtOH) Sigma Aldrich, ACS reagent grade, >99.5%), dichloromethane (Analytical grade, ≥99%) and $H_2O$ (Fisher Scientific , HPLC grade).

**B. Computational details.** All calcuations were performed using the Gaussian 09 computational package.[27] Assignments of transient bands in TEAS were supported with TDDFT vertical excitation energies computed at the B3LYP level using the aug-cc-pvtz basis set, for optimised ground state geometries obtained by MP2 calculations with the aug-cc-pvdz basis set. TVAS spectra were interpreteted using scaled harmonic vibrational frequencies computed at the MP2/aug-cc-pVDZ level of theory. Frequency scaling factors for products of the monomer and dimer photochemistry were determined by scaling the computed 2-AT and $(2\text{-AT})_2$ vibrational frequencies to experimentally measured values.

## 6.3. Results and discussion

The new findings for the photochemistry of the 2-AT monomer, the structure of which is shown in Scheme 6.2, are first presented and discussed. The subsections address the photochemistry in various solvents. The photochemistry of 2-AT dimer $(2\text{-AT})_2$ was studied in DCM, and the results are described in section 6.3.5. The procedures used for band assignments, kinetic fitting, and computational results can be found in the supporting information which will be presented immediately after this chapter.

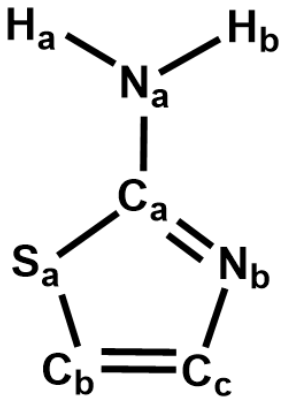


**2-Aminothiazole (2-AT)**

Scheme 6.2- Structure of 2-Aminothiazole (2-AT). Atoms are labelled to assign photochemical pathways.

According to the TDDFT calculations, the 255-nm photoexcitation of 2-AT is expected to induce $S_2 \leftarrow S_0$ and $S_3 \leftarrow S_0$ transitions, with the predicted UV excitation wavelengths of 2-AT shown in Figure 6.1. Natural transition orbital (NTO) analysis of the $S_2$ and $S_3$ states shows both to be optically bright ππ* transitions (see Figure S6.2 of the supporting information). The $S_1$ state is a dark πσ* state, for which the NTOs are shown in Figure 6.1. The $S_1$ states of molecules in solution are typically reached in an ultrafast manner by internal conversion through conical intersections,[28] consistent with the observations reported in sections 6.3.1-6.3.4, and photoproduct channels are therefore assumed to occur selectively from the $S_1$-state PES. In a new collaboration with Dr Basile Curchod (Durham University), high-level calculations are currently being performed to determine the involvement (or otherwise) of higher-lying states in the observed photochemistry. Natural transition orbitals for the $S_1$ state (plotted in Figure 6.1) show πσ* character along the $N_a$-$H_a$, $C_a$-$S_a$ and $C_b$-$S_a$ bonds, suggesting possible N-H fission and various competitive ring-opening pathways which are considered in sections 6.3.1-6.3.5.

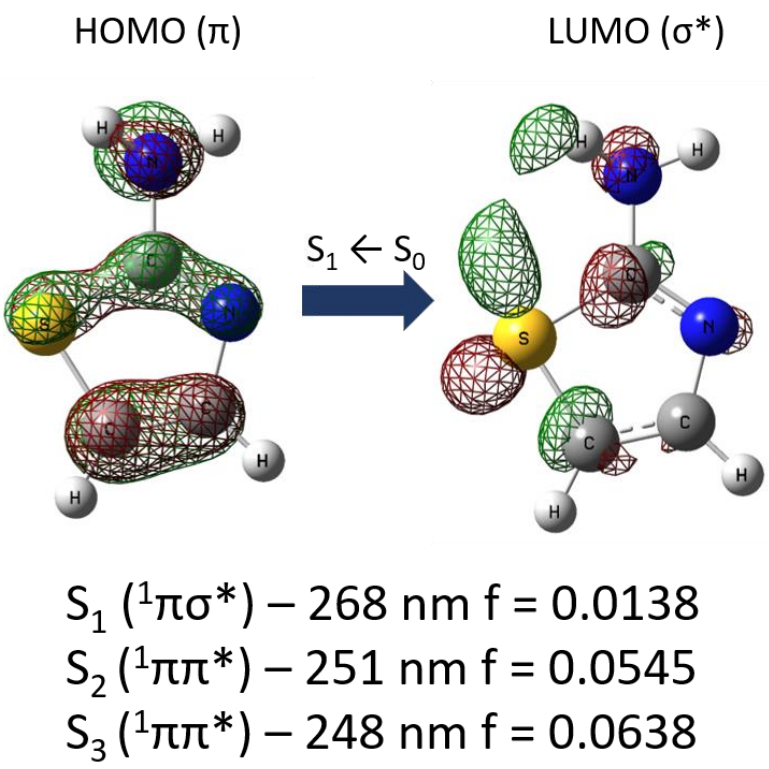


Figure 6.1 – Natural transition orbitals for the $S_1 \leftarrow S_0$ transition of 2-AT and the excitation wavelengths and oscillator strengths (f) for the first three transitions.

### 6.3.1 Photochemistry of the 2-AT monomer in non-polar solvents

The consequences of 255-nm photoexcitation of the 2-AT monomer in apolar solvents are revealed in solutions of cyclohexane from analysis of the TEAS spectra shown in Figure 6.2 and TVAS spectra in Figure 6.3.

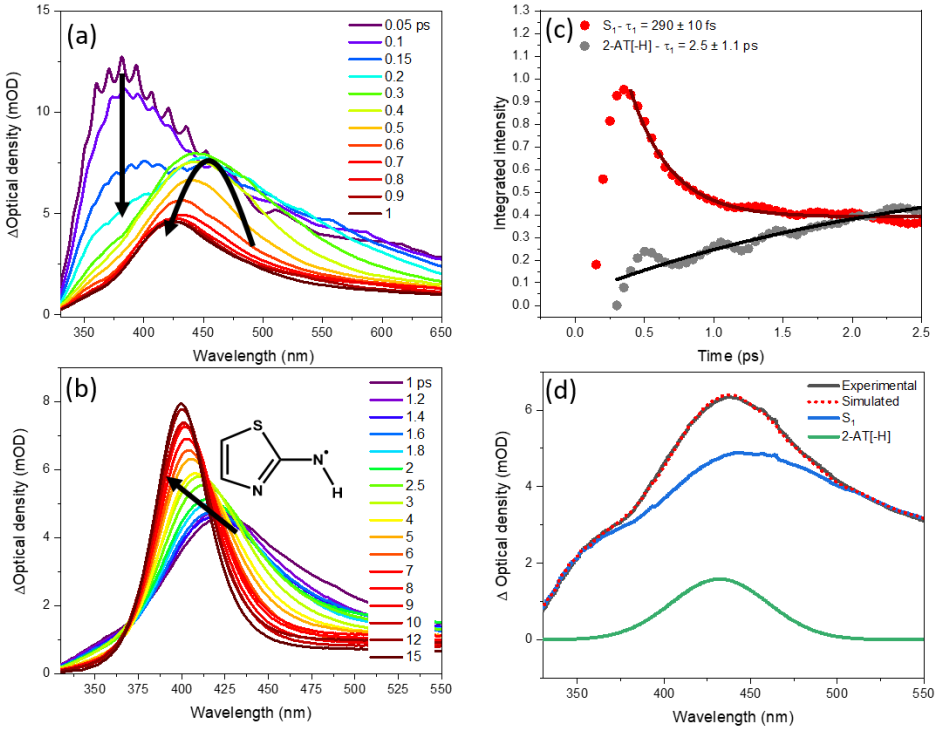


Figure 6.2 – TEAS spectra for the 255-nm photoexcitation of 10 mM 2-AT in cyclohexane for time delays of (a) 0.05 - 1 ps, and (b) 1 - 15 ps. Note the different wavelength scales for panels (a) and (b). Panel (c) shows kinetic fits to time-evolving TEAS integrated band intensities. Dots are experimental data points. The grey points have been multiplied by a factor of 3 to highlight the photoproduct growth. The red experiemntal data points do not fall to zero intensity because of overlapping signal from photoproduct bands which have not been fully seperated in the spectral decomposition. Solid curves are exponential fits, giving the time constants specified in panel (c). Panel (d) shows the decomposition of the experimental data. The spectrum shown is taken at 0.5 ps (black line) and is fit to an early-time basis function (blue) obtained at 0.3 ps, a period when the intensity of the $S_1$ state is at its maximum. The 2-AT[-H] radical band was fit a gaussian function with its centre position and width floated to simulate the effect of vibrational cooling on the spectrum. The red dotted line shows the simulated spectrum.

Immediately after the laser-pulse, a transient absorption band centred at about 375 nm is observed within the instrument response (~150 fs) which is assigned to absorption from higher-lying excited $S_2$ and $S_3$ states of 2-AT directly populated by the 255-nm pulse. The 375 nm band rapidly decays and is replaced by a band centred at 450 nm, which is

attributed to the crossing onto the $S_1$ surface. Although this internal conversion occurs within the estimated instrument response function, systematic changes in the band intensities are resolved in the TEAS spectra on this timescale. The 450 nm band decays with a 290 ± 10 fs time constant and a 415 nm band grows with a 2.5 ± 1.1 ps time constant which is likely because the absorbing species are born with excess vibrational energy, and therefore the growth component of the 415 nm band is rate determined by intermolecular vibrational cooling to solvent molecules. Relaxation of these vibrationally hot molecules causes the 415 nm band to narrow and shift to lower wavelength on a timescale of ~15 ps, until it is centred at 400 nm and remains at a constant intensity for longer than the time duration of the experiment (>1 ns; spectra taken after 15 ps are plotted in Figure S6.3 of the supporting information). The oscillatory structure to the growth component is likely because of a spectral artefact caused by chirp correction. At a 120 mM concentration of 2-AT in DCM, the photoproducts are found to decay over this experimental time duration with a bimolecular rate coefficient of $k \approx 3 \times 10^{10}$ dm$^3$ mol$^{-1}$ s$^{-1}$ which is similar to a diffusion limited rate constant, suggesting reaction with additional 2-AT molecules (see Figure S6.4 of supporting information for kinetic fitting of representative data). However, it is beyond the scope of this work to consider the reactions of the photoproducts any further.

The TVAS spectra in Figure 6.3(a) for photoexcitation of a 5 mM solution of 2-AT in cyclohexane reveal three negative, ground-state bleach (GSB) features at 1525 cm$^{-1}$, 1600 cm$^{-1}$ and 1627 cm$^{-1}$ observed immediately after the laser pulse, and in good agreement with the FTIR spectra of the 2-AT sample shown in Figure 6.4. These spectra show only partial (~50%) recovery of the GSB features at 1525 cm$^{-1}$ and 1627 cm$^{-1}$, but full recovery of the 1600 cm$^{-1}$ GSB. On the basis that a $(2\text{-AT})_2$ feature at 1625 cm$^{-1}$ is found at high concentrations of 2-AT in DCM, with another that strongly overlaps the 1525 cm$^{-1}$ band (see section 6.3.5), the long-lived GSBs at 1525 and 1627 cm$^{-1}$ are suggested to derive from the dimer, which is still present for 5 mM 2-AT in cyclohexane.

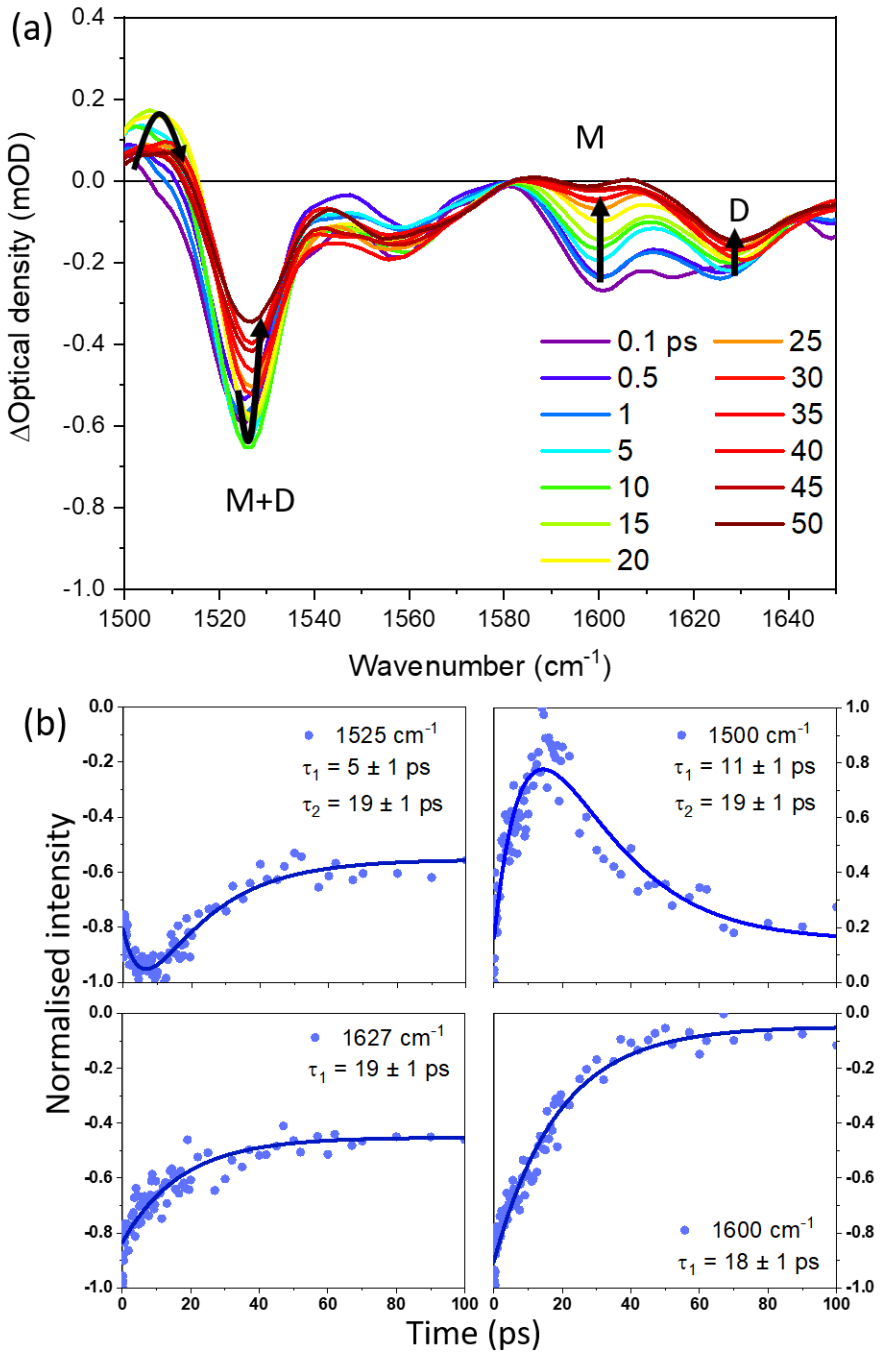


Figure 6.3 – a) TVAS spectra obtained in the wavenumber range from 1500-1650 $cm^{-1}$ for the 255-nm photoexcitation of 5 mM 2-AT in cyclohexane. Monomer and Dimer features are labelled M and D, respectively (see text for a discussion). The arrows show the directions of change of band intensities. b) Kinetic fits for the spectral features labelled by the insets. Dots are experimental data points, and are fitted with exponential or biexponential functions shown as solid curves, giving the specified time constant values.

The apparent full recovery of the 1600 $cm^{-1}$ GSB in cyclohexane solution could be a result of contributions from overlapping photoproducts from the dimer, but a near-full recovery of ground-state 2-AT molecules is consistent with results for the photochemistry of 5 mM 2-AT in DCM (discussed in section 6.3.4) in which dimerization is less favoured. The GSBs in cyclohexane recover with a 18 - 19 ps time constant. The time-evolution of the 1525 $cm^{-1}$ band intensity has also been fit to a 5 ± 1 time constant. This intensity initially becomes more negative, suggesting either the decay of overlapping intermediate bands or reaction of ground state 2-AT. Because this effect is more clearly observed in DCM solutions, this observation is further discussed in section 6.3.4. A positive going band at ~1500 $cm^{-1}$ forms and decays with 11 ± 1 and 19 ± 1 ps time constants respectively. Because the band is formed vibrationally hot (as is shown by its shift to higher wavenumber because of vibrational cooling), and decays to intensity levels close to the baseline, the 1500 $cm^{-1}$ band is assigned to the recovery of vibrationally excited 2-AT in its ground electronic state. Although a dimer contribution cannot be discounted, this interpretation is consistent with DCM solutions where the dimer is less favoured (see section 6.3.4).

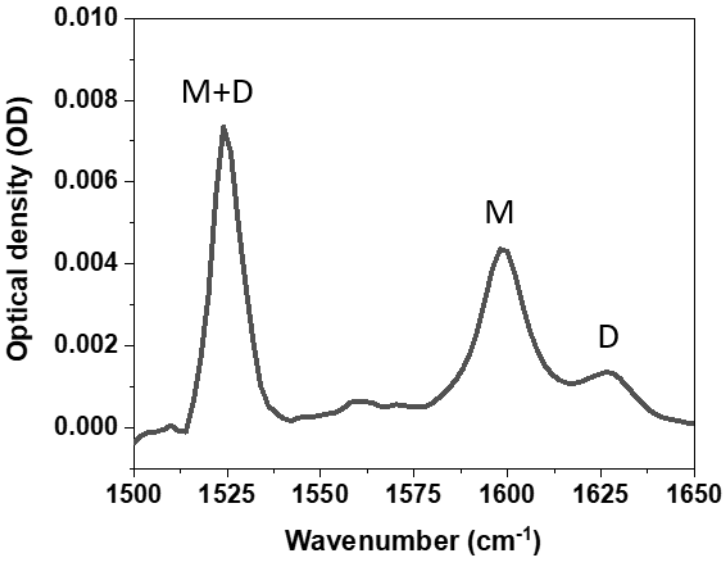


Figure 6.4 – FTIR spectra for 5 mM 2-AT in cyclohexane using a 100 µm pathlength sample cell. Monomer (M) and Dimer (D) peaks are labelled.

Although the presence of $(2\text{-AT})_2$ has been identified in low concentrations of 2-AT in cyclohexane, the contribution of the dimer photochemistry to the formation of photoproducts in TEAS (Figure 6.2) is expected to be insignificant. The basis for this argument is that no significant changes are observed to the photoproduct formation in TEAS spectra obtained at high concentrations of 2-AT in DCM when significant amounts of dimer are present (TEAS spectra are shown in Figure S6.4 of the supporting information).

### 6.3.2 2-AT monomer photochemistry in polar solvents

The effect of photoexciting 2-AT in polar solvents is revealed for solutions in ACN and EtOH. TEAS spectra for 2-AT in ACN are shown in Figure 6.5, with the corresponding spectra for 2-AT in EtOH presented in Figure S6.6 in the supporting information.

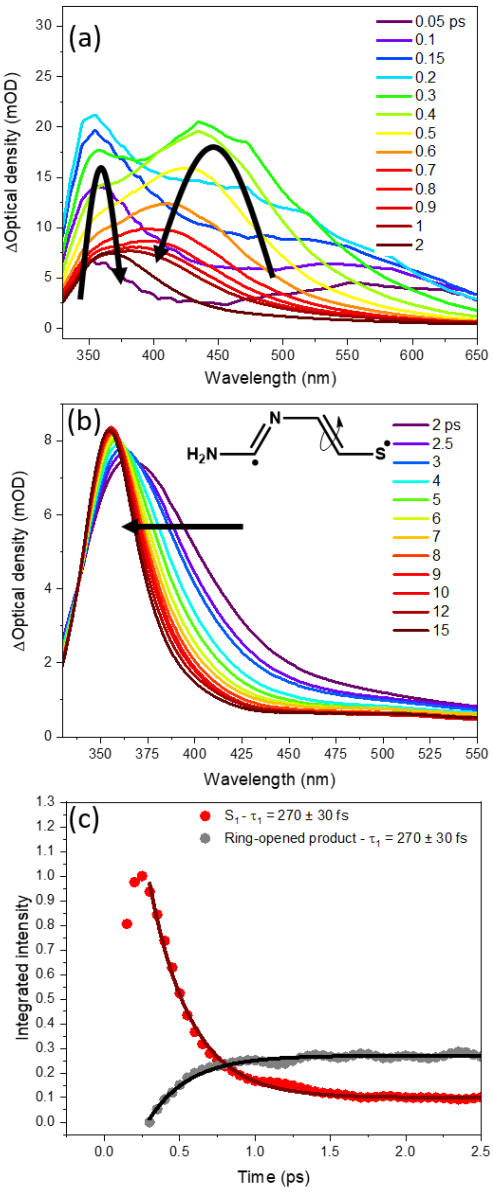


Figure 6.5 – TEAS spectra for the 255-nm photoexcitation of 10 mM 2-AT in ACN for time delays of: (a) 0.05 - 2 ps; (b) 2 - 15 ps. Note the different wavelength scales for panels (a) and (b). Kinetic fits to the first 2.5 ps of dynamics are shown in (c), with dots representing experimental integrated band intensities. The grey data points have been multiplied by a factor of 3. Solid curves are single exponential fits to data points in the range 0.3 – 2.5 ps, giving the time constants specified in panel (c).

Similar to what was observed for 2-AT studies in cyclohexane, a higher-lying excited state of 2-AT is populated within the IRF (~150 fs), and this population rapidly crosses to the $S_1$ surface within the estimated IRF (~150 fs). The $S_1$ state decays to form photoproducts with a 270 ± 30

fs time constant. These photodynamics form vibrationally hot products characterized by a broad absorption band centred at ~375 nm, with band narrowing and shifting to a centre at ~350 nm indicative of vibrationally cooling over ~15 ps. The final band position of the photoproduct is considerably shifted to shorter wavelength compared to 2-AT in cyclohexane solution (see section 6.3.1 and Figure 6.2(b)). Experiments in ethanol solutions give product bands consistent with those for ACN solutions (EtOH spectra are shown in Figure S6.6 within the supporting information).

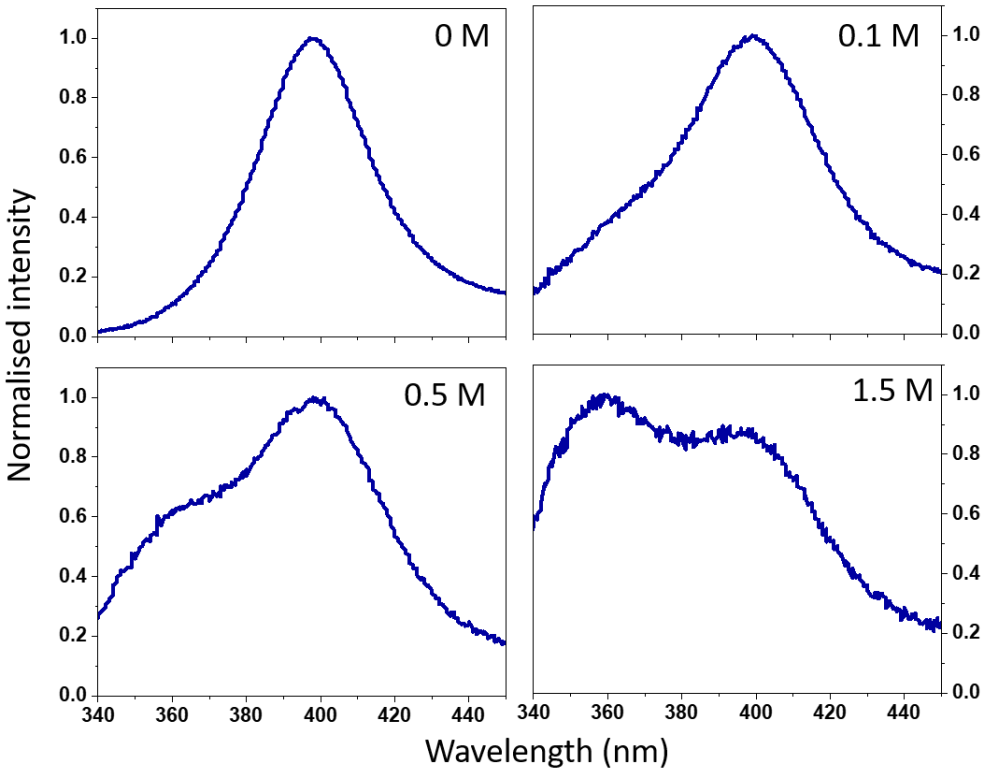


Figure 6.6 – TEAS spectra in the wavelength range 340 – 450 nm for the 255 nm photoexcitation of 10 mM 2-AT in different ratio cyclohexane:ethanol mixtures. All spectra were recorded at a time delay of 100 ps, and have been normalised to a maximum intensity of 1. The concentrations of EtOH are shown in the panels. Comparison of the spectra reveals the formation of a band at ~350 nm which becomes more evident with growing EtOH fraction.

Figure 6.6 shows selected TEAS spectra at 100 ps time delay following the photoexcitation of 2-AT in cyclohexane:ethanol mixtures of different ratios. The spectra reveal the formation of a second band at ~350 nm alongside the ~400 nm band seen in Figure 6.2b as the EtOH fraction increases. The 400-nm band is assigned to the 2-AT[-H] radical in section 6.3.1.

Assuming homogeneous solvent environments in the cyclohexane / ethanol mixtures, the appearance of two features in the presence of a polar co-solvent suggests two different photoproduct species, not simply a shift in band position in different solvents. With increasing solvent polarity, the H-atom ejection pathway appears to become disfavoured because the 400 nm band which is characteristic of the 2-AT[-H] radical is not observed in ACN and EtOH. Instead, competition from a pathway which results in a band at ~350 nm is preferred in polar solvents. Given that the NBO analysis (Figure 6.1) shows considerable $\pi\sigma^*$ character to the $C_a$-$S_a$ and $C_b$-$S_a$ bond, the 350 nm band is likely to be a signature of a ring-opened product. The excess energy liberated by ring-opening might enable twisting around the $C_b$=$C_c$ double bond, forming different possible ring-opened products in their ground electronic state. One candidate photoproduct is illustrated in Figure 6.5b. Assignment of the 350 nm band to this ring-opened product is supported by TDDFT calculation of a strong electronic absorption band at 346 nm. However, a more complete consideration of the possible photoproducts remains to be completed.

The absence of the 400 nm band for 2-AT solutions in ACN (Figure 6.5) could be the result of a larger barrier height to access the region of the adiabatic $S_1$ state with $\pi\sigma^*_{N\text{-}H}$ character responsible for the ejection of the H-atom. This suggestion is supported by the computed cuts through PESs for the $S_1$ state of 2-AT in ACN and cyclohexane shown in Figure 6.7. The PESs predict ~19 kJ mol$^{-1}$ and ~32 kJ mol$^{-1}$ barrier heights for the ejection of the H-atom when using a PCM treatment of cyclohexane and ACN, respectively. However, a more detailed theoretical treatment is currently underway in a collaboration with Dr Basile Curchod (Durham University). Unfortunately, further characterization of intermediates and photoproducts by TVAS experiments, probing the $NH_2$ scissoring and ring-mode stretching region (~1500 cm$^{-1}$) could not be performed for ACN solutions because of significant solvent absorption.

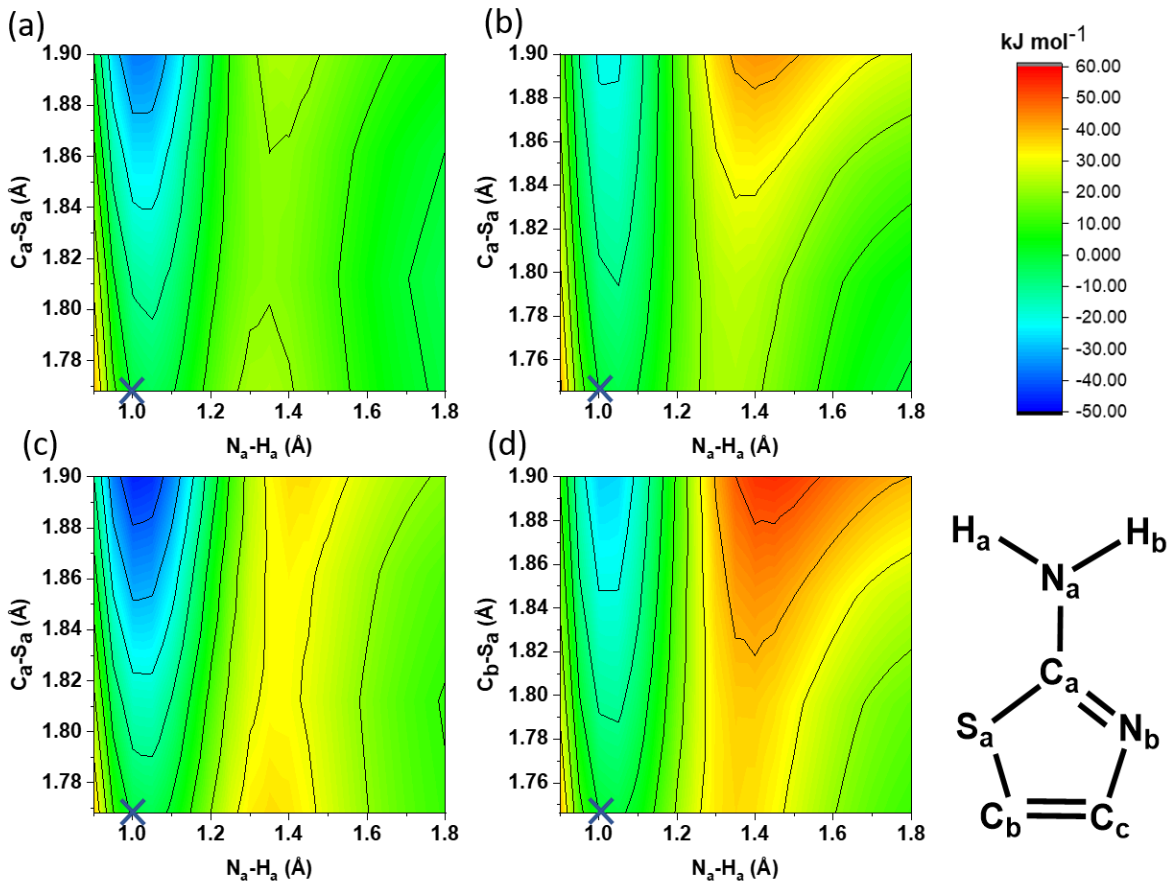


Figure 6.7 – Computed two-dimensional potential energy surfaces for the $S_1$ state of 2-AT constrained to the $C_s$ point group (with structure and coordinate labels shown bottom right) using the B3LYP level of theory with the aug-cc-pvdz basis set, and mapped along selected coordinates, as follows: (a) $C_a$-$S_a$ and $N_a$-$H_a$ in cyclohexane; (b) $C_b$-$S_a$ and $N_a$-$H_a$ in cyclohexane; (c) $C_a$-$S_a$ and $N_a$-$H_a$ in ACN; (d) $C_b$-$S_a$ and $N_a$-$H_a$ in ACN. All other coordinates were fixed at the optimised MP2/aug-cc-pVDZ ground state geometry in the $C_s$ point group. The potential energy surfaces were mapped using $C_s$ symmetry because optimisation of the $NH_2$ group (with all other atoms frozen) in the $S_1$-state resulted in a planar geometry. For this reason, it was assumed that H atoms would rapidly move in the plane of the ring after photoexcitation. Solvents were simulated using the polarizable continuum model. All energies are specified relative to the vertical excitation geometry (shown as a cross), and the colour scale is shown on the top right. Constraining the geometry to $C_s$ symmetry is not expected to alter the ordering of excited states because vertical excitations energies were similar to those obtained from calculations using the $C_1$ point group.

The analysis of possible photochemical pathways competing with N-H scission concentrates on the $C_a$-$S_a$ and $C_b$-$S_a$ ring-opening pathways because the TDDFT calculations predict these to be barrierless on the $S_1$ surface for both ACN and cyclohexane solutions. In polar solvents such as ACN and EtOH, photoexcited molecules may not have sufficient energy localised in the N-H coordinate to exceed the higher barrier for H-atom ejection than is computed for cyclohexane solutions, and the ring-opening pathways therefore dominate the photoproduct formation. The experiments and calculations are unable to predicted which ring-opening pathway(s) are preferred, but further theoretical work exploring the excited-state dynamics of photoexcited 2-AT is underway and will give deeper insights into the photochemical pathways.

### 6.3.4 2-AT in solvents of intermediate polarity

In solutions of intermediate polarity such as DCM and THF, two photoproduct bands are observed with centres at ~365 nm and ~400 nm in DCM, as shown in Figure 6.8. These observations suggest that both the N-H scission and ring-opening photoproduct channels are active in these solvents. The TEAS spectra in THF are reported in Figure S6.7 of the supporting information. TVAS spectra for the photoexcitation of 2-AT in DCM are shown in Figure 6.9 and reveal the formation of three negative-going features within the laser pulse duration. These bands are assigned to the GSB of the 2-AT monomer (FTIR spectra in Figure 6.13 confirm these are 2-AT ground-state bands). There are no significant spectroscopic signatures for the dimer between 0.1 and 15 mM concentrations of 2-AT in DCM.

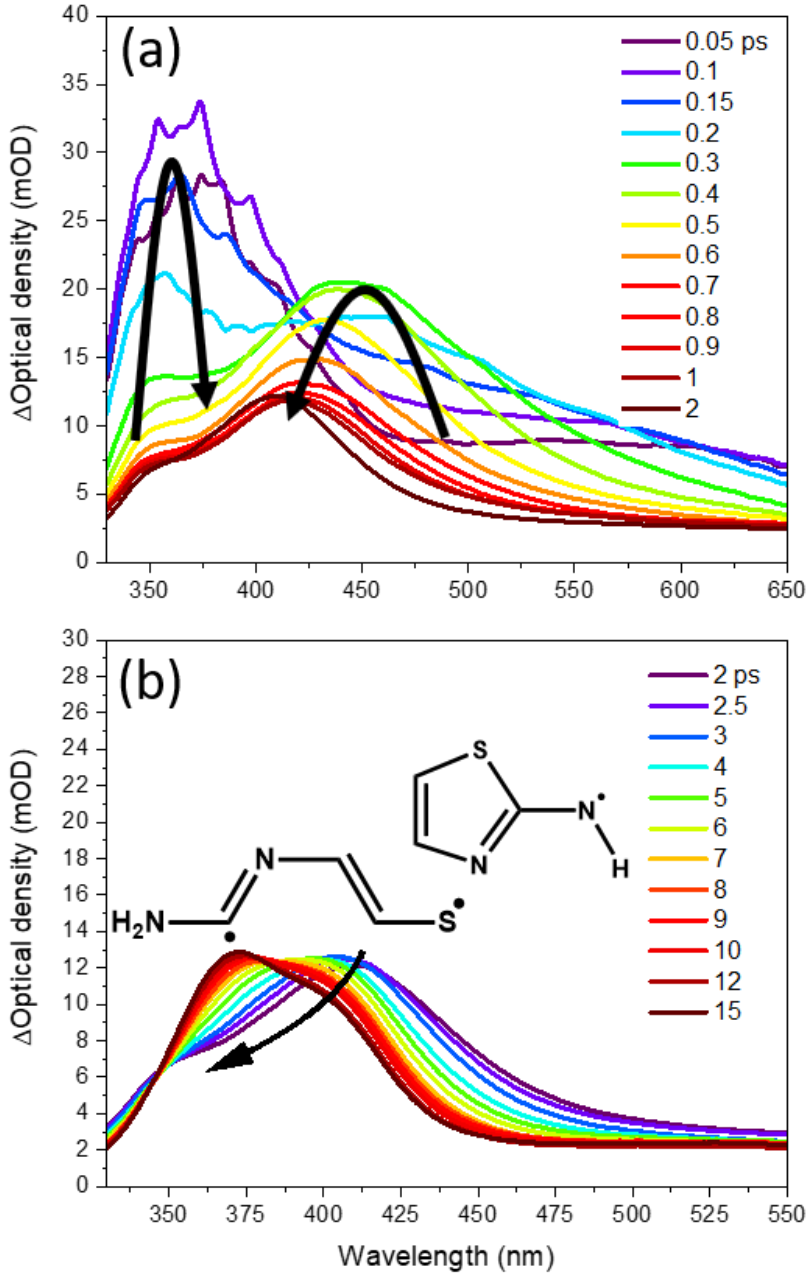


Figure 6.8 – TEAS spectra for the 255 nm photoexcitation of 10mM 2-AT in DCM for periods a) 0.05-2 ps. b) 2-15 ps. Note the different wavelength scales for the two panels.

The TVAS spectra in Figure 6.9 identify that the GSB features of 2-AT recover by ~90%, suggesting the majority of photoexcited 2-AT molecules return to the ground state parent structure. The remaining molecules form the photoproducts discussed previously. The lower GSB recovery fraction in DCM compared to cyclohexane solution suggests that the competing ring-opening channel has a greater propensity to form photoproducts that cannot return to

the parent structure. However, the TVAS spectra obtained in cyclohexane solutions have overlapping contributions from dimer photochemistry, as was discussed earlier, and the apparent differences in ground-state recovery may instead derive from the dimer photodynamics.

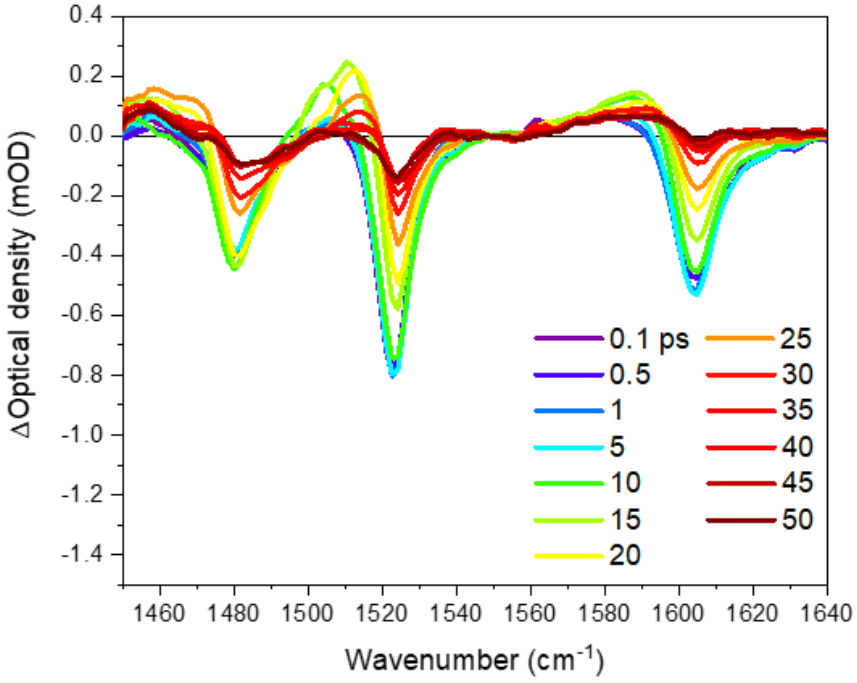


Figure 6.9 - TVAS spectra in the wavenumber range 1650-1640 $cm^{-1}$ for the 255-nm photoexcitation of 5 mM 2-AT in DCM.

Simply integrating the GSB intensities in the spectra plotted in Figure 6.9 as a function of time results in a series of growths and decays (see Figure S6.8 in the supporting information) which are considered to be a result of overlapping intermediate and photoproduct bands. To improve on this analysis, a singular value decomposition was performed to disentangle the different spectral contributions. This section reports the decomposition procedure used for the interpretation of the TVAS spectra of 5 mM 2-AT in DCM.

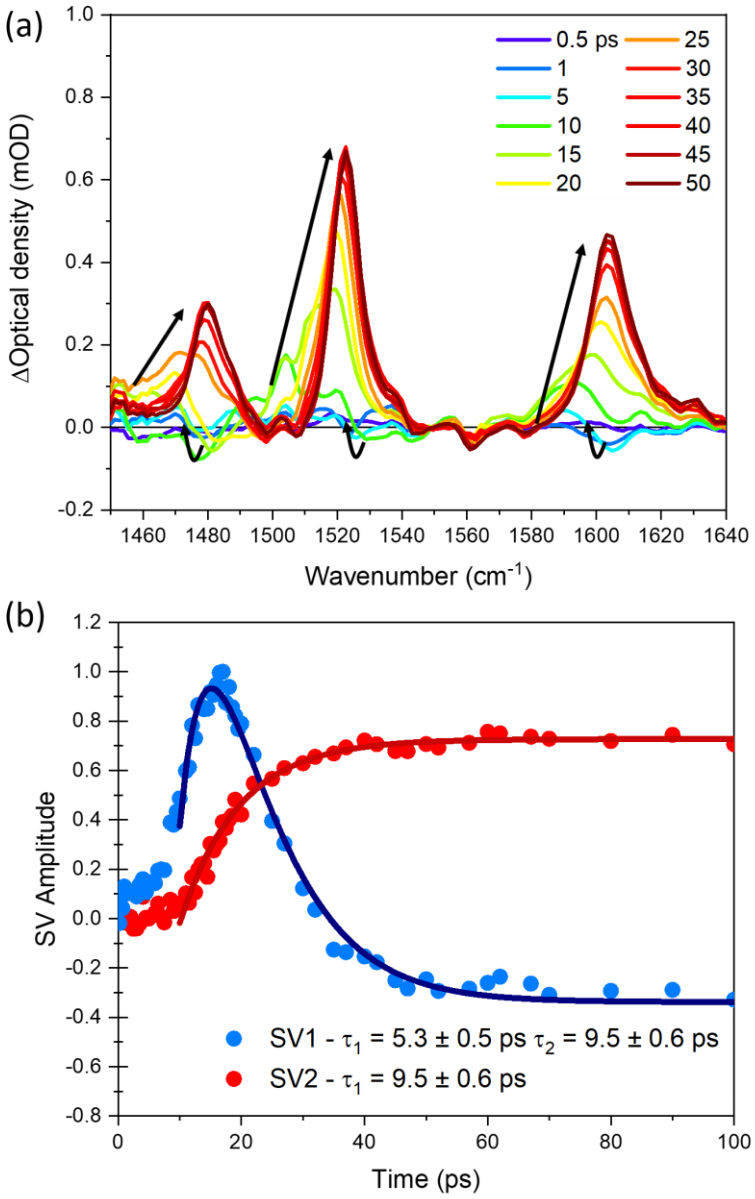


Figure 6.10 – (a) TVAS spectra for the 255-nm photoexcitation of 5 mM 2-AT in DCM. The spectrum taken at 0.1 ps delay has been subtracted from all other time points to highlight the spectral development after the initial excitation. (b) Kinetic fits of the spectral intensities (shown as dots) obtained using singular value decomposition of the spectra in (a). The two SVD components, SV1 and SV2 are shown in blue and red respectively. The time evolution of SV1 has been fit using a biexponential function (shown as solid lines), for which $\tau_1$ was allowed to vary and the $\tau_2$ value was globally fitted using the same exponential function as was applied to SV2.

The singular value decomposition was performed using the KOALA software package.[29] Figure 6.10(a) shows the TVAS spectra obtained after 255-nm photoexcitation of 5 mM 2-AT in DCM,

with subtraction of the 0.1 ps spectrum from all other spectra to emphasize photoproduct development. SVD decomposition of the TVAS spectra in Figure 6.10(a) with two singular values results in the kinetic traces shown in Figure 6.10(b) and simulates 98% of the spectral intensity. The singular value functions are shown in Figure 6.11 as blue (SV1) and red (SV2) traces, and the dotted line compares the sum of these two spectra to an experimental measurement shown as a solid black line.

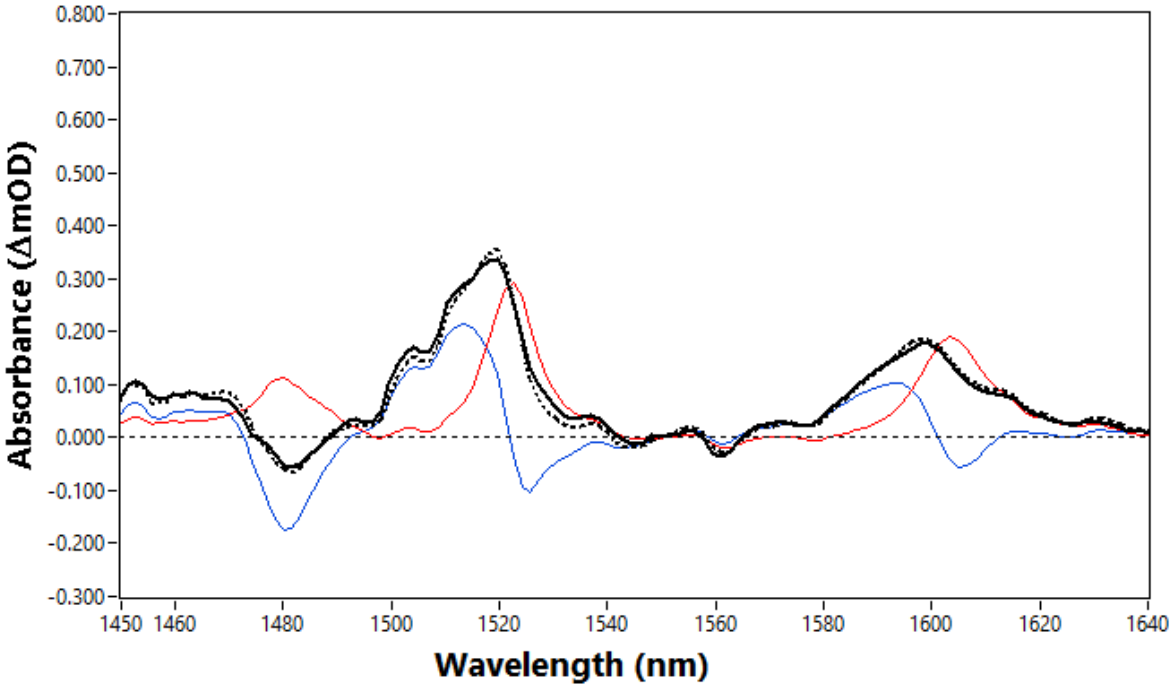


Figure 6.11 – A representative spectrum showing the singular value decomposition in KOALA.[29] The experimental spectrum was taken at a delay-time of 15 ps after the 255-nm photoexcitation of 5 mM 2-AT in DCM. The SV1 basis function is shown in blue and is assigned to ground state 2-AT (corresponding to negative-going features) and vibrationally hot $S_0$ 2-AT molecules (positive-going features). The SV2 basis function is shown in red and is assigned to vibrational ground state $S_0$ 2-AT.

The SV 1 spectral component reveals the decay of spectral intensity for bands centred at 1480, 1525, and 1605 $cm^{-1}$ and its time-dependence fits to a 5.3 ± 0.5 ps time constant. The initial 10 ps of the experimental data points have not been fit because of a gradual rise which is likely to be the result of sequential kinetics or vibrational cooling. Assignment of the 1480, 1525, and 1605 $cm^{-1}$ bands to the excited states of 2-AT is discounted because the TEAS spectra in Figure 6.2 show excited states decay with sub-ps time constants. One possible

explanation for the decay of spectral intensity at 1480, 1525, and 1605 $cm^{-1}$ after the initial photoexcitation is because of the decay of photoproduct bands. On the basis that a similarly observed decay of spectral intensity is observed in cyclohexane (Figure 6.3), where no contribution is expected from ring-opening pathways, a possible assignment is to the 2-AT[-H] radical. However, this is unlikely because computed vibrational frequencies of the 2-AT[-H] radical do not predict three vibrational frequencies within this region (computed vibrational frequencies shown in Table S6.3). Another possible explanation is that the ejected H-atoms are captured by ground state 2-AT molecules, causing a decay in intensity over the region of the GSBs of 2-AT. The time dependence of the SV1 component shows the decay of ground state 2-AT to be accompanied by the growth of bands at 1460 $cm^{-1}$, 1515 $cm^{-1}$, and 1595 $cm^{-1}$. Because the spectral contribution from SV1 reduces with the same time constant as the development of the contribution from SV2, and the band positions in SV2 are in close correspondence with features in the FTIR spectrum of ground state 2-AT, the 1460 $cm^{-1}$, 1515 $cm^{-1}$, and 1595 $cm^{-1}$ bands are assigned to vibrationally hot $S_0$ 2-AT formed by geminate recombination of the 2-AT[-H] radical with its partner H atom, or by H-atom abstraction from a neighbouring solvent molecules.

### 6.3.4 2-AT monomer in water

The 255-nm photoexcitation of the 2-AT monomer in aqueous solution results in the TEAS spectra shown in Figure 6.12.

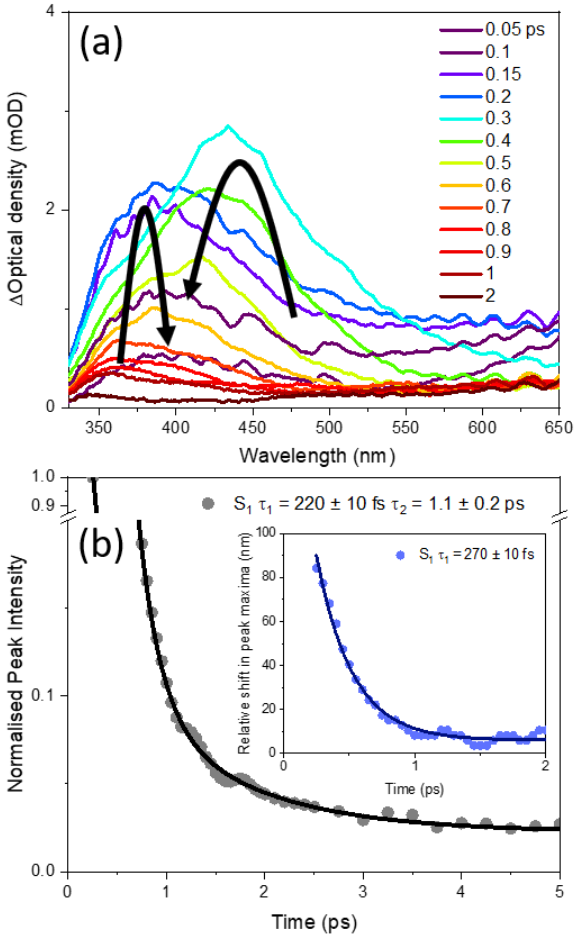


Figure 6.12 – (a) TEAS spectra for the 255-nm photoexcitation of 10 mM 2-AT in water ($H_2O$) for the time window 0.05 - 2 ps. A kinetic fit to the $S_1$-band intensity decay is shown in (b). In this panel, dots are experiemntal data points, normalised to a range from 0 – 1, and plotted for time delays from 0.25 - 5 ps. The oscillations in the experimental datapoints between 1 - 2 ps are a result of allowing the Gaussian fit function centre and width to vary in the fits to data with spectral intensities close to the baseline. The solid curve is a biexponential fit. The inset panel (c) shows a kinetic fit to the shift in maximum wavelength of the transient absorption band.

Absorption from a higher-lying excited state of 2-AT is observed within the IRF (~150 fs), but rapidly decays as population crosses to the $S_1$ surface, giving rise to a band centred at 430 nm that reaches a maximum intensity within ~250 fs of the laser pulse. The 430 nm band then shifts ~80 nm to lower wavelength with a 270 ± 10 fs time constant which is assigned to structural rearrangement in the $S_1$ state, and perhaps to solvation dynamics. The 2-AT $S_1$ state population in $H_2O$ decays with biexponential time-constants of 220 ± 10 fs and 1.1 ± 0.2 ps,

with the slower time constant contributing only ~5% of the decay. The faster time constant is thought to represent relaxation through ring-puckering and ring-opening pathways, but unlike in the other solvents studied (see above), further photoproduct formation is discounted on the basis that no photoproduct bands were observed in the TEAS spectra. Instead, the $S_1$ population reverts to 2-AT in its ground electronic state. The slower component of the relaxation is tentatively attributed to a H transfer mechanism along $H_2O$ wires. This proposal is supported by the quantum mechanical molecular dynamics simulations of Szabla *et al.* for the photochemistry of hydrated 2-Aminooxazole, which revealed the $S_1$ excited-state lifetime of 2-aminooxazole-$H_2O$ clusters to be ~125 fs from ring-puckering and ring-opening pathways, with a longer but minor ~500 fs time constant from a EDPT,[20] in reasonable agreement with the observed excited-state lifetimes for 2-AT. Similar theoretical insights were found for various 2-amino-heterocycles,[19, 21] suggesting a common relaxation mechanism. There is no evidence for the diffusive escape of the H-atom, suggesting that if any N-H bond scission is occurring, there is a preference for geminate recombination to recover the parent ground state 2-AT.

### 6.3.5 2-AT dimer photodynamics in DCM

At higher concentrations of 2-AT in DCM solutions, the propensity to dimerise increases. The FTIR spectra in Figures 6.13(a) and 6.13(b) show that at higher concentrations of 2-AT, additional bands appear at 1490 $cm^{-1}$ and 1625 $cm^{-1}$ which are assigned to $(2\text{-AT})_2$. These band positions are in good agreement with computed frequencies at 1493 $cm^{-1}$ and 1635 $cm^{-1}$, and a further dimer band is predicted at 1538 $cm^{-1}$ which likely overlaps the monomer GSB. Assignment to the 2-IT tautomer is discounted because predicted vibrational frequencies are far outside the level of agreement expected for the computational methods used (see table S6.3 in supporting information). Herein, the frequency scaling factors for products of dimer photochemistry are determined by scaling the computed $(2\text{-AT})_2$ vibrational frequencies to experimentally measured values. Figure 6.13(c) shows a plot of intensity of the 1605 $cm^{-1}$ band (assigned to monomer) as a function of 2-AT concentration. A linear fit was obtained for a 2-AT concentration range of 0.1 – 15 mM and used to determine an extinction coefficient for the monomer of $\varepsilon = (3.7 \pm 0.2) \times 10^{-1}$ $dm^3$ $mol^{-1}$ $cm^{-1}$. At a nominally 120 mM solution of 2-AT in DCM, the dimer exists at a concentration of ~45 mM.

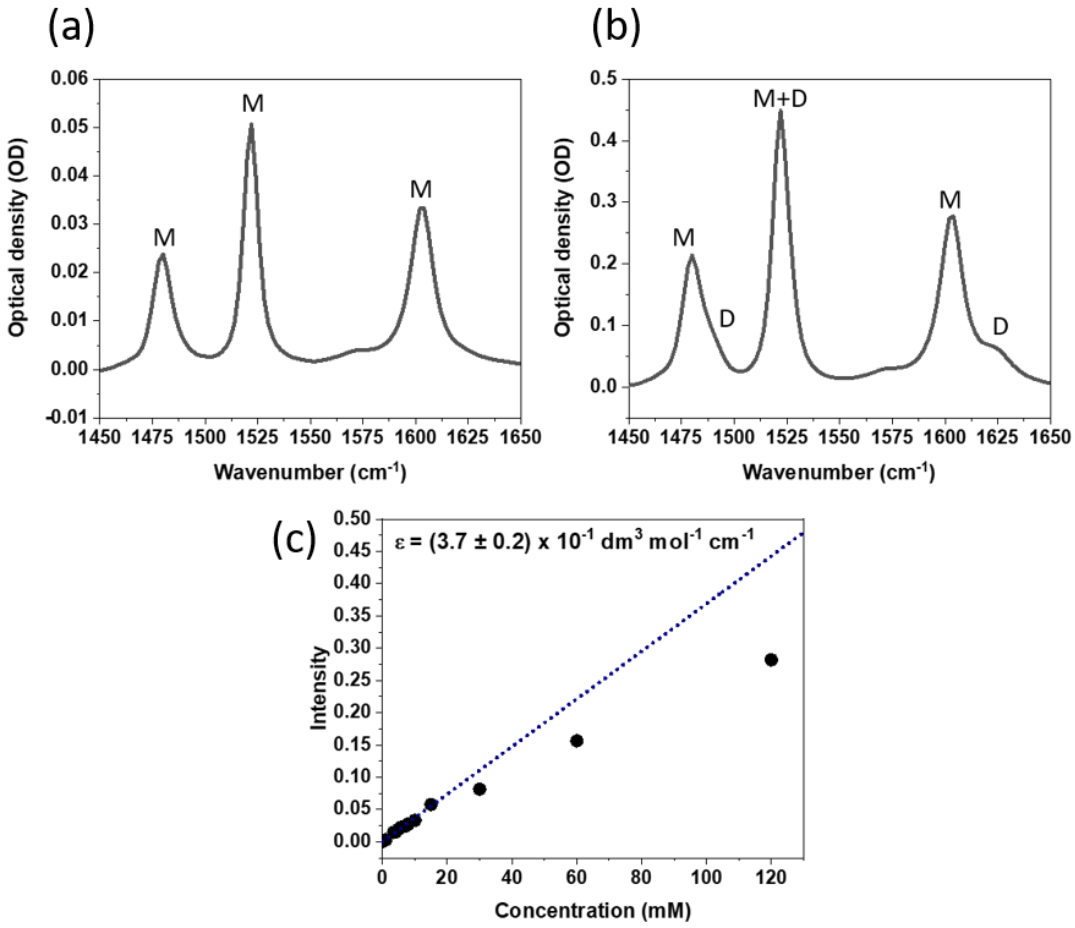


Figure 6.13 – FTIR spectra for 100 μm pathlength samples of: (a) 5 mM 2-AT in DCM; (b) 120 mM 2-AT in DCM. Monomer (M) and Dimer (D) peaks are labelled. A Beer-Lambert plot is shown in (c). A linear fit was obtained up to 15 mM 2-AT and used to determine an extinction coefficient for the monomer.

To characterize the role of dimers, the photochemistry of 2-AT was investigated for the 255-nm photoexcitation of a 120 mM solution of 2-AT in DCM. The resulting TVAS spectra are shown in Figure 6.14(a), with kinetic fits to the photoproduct band intensities in 6.14(b). The negative-going features are assigned to monomer and dimer ground state bleaches (GSBs). Here the focus will be on the photochemistry induced from the dimer, while a detailed discussion of the monomer photochemistry can be found in sections 6.3.1-6.3.4. Particular attention is paid to the 1625 $cm^{-1}$ GSB because this overlaps least with the monomer GSBs. The dimer shows only partial recovery (~15%) of ground state $(2\text{-AT})_2$, suggesting near-complete photo-destruction by either photoproduct formation or dimer dissociation. Positive-going bands centred at 1478 $cm^{-1}$, 1515 $cm^{-1}$ and 1601 $cm^{-1}$ form with a 6.6 ± 0.5 ps

time constant derived from the kinetic fitting of the 1601 $cm^{-1}$ band in Figure 6.14(b), suggestive of photoproducts. The photoproduct forming from the photoexcitation of the monomer is discounted on the basis that at 5 mM concentrations of 2-AT, no evidence was found for the formation of long-lived photoproduct bands in this spectral window. Moreover, the monomer GSB shows nearly complete recovery (~80%). It is possible that minor photoproducts arise from the monomer and dimerise or react with additional 2-AT molecules to form the photoproduct bands seen in Figure 6.14(a). However, this proposition is discounted because of the short timescales for growth of the 1478 $cm^{-1}$, 1515 $cm^{-1}$ and 1601 $cm^{-1}$ bands. TEAS spectra taken for 120 mM 2-AT in DCM (reported in Figure S6.4 in the supporting information) show photoproducts to decay with ~400 ps time constants (see Figure S6.5 of supporting information) from reaction with additional 2-AT molecules, which does not agree with the kinetics observed of the three photoproduct bands in TVAS experiments.

Attribution of the three bands observed by TVAS to photoproducts from the photoexcitation of the dimer is therefore preferred. Here several plausible assignments are proposed. A first candidate is assignment of photoproduct bands to an H-atom ejected radical within a dimer pair (2-AT[-H])(2-AT). When dimerised with a second 2-AT molecule, this radical is computed to have predicted absorption bands at 1474 $cm^{-1}$, 1507 $cm^{-1}$ and 1615 $cm^{-1}$, in reasonable agreement with the observed photoproduct bands. Another possible set of assignments is to 2-IT and $(2\text{-IT})_2$, formed by tautomerisation, as illustrated in scheme 6.1. However, frequency calculations suggest a shift to higher wavenumber relative to 2-AT and $(2\text{-AT})_2$ bands (frequencies are shown in Table S6.3 of the supporting information). Instead, the initially formed $(2\text{-IT})_2$ may undergo a backward tautomerisation of one of the 2-IT units, forming a dimer comprised of 2-IT and 2-AT molecules (2-IT-2-AT). This assignment is supported by computed frequencies at 1485 $cm^{-1}$, 1499 $cm^{-1}$ and 1607 $cm^{-1}$ which are in reasonable agreement with the observed bands.

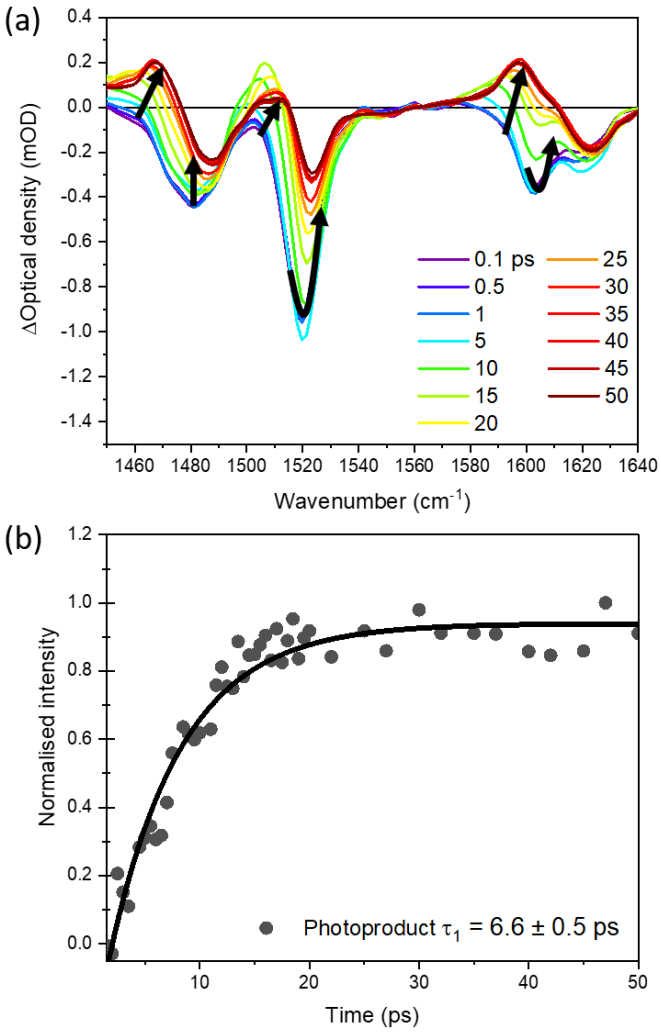


Figure 6.14 – (a) TVAS spectra obtained in the 1450-1640 $cm^{-1}$ region for the 255 nm photoexcitation of 120 mM 2-AT in DCM. (b) A kinetic fit of the intensities of the photoproduct band centred at 1601 $cm^{-1}$. Dots are experimental data points, and are fitted with an exponential function shown as a solid curve.

### 6.5 Conclusions

Transient absorption spectroscopy experiments for solutions of 2-AT in several solvents of different polarity reveal solvent-specific photoproduct pathways. The transient spectra provide evidence for an N-H fission pathway to form radicals by ultrafast H-atom ejection in the case of 2-AT dissolved in non-polar solvents such as cyclohexane. The 2-AT[-H] radical shows a characteristic absorption band centred at ~400 nm. The kinetic growth of the 400-nm radical band intensity reveals periodic oscillations which are assigned to a vibrational coherence in the nascent radical product involving the S-C-N(H) bending coordinate activated

by recoil from the departing H-atom. In polar solvents such as acetonitrile and ethanol, evidence is presented that the N-H fission pathway is inhibited and instead the photochemistry is dominated by heterocyclic ring-opening. TEAS measurements reveal the formation of a ring-opened product via a band centred at ~350 nm. In solvents of intermediate polarity, such as DCM and THF, both N-H fission and ring-opening pathways are active and competitive. Initial calculations mapping portions of the $S_1$ PES suggest that the height of the barrier to N-H bond fission is highly sensitive to the polarity of the solvent, and controls the branching between N-H scission and heterocyclic ring opening dynamics.

To investigate the photochemistry of the 2-AT dimer, transient vibrational absorption spectroscopy experiments were performed at higher solute concentrations. These measurements revealed near-complete photoconversion of the photoexcited dimer and the growth of a photoproduct band. Possible assignments for the photoproduct are suggested, but further theoretical work is needed to provide a definitive interpretation.

To complete this project, TVAS experiments in the region of ~1500 $cm^{-1}$ will be conducted using deuterated ACN as a solvent to eliminate interfering solvent bands. These studies will provide further insights into the photoproduct formation. An attempt will also be made to monitor any ring-opened products using a mid-IR probe window around 2000 $cm^{-1}$. The observed ultrafast dynamics have stimulated the interest of theoretical chemists who are now conducting a more detailed theoretical simulation of the observed photochemistry than the preliminary calculations reported here. The outcomes of these more advanced simulations will undoubtedly provide further insights about the competitive dynamical pathways accessible in the $S_1$ state of 2-AT, and their dependence on solvent environment.

## References


1. Kitadai, N.; Maruyama, S. Origins of building blocks of life: A review. *Geosci. Fron.* **2018,** *9*, 1117-1153.
2. Camprubí, E.; de Leeuw, J. W.; House, C. H.; Raulin, F.; Russell, M. J.; Spang, A.; Tirumalai, M. R.; Westall, F. The Emergence of Life. *Space Sci. Rev.* **2019,** *215*, 56.
3. Sasselov, D. D.; Grotzinger, J. P.; Sutherland, J. D. The origin of life as a planetary phenomenon. *Sci. Adv.* **2020,** *6*, eaax3419.
4. Islam, S.; Bučar, D.-K.; Powner, M. W. Prebiotic selection and assembly of proteinogenic amino acids and natural nucleotides from complex mixtures. *Nat. Chem.* **2017,** *9*, 584-589.
5. Powner, M. W.; Gerland, B.; Sutherland, J. D. Synthesis of activated pyrimidine ribonucleotides in prebiotically plausible conditions. *Nature* **2009,** *459*, 239-242.
6. Sagan, C.; Khare, B. N. Long-wavelength ultraviolet photoproduction of amino acids on the primitive Earth. *Science* **1971,** *173*, 417-20.
7. Pestunova, O.; Simonov, A.; Snytnikov, V.; Stoyanovsky, V.; Parmon, V. Putative mechanism of the sugar formation on prebiotic Earth initiated by UV-radiation. *Adv. Space Res.* **2005,** *36*, 214-219.
8. Ashfold, M. N. R.; Murdock, D.; Oliver, T. A. A. Molecular Photofragmentation Dynamics in the Gas and Condensed Phases. *Annu. Rev. Phys. Chem.* **2017,** *68*, 63-82.
9. Gavrilov, N.; Salzmann, S.; Marian, C. M. Deactivation via ring opening: A quantum chemical study of the excited states of furan and comparison to thiophene. *Chem. Phys.* **2008,** *349*, 269-277.
10. Spesyvtsev, R.; Horio, T.; Suzuki, Y. I.; Suzuki, T. Excited-state dynamics of furan studied by sub-20-fs time-resolved photoelectron imaging using 159-nm pulses. *J. Chem. Phys.* **2015,** *143*, 014302.
11. Miyazaki, J.; Takiyama, H.; Nakata, M. Isocyano compounds newly recognized in photochemical reaction of thiazole: matrix-isolation FT-IR and theoretical studies. *RSC Adv.* **2017,** *7*, 4960-4974.
12. Schalk, O.; Galiana, J.; Geng, T.; Larsson, T. L.; Thomas, R. D.; Fdez. Galván, I.; Hansson, T.; Vacher, M. Competition between ring-puckering and ring-opening excited state reactions exemplified on 5H-furan-2-one and derivatives. *J. Chem. Phys.* **2020,** *152*, 064301.
13. Sellner, B.; Barbatti, M.; Lischka, H. Dynamics starting at a conical intersection: Application to the photochemistry of pyrrole. *J. Chem. Phys.* **2009,** *131*, 024312.
14. Schalk, O.; Geng, T.; Hansson, T.; Thomas, R. D. The ring-opening channel and the influence of Rydberg states on the excited state dynamics of furan and its derivatives. *J. Chem. Phys.* **2018,** *149*, 084303.
15. Adachi, S.; Schatteburg, T.; Humeniuk, A.; Mitrić, R.; Suzuki, T. Probing ultrafast dynamics during and after passing through conical intersections. *Phys. Chem. Chem. Phys.* **2019,** *21*, 13902-13905.
16. Ashfold, M. N. R.; Bain, M.; Hansen, C. S.; Ingle, R. A.; Karsili, T. N. V.; Marchetti, B.; Murdock, D. Exploring the Dynamics of the Photoinduced Ring-Opening of Heterocyclic Molecules. *J. Phys. Chem. Lett.* **2017,** *8*, 3440-3451.
17. Bil, A.; Latajka, Z.; Biczysko, M. Hydrogen detachment driven by a repulsive $^1\pi\sigma^*$ state – an electron localization function study of 3-amino-1,2,4-triazole. *Phys. Chem. Chem. Phys.* **2018,** *20*, 5210-5216.
18. Szabla, R.; Tuna, D.; Góra, R. W.; Šponer, J.; Sobolewski, A. L.; Domcke, W. Photochemistry of 2-Aminooxazole, a Hypothetical Prebiotic Precursor of RNA Nucleotides. *J. Phys. Chem. Lett.* **2013,** *4*, 2785-2788.
19. Janicki, M. J.; Szabla, R.; Šponer, J.; Góra, R. W. Electron-driven proton transfer enables nonradiative photodeactivation in microhydrated 2-aminoimidazole. *Faraday Discuss.* **2018,** *212*, 345-358.

20. Szabla, R.; Šponer, J.; Góra, R. W. Electron-Driven Proton Transfer Along H2O Wires Enables Photorelaxation of πσ* States in Chromophore–Water Clusters. *J. Phys. Chem. Lett.* **2015,** *6*, 1467-1471.
21. Szabla, R.; Šponer, J. E.; Šponer, J.; Sobolewski, A. L.; Góra, R. W. Solvent effects on the photochemistry of 4-aminoimidazole-5-carbonitrile, a prebiotically plausible precursor of purines. *Phys. Chem. Chem. Phys.* **2014,** *16*, 17617-17626.
22. Blank, D. A.; North, S. W.; Lee, Y. T. The ultraviolet photodissociation dynamics of pyrrole. *Chem. Phys.* **1994,** *187*, 35-47.
23. Geng, T.; Ehrmaier, J.; Schalk, O.; Richings, G. W.; Hansson, T.; Worth, G.; Thomas, R. D. Time-Resolved Photoelectron Spectroscopy Studies of Isoxazole and Oxazole. *J. Phys. Chem. A* **2020,** *124*, 3984-3992.
24. Todd, Z. R.; Szabla, R.; Szostak, J. W.; Sasselov, D. D. UV photostability of three 2-aminoazoles with key roles in prebiotic chemistry on the early earth. *Chem. Commun.* **2019,** *55*, 10388-10391.
25. Borisenko, V. E.; Koll, A.; Kolmakov, E. E.; Rjasnyi, A. G. Hydrogen bonds of 2-aminothiazoles in intermolecular complexes (1:1 and 1:2) with proton acceptors in solutions. *J. Mol. Struct.* **2006,** *783*, 101-115.
26. Zeng, Y.; Ren, Y. Density functional theory study of tautomerization of 2-aminothiazole in the gas phase and in solution. *Int. J. Quantum Chem* **2007,** *107*, 247-258.
27. Frisch, M. J.; Trucks, G. W.; Schlegel, H. B.; Scuseria, G. E.; Robb, M. A.; Cheeseman, J. R.; Scalmani, G.; Barone, V.; Mennucci, B.; Petersson, G. A.; Nakatsuji, H.; Caricato, M.; Li, X.; Hratchian, H. P.; Izmaylov, A. F.; Bloino, J.; Zheng, G.; Sonnenberg, J. L.; Hada, M.; Ehara, M.; Toyota, K.; Fukuda, R.; Hasegawa, J.; Ishida, M.; Nakajima, T.; Honda, Y.; Kitao, O.; Nakai, H.; Vreven, T.; Montgomery, J. A., Jr.;; Peralta, J. E.; Ogliaro, F.; Bearpark, M.; Heyd, J. J.; Brothers, E.; Kudin, K. N.; Staroverov, V. N.; Kobayashi, R.; Normand, J.; Raghavachari, K.; Rendell, A.; Burant, J. C.; Iyengar, S. S.; Tomasi, J.; Cossi, M.; Rega, N.; Millam, N. J.; Klene, M. K., J. E.;; Cross, J. B.; Bakken, V.; Adamo, C.; Jaramillo, J.; Gomperts, R.; Stratmann, R. E.; Yazyev, O.; Austin, A. J.; Cammi, R.; Pomelli, C.; Ochterski, J. W.; Martin, R. L.; Morokuma, K.; Zakrzewski, V. G.; Voth, G. A.; Salvador, P.; Dannenberg, J. J.; Dapprich, S.; Daniels, A. D.; Farkas, O.; Foresman, J. B.; Ortiz, J. V.; Cioslowski, J.; Fox, D. J. *Gaussian 09, revision D.01*, Gaussian, Inc: Wallingford, CT, 2013.
28. Kasha, M. Characterization of electronic transitions in complex molecules. *Faraday Discuss.* **1950,** *9*, 14-19.
29. Grubb, M. P.; Orr-Ewing, A. J.; Ashfold, M. N. R. KOALA: A program for the processing and decomposition of transient spectra. *Rev. Sci. Instrum.* **2014,** *85*, 064104.

**Chapter 6 - Supporting Information**

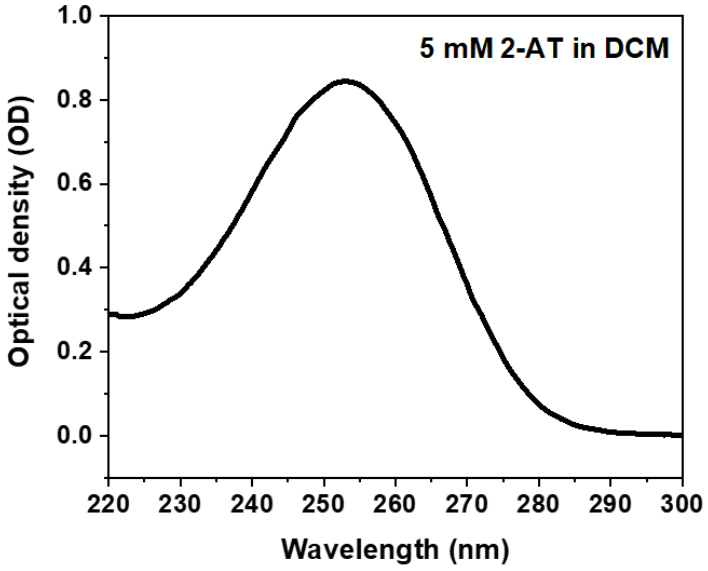


Figure S6.1 – Steady state UV-Vis absorption spectrum in the 220 – 300 nm wavelength region for 5 mM 2-AT in DCM. A pathlength of 300 μm was used, obtaining an optical density < 0.9 OD.

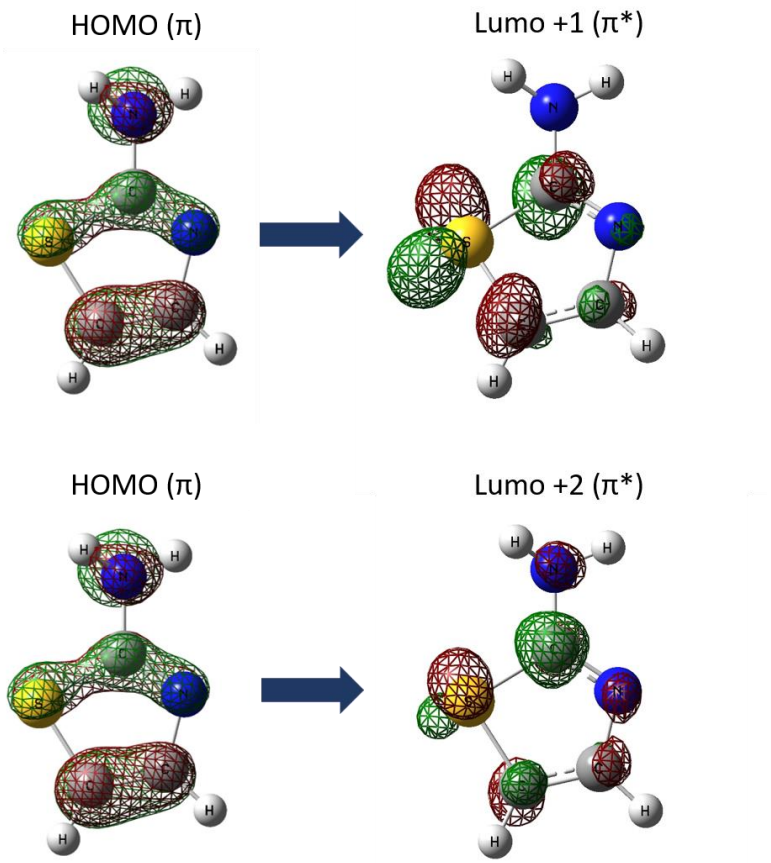


Figure S6.2 – Natural transition orbitals for the $S_2 \leftarrow S_0$ and $S_3 \leftarrow S_0$ transitions of 2-AT. The corresponding plot for the $S_1 \leftarrow S_0$ absorption, and transition probabilities are reported in Figure 6.1 in the main text.

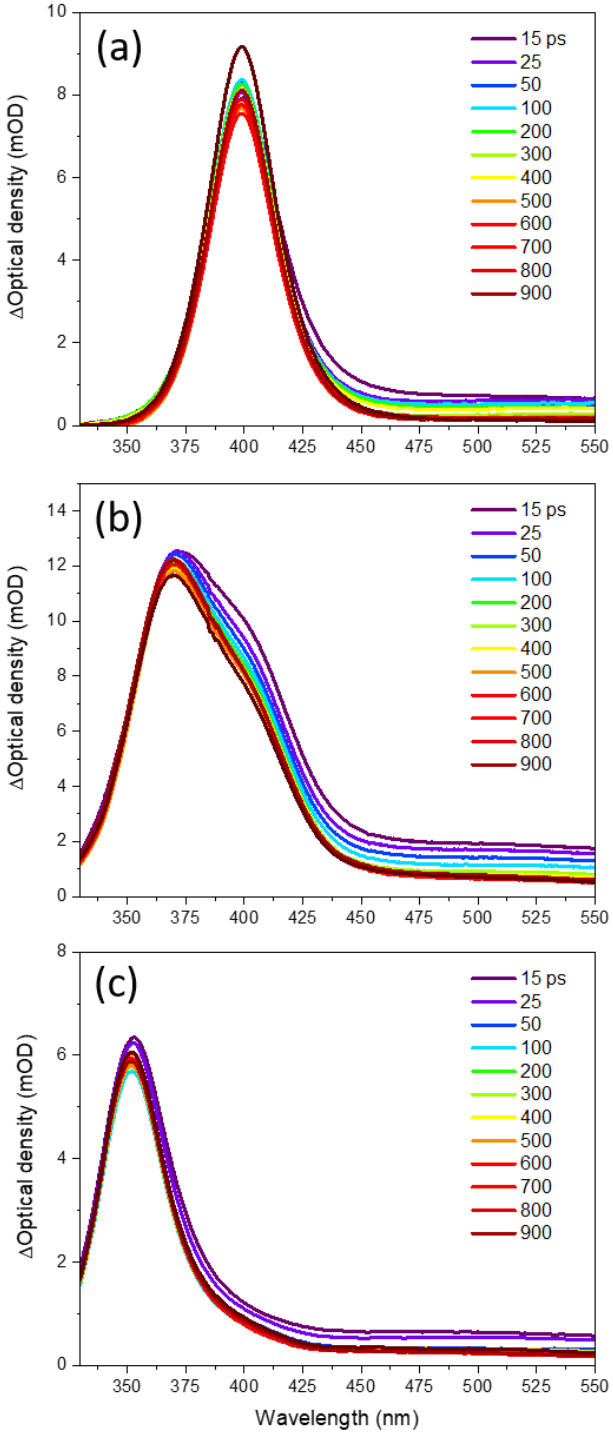


Figure S6.3 – Late time spectra in the 330 – 500 nm wavelength region for: (a) 10 mM 2-AT in cyclohexane; (b) 10 mM 2-AT in DCM; (c) 10 mM 2-AT in ACN.

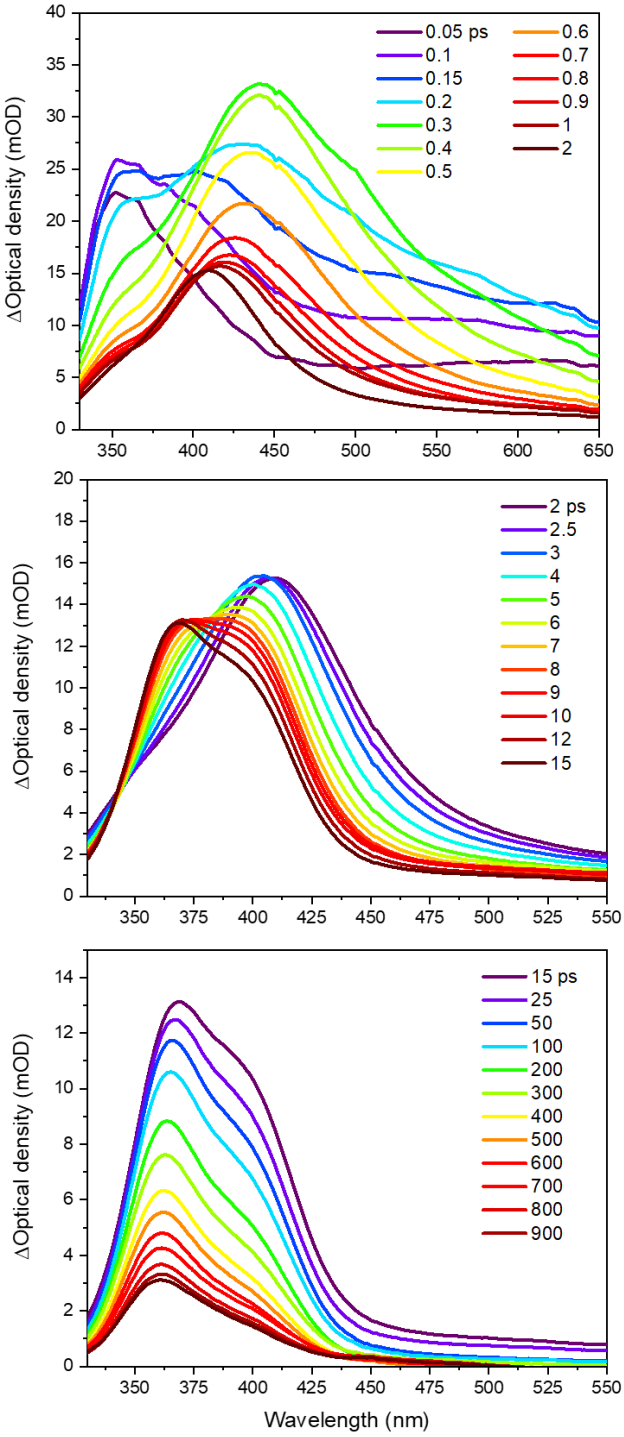


Figure S6.4 – TEAS spectra for the 255-nm photoexcitation of 120 mM 2-AT in DCM for time delays of: (a) 0.05 - 2 ps; (b) 2 - 15 ps; (c) 15 – 900 ps. Note the different wavelength scales for the two panels.

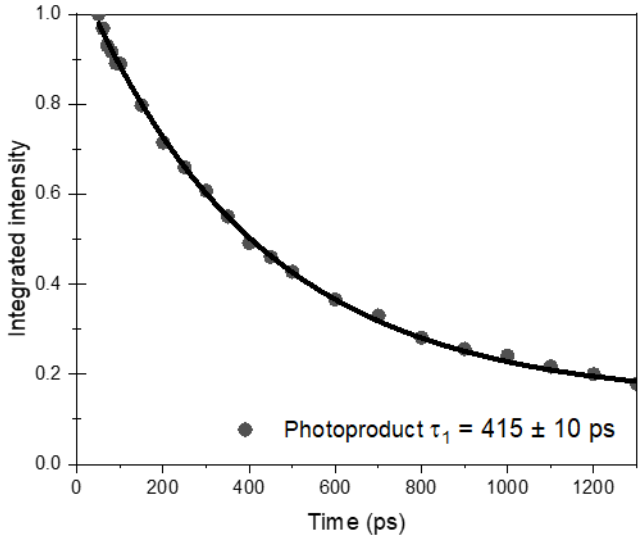


Figure S6.5 - Kinetic plot associated with the decay of the ~365 nm and ~400 nm bands for 120 mM 2-AT in DCM. The 365 nm and 400 nm bands were fit using a single basis function. Circles are experimental measurements which have been fit to an exponential function (solid line).

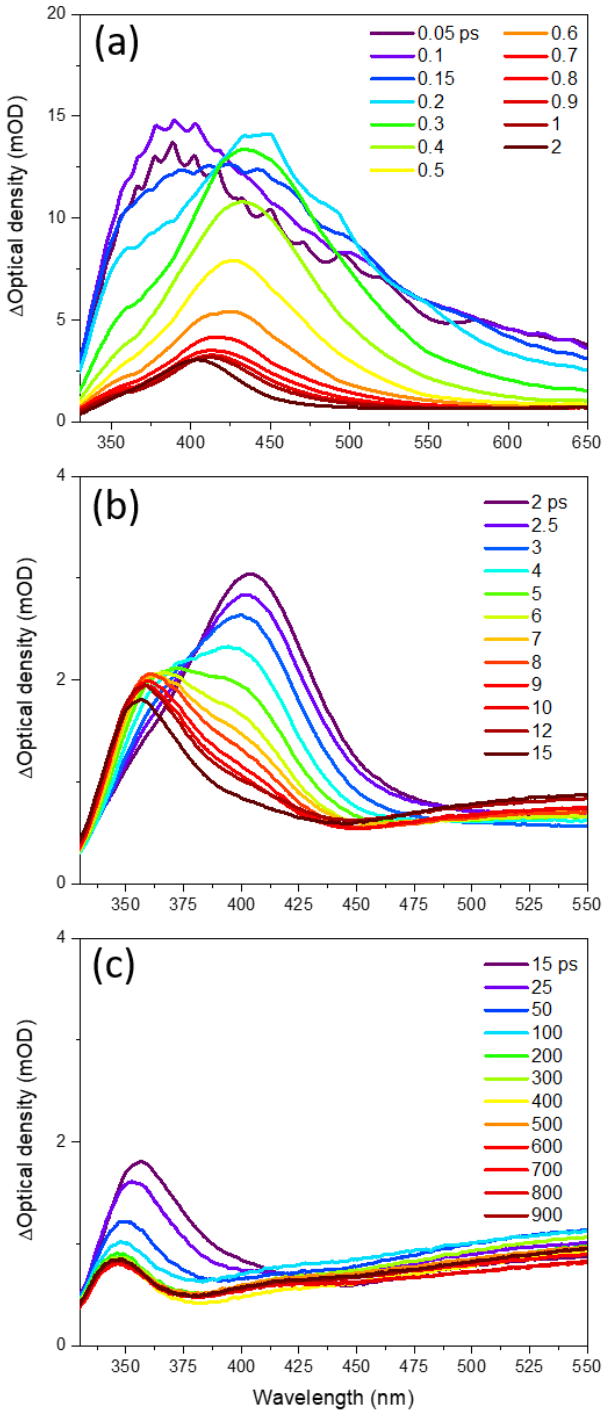


Figure S6.6 – TEAS spectra for the 255-nm photoexcitation of 10 mM 2-AT in EtOH for time delays of: (a) 0.05 - 2 ps; (b) 2 - 15 ps; (c) 15 – 900 ps. Note the different wavelength scales for the panels.

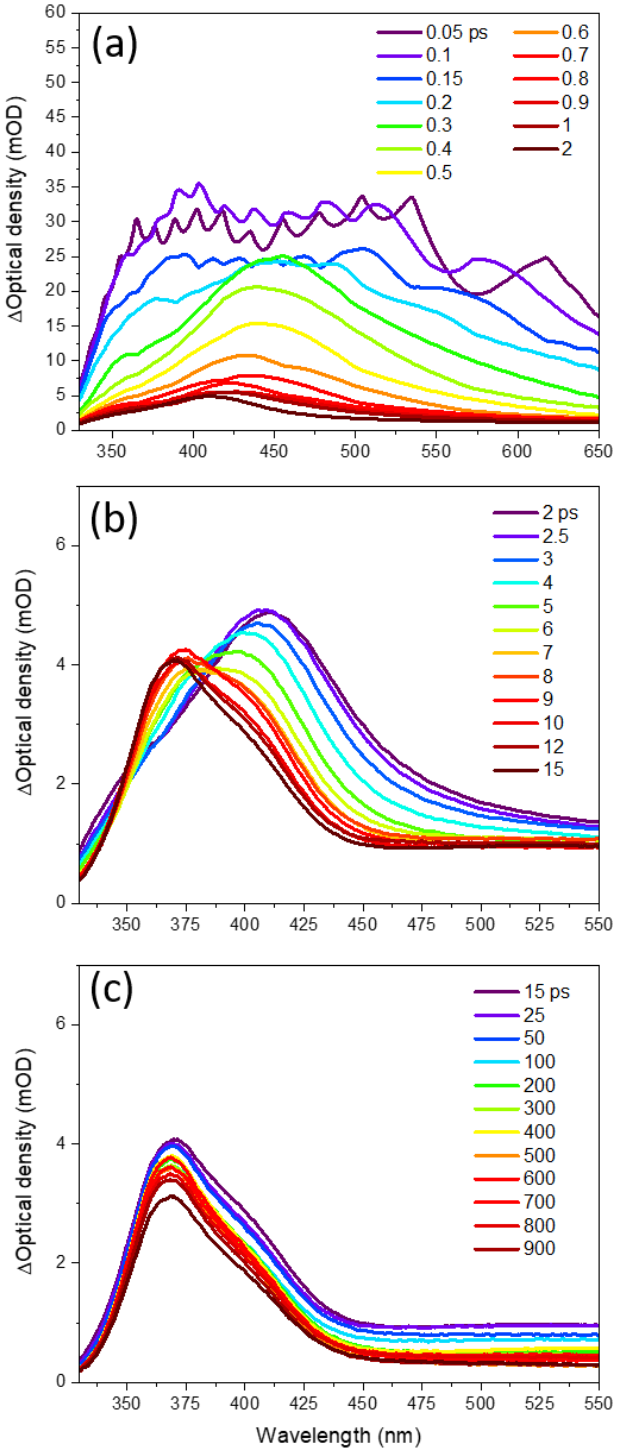


Figure S6.7 – TEAS spectra for the 255-nm photoexcitation of 10 mM 2-AT in THF for time delays of: (a) 0.05 - 2 ps; (b) 2 - 15 ps; (c) 15 – 900 ps. Note the different wavelength scales for the panels.

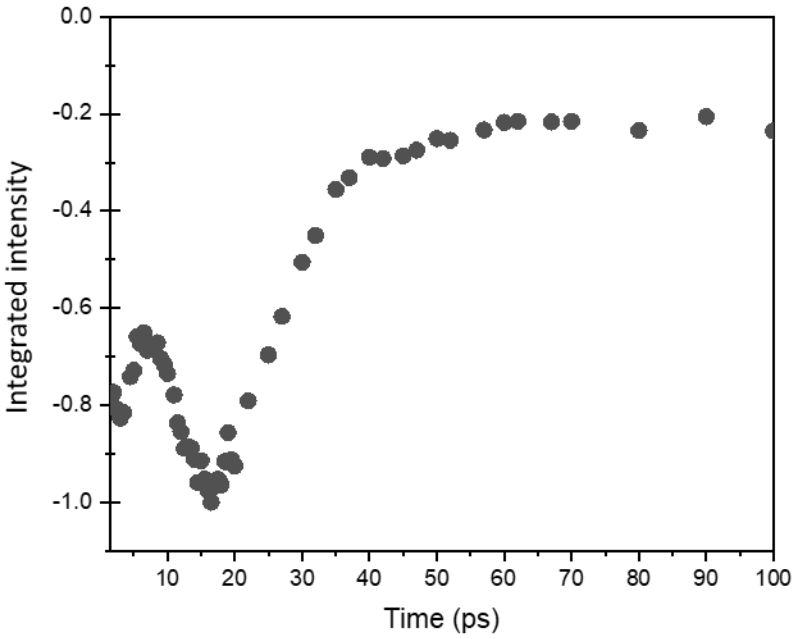


Figure S6.8 – Kinetic plot for the time evolution of the 1480 $cm^{-1}$ band in the TVAS spectra taken for 5 mM 2-AT in DCM (spectra reported in Figure 6.9 in the main text). Dots are experimental data points.

Table S6.1 – Computed and observed vibrational frequencies of 2-AT to determine scaling factors for the corresponding computed vibrational frequencies of monomer photoproducts.

| Computed frequency ($cm^{-1}$) | Observed frequency ($cm^{-1}$) | Scaling factor |
|---|---|---|
| 1627 | 1605 | 0.986 |
| 1550 | 1523 | 0.982 |
| 1489 | 1481 | 0.995 |

Table S6.2 – Computed and observed vibrational frequencies of $(2\text{-AT})_2$ to determine scaling factors for the corresponding computed vibrational frequencies of dimer photoproducts.

| Computed frequency ($cm^{-1}$) | Observed frequency ($cm^{-1}$) | Scaling factor |
|---|---|---|
| 1670 | 1625 | 0.973 |
| 1567 | 1527 | 0.974 |
| 1505 | 1495 | 0.993 |

Table S6.3 – Computed vibrational frequencies of possible photoproducts. Harmonic frequencies of monomer photoproducts were scaled according to the scaling factors reported in Table S6.1, and dimer photoproducts were scaled according to the scaling factors reported in Table S6.2. Numbers in parentheses are IR transition intensities in km $mol^{-1}$.

| Structure | Computed frequency ($cm^{-1}$) | Structure | Computed frequency ($cm^{-1}$) |
|---|---|---|---|
| **2-IT** 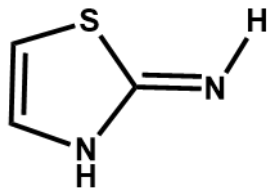 | 1638 (498)<br>1570 (7)<br>1428 (14) | **$(2\text{-IT})_2$** 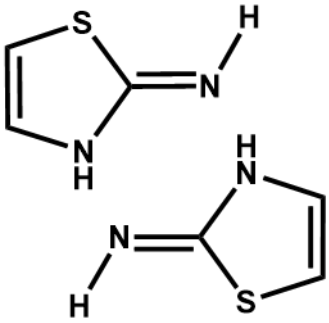 | 1633 (1049)<br>1612 (0)<br>1553 (126)<br>1551 (0)<br>1522 (0)<br>1517 (31) |
| **2-AT[-H]** 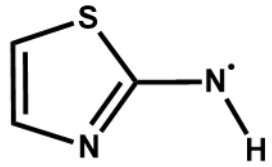 | 1606 (16)<br>1437 (5)<br>1391 (94) | **(2-AT[-H])(2-AT)** 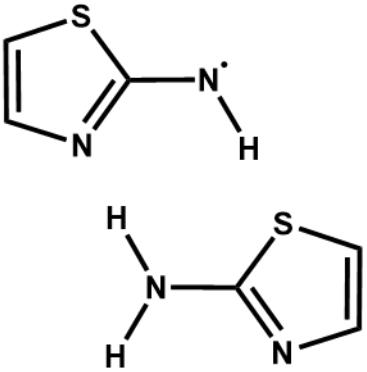 | 1621 (56)<br>1561 (2)<br>1516 (168)<br>1432 (8)<br>1395 (91)<br>1366 (91) |
| **Ring-opened biradical** 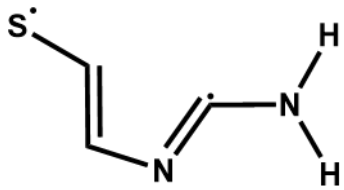 | ~2100 (209)<br>1615 (51)<br>1503 (298) | **(2-AT)(2-IT)** 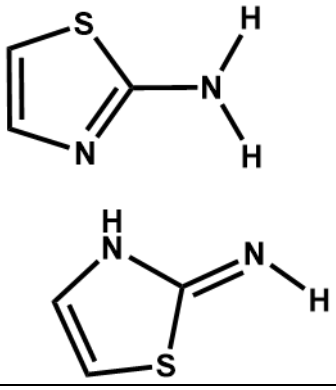 | 1641 (105)<br>1616 (489)<br>1553 (47)<br>1521 (118)<br>1510 (13)<br>1501 (31) |

# Chapter 7 – Conclusions and future work

In this thesis, the roles solvents play in the chemical dynamics of formation of reaction intermediates have been explored using ultrafast transient absorption spectroscopy (TAS). Solvent-solute interactions have been shown to compete with intramolecular rearrangements, influence reaction paths by hydrogen-bonding to reaction intermediates, and change photochemical outcomes.

In Chapter 4, the 255-nm photoexcitation of ethyl diazoacetoacetate in solution was shown to produce carbonyl carbene and ketene intermediates in <300 fs. The ketene intermediates formed vibrationally hot, as was shown by the narrowing and shifting to higher wavenumber of a mid-infrared absorption band over several picoseconds. A slower (>1 ns) pathway to ketene products was also identified from the rearrangement of ground state carbonyl carbenes in cyclohexane. In nucleophilic solvents such as acetonitrile and tetrahydrofuran, reaction of the carbene with solvent molecules to form ylides was shown to compete with ketene formation. A future extension of this work would be investigation of the effects of π-donor solvents such as benzene which have been postulated to form π-donor ylides, but evidence for their formation has been indirect,[1] or lacked the time resolution needed to observe the kinetics of carbene-solvent complexes.[2] Chapter 4 also reports a study of the mechanism for alcohol reactions with carbonyl carbenes to form ethers. Experimental and computational evidence was presented to show that the alcohol adds to the carbene in a concerted manner, forming an enol intermediate and bypassing the previously accepted ylide pathway. These results indicate a need for further study of the reactions and mechanisms of carbonyl carbenes to explore more widely how the carbonyl functional group may participate in reactions. Candidate reactions are N-H and S-H insertions which have received little attention to date.

The studies reported in Chapter 5 demonstrated that the 270-nm photoexcitation of ethyl diazoacetate readily produced carbene intermediates, and further reaction with tetrahydrofuran produced ylide intermediates in competition with C-H insertion reactions. Using transient vibrational absorption spectroscopy (TVAS), the specific solvation dynamics of the THF-derived ylide were revealed in ethanol, chloroform, dichloromethane, and cyclohexane. Characteristic carbonyl band shifts identified the formation of hydrogen bonds and reflected the change in structure of the ylide. The specific interaction of methanol with

the THF-derived ylide was further characterised using quantum chemical (MP2) calculations and DFT-based atom-centred density matrix propagation trajectories which revealed preferential interaction of methanol with the α-carbonyl group. The role of solvents in the Wittig reaction has been examined in numerous synthetic studies,[3-9] with the use of hydrogen-bonding solvents shown to lead to changes in reaction outcomes which could not be explained by a solvent's bulk properties. These changes are therefore postulated to be a result of hydrogen-bonding interactions to the phosphorus ylide intermediates.[3, 5, 9] However, direct observations of hydrogen-bonded complexes during Wittig reactions remain scarce. The work reported here proved TVAS to be a sensitive technique for detecting solvent or co-solute hydrogen-bonding to a ylide, and extension to the investigation of solvation of zwitterionic intermediates in Wittig reactions would be of significant value for future design of synthetic strategies to control reaction outcomes. The phosphorus-based ylide required for a Wittig reaction could be synthesised by photoexciting ethyl diazoacetate in the presence of a substituted phosphine ($PR_3$).

Recently, it has become possible to measure chemical dynamics over femtosecond to microsecond time-durations in a single experiment.[10] The Wittig reaction would be an excellent candidate for these experiments because numerous reaction steps and intermediates could be directly observed by TAS, and the influence of solvation on each reaction-step outcome could be investigated. Lithium salts can also alter the outcomes of reactions which involve the formation of zwitterionic intermediates, and are postulated to stabilise the negative charge on the intermediate.[6, 11-12] An interesting extension of the reported studies would be to investigate how ionic salts, or indeed ionic liquid solvents, affect the dynamics of hydrogen-bonded solvent-solute complexes formed during organic reactions. The use of ionic liquids in Wittig reactions has already been tested extensively in synthetic experiements,[13-16] but in-depth mechanistic understanding is still lacking. Stabilisation by coordination to different charged sites of the ylide could offer a facile route to tune product outcomes.

In Chapter 6, study of the photochemistry of 2-Aminothiazole (2-AT) in various solvents was reported. The results identified that UV excitation of 2-AT at 255 nm induced competing N-H bond fission and ring-opening pathways, and the choice of solvent changed the preferred outcome. The reason for this solvent-controlled photochemical selectivity was

traced to different $S_1$-state energy barriers to access the dissociative $\pi\sigma^*$ electronic state responsible for N-H bond scission in polar and non-polar solvents. The 255-nm photoexcitation of the $(2\text{-AT})_2$ dimer was also explored, and a photoproduct band unique to the dimer was identified and tentatively assigned. The computational results presented in this chapter provided preliminary insights into the effects of solvation on the 2-AT photochemistry, but higher-level calculations and wavepacket dynamical simulations are now required to confirm precisely how different solvents affect the photochemistry of 2-Aminothiazole.

Although choice of solvent is known to affect product outcomes of many synthetic reactions, for example influencing reaction rates, product yields and stereochemistry, the fundamental mechanistic reasons are often not well understood. By observing transient solvent interactions with reactive intermediates, and changes to mechanistic steps using ultrafast spectroscopy methods, the work presented in this thesis contributes to improving this understanding. It demonstrates that TAS can address complex mechanistic questions, and therefore has great potential for informing the design of new synthetic strategies.

**References**


1. Wang, J.; Kubicki, J.; Peng, H.; Platz, M. S. Influence of Solvent on Carbene Intersystem Crossing Rates. *J. Am. Chem. Soc.* **2008,** *130*, 6604-6609.
2. Moss, R. A.; Wang, L.; Weintraub, E.; Krogh-Jespersen, K. The Solvation of Carbenes: π and O-Ylidic Complexes of p-Nitrophenylchlorocarbene. *J. Phys. Chem. A* **2008,** *112*, 4651-4659.
3. Robiette, R.; Richardson, J.; Aggarwal, V. K.; Harvey, J. N. On the Origin of High E Selectivity in the Wittig Reaction of Stabilized Ylides: Importance of Dipole−Dipole Interactions. *J. Am. Chem. Soc.* **2005,** *127*, 13468-13469.
4. Pandolfi, E. M.; López, G. V.; Días, E.; Seoane, G. A. Solvent Effect in the Wittig Reaction Under Boden's Conditions. *Synth. Commun.* **2003,** *33*, 2187-2196.
5. Aksnes, G.; Berg, T. J.; Gramstad, T. Temperature and solvent effects in Wittig reactions. *Phosphorus. Sulfur. Silicon. Rel. Elem.* **1995,** *106*, 79-84.
6. Hwang, J.-J.; Lin, R.-L.; Shieh, R.-L.; Jwo, J.-J. Study of the Wittig reaction of benzyltriphenylphosphonium salt and benzaldehyde via ylide-mediated phase-transfer catalysis: Substituent and solvent effects. *J. Mol. Catal. A: Chem.* **1999,** *142*, 125-139.
7. Wu, J.; Zhang, D.; Wei, S. Wittig Reactions of Stabilized Phosphorus Ylides with Aldehydes in Water. *Synth. Commun.* **2005,** *35*, 1213-1222.
8. El-Batta, A.; Jiang, C.; Zhao, W.; Anness, R.; Cooksy, A. L.; Bergdahl, M. Wittig Reactions in Water Media Employing Stabilized Ylides with Aldehydes. Synthesis of α,β-Unsaturated Esters from Mixing Aldehydes, α-Bromoesters, and $Ph_3P$ in Aqueous $NaHCO_3$. *J. Org. Chem.* **2007,** *72*, 5244-5259.
9. Westman, G.; Wennerström, O.; Raston, I. On the effect of cyclodextrin on the Z/E-selectivity of Wittig Reactions with semistabilized ylides. *Tetrahedron* **1993,** *49*, 483-488.
10. Koyama, D.; Donaldson, P. M.; Orr-Ewing, A. J. Femtosecond to microsecond observation of the photochemical reaction of 1,2-di(quinolin-2-yl)disulfide with methyl methacrylate. *Phys. Chem. Chem. Phys* **2017,** *19*, 12981-12991.

11. Hooper, D. L.; Garagan, S.; Kayser, M. M. Lithium Cation-Catalyzed Wittig Reactions. *J. Org. Chem.* **1994,** *59*, 1126-1128.
12. Uchiyama, Y.; Ohtsuki, T.; Murakami, R.; Shibata, M.; Sugimoto, J. (E)-Selective Wittig Reactions between a Nonstabilized Phosphonium Ylide Bearing a Phosphastibatriptycene Skeleton and Benzaldehydes. *Eur. J. Org. Chem.* **2017,** *2017*, 159-174.
13. Firaha, D. S.; Gibalova, A. V.; Hollóczki, O. Basic Phosphonium Ionic Liquids as Wittig Reagents. *ACS Omega* **2017,** *2*, 2901-2911.
14. Le Boulaire, V.; Grée, R. Wittig reactions in the ionic solvent [bmim][BF4]. *Chem. Commun.* **2000**, 2195-2196.
15. Fresneda, P. M.; Blázquez, J. A. Synthesis of β-carbolines using microwave-assisted aza-Wittig methodology in ionic liquids. *Tetrahedron Lett.* **2012,** *53*, 2618-2621.
16. Valizadeh, H.; Vaghefi, S. One-Pot Wittig and Knoevenagel Reactions in Ionic Liquid as Convenient Methods for the Synthesis of Coumarin Derivatives. *Synth. Commun.* **2009,** *39*, 1666-1678.